University of Reading

Self-Assembly and Bioactivity of Peptides for Therapeutic Applications

A Thesis submitted for the degree of Doctor of Philosophy

Department of Chemistry

Charlotte Jennifer Chante Edwards-Gayle

November 2019

Declaration

I can confirm that this is my own work and the use of material from other sources has been properly and fully acknowledged

[redacted]

Charlotte Jennifer Chante Edwards-Gayle

Acknowledgements

I would sincerely like to thank my supervisor Professor Ian Hamley for giving me the opportunity to undertake this PhD. I will always be grateful for him taking a chance on me, coming into this studentship without a Masters I felt underprepared. His mentorship, expertise, knowledge and guidance have driven me to become a better researcher. I am thankful he allowed me to participate on a broad range of projects, which has made the whole experience both challenging and stimulating. I would also like to thank Dr Robert Rambo, for his support through my PhD, allowing me to spend time learning more about synchrotrons, and supporting me to share my work at SAS2018, which was an amazing experience, my first time ever outside of Europe.

I would like to give a big thankyou to Dr Valeria Castelletto, for her mentorship and comradeship in the lab. She was very kind to me throughout, and I always enjoyed our beamtimes together (minus SOLEIL!). I would like to thank Dr Fran Greco for her training in tissue culture and making me feel like part of the Greco group. I would like to also thank Dr Glyn Barrett, for his training in bacterial assays, guidance, and great cups of tea. I'd like to thank the Diamond guys, Nikul, Nathan and Katsuaki for making my times at Diamond entertaining. Thank you to other collaborators, Dr Janne Ruokolainen, Dr Jani Seitsonen and Dr Mehdi Reza, for Cryo-TEM images. Dr Nicholas Spencer for XRD measurements. Nicholas Michael for mass spec. Amanpreet Kaar and Dr Peter Harris for training on SEM and TEM.

Next, I'd like to thank all my friends at Reading who have made this PhD. I'd like to thank Jessica Hutchinson, for all the trips and funny times we had together. Some of my best PhD memories are with you, and I know we will be lifelong friends. I'd like to thank Marleen Wilde, for her friendship, support and for genuinely helping me to get out of the office/lab. I'd like to thank Az and Irene, for their company in tissue culture. I'd also like to thank Aina, Adam, Alex, Evita, Jasraj, Lewis, Sam and Zoe for your friendship and entertainment. In particular, a big thank you to the little office, Jessi, Sara, Jully and Nada, thanks for the jokes and support.

Finally, I'd like to thank my family. My grandparents, for their support, love and inspiring me to be the best I can be (and giving me a home for a while!). My mum, the best mother anyone could ask for. Thank you for raising me, teaching me to be strong, and making our home feel complete. Lastly, my partner Fraser, for, his love, encouragement and support. Thank you for keeping my feet on the ground.

Abstract

Peptides are an attractive platform to make new and novel constructs for therapeutic applications due to their biocompatibility, biodegradability and biofunctionality. Peptides that self-assemble may have enhanced *in vivo* stability and may be able to self-deliver. Furthermore, peptides can be modified to enhance their *in vivo* stability through lipidation, PEGylation and other modifications. This thesis aims to explore the self-assembly and bioactivity of small oligopeptides, telechelic tyrosine functionalised PEGylated peptides and peptide hormones with potential therapeutic applications.

With the rise in cases of antimicrobial resistance, there is a great amount of interest in the development of alternate medicines to combat these issues. Short cationic peptides are beginning to show great potential in this area, due to their 'multi-hit' strategy and relatively cheap cost of synthesis. The self-assembly and lipid interactions of a group of surfactant-like peptides (SLPs) and peptide bola-amphiphiles containing arginine and alanine are examined. It is apparent that the size of the hydrophobic block causes increased aggregation propensity and increased structural ordering. The cytocompatibility of the SLPs and bola-amphiphiles is measured, revealing that cytotoxicity is not linked to molecular weight. The SLPs are more cytocompatibile than the bola-amphiphiles. These peptides show activity at cytocompatibile concentrations against *P.aeruginosa*, a bacterial species on the World Health Organisations list of species that require new treatments.

Further to this, the self-assembly and bioactivity of two short symmetrical AMPs, consisting of arginine and phenylalanine was examined. These peptides were found to have weak self-assembly behaviour, but strong interactions with many different *Pseudomonas* bacteria, with particularly strong interactions with *P.aeruginosa*. The peptides alter the structure of liposomes based on the composition of the *P.aeruginosa* membrane, with the most active peptide, R_4F_4, completely disrupting vesicle formation. The peptide R_4F_4 disrupts biofilm formation and interacts with cyclic diguanylate (c-di-GMP), a regulator of biofilm formation and dispersion in the species.

Materials functionalised with tyrosine may be of interest for enzyme responsive materials. The self-assembly of tyrosine functionalised telechelic PEO-star conjugates at native pH and pH 12 was examined These conjugates were found to self-assemble into a mixture of spherical globules and fibres. The self-assembly of the lower molecular weight conjugate was disrupted by pH adjustment. The larger conjugate formed mixed long straight fibres and smaller globules when adjusted to pH 12. These conjugates did not form hydrogels and were proved to be cytocompatible at sufficiently high concentration. Self-assembled hormones may have prolonged half-lives and increased stability *in vivo*. Peptide hormone oxytocin has found to be heat unstable, affecting its performance in developing nations. Probing conditions for self-assembly may improve the stability. Thus, the assembly of the peptide hormone oxytocin and analogues was examined. The self-assembly of oxytocin was inconclusive when examined by biophysical techniques. Analogue carbetocin was found to not aggregate at native pH. Oxytocin was found to form a self-standing β-sheet gel at 2 wt% and pH 12, whereas carbetocin appeared slightly crystalline under these conditions. A lipidated variant of oxytocin was found to be insoluble and to assemble into irregular aggregates in ethanol. Overall, this thesis examines through biophysical techniques and bioassays, different peptides with a range of potential therapeutic applications, contributing to the understanding of short antimicrobial peptides.

Contents

Chapter 2:Self-assembly and bioactivity of peptide bola-amphiphiles and surfactant-like peptides containing Alanine and Arginine……………………………………………66

Chapter 4: Self-assembly of Telechelic Tyrosine End-Capped PEO Star polymers in Aqueous Solution……………………………………………………………………...149

List of Figures

List of Tables

List of Abbreviations

PA	Peptide Amphiphile
SLP	Surfactant-like peptide
CAC	Critical aggregation concentration
CD	Circular Dichroism
UV	Ultra-violet
FTIR	Fourier Transform Infrared Spectroscopy
XRD	X-ray fibre diffraction
DSC	Differential scanning calorimetry
EM	Electron Microscopy
TEM	Transition Electron Microscopy
SEM	Scanning Electron Microscopy
SAXS	Small-angle X-ray scattering
AMP	Antimicrobial Peptide

List of Publications

Charlotte Edwards-Gayle, Valeria Castelletto, Ian W. Hamley, Glyn Barrett, Francesca Greco, Daniel Hermida Merino, Robert P. Rambo, Jani Seitsonen, Janne Ruokolainen. "Selective Antibacterial Activity and Lipid Membrane Interactions of Arginine-Rich Amphiphilic Peptidess" *ACS Appl. Bio Mater.* 2020, 3(2) 1165-1175 *For writing the paper, and all assays included in the paper, apart from the synthesis of the peptide.*

Charlotte Edwards-Gayle, Valeria Castelletto, Ian W. Hamley, Glyn Barrett, Francesca Greco, Daniel Hermida Merino, Robert P. Rambo, Jani Seitsonen, Janne Ruokolainen. "Self-Assembly, Antimicrobial Activity, and Membrane Interactions of Arginine-Capped Peptide Bola-Amphiphiles" *ACS Appl. Bio Mater.* 2019, 25, 2208-2218 *- For writing the paper, all assays included in the paper, apart from the synthesis of the peptide.*

Charlotte J. C. Edwards-Gayle, Francesca Greco, Ian W. Hamley, Robert P. Rambo, Mehedi Reza, Janne Ruokolainen, Dimitrios Skoulas, Hermis Iatrou. "Self-Assembly of Telechelic Tyrosine End-Capped PEO Star Polymers in Aqueous Solution" *Biomacromolecules.* 2018, 19(1), 167-177 *For writing the paper, all assays included in the paper, apart from the synthesis of the peptide,.*

Charlotte J. C. Edwards-Gayle and Ian W. Hamley. "Self-assembly of bioactive peptides, peptide conjugates, and peptide mimetic materials" *Org. Biomol. Chem.*, 2017,15, 5867-5876 *Review article*

Valeria Castelletto, Charlotte J C Edwards-Gayle, Francesca Greco, Ian W Hamley, Jani Seitsonen, Janne Ruokolainen "Self-Assembly, Tunable Hydrogel Properties and Selective Anti- Cancer Activity of a Carnosine-Derived Lipidated Peptide" *ACS Appl. Mater. Interfaces. 2019* 11(37) 33573-33580 *For cell viability measured for different cancer strains with peptide solutions and hydrogels, gel drug uptake and leakage assays, critical aggregation concentration measurements, and writing these sections.*

Valeria Castelletto, Charlotte Edwards-Gayle, Ian W. Hamley , Juliane Pelin, Wendel A. Alves, Andrea M. Aguilar, Jani Seitsonen, Janne Ruokolainen. "Self-Assembly of a Catalytically Active Lipopeptide and Its Incorporation into Cubosomes" *ACS Appl. Bio Mater.* 2019, 2(8) 3639-3647 *For cell viability assays, and contribution to SAXS data collection.*

Valeria Castelletto, Charlotte J. C. Edwards-Gayle, Ian W. Hamley**,** Glyn Barrett, Jani Seitsonen, Janne Ruokolainen "Peptide-Stabilized Emulsions and Gels from an Arginine-Rich Surfactant-like Peptide with Antimicrobial Activity" *ACS Appl. Mater. Interfaces.* 2019,11(10), 9893-9903 *For cell viability assays, antimicrobial screening and contribution to SAXS data collection.*

Manuel Hartweg, Charlotte J. C. Edwards-Gayle, Elham Radvar, Dominic Collis, Mehedi Reza, Michael Kaupp, Jan Steinkoenig, Janne Ruokolainen, Robert Rambo, Christopher Barner-Kowollik, Ian W. Hamley, Helena S. Azevedo and C. Remzi Becer "Ugi multicomponent reaction to prepare peptide–peptoid hybrid structures with diverse chemical functionalities" *Polym. Chem.* 2018, **9**, 482-489 *For physical characterisation (circular dichroism, SAXS with form-factor fitting, and TEM) of the petide-peptoid molecules.*

Jessica A. Hutchinson, Ian W. Hamley, Charlotte J. C. Edwards-Gayle, Valeria Castelletto, Cristian Piras, Rainer Cramer, Radoslaw Kowalczyk, Jani Seitsonen, Janne Ruokolainen and Robert P. Rambo "Melanin production by tyrosinase activity on a tyrosine-rich peptide fragment and pH-dependent self-assembly of its lipidated analogue" *Org. Biomol. Chem.* 2019, 17, 4543-4553 *For cell culture measurements, and contribution to SAXS data collection.*

Valeria Castelletto, Ruth Barnes, Kimon andreas Karatzas, Charlotte Edwards-Gayle, Francesca Greco, Ian W Hamley, Robert Rambo, Jani Seitsonen, Janne Ruokolainen. "Restructuring of Lipid Membranes by an Arginine-Capped Peptide Bola-amphiphile" *Langmuir*. 2019, 35(5),1302-1311 *For cell viability measurements, and contribution to SAXS data collection.*

Mohammad Aref Khalily, Hakan Usta, Mehmet Ozdemir, Gokhan Bakan, F. Begum Dikecoglu, Charlotte Edwards-Gayle, Jessica A. Hutchinson, Ian W. Hamley, Aykutlu Dana and Mustafa O. Guler "The design and fabrication of supramolecular semiconductor nanowires formed by benzothienobenzothiophene (BTBT)-conjugated peptides" *Nanoscale*, 2018,10, 9987-9995 *For SAXS sample preparation and measurement, and primary data analysis (subtraction).*

Valeria Castelletto, Ruth Barnes, Kimon andreas Karatzas, Charlotte Edwards-Gayle, Francesca Greco, Ian W Hamley, Robert Rambo, Jani Seitsonen, Janne Ruokolainen. "Arginine-Containing Surfactant-Like Peptides: Interaction with Lipid Membranes and Antimicrobial Activity" *Biomacromolecules*. 2018, 19(7), 2782-2794. *For cell viability measurements, and contribution to SAXS data collection.*

Elif Arslan, Meryem Hatip, Ozge Uysal, Dikecoglu, Ahmet Emin Topal, Ruslan Garifullin, Alper Devrim Ozkan, Aykutlu Dâna, Daniel Hermida Merino, Valeria Castelletto, Charlotte Edwards-Gayle, Sefer Baday, Ayse Begum Tekinay, Mustafa O. Guler. "Supramolecular Peptide Nanofiber Morphology Affects Mechanotransduction of Stem Cells" *Biomacromolecules.* 2017, 18(10), 3114-3130. *For SAXS sample preparation and measurement, and primary data analysis (subtraction)*

Chapter 1

Introduction

This chapter has been in-part published in the review article titled "Self-assembly of bioactive peptides, peptide conjugates, and peptide mimetic materials" C.J.C.Edwards-Gayle and I.W.Hamley, 2017, Org. Biomol. Chem., 2017,15, 5867-5876

1.1 Peptides

Peptides are small oligomeric molecules consisting of amino acids. In nature, there are 20 amino acids (Figure 1.1),[1–3] encoded in the genetic code of eukaryotes and prokaryotic organisms. In addition to this, there are thousands more amino acids which are created through post-translational modifications and synthetically. Each amino acid consists of a α-carbon, amino group, carboxyl group, hydrogen, and variable group R, which dictates the properties of the amino acid. The exceptions to this are glycine (for which the R group is hydrogen, making it non-chiral), and proline, which is an imino acid.

Peptide bonds are formed through a condensation reaction between an amine and a carboxyl group. For example, two amino acids may react together in this way to form a dipeptide (Figure 1.2).[4] Peptide bonds are sterically hindered, due to electron delocalisation. This results in cis-trans isomerisation and resonance. When multiple amino acids react in this way, polypeptides and proteins may be formed. It is commonly stated that a peptide is below 50 amino acids in length and a protein above, although there are some exceptions to this rule.[5]

Peptides and proteins may form higher order structures. Primary structure describes the linear amino acid sequence. Secondary structure defines formation of more ordered structures for example α-helices and β-sheets (Figure 1.4), which are held together through hydrogen bonding. This is largely dictated by which amino acids are present in the sequence, as different amino acids have greater tendencies to form different conformations (Figure 1.3).[6] This can enable a degree of intelligent design, where amino acid residues can be selected in order to try to generate specific secondary structure, for example, selecting amino acids with high β-sheet propensity, with the aim to form β-sheet fibrils. Amino acids are also optically active, giving 'handedness' to structures (Figure 1.2). Natural amino acids synthesised on the ribosome are L-isomers which, in turn, makes right-handed α-helices the energetically favoured conformation.[2] D-amino acids occur synthetically, occasionally post translationally or in some bacteria. D-amino acids would form left-handed α-helices. When these structures fold further, they are described as tertiary and when multiple domains of folded polypeptides come together, quaternary structures are formed. Although folding is not a fully understood phenomenon, it is thought to be mainly driven by the hydrophobic effect, with contribution also from attractive forces: hydrogen bonds, electrostatic interactions, Van der Waals forces as well as covalent disulphide cross bridges formed by cysteine residues.

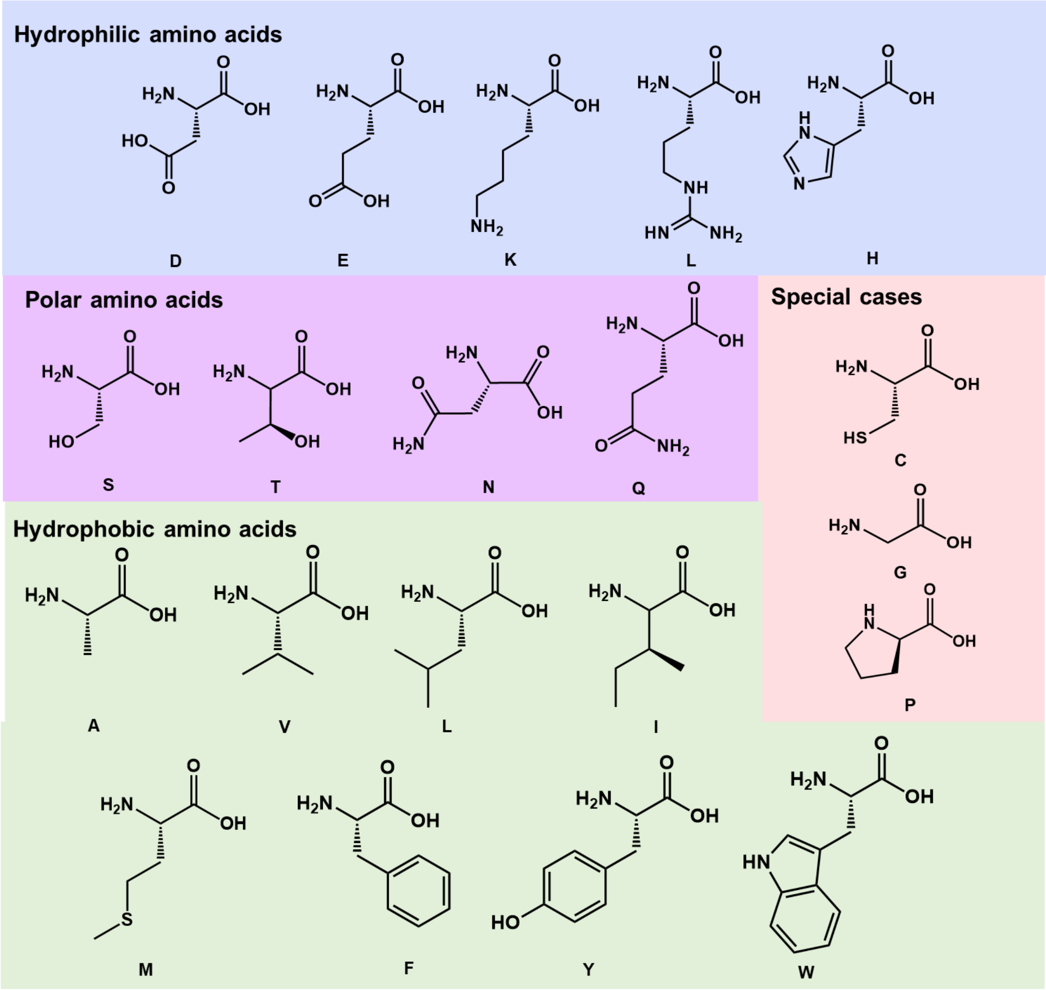

D	*Asp*	*Aspartic acid*	***Q***	*Gln*	*Glutamine*	***M***	*Met*	*Methionine*
E	*Glu*	*Glutamic acid*	***C***	*Cys*	*Cysteine*	***F***	*Phe*	*Phenylalanine*
K	*Lys*	*Lysine*	***G***	*Gly*	*Glycine*	***Y***	*Tyr*	*Tyrosine*
R	*Arg*	*Arginine*	***P***	*Pro*	*Proline*	***W***	*Trp*	*Tryptophan*
H	*His*	*Histidine*	***A***	*Ala*	*Alanine*			
S	*Ser*	*Serine*	***V***	*Val*	*Valine*			
T	*Thr*	*Threonine*	***L***	*Leu*	*Leucine*			
N	*Asp*	*Asparagine*	***I***	*Ile*	*Isoleucine*			

Figure 1.1. *Amino acids classified based on their solubility.*

Peptides are an attractive platform due to their chemical diversity, biocompatibility, resemblance with proteins, feasibility to synthesise in large quantities and their use as building blocks for creating large assembled structures. [7]

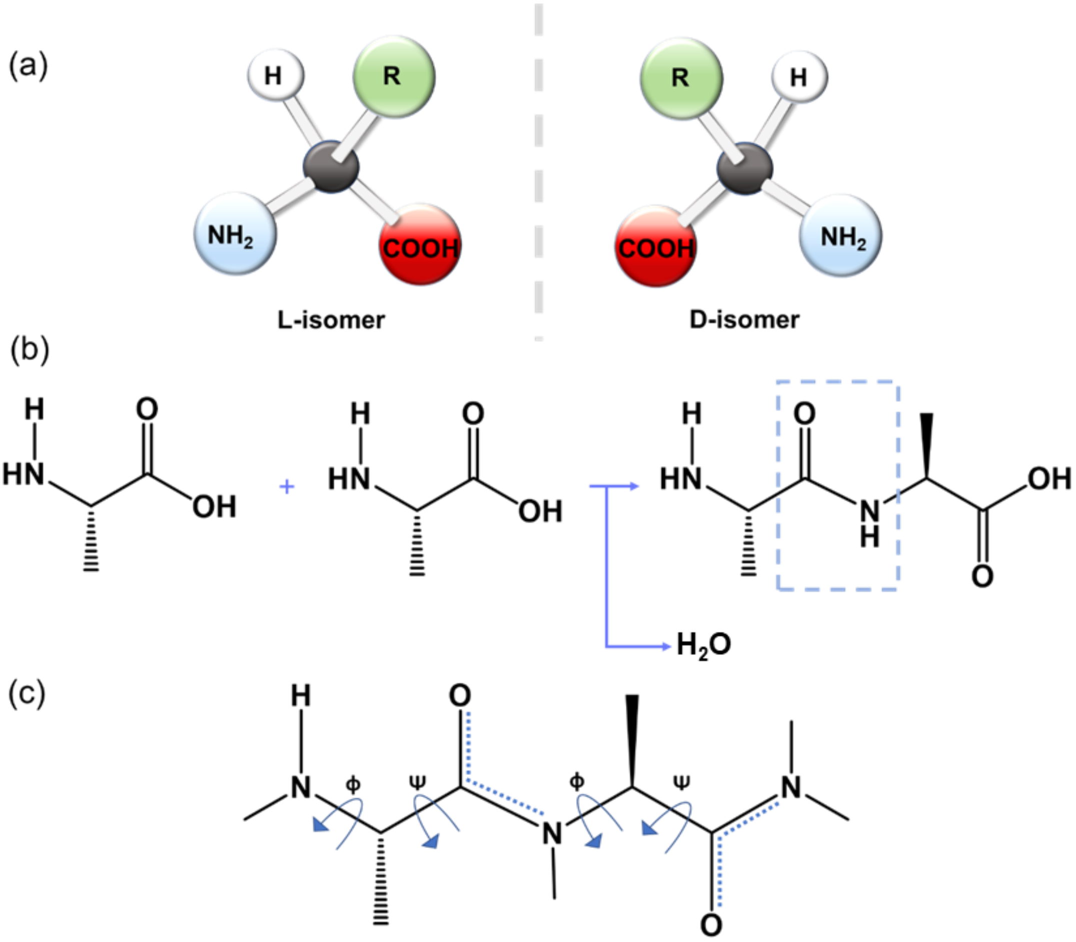

Figure 1.2. *a) Stereoisomers of amino acids, b) the formation of the peptide bond and c) structure of the peptide showing flexible bonds phi and psi, and sterically hindered amide/peptide bond, due to resonance.*

1.2 Peptide Self-assembly

Self-assembly is defined as the ability of a molecule, without the guidance of external factors, to associate through non-covalent interactions to form highly ordered 3-dimensional structures. [8–12] This occurs through a bottom-up approach. Most self-assembling molecules are amphiphilic, having both hydrophobic and hydrophilic components,[9] although there are some exceptions to this.[13,14] Lipids are perhaps the simplest molecule displaying amphiphilicity, with a hydrophilic head group, and a hydrophobic tail group. These molecules self-assemble with the degree of saturation in the lipid chain, among other variables, dictating the packing of the molecules.

Peptides and proteins are more complex in their amphiphilicity. This is largely due to folding, giving rise to ‘faces’, each of which are exposed to different environments. For example a β-sheet peptide may contain alternating hydrophilic and hydrophobic residues, resulting in the side chains being exposed on opposite sides of the sheet.[15]

Self-assembly is commonly found in nature. A natural example of a self-assembled structure is the phospholipid bilayer, which is the basis of cell membranes, vesicles and organelle membranes in cells and bacteria.[16] Another example is microtubules, which are cytoskeletal components of eukaryotic and some prokaryotic cells. Microtubules have many functions in eukaryotic cells, including cargo transport of vesicles, and are a main component of the mitotic spindle in cell division which contracts to pull apart chromosomes and assist in maintain cell shape. Additionally in prokaryotes, they make up the internal structure of cilia and flagella in bacteria enabling movement.[17,18] Other examples include protein folding in enzymes, other protein molecular machine assemblies, DNA double helix formation and the formation of the virus protein capsid around a nucleic acid core.[19]

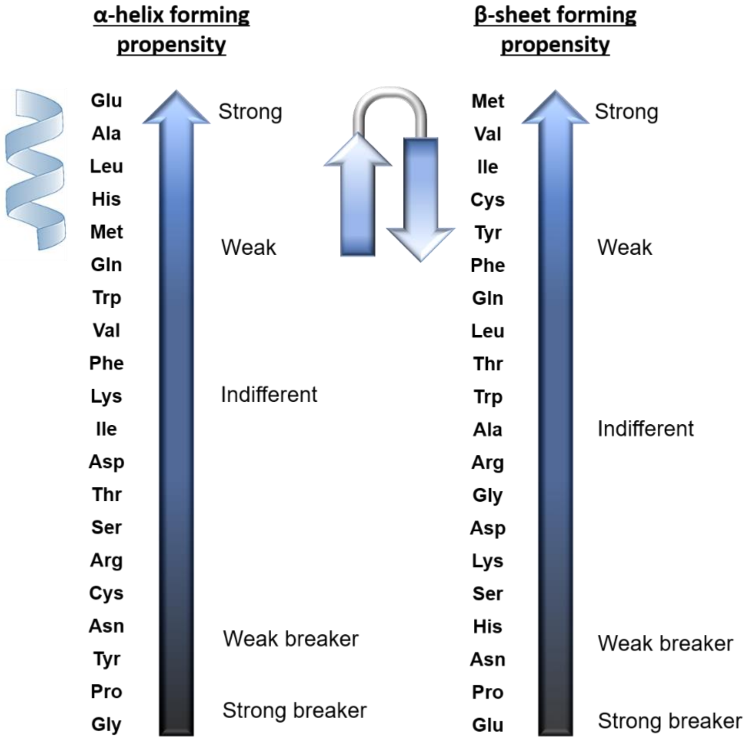

Figure 1.3. *Amino acid structure forming propensities calculated experimentally.*[20]

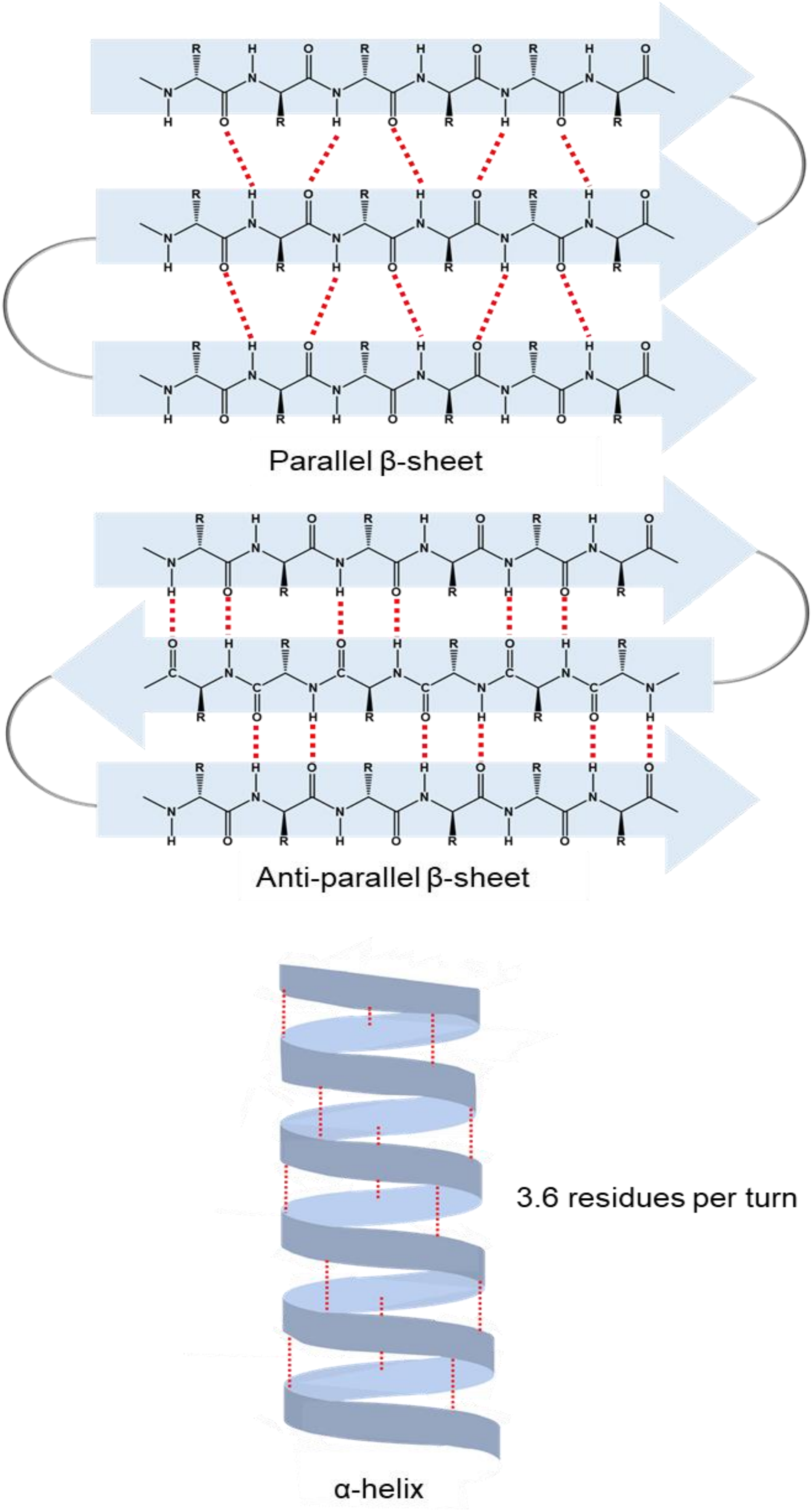

Figure 1.4. *Common secondary structures formed by peptides and proteins.*

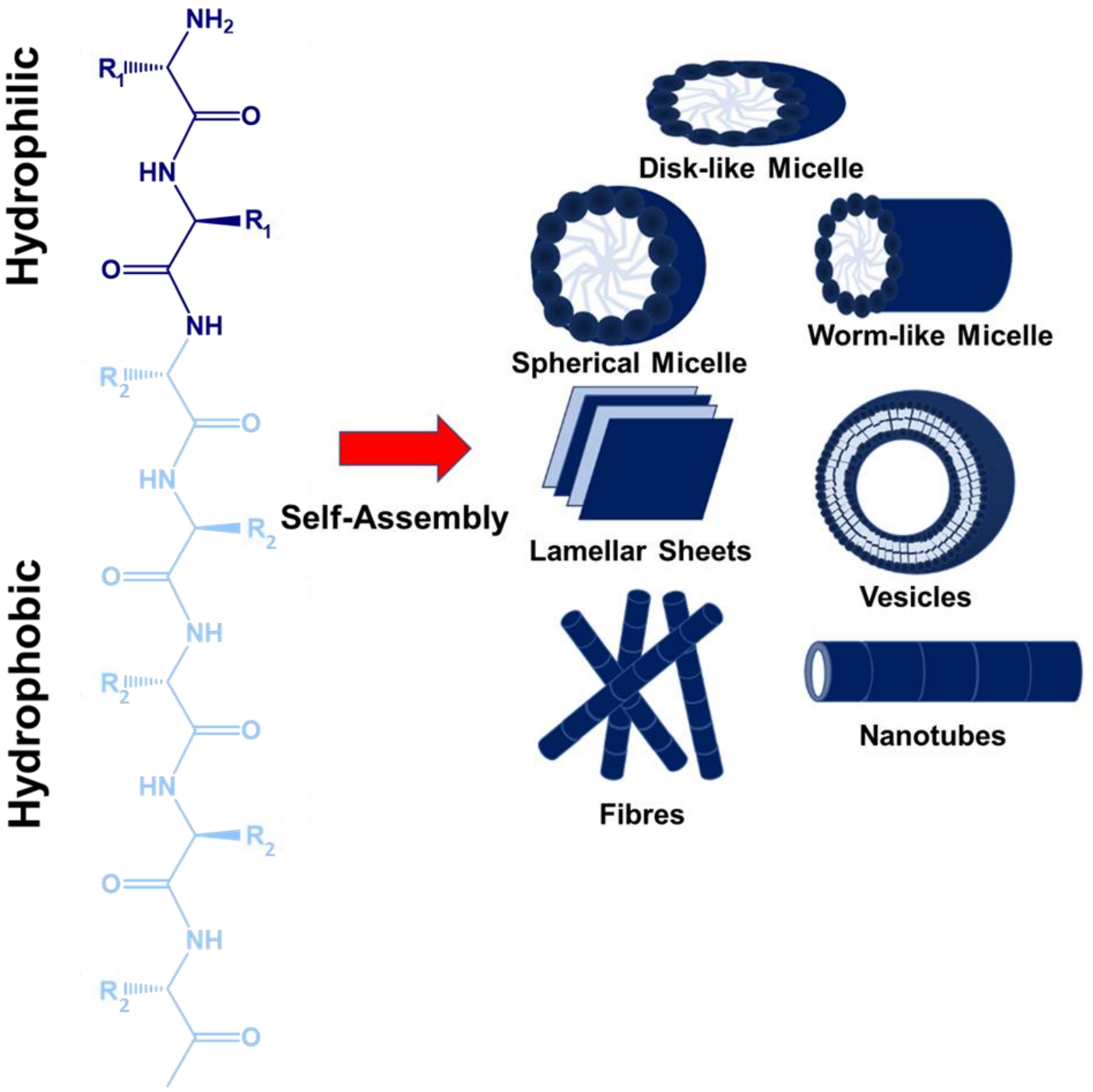

Figure 1.5. *Possible self-assembled structures of peptide amphiphiles. Amphiphilic peptides may assemble into secondary structure through inter and intra molecular interactions (e.g electrostatic interactions and hydrogen bonding), and continue to aggregate into larger self-assembled structures. Where R1 is a hydrophobic group, and R2 is a hydrophilic group (see figure 1.1)*

Some of the most common self-assembled structures (Figure 1.5) include micelles, vesicles and fibrillar structures (nanotubes, fibres).[21] Micelles can be spherical, worm-like or disk-shaped assemblies and form spontaneously above a critical micelle concentration and temperature.[22,23] Vesicles are spherical lamellar structures which are hollow, surrounding an aqueous core. Fibres are cylindrical structures which can be either rigid or flexible. Nanotubes are lamellar structures which are tube-like in shape and hollow. In nanotubes, hydrophilic surfaces are exposed to the inner and outer aqueous environments, whilst hydrophobic residues pack together between hydrophilic interfaces.[24] Peptides and proteins may assemble further from these tertiary structures, to form networks of packed self-assembled fibrils, which may result in the formation of hydrogels.

Hydrogen bonding between the backbone of peptide chains is an important factor in peptide self-assembly, as it drives longitudinal packing of peptide monomers into β-sheets. Inter β-sheet interactions among side chains of peptide molecules regulate the lateral packing of the β-sheet at a slow rate compared to the fast growth in the hydrogen-bonding direction. Packing of β-sheets, which are naturally twisted due to chirality, favours reduced twisting. Lateral interactions overcome the energy penalty due to untwisting.[15] Thus, the final assembled morphologies are the result of these confinements, interactions and/or their interplay.[15]

Self-assembly can be characterised by a number of physical techniques. Fluorescence can be used to detect aggregation concentrations, with probes specialised to structure types. Circular Dichroism (CD),[25–28] Fourier-transform infra-red spectroscopy (FTIR)[29–32] and X-ray fibre diffraction (XRD)[32,33] are used to characterise secondary structure formation. Scattering techniques (e.g SAXS[32,34,35]) and several microscopy techniques are used to characterise self-assembled structures.[32]

1.3 Drivers of folding and self-assembly

Peptide/protein folding and self-assembly is driven by non-covalent forces to form ordered structures ranging from the nanometer to micron size.[36] These non-covalent interactions include Van der Waals forces, hydrophobic interactions, electrostatic interactions, hydrogen bonding and π-π stacking (aromatic) interactions.[9,11] These interactions are enough to stabilise these robust structures, and in turn, allows the structure to be influenced by a number of factors including temperature, pH, concentration and pressure. These factors may be exploited in the creation of new materials, providing a degree of tunability, for example pH responsive materials.

Hydrogen bonding is a non-covalent bond which forms when hydrogen is bonded to an electronegative donor, which interacts with an electronegative acceptor.[37–39] The acceptor needs to have a non-bonding electron pair. In peptides, the donors and acceptors are usually oxygen (O) atoms or nitrogen (N) retrospectively, particularly NH_2 groups and OH groups, although C=O groups also can act as acceptors. Hydrophilic amino acid residues can form hydrogen bonds with water molecules, but hydrophobic residues cannot, which is a large driver of hydrophobic collapse. Hydrogen bonds are the strongest noncovalent, with an estimated energy of 12-30 kJ mol^{-1}. Hydrogen bonds are highly directional, with the strongest bonds being found when all molecules are in a straight line (180 ^{o}C bond angles). For example, anti-parallel β-sheets (Figure 1.4) are more stable than parallel β-sheets as the hydrogen bonding pattern is more optimal.

Electrostatic interactions include ionic and permanent dipole interactions.[40] Ionic bonds, the strongest electrostatic interaction (20 kJ mol^{-1}), are attractions between positive and negative groups of ions. Only the charged amino acids are able to form electrostatic interactions (D,E,G,L,K,H). Ion-polar and polar-polar electrostatic interactions also occur through a similar principle, with negative dipoles interacting with positive dipoles.

Van der Waals forces is a term used to describe a collective group of weak interactions between atoms which are positioned closely.[41] Atoms may be electrically neutral, however as the electron cloud is dynamic, electrons are constantly moving. This can cause areas of the atom to become more electron rich than other parts, leading to temporary weak positive and negative dipoles. A negative charge on an atom will cause repulsion of the electron cloud of the neighbouring atom, thus creating a temporary positive dipole in the neighbouring atom. Van der Waals forces can operate between any two atoms and is distant dependent. Van der Waals are important in the hydrophobic effect, which causes peptides to form structures, as it is the primary interaction between hydrophobic groups in the core of structures.

Aromatic amino acid groups, Tyr, Trp and Phe, may form π-π stacking interactions,[42] which is an important non-covalent interaction that plays a role in self-assembly and amyloid fibril formation.[42] These interactions are the result of electrostatic attraction between π electron clouds, and the different arrangements can be seen in Figure 1.6.

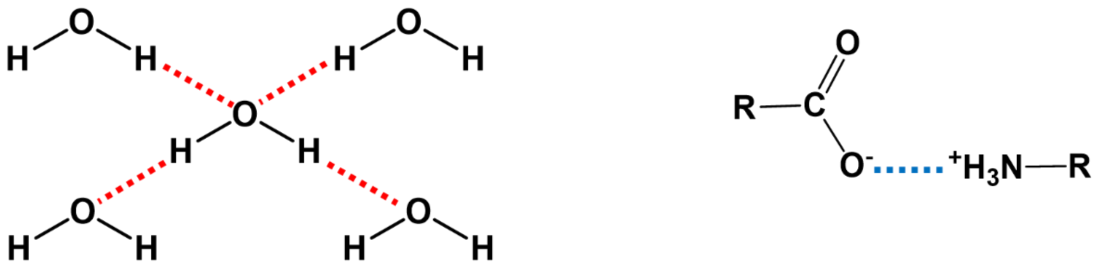

Hydrogen Bonding

Ionic Interaction

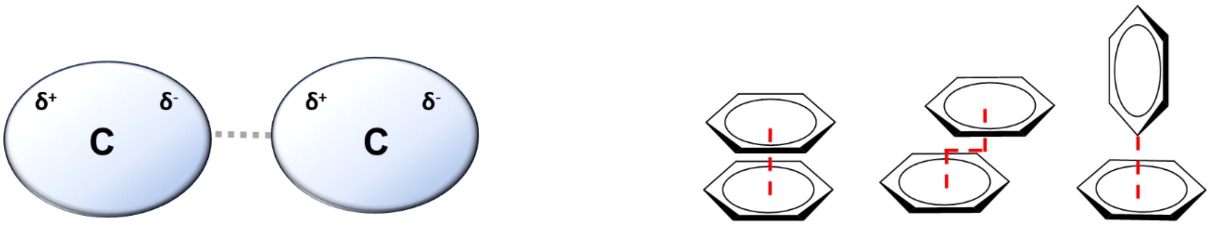

Dipole Interactions
Temporary/Permanent

π-stacking interactions

Figure 1.6. *Non-covalent interactions which drive self-assembly.*

1.4 Biophysical Methods to Study Self-Assembly

1.4.1 Fluorescence spectroscopy

Critical aggregation concentrations are mainly determined using fluorescence spectroscopy. Fluorescence spectroscopy works through the excitation of electrons to the singlet state. Once excited, the electron relaxes back down to the ground state (Figure 1.7). As it relaxes, the electron releases a wavelength of light, that usually has a longer wavelength than the wavelength used to excite. This is known as the Stokes shift. Fluorescence instruments contain a light source, a sample holder and a detector. A beam of light is passed through the sample, at a specific wavelength, and the light emitted (emission spectrum) or absorbed (excitation spectrum) is measured by the detector.

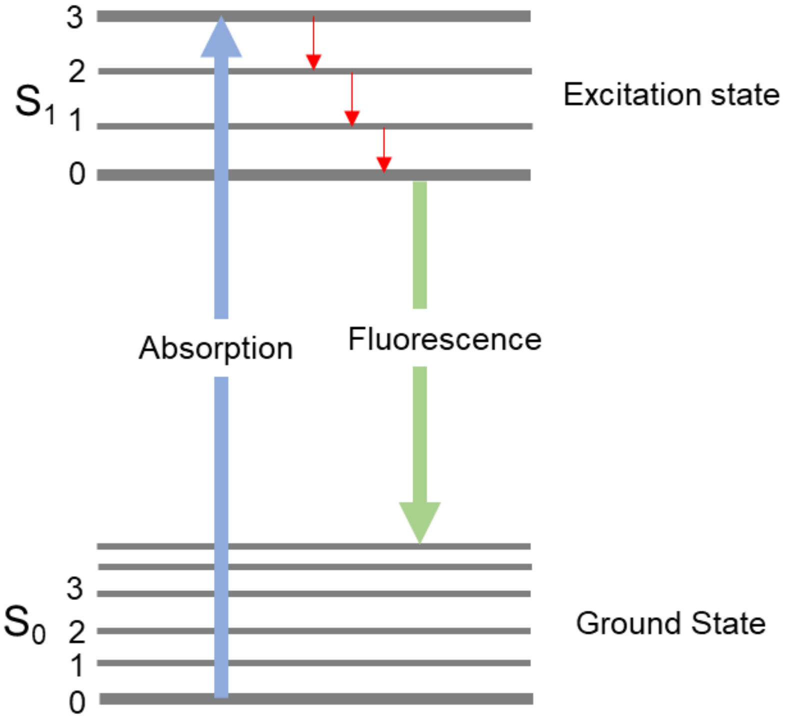

Figure 1.7. *Illustration of the Jablonski diagram to show fluorescence states.*

Compounds that fluoresce are known as fluorophores, and usually contain aromatic groups. Aggregation concentrations of peptides can be measured using intrinsic tyrosine, tryptophan and phenylalanine fluorescence, or fluorescent probes such as 8-Anilinonaphthalene-1-sulfonic acid (ANS),[43] pyrene[44,45] and thioflavin T.[46–48] The amino acid residues and probes (aside from ThT) have generally increased intensity when bound to hydrophobic environments, whereas Thioflavin T has increased fluorescence when bound to β-sheet amyloid fibres.[47]

Several factors affect the fluorescence spectrum. Fluorescence is directly proportional to absorbance, shown by the Beer-Lambert law:

$$A = \varepsilon c l$$

Where A is absorbance, ε is the molar extinction coefficient (M^{-1} cm^{-1}) , L is the pathlength (cm) and c is the concentration (M). Thus, concentration of the sample, pathlength of the cuvette, self-absorption of the sample can all affect the fluorescence of a sample.

1.4.2 Circular Dichroism (CD)

Circular dichroism is a technique used to examine the secondary structure of chiral molecules, through plane polarised light.[25,26,49] Plane polarised light can be seen as being made up of two equal circularly polarised components, with one rotating clockwise (right-handed) and one anti-clockwise (left-handed). Circular Dichroism measures the difference in absorption of these two components. If a compound is not chiral, or exists as a racemic mixture, then no signal is obtained as there is no absorption or equal left and right absorption which cancel out. Chiral molecules, for example peptides and proteins, have unequal absorption of left and right-handed circularly polarised light, which produces a non-zero CD signal. The change in absorption is written as:

$$\Delta A = A_L - A_R$$

Where ΔA is change in absorbance, A_L is left-handed circularly polarised light, and AR is right-handed circularly polarised light.

The CD spectrum in the far UV can be used to measure secondary structure, and to estimate the percentage of each secondary structure present. Each secondary structure has distinct peaks in the far UV region (Figure 1.8). [25,26,49] Circular Dichroism data is presented predominantly in this thesis as molar ellipticity which is calculated through the following equation:

$$[\theta] = \frac{\theta}{10\,CL}$$

Where [θ] = molar ellipticity in deg cm^2 $dmol^{-1}$, θ = ellipticity in mdeg (m^o), L = path length in cm, and C = concentration in Moles (M)

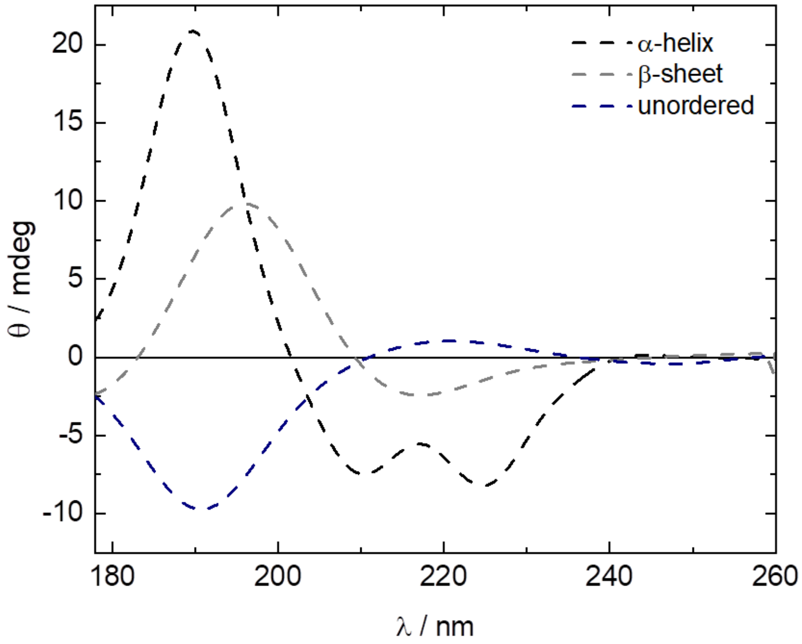

Figure 1.8. *Schematic of typical circular dichroism profiles for different secondary structures.*

1.4.3 Fourier Transform Infrared Spectroscopy (FTIR)

Fourier Transform InfraRed spectroscopy can also be used to characterise the secondary structure of peptides and proteins. Infrared radiation excites vibrational transitions in molecules, and the ability of the molecule to absorb infrared depends on the polarity, strength and positioning of the vibrating molecule, thus molecules are influenced by intra and inter-molecular interactions. [30,31,50,51]

In an FTIR instrument, an infrared source produces a broad spectrum of infrared light wavelengths which are split into two paths using a half-silvered mirror. This light is then reflected back onto a beam splitter by two mirrors, one of which is moveable, where it is recombined and focused onto the sample. The intensity of light striking the detector is measured as a function of mirror position. This is then Fourier-transformed to produce the final plot of intensity vs wavenumber.

For peptides and proteins, two of the most important regions in the FTIR spectrum are the Amide I region, which ranges from 1600 cm^{-1} to 1700 cm^{-1}, and Amide II region, which ranges from 1510 cm^{-1} to 1580 cm^{-1}. Secondary structure assignments can be seen in Table 1.1.

Table 1.1 *Wavelength vibrations in FTIR that correspond to secondary structures.*

Secondary Structure	**Wavelength (cm^{-1})**
β-sheet	1613-1637 1682-1689
α-helix	1645-1662
Unordered	1637-1645
Turns	1637-1645

1.4.4 X-ray fibre diffraction (XRD)

X-ray Fibre diffraction (referred to as XRD) is a type of X-ray diffraction which is used to determine repeat distances in periodically repeating and partly ordered but non-crystalline structures. XRD is commonly used to examine the structure of amyloid like fibres for this reason. An ideal fibre pattern of an oriented fibre exhibits 4-quadrant symmetry, with the perpendicular direction being called the equator of the fibre, and the meridian being the axis of the fibre.

The technique is analogous to wide angle X-ray scattering (WAXS), which is similar to small angle X-ray scattering (SAXS, discussed in section 1.4.7), but the detector sample distance is closer. This means wider angles are measured in the diffraction pattern. Regularly spaced atoms in a crystalline structure can be measured by determining the d-spacing using Bragg's law. Here in this thesis, it is used to investigate the structure of peptide and peptide conjugates which have the ability to form dried stalks.

1.4.5 Electron Microscopy

The four types of electron microscopy used in this thesis are transition electron microscopy (TEM), scanning electron microscopy (SEM), Cryo-TEM and Cryo-SEM. [52]

Transmission electron microscopy is a high-resolution technique, where a beam of electrons is transmitted through the sample with different density. Electrons have a much shorter wavelength than visible light, enabling up to 1000 times higher resolution from TEM. This enables nanostructures to be examined with this technique. Samples must be below 100 µm in thickness, which increases the complexity of sample preparation for biological samples. Biological samples including peptides, often require negative staining to increase the electron density difference (contrast) of the sample to reveal the structure, for example a heavy metal salt such as uranyl acetate. [52]

Whilst TEM can give a detailed information on nanostructures, scanning electron microscopy (SEM) can give useful information about the surface topography of a structure (for example a hydrogel or a bacterial cell). Scanning electron microscopy produces images by scanning the surface of the sample with a focused electron beam. SEM has a lower resolution than TEM.

For both microscopy techniques, the electron beam is emitted from a negatively charged electron gun, which most commonly either tungsten filament cathode or a lanthanum hexaboride (LaB6) source. The electrons are accelerated by a series of anodes under vacuum at high voltage. For TEM voltage ranges from 60-200 keV, and for SEM this voltage ranges from 0.2-40 KeV.

Both instruments have a series of lenses to focus the beam, which are composed of copper coil wires. The main types of lenses are the condenser lens, which is used as the primary way to focus the beam on the sample, the objective lens, which focuses and magnifies the lens, and the projector lens used to focus the image further and project it onto an imaging device. Apertures can be used in EM to decrease the beam intensity, filter out electrons which are scattered to high angles. High angle electron scattering can lead to diffraction, chromatic or spherical aberrations. In SEM and TEM there are two apertures, the condenser aperture which controls beam size on the sample, and the objective aperture, which selects which electrons contribute to the image, thus affecting the overall contrast. [52]

As both instruments are under vacuum, samples need to be dry in order to be imaged. For self-assembled samples, and amphiphilic molecules that require hydration to be in the correct orientation, this can be a limiting factor. Some molecules will form different morphologies in the dried form, for example some peptides may transition upon drying to a β-sheet structure, leading to fibril formation. Biological samples also need to be dehydrated through a ethanol gradient and then dried. Thus, cryo-TEM and cryo-SEM which involves the swift freezing of samples, allowing them to be imaged in the solution state can have a large advantage over SEM and TEM.

1.4.6 Small angle X-ray Scattering (SAXS)

Small angle X-ray scattering (SAXS) is a powerful method to study the structural properties of materials at the nanoscale. It is a non-destructive, accurate method that requires little sample preparation. Originally developed in the 1930s to study metal alloys,[53] it has been shown to be useful for many other purposes including polymers, colloids and biological macromolecules. There have been two milestones that have increased the popularity of the technique. The first was in the 1970s, with the appearance of intense synchrotron sources. The second, in the 1990s, was associated with computational advances and methods allowing for high throughput SAXS.[35] Recent progress in instrumentation and analysis methods has led to an increasing number of applications of this technique for biomacromolecule studies in solution state, allowing for example self-assembly to be studied in solution or in hydrogels.[35]

SAXS measurements on solutions are typically performed when molecules are randomly orientated in solution resulting in no diffraction peaks being observed, and all orientation information is lost. It is still possible to obtain information on magnitudes of the interatomic distances, such that the overall structural parameters, even low-resolution shapes of particles can be obtained. This enables SAXS to be used to determine the overall shape of proteins or self-assembled structures in solution. This is a useful and important tool, as many crystallographic high resolution studies, structures of peptides and proteins do not accurately represent conformation in solution, as the energetically favourable conformation for crystallisation is often different from how the peptide would behave in solution. New SAXS approaches include time resolution, assessment of oligomeric states of macromolecules and proteins, chemical equilibria and reaction kinetics.[34]

1.4.6.1 Solution-SAXS

Solution SAXS is a powerful technique to study self-assembly in solution. Scattering is isotropic, and photons are collected on a 2D detector. To overcome this, the image is radially averaged to obtain scattering intensities, as a function of the momentum of transfer or wavevector, q :

$$q = \frac{4\pi \, sin\theta}{\lambda}$$

Where λ is equal to the wavelength of the incident beam, θ is half the angle of incidence (angle between incident beam and scattered radiation). A typical scattering curve will have intensity plotted against q in nm^{-1} or Å dependent on instrumentation (figure 11b). The q-range is determined by experimental set-up.

During an experiment, scattering of the dissolved particles and that from the pure solvent are separately collected. The scattering of the pure solvent is subtracted from that of dissolved particle. The difference in signal is proportional to the concentration of the solution, and to the difference in electron density between particle Pp and solvent Ps. For biological molecules, including peptides, the density of the particle is can be only slightly higher than that of the corresponding aqueous buffer, meaning that the useful subtracted signal may be small. This means that background noise can be a problem with the technique, therefore equipment needs to be optimised to reduce background scattering as much as is possible. [35]

For a monodisperse system, consisting of non-interacting identical particles, the scattering intensity from a single particle averaged over all orientations is proportional to the background-corrected intensity *I(q)*, as such that:

$$I(q) = I(q)_{\Omega} = A(q)A^{*}(q)_{\Omega}$$

Where the scattering amplitude, *A(q)* is a Fourier transformation of excess scattering length density, and Ω is the solid angle in the reciprocal space of the scattering.

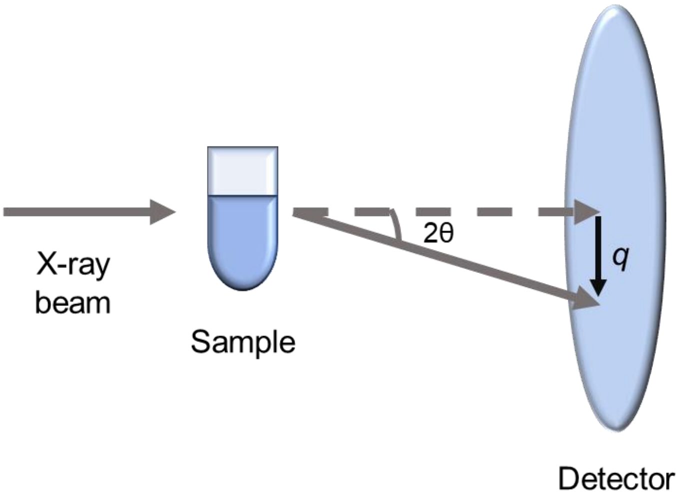

Figure 1.9 A typical SAXS experiment. *When a monochromatic beam hits the sample, photons are scattered. The scattered photons are collected by a 2D detector, and the data is radially averaged in order to obtain a scattering curve.*

1.4.6.2 Computation of overall parameters

Guinier analysis, developed in the 1930s, is still the most straightforward way to determine the radius of gyration (R_g) and forward scattering $I(q)$.[54] The radius of gyration is a model independent size parameter, that can eventually be used to calculate the particle dimensions if a model is found. The Guinier approximation for a monodisperse system is:

$$I(q) = I(0).\exp(-\frac{1}{3}\,{R_g}^2\,q^2)$$

This approximation is valid for the range $q.R_g < 1.3$.[35] In practice R_g and $I(0)$ are determined through a Guinier plot, a plot of ln[I(s)] against q^2. The slope is equal to R_g, and the intersection with the ordinate is the forward scattering intensity. A linear Guinier plot is a good indicator of sample quality and monodispersity.[35] However, complementary techniques, for example dynamic light scattering, should be used to confirm this.[55] Non-linear Guinier plots can be due to a number of reasons for example polydispersity, improper background subtraction and interparticle interactions. As the Guinier region is influenced by interactions, non-specific aggregation this can result in a sharp increase at low angles and overestimation of both R_g and I(0). Although this effect is not ideal, it does have some uses, for example finding crystallisation conditions of a peptide/protein.

Polydisperse samples can still be measured using techniques such as size-exclusion SAXS (SEC-SAXS), which separates fractions within a sample before running them into the beamline. It can also be used to detect different aggregation states. For example, if a self-assembling peptide has partial assembly to fibres and partial assembly to spherical micelles it is possible to separate the two assemblies through a size exclusion column, and load both onto the beam as they are eluted separately.

The Guinier approximation provides a way to access *I(0)*. Overall the Guinier method provides size information, data quality, interactions and oligomeric state. Today, it can be calculated automatically by computer programmes.[35]

1.4.6.3 Modelling SAXS structure

Every particle has an associated form factor (an interference pattern describing every wave that is scattered by every atom inside the particle) that is characteristic to its structure. Overall size is determined primarily by the slope at low *q*, the final slope at high *q* bears the surface information (Porod's region). Shape and internal distribution information are determined through the oscillating part of the middle section of the form factor. Rough classifications into globular, cylindrical and lamella shape can be done by investigating the power law form factor at small angles. On a double logarithmic scale, an initial slope of q^0 indicate globular objects, q^{-1} indicates cylindrical shape, and q^{-2} equates to lamellar objects.[34] When q values exceed this, the objects are too large for the resolution limit and only the Porod region (region observed that gives information about structure surface, toward q max) is observed.[34]

One method of investigating overall shape is to do a Fourier-transform, and the resulting curve p(r) is the "pair-distribution distance function". This produces a histogram of distances found inside the particle. This gives an initial idea of the shape.[35]

From here it is possible to perform model calculations to determine relative positioning and orientations. They involve repeated calculations of pair-distribution distance functions, and comparisons with experimental curves. *Ab initio* modelling, such as a dummy bead modelling algorithm can be used to build models for particles of different shapes based on beads. Rigid-body modelling requires all atomic points (although this can be overcome by combination with ab initio techniques).[34] There are many computer programmes available that can perform modelling functions.

For self-assembled structures, it is possible to model them using form-factor fitting. This is the modelling method used predominantly in this thesis. This is based on using the SAXS profile to select and fit the data to different shaped models through adjusting various parameters. Programmes such as SASfit can be used to model structures using this method. Through this it has been possible to model spheres, core-shell and cylindrical micelle structures, bilayers, fibres and nanotube assemblies, with various degrees of polydispersity and backgrounds[56]

Sphere

$$\lim_{Q=0} I_{Sphere}(Q,R) \;=\; \left(\frac{4}{3}\pi R^3 \Delta\eta\right)^2$$

Where Q = forward scattering, Δη = the difference in the scattering length density between the particle and the matrix, and R is the radius.

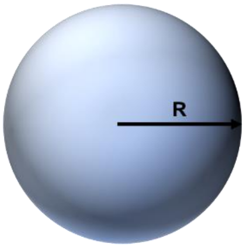

Spherical Shell

$$\lim_{Q=0} I_{Sphere}(Q, R_1, R_2, \Delta\eta, \mu\,) \;=\; \left(\frac{4}{3}\pi\Delta\eta\left[R_1^3 - R_2^3(1-\;\mu\right]\right)^2$$

Where Q = forward scattering, Δη = the difference in the scattering length density between the shell and the matrix, and R1 is the overall radius, R2 is the radius of the core, μ is the scattering contrast of the shell

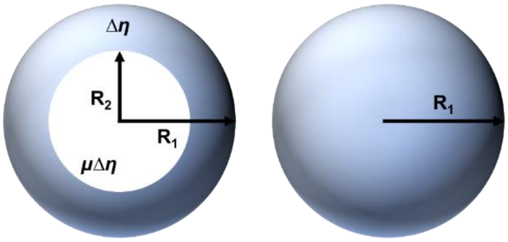

Long Cylindrical shell

$$I_{longCylindricalshell}(Q) = P'(Q)P_{cs}(Q)$$

$$P'(Q) = 2\frac{Si(QL)}{QL} - \left(\frac{sin(QL/2)}{QL/2}\right)^2$$

$$Si(x) = \int_o^x \frac{\sin t}{t}\,dt$$

$$P_{cs}(Q) = \left(2\frac{J_1(QR)}{QR}\ (\eta_{core} - \eta_{shell})R^2L\pi + 2\frac{J_1(Q(R+t))}{Q\,(R+t)}\ (\eta_{shell} - \eta_{solv})(R+t)^2L\pi\right)^2$$

Where R is the radius of the core, t is the thickness of the shell, L is the length of the cylinder, Q is the forward scattering, η_{core} *is the scattering length density of the core,* η_{shell} *is the scattering length density of the shell,* η_{colv} *is the scattering length density of the solvent. For long cylindrical shell, the approximation only holds for cylinders much greater in length that radius of the cylinder.*

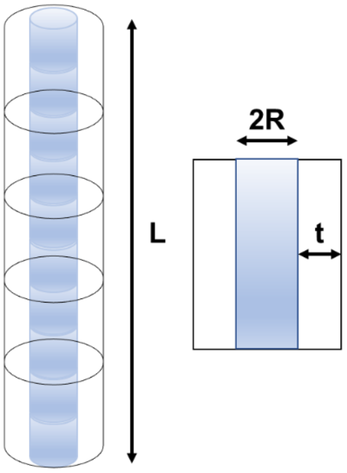

Long Cylinder

$$Si_{\frac{x}{2}}(x) = \left(Si(x) + \frac{\cos x}{x} + \frac{\sin x}{x^2}\right)\ x \to \infty\ \frac{\pi}{2}$$

$$\Lambda_1(x) = \frac{2}{x}J_1(x)$$

$$\Lambda_2(x) = \frac{8}{x^2}J_2(x)$$

$$\omega(x) = \frac{8}{x^2}(3J_2(x) + J_0(x) - 1)$$

$$\phi Long(q,R,L) = \left(\Delta\eta\pi R^2L\right)^2\frac{2}{QL}\left\{Si_{\frac{x}{2}}(QL)\Lambda_1^2(QR) - \frac{\omega(2QR)}{QL} - \frac{\sin\,(QL)}{(QL)^2}\right\}$$

Where $J_n(x)$ *are the regular cylindrical Bessel function of order n. R is the radius and L is the length. The approximation for a long cylinder is valid when L > 2R*

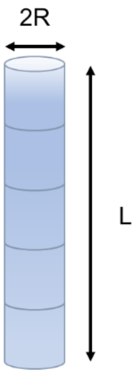

Flat Cylinder

$$\Lambda_1(x) = \frac{2}{x} J_1(x)$$

$$I_1(x) = \int_0^x \Lambda(x')dx' = 2xJ_0(x) - 2J_1(x) - \pi x[J_0(x)H_1(x) - J_1(x)H_0(x)]$$

$$I_0(x) = \frac{I_1(x) + x\Lambda_1(x)}{2}$$

$$\Omega(x) = \frac{2}{x}[I_0(x) - 2J_1(x)]$$

$$\chi(x) = \left(\frac{sin(x/2)}{x/2}\right)^2$$

$$\phi flat(q,R,L) = \left(\Delta\eta\pi R^2 L\right)^2 \frac{8}{(2qR)^2} \left\{\chi(qL) + \frac{I_1(2QR)\Omega(qL)}{2qR} - \Lambda_1\,(2qR)\right\}$$

H_a(x) is the Struve function of order a and Jn(x) are the regular cylindrical Bessel function of order n.

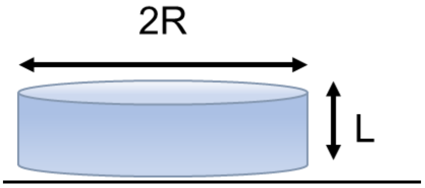

Porod Cylinder

$$\phi_{Porod}(q,R,L) = p\left(\frac{2R}{L}\right)\phi_{flat}(q,R,L) + \left(1 - p\left(\frac{2R}{L}\right)\phi_{long}(q,R,L)\right)$$

$$\boldsymbol{p(x)} = \begin{cases} \mathbf{1} & \boldsymbol{for\ x > \frac{5}{4}} \\ \mathbf{2}\left(\boldsymbol{x - \frac{3}{4}}\right) & \boldsymbol{for\ \frac{3}{4} \leq x \leq \frac{5}{4}} \\ \mathbf{0} & \boldsymbol{for\ x < \frac{3}{4}} \end{cases}$$

Only a good approximate when L = 2R.

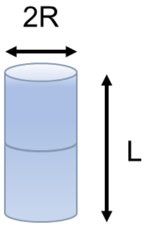

The quality of the fit is assessed through examining the residuum (deviation between the data set and the fit), which is examined through the chi (χ) square test:

$$\chi^2 = \frac{1}{N - m} \sum_{i=1}^{N} \left(\frac{I_{exp}(q_i) - I_{th}(q_i)}{\Delta I(q_i)} \right)$$

Where N is the number of data points, m is the number of fit parameters, $I_{exp}(q_i)$ is the experimental data, $I_{th}(q_i)$ is the fitting function. A good fit is achieved when χ^2 is close to 1.

1.5 Peptide Amphiphiles (PA's) and Amphiphilic Peptides

The classical model of a peptide amphiphile (PA) was defined by Stupp (Figure 1.10). [57] This model has multiple sections. Firstly, a hydrophobic tail group, usually an alkyl group, which leads to hydrophobic interactions. Secondly, a peptide sequence that can form intermolecular hydrogen bonds, which determines the interfacial curvature of self-assembly. Next, a section of charged amino acids to promote solubility and finally a functional peptide epitope that has bioactivity.[57] Although the classical model of peptide amphiphiles are defined as such, other peptides which are amphiphilic, with both charged and uncharged parts and without lipid tails, have also been shown to have remarkable self-assembly abilities.

The amphiphilicity of these molecules drives self-assembly, which draws the functional/hydrophilic part of peptide group to the surface of the structure. Self-assembly occurs above a critical aggregation concentration (*cac*). The cac can be measured using fluorescence methods, light scattering or proton NMR solubility.[9]

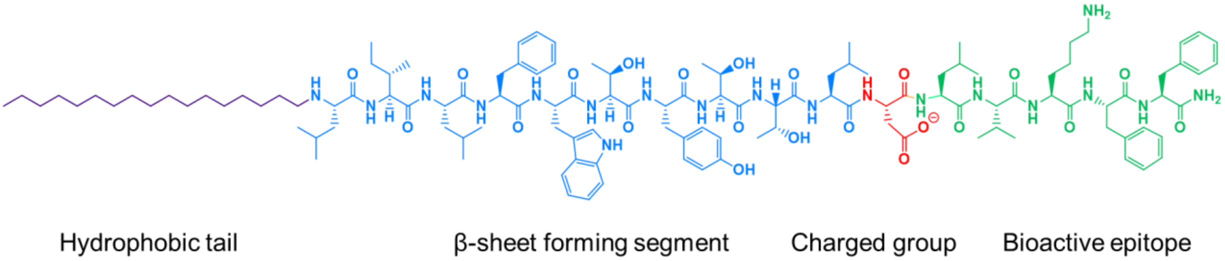

Figure 1.10. *Typical structure of a peptide amphiphile showing the four domains that are typically required for self-assembly, though variations of this structure have been shown to self-assemble.*[57]

Self-assembly of peptide amphiphiles and amphiphilic peptides has been widely-studied due to their potential to assemble into a large range of novel nanostructures which are of interest commercially and biomedically. These structures can be monolayer based (for example micelles), or bilayer based (for example vesicles).[58] The self-assembled structure of a peptide can largely be controlled by amino acid sequence, length of sequence and lipidation. Thus, they are a malleable tool in order to make novel biomaterials. Some of their potential uses include drug delivery, tissue engineering and antimicrobial agents.[9]

1.6 Surfactant-like Peptides (SLP's)

Surfactant-like peptides (SLPs) are peptides containing sequences of both hydrophobic and hydrophilic amino acids (Figure 1.11.), which self-assemble in a similar way to PAs. Popular examples of this include A_6R,[59] A_6D and V_6D.[60] Alanine-containing SLPs have found to self-assemble into more stable structures due to stronger hydrophobic interactions, in contrast to other hydrophobic amino acid residues.

SLPs tend to feature 1-2 charged amino acids that form a hydrophilic head group, and 4 or more consecutively hydrophobic amino acids.[61] Early studies of self-assembly of this group showed that in water, they undergo self-assembly to from bilayer nanovesicles and nanotubes, with an average diameter of 30-50nm).[62] Nanotubes are thought to form from bilayers of peptide molecules, which resemble sheets. These sheets then roll up to form tubes, which have a defined diameter, and continue to grow from the edges. More recently, SLPs have been prepared that form micelles through packing of hydrophobic tails or nanofibers. Two variants of A_6K were shown to have differences in assembly due to deprotection of the C-termini or the pH of the solution. A_6K with the sequence Ac-AAAAAAAK-CONH$_2$ were observed to form nanofibers at low pH and pH 6, and amorphous aggregates at high pH. When the protecting NH_2 group at the C-termini was removed, leaving the sequence Ac-AAAAAAAK-COOH (named $A6K^{\pm}$), it was shown to form short nanofibers at low pH, longer fibres at pH 5, and nanospheres at high pH.[44] This was studied using atomic force microscopy, dynamic light scattering and transition electron microscopy (TEM). The difference at high pH was thought to be due to the ability of the carboxyl group in the second variant to disassociate. The uncapped version of A_6K has also been shown to form single layer nanotubes at high concentrations using cryo-TEM and SAXS (small angle-x-ray scattering), and NMR.[63,64]

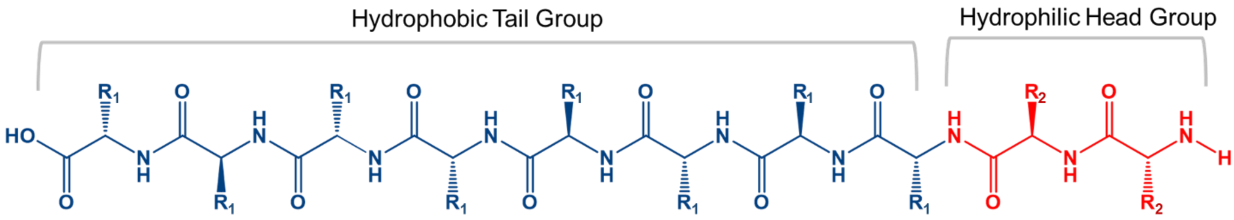

Figure 1.11. *Structure of a SLP, where the hydrophobic tail group and hydrophilic head group can vary in size, where R_1 is a hydrophobic group and R_2 is a charged group.*

SLPs have promising potential to be used in the study of membrane proteins because, like lipids, they can form layered structures. Membrane protein purification is a complex process due to the size and interactions membrane proteins have with the lipid bilayer. Surfactant-like peptides could be used to bind the hydrophobic section of the membrane protein and sequester it from water, thus preventing denaturation. For example, surfactant-like peptides have been shown to enhance the stability of bovine rhodopsin, a G-protein coupled receptor.[62] They also have promising antimicrobial applications.[59]

1.7 Peptide Bola-amphiphiles

A bola-amphiphile is a molecule described as having two hydrophilic head groups joined together through a hydrophobic core group.[65] This type of peptide are naturally found in membranes of some extremophile archaebacteria, which have monolayer assemblies as membranes as opposed to the standard bilayer structures of normal lipid membranes (Figure 1.12). This improves their stability in harsh conditions.[66] Aside from this, peptide bola-amphiphiles can consist of amino acids alone and be rather short in sequence, or have other groups (for example an alkyl core group) with longer sequences.

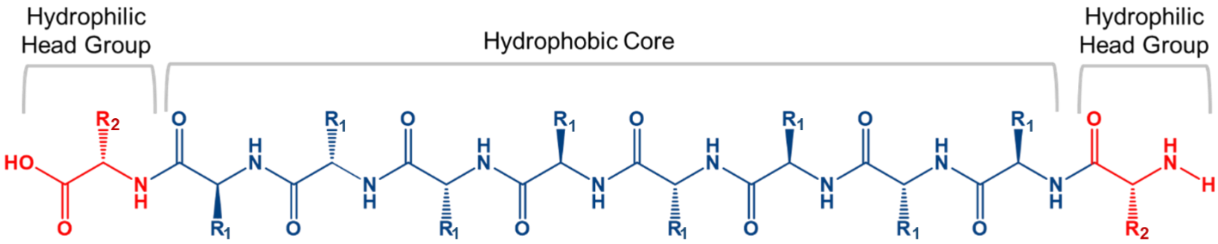

Figure 1.12. Generic structure of a peptide bola-amphiphile, where the hydrophobic core and hydrophilic head group can vary in size, where R_1 is a hydrophobic group and R_2 is a charged group.

The self-assembly of a group of short bola-amphiphiles, with sequence KA_nK (where n ranges between 3 and 8) has been investigated.[67] KA_3K was found to not self-assemble, however when increasing the length of the alanine chain length between 4 and 8, self-assembly into nanofibers was observed. Interestingly, despite these peptides binding to ThT and having birefringence which is characteristic of amyloid fibres, the secondary structure determined through circular dichroism (CD) was disordered. Moreover, peptides with different hydrophilic capping groups were examined, those with arginine (RA_6R), glutamic acid (EA_6R) and threonine (TA_6T) forming spherical structures, compared to serine (SA_6R), lysine (KA_6K) and aspartic acid

(DA_6D) which form nanofibers.[67] This group also examined the effect of replacing alanine in the hydrophobic core with other amino acids, and found that as long as the core remained hydrophobic nanofibers formed, however, the substitution of hydrophilic residues resulted in a loss of nanofiber formation.[67]

Recently, Guan and co-workers studied dendritic peptide bola-amphiphiles, which were shown to be able to transport siRNA (silencing RNA) into primary adipocytes and hepatocytes without disturbing the normal metabolic interactions of the cells.[68] siRNA transportation into the cell is important for tissue engineering, and in diseases where stopping the transcription of certain mRNA (thus affecting protein composition) is important. The dendritic peptides consist of a fluorocarbon core, which increases the stability of the dendrimer in the cytoplasm, assists cellular uptake and increases self-assembling propensity. Attached to this are two L-lysine residues, connected through a disulphide linker. This disulphide linker provides stimuli responsive release of siRNA. The dendrimers were functionalised with tryptophan and histidine to increase binding and buffering respectively.[68]

The construction of a group of bola-amphiphile like peptides which mimic collagen was also examined.[69] These sequences contain two hydrophilic head groups consisting of L-aspartic acid, linked together through repetitive triple helical core groups, which are similar to the architecture of collagen. These peptides, $D_2(GPO)_7D_2$ and $D_2(PPG)_{12}D_2$ were found to assemble into nanospheres, which were stable across a broad range of pH conditions.[69]

Two short bola-amphiphiles containing eight amino acids were found to have remarkable self-assembling properties. Peptide RFL_4FR was found to self-assemble into cytocompatibile β-sheet nanosheets,[70] which over time fold into nanotubes.[70] Peptide EEL_4FE was found to form nanosheets, transitioning from β-sheet to disordered secondary structure upon nanotube formation.[71]

Therefore, peptide and peptide-functionalised bola-amphiphiles may have a range of applications including studying model systems, membrane modelling of extremophile bacteria, siRNA transporters, collagen-mimetic materials and antimicrobials.

1.8 Lipopeptides

Self-assembling amphiphilic lipopeptides are a class of molecules defined as having a one or more lipid chains attached to a peptide head group. The self-assembly of this class is thought to depend upon the hydrophile/lipophile balance (HLB).[12] They offer advantages compared to peptides, as they offer increased amphiphilicity and are compatible with the phospholipid bilayer (which makes up cell membranes), enabling them to deliver actives into cells via endocytosis. Additionally, self-assembly of lipopeptides facilitates the presentation of peptide functionalities at high density at the surface of nanostructures (micelles, vesicles and fibrils) and increase the *in vivo* stability.[11,12]

Many naturally expressed bioactive lipopeptides contain one lipid chain (C_{14}-C_{18}) with a cyclic head group. Cyclisation is thought to have evolved to reduce proteolysis, thus enhancing *in vivo* stability. However, these conformational peptide constraints may be relevant to bioactivity. In bacteria, many naturally occurring amphiphilic lipopeptides are produced as part of a host defence response against other organisms.[72] This has many interesting uses clinically. An example is daptomycin, produced by gram positive bacteria, *Streptomyces roseoporous*, which is used to treat MRSA and self-assembles into micelle structures.[73,74]

Synthetic amphiphilic lipopeptides tend to be based on a bio-derived sequence, often containing a linear peptide head group with 1-3 (usually palmitoyl) lipid chains attached. An example is Toll-like receptor agonists (TLRs). TLRs are transmembrane proteins which are part of the innate immune response, making them an important therapeutic target. Agonists of TLRs were designed based on the Pam_3Cys peptide (where Pam denotes a C_{16} chain). This synthetic peptide has been shown to stimulate cytotoxic T lymphocyte (CTL) responses against cells infected with influenza virus.[75] Another related lipopeptide to this is $Pam_3CysSer_2$ which has been shown to stimulate antibodies against foot and mouth disease.[76] Pam_1CKS_4 and Pam_2CSK_4 have been shown to self-assemble into spherical micelles in contrast to Pam_3CSK_4 which forms bilayer based structures.[77]

1.9 PEGylation and other modifications

Attachment of polymer chains to peptides can increase *in vivo* stability through the reduction of proteolysis / promoting album binding. One such way is to PEGylate peptides.[78] PEGylation is covalently attaching polyethylene glycol (PEG) or polyethylene oxide (PEO) to a peptide chain. This can increase the molecular weight, increasing resistance to enzymatic degradation. PEG is an attractive polymer for attachment as it is FDA approved, meaning it has huge potential in the area of developing drug delivery technologies and extending drug half-lives.[79,80]

PEGylation has resulted in a mixture of positive and negative results. For example, the PEGylation of gut peptide $PYY_{3\text{-}36}$, which is involved in several stomach processes including feeling full after eating, was examined. It was shown that PEGylation extended the circulation half-life of the peptide in a mouse model, but eliminated its activity.[81] To overcome this issue, attaching PEG through a hydrolysable linker was found to restore activity.[81] Recently, Hamley and co-workers examined the effects PEGylation of $PYY_{3\text{-}36}$ had on self-assembly by attaching short oligoPEG chains in several regions across the peptide.[82] PEGylation was found to inhibit peptide aggregation, shown through fluorescence studies, although α-helical secondary structure was observed.[82] Thus PEGylation can increase stability, decrease activity dependent on method of attachments, and increase solubility/ prevent or increase self-assembly dependent on the length of the PEG chain.

Hamley and co-workers reported the gel-sol transition of PEO conjugates with hydrophobic dipeptides, including dityrosine and diphenylalanine.[83] One conjugate with a di-tyrosine cap and a C-terminal Fmoc protecting group was found to undergo a gel-sol transition period near body temperature, driven by loss of β-sheet structure associated with extended fibril formation.[83] The self-assembly of three conjugates, Tyr_5-PEO2K-Tyr_5, Tyr_5-PEO6K-Tyr_5 and Tyr_3-PAla-Tyr_3 (PAla = poly(L-alanine), was examined.[84] Tyr_5-PEO2K-Tyr_5 and Tyr_3-Pala-Tyr_3 were shown to have poor solubility in water until adjusted to pH 12, whereas Tyr_5-PEO6K-Tyr_5 showed good solubility. All three polymer conjugates were shown to assemble into β-sheet fibrillar structures probed by cryo-TEM. Interestingly, hydrogel formation was not observed for any samples, in contrast to the previous work, up to 20 wt%.[84]

Other modifications aside from PEGylation that can increase stability can include the substitution of L-amino acids to D-amino acids. Mammalian enzymes do not recognise D-amino acids, therefore this can delay their enzymatic breakdown.[85,86] Moreover, the addition of carbohydrates (glycosylation),[87] conjugation to protein serum albumin[88] or changing the position of the R-functional group to the nitrogen as in peptoids, are other techniques to improve peptide stability.[89]

1.10 Hydrogels

Hydrogels can often form as the result of a higher order of self-assembly beyond the structures described above. A hydrogel is defined as a water swollen, cross-linked polymeric network. It is produced by simple reactions between one or more monomers, retaining water but not dissolving. Some hydrogels are able to absorb large amounts of water and they may also be designed to have mechanical properties similar to natural tissue. Hydrogel formation can be very dependent upon temperature, pH, concentration of polymer/peptide or salts.[90]

Hydrogels can be made of natural or synthetic materials, and can be prepared through use of homopolymers, copolymers or multi-polymer networks. Homopolymeric hydrogels contain one polymer, copolymer networks contain two or more polymers interacting with each other to form the fibrillar network, and co-networks contain two independent fibril forming monomers. They can be non-crystalline, semi-crystalline or crystalline.[90] Formation can occur through covalent interactions between monomers, or through electrostatic interactions, hydrogen bonding, Van der Waals and/or ionic interactions.

Peptides and peptide conjugates have the ability to form hydrogels. Hydrogelation is a hierarchical process, which occurs with continuing self-assembly.[91] For example, for fibre-based hydrogels, self-assembly might occur from β-sheet peptides to nanofibers. These fibres may then elongate in three dimensions, leading to increased fibre length and entanglement, ultimately leading to fibrillar network formation. These complex networks of peptides may then entrap water, thus providing a self-supporting hydrogel. Peptides and peptide conjugates with other secondary structures, for example α-helical, have also been shown to be able to form hydrogels.[92]

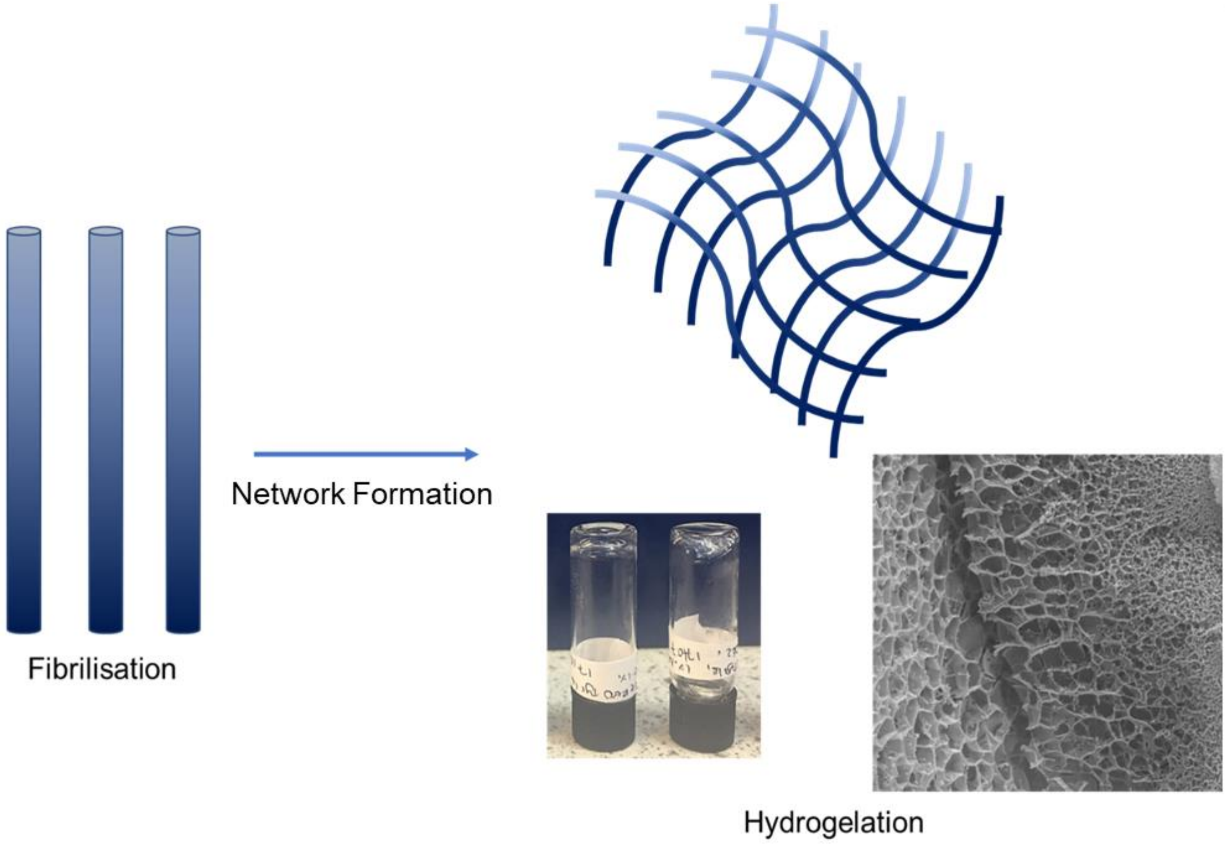

Figure 1.13. *Simplified schematic of hydrogel formation*

Hydrogels designed for biomedical applications must be cytocompatible. Synthetic hydrogels are more likely to induce immune inflammatory response, which could have potential cytotoxic and thus detrimental effects. Natural hydrogel polymers, for example peptide, or peptide functionalised polymer hydrogels,[83,93–98] are more likely to be biocompatible. A number of other physical parameters, for example degradation and performance (e.g. cell adhesion) must also be considered. The mechanism by which the hydrogel forms is important. Gels formed by ionic cross-linking may be prematurely degraded *in vivo* due to salts in body fluids, making covalent cross-linking preferred. Some examples of other naturally occurring polymers include fibrin, collagen and gelatin and hyaluronate. The most popular FDA-approved synthetic polymers are poly(acrylic acid) derivatives and poly(ethylene oxide) (PEO).[99]

Hydrogels have also been shown to have applications in cell culturing. Peptide hydrogels for cell culturing must mimic the extracellular matrix and incorporate peptide adhesion motifs. Peptide RGD, is one of the most widely used peptide sequences for this purpose. A Fmoc-RGD peptide was shown to form β-sheet secondary structure, and to self-assemble into amyloid fibrils. The hydrogel formed by Fmoc-RGD was shown to be capable of sustaining cells and supporting fibroblasts compared to a control scrambled sequence.[100] Other applications for peptide and peptide conjugate hydrogels include biosensors,[101] regenerative medicine and tissue engineering,[102–112] and slow release drug delivery systems.[80,113–117] The applications described below are those most relevant to this thesis.

1.11 Therapeutic applications

Peptide amphiphiles have many applications. Some applications, including biomineralization,[118–120] membrane stability enhancement[121–124] and antibody production[125,126] are not covered here but are described in detail elsewhere.[8,127] The applications presented below are those most relevant to this thesis.

1.11.1 Tissue scaffolds

Tissue scaffolds are engineered materials that mimic the extra-cellular matrix (ECM), and are designed to allow cell attachment/migration, enable diffusion of desired molecules, exert mechanical and biological influences to modify the behaviour of the cell phase, or to deliver and retain cells and biochemical factors. Peptide amphiphiles (PAs) have been shown to have potential applications in this field.

One of the most commonly studied cell adhesion motif is the integrin recognition motif RGDS from fibronectin. Terrill's group attached RGD units either through amino or carboxyl units to dialkyl lipid chains. They also prepared a conjugate which contained loops connected by linkers to dialkyl chains on both sides.[128] It was found that lipid chain attachment to the RDG peptide affected the spreading of melanoma (tumour associated with skin cancer). Amino conjugated PA was found to show no spreading, whilst the looped PA was found to show concentration-dependent spreading, and indiscriminate spreading was observed for the carboxyl coupled PA. Further studies based on liposomes revealed that spontaneous metastasis could be inhibited by RGD-based PAs.[129]

PAs have also been shown to have promise in regenerative medicine. PA nanofibril gels containing peptides incorporating a cell adhesion motif, IKVAV have been observed to encapsulate cells and rapidly differentiate them into neurones.[130] This same PA has been shown to be effective in a mouse model for treating spinal cord injury, the self-assembling nanofibers inhibiting glial scar formation and promotion of axon elongation. Other PAs have been shown to be effective in cartilage regeneration using bone marrow-derived stem and progenitor cells.[131]

Cosmetic lipopeptide amphiphile Matrixyl (C_{16}-KTTKS), shown to stimulate collagen and fibronectin production in fibroblasts, undergoes self-assembly in aqueous solution.[127] At neutral pH, it has been shown to have β-sheet secondary structure and form bilayer-based nanotapes[63] which are stable between the pH range of 3-7 at room temperature. However, pH reduction/increase[132] or increased temperature[133] favours random coil secondary structure, and spherical micelle self-assembly.

1.11.2 Delivery and cell internalization

Transportation of hydrophobic drugs and other active molecules into cells is an important and ongoing biomedical challenge. PA-based nanocarrier systems have shown potential and are usually designed based upon natural sequences. An example is a PA comprising of a tandem dimer, containing binding sites for LDL (low-density lipoprotein) receptor and cell-surface heparin sulphate proteoglycans. Internalisation of the PA into brain capillary endothelial cells was imaged using fluorescent techniques, showing potential drug transport applications.[134] Another example of a delivery system is a PA containing cell adhesive MMP-2 (matrix metalloprotease-2) sensitive peptide domain, which was shown to form fibrillar hydrogels. This PA can deliver anti-cancer agent cisplatin through enzymatic degradation.[135]

Cationic PAs have also been shown to be useful in gene therapy. The PAs H_5R_{10} and $H_{10}R_{10}$ were conjugated to cholesterol.[136] They were shown to assemble into cationic micelles, which lead to increased localization charge and increased DNA binding. $H_{10}R_{10}$ was shown to stimulate higher gene expression, probed through use of a reporter gene in HEK293 and Hep62 cells.[136] Moreover, $A_{12}H_5K_{10}$ and $A_{12}H_5K_{15}$ were also investigated.[137] Through the same reporter assay, these PAs were shown to have improved gene expression compared to non-amphiphilic control peptide, and a more favourable cytotoxicity profile compared to polyethyleneimine (PEI), a commonly used synthetic DNA-condensing polymer. Simultaneous delivery of genes (either p53 tumour suppressor or luciferase reporter gene) and doxorubicin was examined using Ac-$(AF)_6H_5K_{15}$-NH_2.[138] This PA self-assembled into micelles with the ability to encapsulated condensed DNA and doxorubicin, with delivery efficiency and in vitro expression examined in HePG2 cells.

It has also been possible to use PAs to study endocytosis. One such PA, based on p53 tumour suppressor, comprised of this pro-apoptotic peptide attached to C_{16} lipid chain. Internalization was investigated using fluorescent methods. This PA was shown to self-assemble into rod-shaped micelles. FRET (fluorescence resonance energy transfer) showed internalization of monomers into SJSA-1 human osteosarcoma cells as opposed to micelles, and uptake was enhanced by lipidation.[139]

1.11.3 Peptide Hormones

Hormones are tightly regulated chemical messengers produced by the endocrine system, to regulate growth, development, tissue function, metabolism, sleep, reproduction, mood and sexual function.[11,140] In the endocrine system there are two major types of hormone, steroid hormones which are water-insoluble hormones, and peptide hormones which are water soluble hormones. Steroid hormones generally interact through permeating cells with intracellular targets, e.g. DNA. Peptide hormones generally act on the surface of target cells, binding to specific receptors on membrane surfaces which trigger downstream signalling cascades.

Imbalance of peptide hormones can cause disease, for example type II diabetes, which is caused by cells becoming insensitive to peptide hormone insulin, due to repeatedly high levels in the blood stream.[141] Peptide hormones may also be used therapeutically. One example is insulin, which is used to treat type I diabetes, caused by the pancreas not making enough to control blood sugar levels.[142] Another example is oxytocin, which is both produced naturally by the pituitary gland, playing a role in social bonding, and is used as a therapeutic during childbirth to induce labour and prevent excessive blood loss.[143,144] Oxytocin is heat sensitive, limiting it’s therapeutic use. Thus an analogue of oxytocin, Carbetocin, was developed as an alternative therapeutic for areas where correct storage cannot be guaranteed.[145]

There is increased interest in peptide hormones that may be able to self-assemble to increase efficacy and stability in vivo. One example is oxyntomodulin, a 29 amino acid long peptide hormone, expressed naturally as an appetite suppressant. Oxyntomodulin was found to have increased activity in rats, when injected in a nanofibril conformation. The self-assembly is reversible, causing slower release of the active in vivo.[146] Peptide YY (PYY_{3-36}) is a gastrointestinal peptide hormone that has been shown to reduce calorific intake in mice when higher levels are present. PYY, which has an α-helical secondary structure, has a short half-life *in vivo*, therefore there is interest in chemical modifications to increase stability,[147] such as PEGylation mentioned in Section 1.7.

1.11.4 Antimicrobial Peptides

The increased prevalence of multi antibiotic-resistant pathogens has been listed by the World Health Organisation (WHO) as one of the biggest threats to modern day healthcare, food security and development.[148] Antimicrobial resistance is the reduced effectiveness of a previously active substance against a microbe, where the microbe has evolved this resistance through changes in one/a combination of factors including, but not limited to, gene expression, membrane composition and enzyme expression. This process occurs naturally, although is accelerated by the over usage of antibiotics in medicine and agriculture, and the lack of development of new actives by pharmaceutical companies.[149] Table 1.2. lists the bacteria that are prioritised by the most important targets for new therapies, as listed by the WHO.[148]

Antimicrobial peptides (AMPs) are attracting attention as an alternative to conventional antibiotics, and can target a range of microbes including viruses, fungus, bacteria and parasites. They have several attractive qualities.[149–152] Firstly, they are highly effective against gram-negative bacteria, which are harder to target due to their double membrane cell wall.[153] Secondly, AMPs commonly interact non-specifically with microbes, leading to a ‘multiple-hit’ strategy, enabling to kill microbes through more than one antimicrobial mechanism at the same time, increasing the likelihood of targeting multi-drug resistant bacteria.[154,155] Another advantage of this non-specificity is that is harder for the microbe to develop resistance, as the AMP does not target one specific protein/pathway. Finally, the rapid action of AMPs (with some able to kill microbes in seconds) also increases the difficulty for microbes to develop resistance. [156]

Table 1.2. *Priority list devised by the World Health Organisation (WHO) of resistant bacteria species.* [148]

	Species	Gram	Resistant to
Critical	*Acinetocater baumanni*	-ve	Carbapenem
	Pseudomonas aeruginosa	-ve	Carbapenem
	Enterobacteriacae (including E.coli)	-ve	Carbapenem, ESBL-producing
High	*Enterococcus Faecium*	+ve	Vancomycin
	Staphylococcus aureus	+ve	Methicillin, Vancomycin
	Helicobacter pylori	-ve	Clarithromycin
	Camplyobacter Spp.	-ve	Fluoroquinolone
	Salmonellae	-ve	Fluoroquinolone
	Neisseria gonorrhoeae	-ve	Cephalosporin
Medium	*Streptococcus pneumoniae*	+ve	Penicillin
	Haemophilus influenzae	-ve	Ampicillin
	Shigella	-ve	Fluoroquinolone

1.11.4.1 Structure and classification.

Antimicrobial peptides, (AMPs) are generally oligopeptides, ranging in lengths from 5 amino acids to 100 amino acids. [149–152] long. Most AMPs are cationic, due to the abundance of lysine and arginine residues,[157–160] allowing AMPs to interact with the anionic microbe membrane. AMPs also contain ~40% hydrophobic residues, making them amphiphilic.[152] This enables AMPs to interact with both the phospholipid head group (hydrophilic part) and the lipid tail group (hydrophobic part). Due to the cationic charge of the majority of AMPs, they are often referred to as cationic antimicrobial peptides, or, in the case of natural AMPs, cationic host-defence peptides. There are also naturally occuring of AMPs with low positive charge, neutral charge and anionic charge, for example dermcidin secreted from sweat glands in humans.[161,162] Some other important amino acids frequently found in both naturally occurring and synthetic AMPs are proline,[163] tryptophan,[149,152,164] cysteine,[165] glycine,[166,167] and histidine.[168]

Due to the high diversity of AMPs, they are generally categorised into four groups based on their secondary structure. These are: β-sheet forming, α-helical forming, extended or loop structures.[169,170] The most studied class of these is α-helical forming antimicrobials, which include magainin,[171] indolin, ,[172] and LL-37.[173,174] β-sheet forming AMPs usually consist of two β-sheet strand structures stabilised by S-S bridges.

Some AMPs are cyclic, and do not fit into these four classes. Some examples include surfactin, iturins and lichenysin, which have antifungal properties[175]. Surfactin, produced by *B.subtilis*, has the ability to reduce the surface tension of water to 27 mN m^{-1} at concentrations as low as 20 µM. This peptide self-assembles into spherical micelles in bulk aqueous solution, and adopts a more globular conformation at the interface (for example air/water).[12,176] Several cyclic peptides have been approved by the FDA, including Oritavancin and Dalbavancin, which are used to treat skin infections.

1.11.4.2. Mechanism of action

AMPs which are α-helical or β-sheet forming generally target the anionic lipopolysaccharide layer of the cell membrane on microorganisms, which is ubiquitous. Eukaryotic membranes (found in animals and plants), which are rich in cholesterol and low in negative charge may not be targeted by AMPs. Methods by which antimicrobial peptides interact with membranes are listed in Table 1.3. As well as membrane interactions, some extended structures have been observed to be bactericidal by moving across membranes and interacting with DNA sequences or metabolic enzymes.

Table 1.3. *Mechanisms of action by AMPs.*[154]

Interaction Model	Mechanism	Ref
Detergent-like / Carpet Model	Peptide coats a small area of the membrane, leading to bilayer penetration and pore formation	177–179
Membrane Thinning	Peptides insert themselves into one side of the bilayer, causing gaps in the lipid bilayer molecules, causing thinning	180,181
Aggregate	Peptides stick parallel to the membrane surface, then reorientation occurs causing peptide spheres to form inside the membrane	182
Toroidal Pore	Peptides are orientated with the hydrophobic region associated with the centre part of the lipid bilayer, and hydrophilic regions facing the pore.	183,184
Barrel-Stave	Staves form parallel to the membrane, which the further assemble into barrelles which insert into the bilayer.	185–187

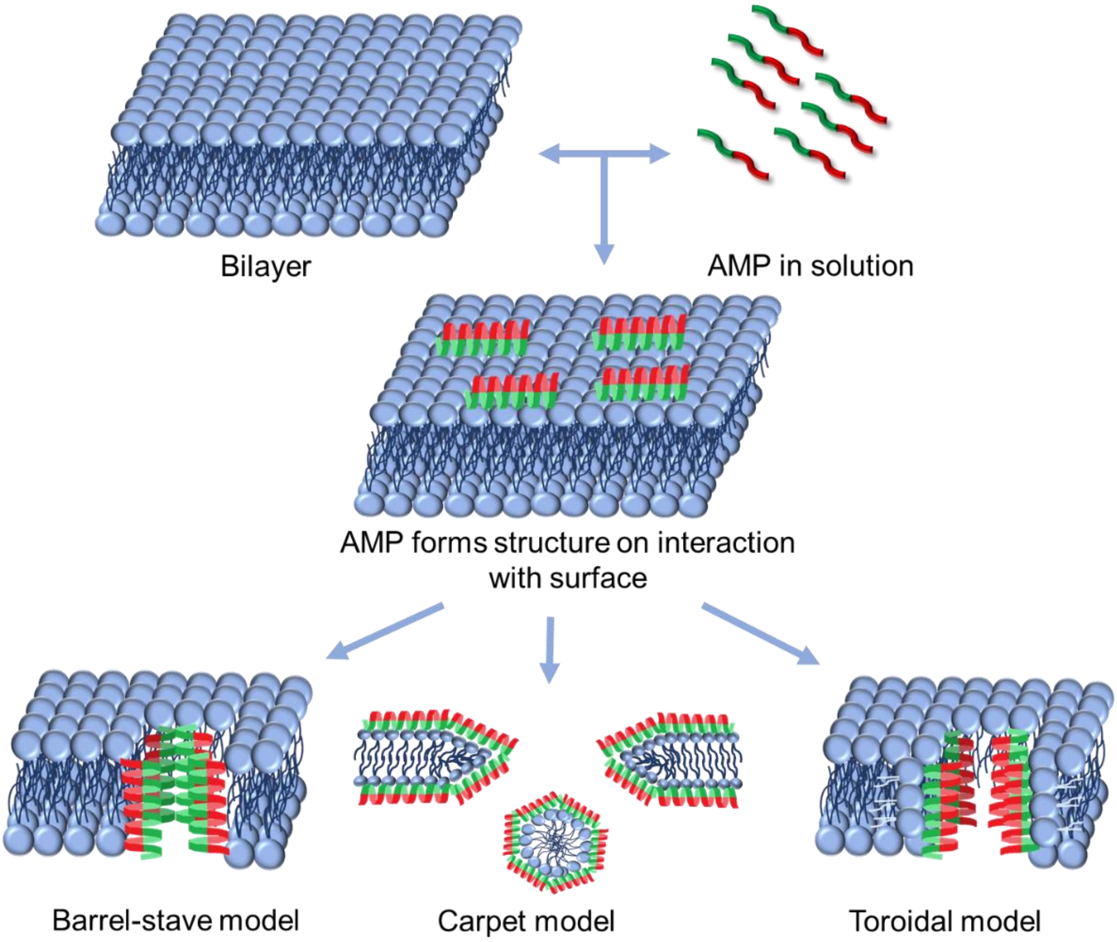

Figure 1.14. *Mechanism of membrane interactions of AMPs.*

1.11.4.3 Clinical antimicrobial peptides

To date, very few AMPs are available clinically. One of the most known AMP is Daptomycin. Daptomycin was approved as an antibiotic by the FDA in the mid-1980s. Several other AMPs are in use in other areas of the world, with many more in clinical trials, (listed in Table 1.2). Daptomycin self-assembles into micelles that assist delivery to the bacterial cell membrane, which was previously thought to be Ca^{2+} dependent.[188] However, recently Hamley and co-workers proved daptomycin could self-assemble into micelles spontaneously in aqueous solutions, with and without Ca^{2+}.[74]

The mechanism by which Daptomycin causes bacterial cell death is unclear.[188] Daptomycin inserts into the lipid bilayer, a process which is largely dependent on the presence of lipid PG (discussed in section 1.12.1). After this, there are two possible mechanisms of action. The first is linked to membrane depolarisation due to Daptomycin forming pore structures in the membrane, resulting in ion leakage and loss of membrane potential. The second proposed model involves Daptomycin aggregating at the membrane surface, causing bending and pore formation.[188]

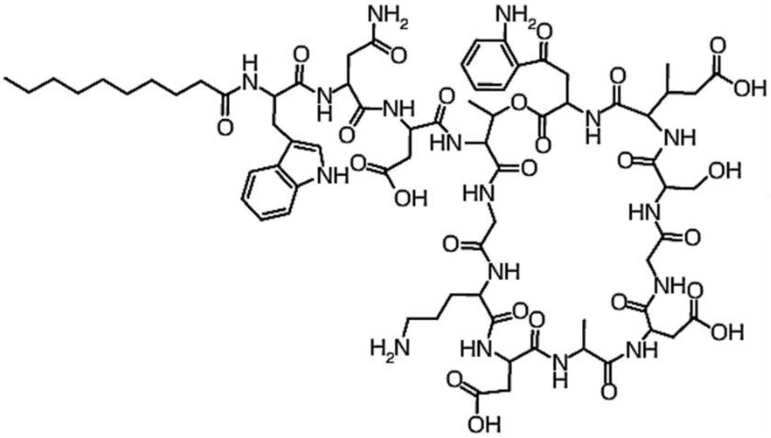

Figure 1.15. *Daptomycin. This peptide has an anionic charge and disrupts the membrane of gram-positive bacteria.*

There are a large number of AMP’s under clinical investigation (Table 1.4.). Interesting actives include several pre-clinical trial AMPs, such as Novamycin (RRRRRRRRRRRRR)[189] Novarifyn (RRRFRFFFRFRRR)[190] and D2A21 (FAKKFAKKFKKFAKKFAKFAFAF).[191] These are rich in arginine, alanine and phenylalanine, which are residues used in this thesis to construct potential short AMP’s.

Table 1.4. *AMPs in clinical trials or preclinical trials*[156]

Name	Structure	Net charge	Target	Mechanism	Administration	Ref
In use						
Nisin A	Polycyclic CP	+	*E.coli, S.aureus*	Membrane disruption / Immunomodulation	Food preservative	192
Gramicidin S	Cyclic, cationic, β-sheet	+	*E.coli, S.aureus*	Membrane disruption	Topical	193
Polymixin	Polycationic, lipopeptide	+	*K.pneumonia, A.baumannii*	Membrane disruption	Oral / Intravenous	194
Daptomycin*	Anionic, cyclic, lipopeptide	-	MRSA, VRE	Membrane disruption	Intravenous	195
Clinical trial Stage III						
Pexiganan	α-helical, cationic, amphiphilic	+	Diabetic foot ulcers	Membrane disruption / Immunomodulation	Topical	196
Surotomycin	Macrocyclic, lipopeptide	-	*C.difficile*	Membrane disruption	Oral	197
Ramoplanin	Macrocyclic Lipopeptide	+	G(+) (VRE, *C.difficile*)	Cell wall synthesis	Oral	198
D2A21	α-helical, cationic, amphiphilic	+	Burn wound infections	Membrane disruption	Topical	191
SGX942	Cationic	+	Oral mucositis	Immunomodulation	Oral rinse	199
PXL01	Cationic	+	Postsurgical adhesions	Immunomodulation	Topical	200
POL7080	Cationic, macrocyclic	+	*p.aerguinosa k.pneumonaie*	LptD binding	Intravenous	201
Clinical trial stage II						
EA-230	Short peptide	-	Sepsis and Renal Failure protection	Immunomodulation	Intravenous	202
Delmitide	Cationic	+	Inflammatory bowel disease	Immunomodulation	Topical	155

Ghrelin	α-helical, cationic, amphiphilic lipopeptide	+	Chronic respiratory failure	Immunomodulation	Intravenous	203
C16G2	α-helical, cationic, amphiphilic	+	Tooth decay by *S.mutans*	Membrane disruption	Mouth wash	204
DPK-060	Radom coil, cationic	+	Acute external otitis	Membrane disruption / Immunomodulation	Ear drops	205
PAC113	α-helical, cationic, amphiphilic	+	Oral candidiasis	Membrane disruption / Immunomodulation	Mouth rinse	191
LTX-109	Cationic, amphiphilic	+	G(+) MRSA skin infections, impetigo	Membrane disruption	Nasal Topical	206
Clinical trial stage I						
hLF1-11	α-helical, cationic, amphiphilic	+	MRSA, *K.pneumonaie*, *L.monocytogenes*	Membrane disruption / Immunomodulation	Intravenous	207
Wap-8294A2	Macrocyclic, thioesther	+	G(+) bacteria (VRE, MRSA)	Membrane disruption	Topical	208
Friulimicin B	Macrocyclic, lipopeptide	-	Pneumonia, MRSA	Membrane disruption	Intravenous	209
Pre-clinical						
Novamycin	Cationic	+	Fungal infections	Membrane disruption	Topical	189
Novarifyn	Cationic, amphiphilic	+	Broad-spectrum G(+) and G(-)	Membrane disruption	Topical	190
D2A21	α-helical, cationic, amphiphilic	+	Skin infections, *P.aeruginosa*	Membrane disruption	-	191
HB1345	Cationic, lipopeptide	+	Skin infections, acne	Immunomodulation	Topical	210

1.11.4.4 Challenges of AMPs

The main challenge AMPs face is *in vivo* stability. Naturally occurring and synthetic AMPs can be readily degraded by proteolytic enzymes. One way to overcome this is to use chemical modifications, for example lipidation,[211] insertion of D-amino acids into cleavage sites, macro-cyclisation of the C and N termini, and/or the insertion of noncanonical amino acids or peptide-mimetic materials. Another method to overcome this to transport the peptide in a delivery system, which can lead to targeted release.[12,85,156]

Self-assembly may also increase efficacy by increasing the local concentration of the AMP. One example is LL-37, which forms dimers on gram-negative bacteria membranes, leading to the formation of toroidal holes.[173,174,212] Moreover the cell penetrating peptide TAT (YGRKKRRQRRR) peptide from HIV retrovirus, [213,214] had increased antimicrobial strength and membrane translocation when conjugated to polyarginine and cholesterol. This drove self-assembly into micelles, and has shown to be effective in rabbit and mouse models against *S.aureus.*[215]

AMPs are also easily affected by different conditions including physiological salt conditions and pH, which can cause loss of electrostatic interactions between the cell membrane and peptide to occur. Additionally, AMPs can indirectly bind to serum proteins (e.g. albumin) thus losing efficacy. Some AMPs have also been reported to interact with mammalian cells as well as bacterial cells, inducing toxicity.[150,151,156,165]

Manufacturing AMP’s through solid phase synthesis is expensive.[156] One method to overcome this is to use short peptides. Small synthetic peptides (peptides below 10 aa) could be a good alternative to reduce the cost of synthesis. Synthetic short peptides containing arginine and tryptophan have been shown to be sufficient in killing bacteria, when using sequences $[RW]_n$-NH_2 where n = 1-5.[216] Overall the optimum length was found to be 3 repeating units as though higher units displayed higher activity, the toxicity to red blood cells was also increased. Moreover, lysine-based di- and tri- PAs showed that antimicrobial activity on Gram-positive and Gram-negative bacteria occurred through leakage, caused by cell membrane disruption.[175] Other methods of peptide synthesis including bioengineering and fermentation.

1.12 Lipid Bilayers

In the design of peptides which can be used therapeutically, it is important to consider their interactions with lipid bilayers. Lipid bilayers surround nearly all cell types, providing basic structural support. Bilayers act as a barrier both against outside molecules, and to stop various molecules (e.g. proteins, ions, organelles) from diffusing out. Compositions of membranes differ depending on species and the kingdom from which the organism originates. Thus, consideration of peptide interaction with the lipid bilayer is essential in the consideration of peptides for therapeutic use. Interaction with lipid bilayers can be examined in three main ways; 1) biophysical membrane models 2) in vitro models and 3) in vivo models.

1.12.1 Components of Lipid Bilayers

Membranes mainly consist of 3 major types of lipid (Figure 1.16)[217–220] The main components of lipid bilayers in animal and bacteria cells are phospholipids. Phospholipids are amphipathic molecules containing glycerol linked to a phosphate head group and two hydrocarbon chains. The most abundant structures of different phosphate headgroups can be seen in figure 1.16. The second class of lipids are sphingosines, which have a core of 1-amino-2-hydroxyethane, with substitutions. Sphingosines contain a choline derivative sphingomyelin (SP) which is similar to phosphatidyl choline (PC) in terms of headgroup and no charge. Alternatively, sphingosine head groups may also have complex sugars, broadly classed as glycolipids, which are present in some human cell types. Sphingosines also have hydrocarbon fatty acid chains. The final lipid class found in membranes are sterols. Sterols are structurally very different from the other groups of membrane lipids. The bacterial equivalent of sterols are hopanoids (Figure 1.13). [218,221]

Two of the three major groups, of lipids contain acyl groups. These acyl groups generally range from C_{12}– C_{30} and give a huge amount of variation to the lipid classes found in biomembranes. It is very rare that the two fatty acids attached to the functional head groups are identical. The length of the fatty acids and the amount of saturation ultimately determines the fluidity of the bilayer.[218]

All these classes of membrane lipid are amphiphilic, which leads to spontaneous self-assembly into bilayers in aqueous environments, with the lipid tails facing inward, and the polar head groups facing the solution. This then assembles further into either vesicles/liposomes or micelle like structure to ‘seal-off’ the hydrophobic region from the aqueous environment.

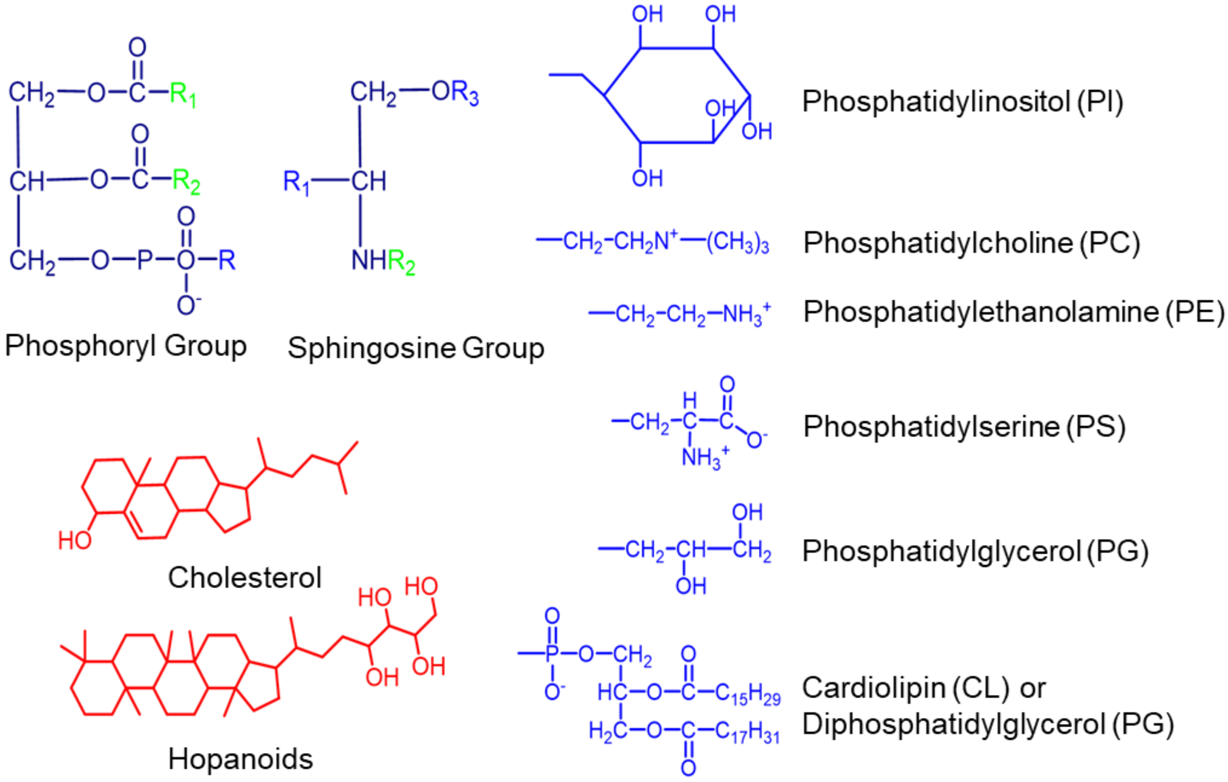

__Figure 1.16.__ the phosphoryl head group, and sphingosine head group, where R blue groups have one of the righthand side head groups attached, and the green R groups generally have acyl chains attached. In the red are the sterols and hopanoids groups.

Generally, biological membranes are asymmetric due to the composition of lipids, as well as proteins and sugars.[222,223] The degree of asymmetry can range depending on cell type, from complete symmetry (PC in blood platelet membranes) to unilateral (e.g. PS in rat erythrocytes).[221] Some of these asymmetric variations can be documented in liposome preparations, for example PC/PE mixtures showing PC has preference for the outer face and PE for the inner face of the vesicle.[223] The asymmetry strongly depends on deviation from complete homogeneity of lateral mixing membrane components. Biological membranes are found in lamellar phase symmetry, however other structures have been observed in artificial membranes through heating (Figure 1.17).[193,224,225]

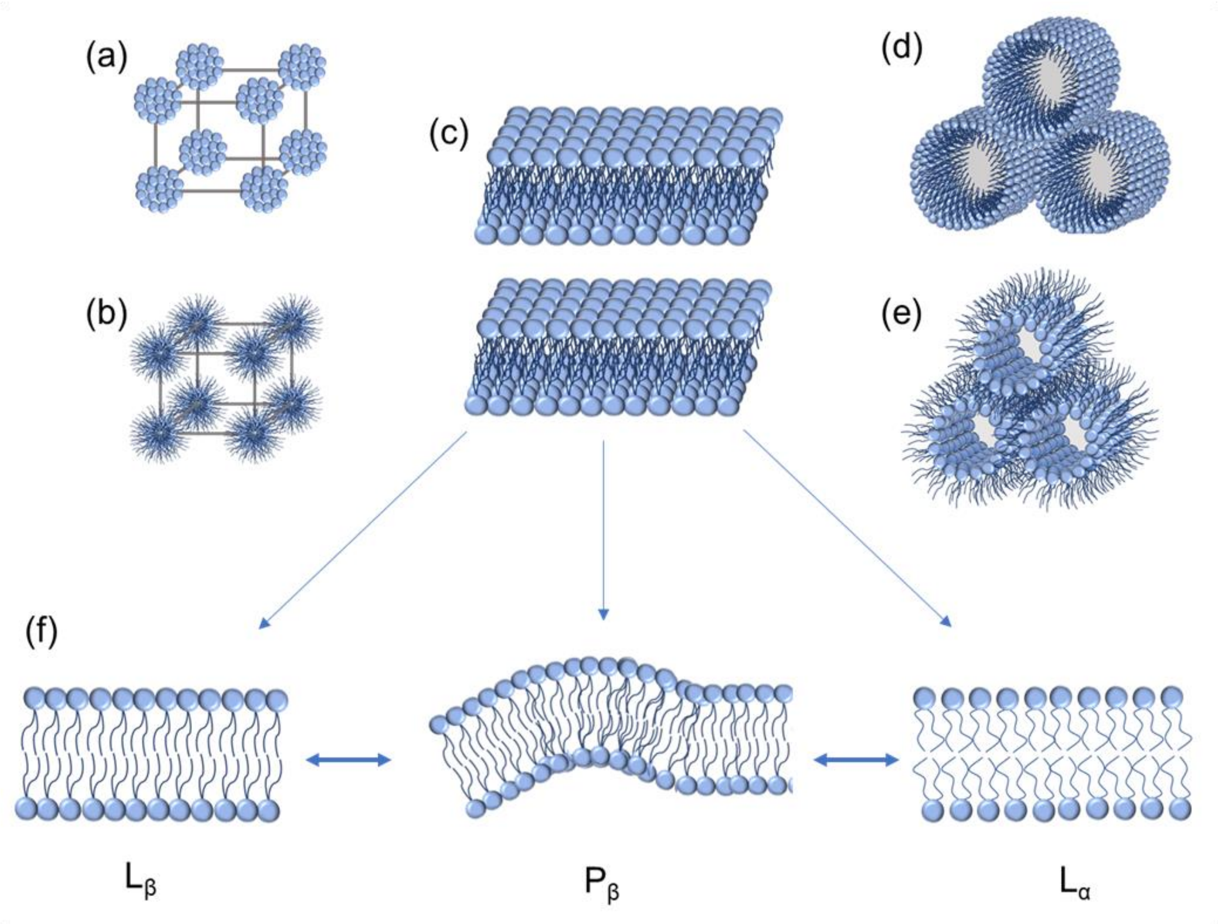

Figure 1.17. *Different types of structures of lipid micelles or membranes. a) cubic phase in aqueous (aq) solvent and b) cubic phase in organic solvent, c) lamellar phase in aqueous solvent, the form generally of most cell bilayers, d) hexagonal phase symmetry in aq solvent e) hexagonal phase in organic solvent and f) different temperature phases within the lamellar phase,* L_β*= lamellar solid crystalline phase,* P_β *= the transition phase and* L_α*= the liquid crystalline phase.*

Although membranes are ubiquitous to all cells, there are composition differences between groups of cells (Table 1.5). The most abundant phospholipids in animal cells are PC, PS and PE, with cholesterol. Generally bacteria contain no sphingolipids and trace amounts of steroids. The major components of bacterial membranes are cardiolipin, PE and PG (with no PC), with hopanoids. Overall this gives bacteria membrane a greater negative charge than the mammalian membrane.[218]

Table 1.5. *Lipid headgroup ratios in different membranes found in bacteria and humans.* [218,221] .

	CL	PG	PE	PC	PS	Sphingomyelin	Cholesterol
Gram Negative Bacteria							
E.coli	5	15	80	-	Trace	-	-
E.cloacae	3	21	74	-	-	-	-
K.pneumoniae	6	5	82	-	-	-	-
P.aeruginosa	11	21	60	-	-	-	--
Gram positive							
S.aureus	42	58	-	-	-	-	-
S.pneumoniae	50	50	-	-	-	-	-
B.cereus	17	40	43	-	-	-	-
Human Cell types							
Liver plasma cell	-	-	7	24	4	19	17
Red blood cell	-	-	18	17	7	`8	23
Myelin	-	-	`5	10	9	8	22
Mitochondrion	12	-	28	44	2	0	3
ER	-	-	17	40	5	5	6

CL is cardiolipin, PG is phosphatidyglycerol, PE is phosphatidylethanolamine, PC is phosphatidylcholine, PS is phosphatidylserine

1.12.2 Physical States of Membranes

Temperature changes in bilayers result in mesomorphic states. Below the transitional temperature T_m, membranes exist in the solid crystalline L_β phase.[226–228] In the L_β phase, there is very little lateral movement of the acyl chains in the phospholipids, and the acyl chains will mainly be in trans confirmation. Above the transition temperature, the membrane will mainly exist in the liquid crystalline L_α phase. This permits free rotation of the acyl chains around the normal axis plane, which leads to the formation of rotamers of acyl chains. Overall the effect of this is increased volume of the bilayer and decreased membrane viscosity in the L_α phase. This is because in the L_β phase, the acyl chain is more condensed, 0.2-0.23 nm^2 per chain, whereas in the L_α phase the alkyl chains have more rotational freedom, and will take up around 0.3-0.4 nm^2 per chain.[16,218,229] In the transition L_α to L_β phase and vice versa, there is a pre-transition phase, P_β phase, which is characterised by a ripple distortion of the bilayer plane.

The L_β and L_α phases are not well separated phases. Actually, there are defects in the lattice parameters of both L_β and L_α phases, the number of which increases upon heating. These defects give rise to domain formation of areas of the bilayer that will transition faster and areas that will transition slower. Thus, if the transition is approached on heating, islands of fluid lipid are observed, floating on a 'sea' of crystalline solid phase, and if the transition is approached from cooling, islands of solid float on a 'sea' of liquid. [226–228] The interfacial sites between these islands are the areas with higher amounts of permeability to molecules.

Sterols and hopanoids also affect the transition temperature. [221,226–228] Sterols have rigid four-ringed cores which in the L_α phase prevents adjacent acyl chains from freely rotating, thus increasing rigidity. In the L_β phase, sterols remain *in situ*, preventing surrounding phospholipids from forming crystal lattice structures. Thus, increase in sterols or hopanoid content in the membrane gradually abolishes the transition from L_α to L_β and vice versa, without shifting the melting temperature, T_m. For membranes consisting of PC mixed with cholesterol, the T_m observed by DSC was not present at 22% cholesterol and above.[230]

The temperatures at which lipids transition is largely dependent on many factors, including the length, saturation, positioning of C=C bonds, branching and positioning of the acyl chain to the polar head group, charge of the overall phospholipid, and which head group the phospholipid has. PE has the highest melting temperature, followed by PS, and then PC and PG which are equivalent. In nature, tight regulation on the fluidity of the membrane is essential for survival. Several types of extremophile bacteria alter their alkyl lipid chain lengths based on their immediate environment in order to maintain membrane fluidity.[229]

1.12.2 Biophysical methods to study membrane interactions

Membrane models can be made in vitro using commercially available lipids. Both the selection of lipids, and ratios of phospholipids/sphingolipid/sterols can be varied to make simplified models of specific cell types or organisms. The majority of membrane lipids used to make models are phospholipids as they are the most abundant lipid in membranes. Phospholipids can form a range of structures including disks, bilayers, monolayers and vesicles (which can be multi-lamellar or unilamellar), depending on preparation. Moreover, they generally have well characterised phase diagrams, [231] and can form in a variety of different buffers, making them a convenient tool in understanding mechanisms and interactions.

Models can be examined using a number of techniques including differential scanning calorimetry,[232–234] small-angle X-ray scattering, fluorescence (to examine leakage),[235] dynamic light scattering[236] and microscopy techniques. [59,232,233,237–240]

1.12.3 In-vitro methods

1.12.3.1 Bacteria

Although membrane models can be well characterised, giving an idea about potential interactions, bacteria are much more complex than biophysical models. As well as having membranes, bacteria also have cell walls and periplasm. These combined structures are called the bacterial envelope. Bacteria can be categorised as Gram-negative or Gram-positive, depending on whether they bind the Gram stain, which ultimately shows large differences in the envelope structure. [241–243]

Gram-positive bacteria have a thick layer of peptidoglycan in their envelope. Peptidoglycan is a mesh like polymer composed of sugars and amino acids, which gives the bacterial cell wall rigidity. These layers also contain teichoic acids, which often carry oligosaccharide chains and D-alanine residues. [242]

Gram-negative envelopes are much more complex, thus they are harder to find actives against. The Gram-negative cell wall is mainly composed of outer membrane. The outer membrane is made up of an outer part, made up of lipid A, core and liposaccharides and porins. [241,243] The inner leaf is made up of phospholipids. In between the outer membrane and the cell membrane, there is the periplasmic space. The periplasmic space is defined as being a gel-like space, consisting of numerous proteins and a loosely ordered peptidoglycan layer. The outer membrane is connected to the peptidoglycan layer through lipoproteins. The complexity of the bacteria envelop increases the difficulty of AMPs-induced the membrane disruption. [241,243]

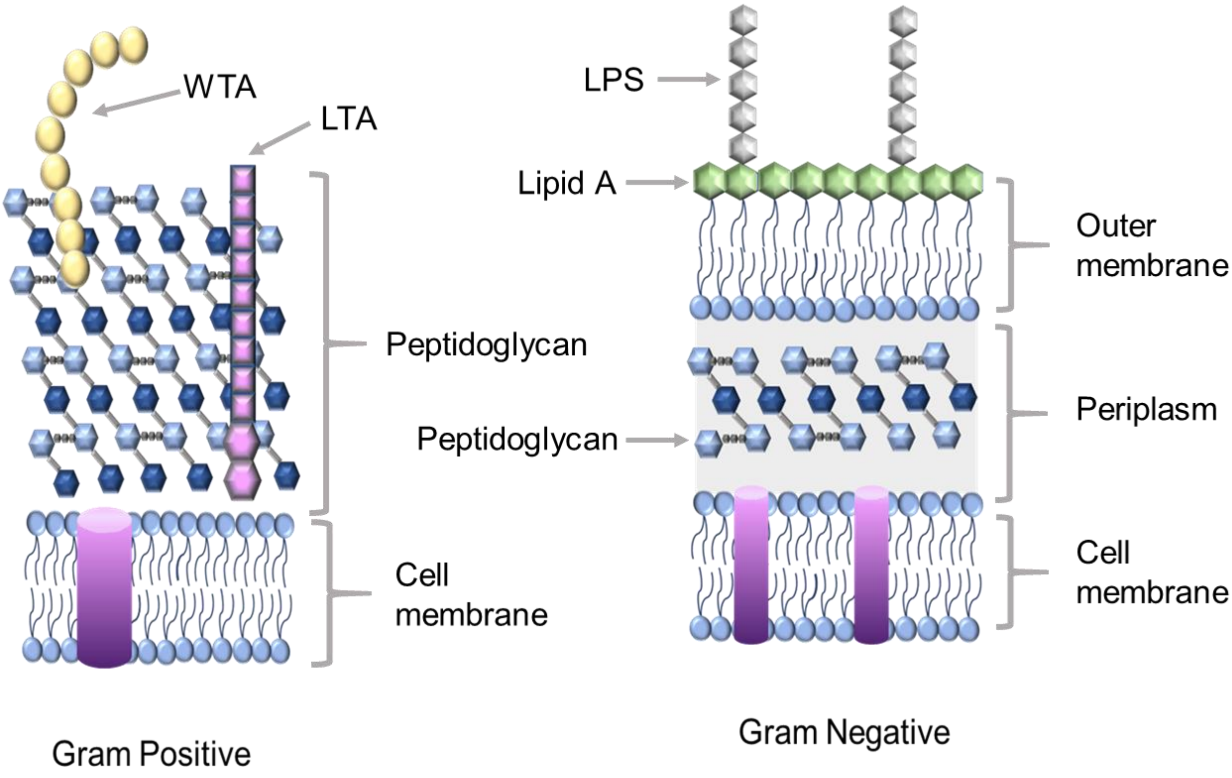

Figure 1.18. *Schematic of Gram positive and negative membranes, where WTA is wall teichoic acids, LTA is lipoteichoic acids and where LPS is lipopolysaccharides.*

Some bacteria may form biofilm matrices. Biofilm matrices form when free floating bacteria attach to a surface by secreting EPN (extracellular polymeric network) which is made up of sugars, proteins and nucleic acids. This enables bacteria to stick together, and attracts more bacteria to the site eventually ending up as a large 3D network.[244] Parts of this network may then break off and establish themselves elsewhere. Biofilm networks account for 80% of the infections in the human body, and can grow on implanted devices, for example *P.aeruginosa* can grow on catheters in a biofilm network.[244] The ability of bacteria to form biofilm networks increases the difficulty for actives to access the bacterial population. All the bacteria listed in Table 1.2 are able to form biofilms.

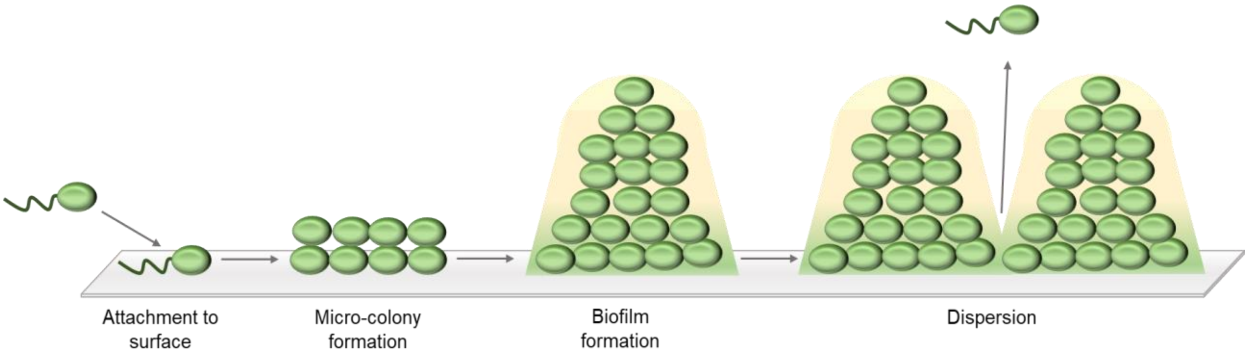

Figure 1.19. *Scheme of biofilm formation.*

One of the major regulators of biofilm formation is secondary messenger molecular 3’,5’-cyclic diguanylic acid (c-di-GMP).[245–247] A secondary messenger molecule is a molecule realised by a cell in response to a primary signal (or primary messenger molecule). Secondary messengers regulate physiological changes to the cell including proliferation, apoptosis, migration, survival and can trigger signalling cascades. In bacteria, c-di-GMP is a key regulator of numerous functions including differentiation, cell cycle, biofilm formation and dispersion, virulence and motility. Specifically for biofilms, low levels of c-di-GMP are associated with planktonic existence and high levels are associated with biofilm formation.[246] Recently proline-rich peptides were shown to be able to bind this secondary messenger, inhibiting the growth of *P.aeruginosa*. Thus c-di-GMP is an important target for AMPs.

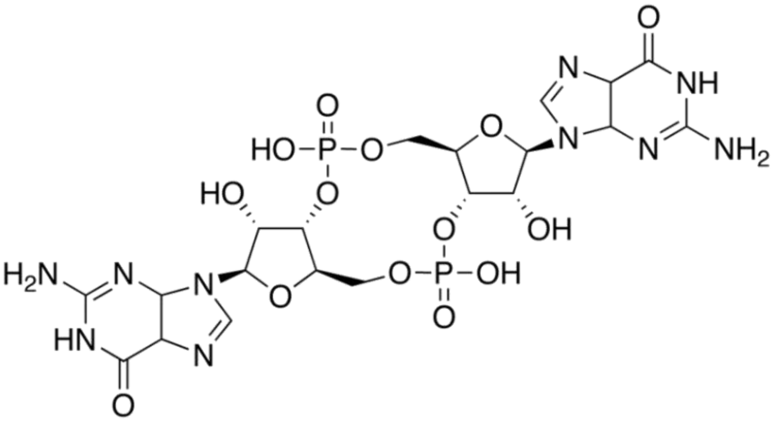

Figure 1.20. *Secondary messenger c-di-GMP, an important regulator of biofilm formation.*

1.12.3.2 Human cells

Human cells also have increased complexity compared to lipid models, due to the occurrence of many different proteins attached or associated with the membrane. Moreover, different cell types have different lipid compositions (Table 1.4) All types of eukaryotic cell have glycolipids on their outer surface that have important functions in cell interactions, cell recognition, protection and provide electrical effects. The most complex glycolipid are the gangliosides, which contain oligosaccharides with net negative charge.[221]

In vitro cell culture is often used as a first line examination of either activity or toxicity screening when examining new materials.[248] Peptides that are thought to target cancer may be tested in vitro cancer cell lines, or peptides for other uses may be tested in normal cell lines. Primary cells are extracted directly from a human/animal and are grown in media. These cells usually have a limited life-span but maintain more of the markers and characteristics seen in vivo. Cell lines (or secondary cells) are immortalised cells, taken from a host and grown from a single cell. Cell lines are easier to culture and manipulate. Due to years of circulation, most cell lines differ genetically and phenotypically from their original host. It is important to screen cell lines which are appropriate for the application. For example, if the application is intravenous, it is important to test against blood cell lines as well as the target tissue. [248]

1.12.5 In-vivo studies

In vivo studies are the final line of testing, which is stringently regulated. In vivo testing detects whether the active 1) goes to the correct place, without off-targets which result in toxicity/inflammation response, 2) can distinguish between target and non-target cells, for example an AMP would need to target bacterial cells, not host cells and 3) has good efficacy. In vivo studies present a range of complications and are thus are outside the scope of this thesis.

1.13 Aims and Objectives

This thesis aims to examine different peptides with potential therapeutic applications, using physical characterisation and in vitro studies using cell culture and bacteria. More specifically the aims are as follows:

- To investigate the self-assembly, membrane interactions and bioactivity through human cell culture and bacterial studies of short peptide sequences containing arginine and alanine, with A_nR or RA_nR structures. To examine the effect of hydrophobic block length and positioning on bioactivity and self-assembly. These peptides are hypothesised to have antimicrobial activity; thus experiments focus on whether this activity occurs in the physiological range, and whether this activity is predominantly due to membrane disruption.

- To investigate the self-assembly, membrane interactions and bioactivity of short symmetrical peptides rich in phenylalanine and arginine, using cell culture and bacterial studies, both in solution and in the biofilm matrix, and to examine their interactions with messenger molecule ci-d-GMP through biophysical techniques. These peptides are hypothesised to have antimicrobial activity, higher activity than the AnR or RAnR due to the cationic charge of these peptides being increased. Experiments focus on whether this activity occurs in the physiological range, and whether this activity is predominantly due to membrane disruption.

- To investigate the self-assembly and cytocompatibility of tyrosine-capped telechelic PEO-star conjugates of different sizes, for use as enzyme responsive delivery material, and hydrogels which may be used as tissue scaffolds.

- To investigate the self-assembling properties of neuropeptide hormone Oxytocin and heat stable derivative Carbetocin using biophysical characterisation techniques.

1.14 References

(1) Daura, X.; Gademann, K.; Jaun, B.; Seebach, D.; van Gunsteren, W. F.; Mark, A. E. Peptide Folding: When Simulation Meets Experiment. *Angew. Chemie Int. Ed.* **1999**, *38* (1/2), 236–240.

(2) Kaul, R.; Balaram, P. Stereochemical Control of Peptide Folding. *Bioorganic Med. Chem.* **1999**, *7* (1), 105–117.

(3) Esser, R.; Grotendorst, P. G. J.; Lewerenz, M.; BÜrgi, R.; Daura, X.; Mark, A. E.; Van Gunsten, W. F.; Bellenda, M.; Mammi, S.; Peggion, E. Reversible Peptide Folding in Dmso By Molecular Dynamics Simulation. *Mol. Dyn. Parallel Comput.* **2000**, 342–343.

(4) Zhao, X.; Pan, F.; Lu, J. R. Recent Development of Peptide Self-Assembly. *Prog. Nat. Sci.* **2008**, *18* (6), 653–660.

(5) Kent, S. B. H. Total Chemical Synthesis of Proteins. *Chem. Soc. Rev.* **2009**, *38* (2), 338–351.

(6) Fujiwara, K.; Toda, H.; Ikeguchi, M. Dependence of α-Helical and β-Sheet Amino Acid Propensities on the Overall Protein Fold Type. *BMC Struct. Biol.* **2012**, *12* (18), 6–15.

(7) Mandal, D.; Tiwari, R. K.; Nasrolahi Shirazi, A.; Oh, D.; Ye, G.; Banerjee, A.; Yadav, A.; Parang, K. Self-Assembled Surfactant Cyclic Peptide Nanostructures as Stabilizing Agents. *Soft Matter* **2013**, *9* (39), 9465–9475.

(8) Stupp, S. I. Self-Assembly and Biomaterials. *Nano Lett.* **2010**, *10* (12), 4783–4786.

(9) Dehsorkhi, A.; Castelletto, V.; Hamley, I. W. Self-Assembling Amphiphilic Peptides. *J. Pept. Sci.* **2014**, *20* (7), 453–467.

(10) Hamley, I. W. Self-Assembly of Amphiphilic Peptides. *Soft Matter* **2011**, *7*, 4122–4138.

(11) Hutchinson, J. A.; Burholt, S.; Hamley, I. W. Peptide Hormones and Lipopeptides: From Self-Assembly to Therapeutic Applications. *J. Pept. Sci.* **2017**, *23* (2), 82–94.

(12) Hamley, I. W. Lipopeptides: From Self-Assembly to Bioactivity. *Chem. Commun.* **2015**, *51* (41), 8574–8583.

(13) Gour, N.; Chandra Kanth, P.; Koshti, B.; Kshtriya, V.; Shah, D.; Patel, S.; Agrawal-Rajput, R.; Pandey, M. K. Amyloid-like Structures Formed by Single Amino Acid Self-Assemblies of Cysteine and Methionine. *ACS Chem. Neurosci.* **2019**, *10* (3), 1230–1239.

(14) Uyaver, S.; Hernandez, H. W.; Gokhan Habiboglu, M. Self-Assembly of Aromatic Amino Acids: A Molecular Dynamics Study. *Phys. Chem. Chem. Phys.* **2018**, *20* (48), 30525–30536.

(15) Zhou, P.; Deng, L.; Wang, Y.; Lu, J. R.; Xu, H. Different Nanostructures Caused by Competition of Intra- and Inter-β-Sheet Interactions in Hierarchical Self-Assembly of Short Peptides. *J. Colloid Interface Sci.* **2016**, *464*, 219–228.

(16) Marsh, D. Thermodynamics of Phospholipid Self-Assembly. *Biophys. J.* **2012**, *102* (5), 1079–1087.

(17) Johnson, K. A.; Borisy, G. G. Thermodynamic Analysis of Microtubule Self-Assembly in Vitro. *J. Mol. Biol.* **1979**, *133* (2), 199–216.

(18) Gardner, M. K.; Charlebois, B. D.; Janosi, I. M.; Howard, J.; Hunt, A. J.; Odde, D. J. Rapid Microtubule Self-Assembly Kinetics. *Cell* **2011**, *146* (4), 582–592.

(19) Mandal, D.; Nasrolahi Shirazi, A.; Parang, K. Self-Assembly of Peptides to Nanostructures. *Org. Biomol. Chem.* **2014**, *12* (22), 3544–3561.

(20) Chou, P. Y.; Fasman, G. D. Prediction of Protein Conformation. *Biochemistry* **1974**, *13* (2), 222–

245.

(21) Stendahl, J. C.; Rao, M. S.; Guler, M. O.; Stupp, S. I. Intermolecular Forces in the Self-Assembly of Peptide Amphiphile Nanofibers. *Adv. Funct. Mater.* **2006**, *16* (4), 499–508.

(22) Torchilin, V. P. Micellar Nanocarriers: Pharmaceutical Perspectives. *Pharm. Res.* **2007**, *24* (1), 1–16.

(23) Tu, R. S.; Tirrell, M. Bottom-up Design of Biomimetic Assemblies. *Adv. Drug Deliv. Rev.* **2004**, *56* (11), 1537–1563.

(24) Kita-Tokarczyk, K.; Grumelard, J.; Haefele, T.; Meier, W. Block Copolymer Vesicles - Using Concepts from Polymer Chemistry to Mimic Biomembranes. *Polymer (Guildf).* **2005**, *46* (11), 3540–3563.

(25) Greenfield, N. J. Applications of Circular Dichroism in Protein and Peptide Analysis. *TrAC - Trends Anal. Chem.* **1999**, *18* (4), 236–245.

(26) Greenfield, N. J. Using Circular Dichroism Spectra to Estimate Protein Secondary Structure. *Nat. Protoc.* **2007**, *1* (6), 2876–2890.

(27) Hirst, J. D.; Colella, K.; Gilbert, A. T. B. Electronic Circular Dichroism of Proteins from First-Principles Calculations. *J. Phys. Chem. B* **2003**, *107* (42), 11813–11819.

(28) Woody, R. W. Circular Dichroism Spectrum of Peptides in the Poly (Pro) II Conformation. *J. Am. Chem. Soc.* **2009**, *131* (23), 8234–8245.

(29) Barth, A. The Infrared Absorption of Amino Acid Side Chains. *Prog. Biophys. Mol. Biol.* **2001**, *74* (2000), 141–173.

(30) Barth, A. Infrared Spectroscopy of Proteins. *Biochim. Biophys. Acta* **2007**, *1767* (9), 1073–1101.

(31) Barth, A.; Haris, P. I. Biological and Biomedical Infrared Spectroscopy; IOS Press, 2009; Vol. 2.

(32) Castelletto, V.; Hamley, I. W. Methods to Characterize the Nanostructure and Molecular Organization of Amphiphilic Peptide Assemblies. In *Peptide Self-Assembly: Methods and Protocols*; Nilsson, B. L., Doran, T. M., Eds.; Springer New York: New York, NY, 2018; pp 3–21.

(33) Parker, M. W. Protein Structure from X-Ray Diffraction. *J. Biol. Phys.* **2003**, *29* (4), 341–362.

(34) Schnablegger, H.; Singh, Y. The SAXS Guide: Getting Acquainted with the Principles. *Ant. Paar* **2013**, 124.

(35) Blanchet, C. E.; Svergun, D. I. Small-Angle X-Ray Scattering on Biological Macromolecules and Nanocomposites in Solution. *Annu. Rev. Phys. Chem.* **2013**, *64* (November 2012), 37–54.

(36) Branco, M. C.; Schneider, J. P. Self-Assembling Materials for Therapeutic Delivery. *Acta Biomater.* **2009**, *5* (3), 817–831.

(37) Luzar, A.; Chandler, D. Hydrogen-Bond Kinetics in Liquid Water. *Nature* **1996**, *379*.

(38) Buckingham, A. D.; Del Bene, J. E.; McDowell, S. A. C. The Hydrogen Bond. *Chem. Phys. Lett.* **2008**, *463* (1–3), 1–10.

(39) Lippincott, E. R.; Scheoeder, R. One-Dimensional Model of the Hydrogen Bond. *J. Chem. Phys.* **1955**, *23*, 1099.

(40) Beer, P. D.; Gale, P. A.; Smith, D. K. Supramolecular Chemistry; Oxford University Press, 1999.

(41) Steed, J. W.; Atwood, J. L.; Gale, P. A. Definition and Emergence of Supramolecular

ChemistryAdapted in Part from Supramolecular Chemistry , J. W. Steed and J. L. Atwood, Wiley: Chichester, 2nd Ed., 2009. . In *Supramolecular Chemistry*; 2012.

(42) Mcgaughey, G. B.; Gagne, M.; Rappe, A. K. π-Stacking Interactions. **1998**, *273* (25), 15458–15463.

(43) Hawe, A.; Sutter, M.; Jiskoot, W. Extrinsic Fluorescent Dyes as Tools for Protein Characterization. *Pharm. Res.* **2008**, *25* (7), 1487–1499.

(44) Qiu, F.; Chen, Y.; Zhao, X. Comparative Studies on the Self-Assembling Behaviors of Cationic and Catanionic Surfactant-like Peptides. *J. Colloid Interface Sci.* **2009**, *336* (2), 477–484.

(45) Jones, R. R.; Castelletto, V.; Connon, C. J.; Hamley, I. W. Collagen Stimulating Effect of Peptide Amphiphile C16-KTTKS on Human Fibroblasts. *Mol. Pharm.* **2013**, *10* (3), 1063–1069.

(46) Giri, K.; Bhattacharyya, N. P.; Basak, S. PH-Dependent Self-Assembly of Polyalanine Peptides. *Biophys. J.* **2007**, *92* (1), 293–302.

(47) Levine, H. Thioflavine T Interaction with Synthetic Alzheimer's Disease B-amyloid Peptides: Detection of Amyloid Aggregation in Solution. *Protein Sci.* **1993**, *2* (3), 404–410.

(48) LeVine, H. Quantification of β-Sheet Amyloid Fibril Structures with Thioflavin T. *Methods Enzymol.* **1999**, *309*, 274–284.

(49) Greenfield, N. J. Using Circular Dichroism Specrea. *ProQuest Diss. Theses* **2009**, *1* (6), 2876–2890.

(50) Stuart, B. H. Infrared Spectroscopy: Fundamentals and Applications; Wiley, 2004.

(51) Barth, A. The Infrared Absorption of Amino Acid Side Chains. *Prog. Biophys. Mol. Biol.* **2000**, *74* (3–5), 141–173.

(52) Reimer, L.; Kohl, H. Transmission Electron Microscopy Physics of Image Formation; 2008.

(53) Guinier, A. La Diffraction Des Rayons X Aux Tres Petits Angles: Applications a l'etude de Phenomenes Ultramicroscopiques. *Ann. Phys. (Paris).* **1939**, *12*, 161–237.

(54) Gelain, F.; Cigognini, D.; Caprini, A.; Silva, D.; Colleoni, B.; Donegá, M.; Antonini, S.; Cohen, B.; Vescovi, A. New Bioactive Motifs and Their Use in Functionalized Self-Assembling Peptides for NSC Differentiation and Neural Tissue Engineering. *Nanoscale* **2012**, *4* (9), 2946.

(55) Jacques, D. A.; Guss, J. M.; Svergun, D. I.; Trewhella, J. Publication Guidelines for Structural Modelling of Small-Angle Scattering Data from Biomolecules in Solution. *Acta Crystallogr. Sect. D Biol. Crystallogr.* **2012**, *68* (6), 620–626.

(56) Breßler, I.; Kohlbrecher, J.; Thünemann, A. F. *SASfit* : A Tool for Small-Angle Scattering Data Analysis Using a Library of Analytical Expressions. *J. Appl. Crystallogr.* **2015**, *48* (5), 1587–1598.

(57) Cui, H.; Webber, M. J.; Stupp, S. I. Self-Assembly of Peptide Amphiphiles: From Molecules to Nanostructures to Biomaterials. *Biopolymers* **2010**, *94* (1), 1–18.

(58) Löwik, D. W. P. M.; van Hest, J. C. M. Peptide Based Amphiphiles. *Chem. Soc. Rev.* **2004**, *33* (4), 234–245.

(59) Dehsorkhi, A.; Castelletto, V.; Hamley, I. W.; Seitsonen, J.; Ruokolainen, J. Interaction between a Cationic Surfactant-like Peptide and Lipid Vesicles and Its Relationship to Antimicrobial Activity. *Langmuir* **2013**, *29* (46), 14246–14253.

(60) Vauthey, S. Molecular Self-Assembly of Surfactant-like Peptides to Form Nanotubes and Nanovesicles. *Proc. Natl. Acad. Sci.* **2002**, *99* (8), 5355–5360.

(61) Zhang, S. Fabrication of Novel Biomaterials through Molecular Self-Assembly. *Nat. Biotechnol.* **2003**, *21* (10), 1171–1178.

(62) Zhao, X. Design of Self-Assembling Surfactant-like Peptides and Their Applications. *Curr. Opin. Colloid Interface Sci.* **2009**, *14* (5), 340–348.

(63) Castelletto, V.; Hamley, I.; Perez, J.; Abezgauz, L.; Danino, D. Fibrillar Superstructure from Extended Nanotapes Formed by a Collagen-Stimulating Peptide Amphiphile. *Chem. Commun. (Camb).* **2010**, *46* (48), 9185–9187.

(64) Middleton, D. A.; Madine, J.; Castelletto, V.; Hamley, I. W. Insights into the Molecular Architecture of a Peptide Nanotube Using FTIR and Solid-State NMR Spectroscopic Measurements on an Aligned Sample. *Angew. Chemie* **2013**, *52* (40), 10537–10540.

(65) Fuhrhop, J. H.; Wang, T. Bolaamphiphiles. *Chem. Rev.* **2004**, *104* (6), 2901–2938.

(66) Valentine, D. L. Adaptations to Energy Stress Dictate the Ecology and Evolution of the Archaea. *Nat. Rev. Microbiol.* **2007**, *5* (4), 316–323.

(67) Santoso, S.; Hwang, W.; Hartman, H.; Zhang, S. Self-Assembly of Surfactant-like Peptides with Variable Glycine Tails to Form Nanotubes and Nanovesicles. *Nano Lett.* **2002**, *2* (7), 687–691.

(68) Eldredge, A. C.; Johnson, M. E.; Cao, Y.; Zhang, L.; Zhao, C.; Liu, Z.; Yang, Q.; Guan, Z. Dendritic Peptide Bolaamphiphiles for SiRNA Delivery to Primary Adipocytes. *Biomaterials* **2018**, *178*, 458–466.

(69) Yao, L.; He, M.; Li, D.; Liu, H.; Wu, J.; Xiao, J. Self-Assembling Bolaamphiphile-like Collagen Mimetic Peptides. *New J. Chem.* **2018**, *42* (9), 7439–7444.

(70) Hamley, I. W.; Burholt, S.; Hutchinson, J.; Castelletto, V.; Da Silva, E. R.; Alves, W.; Gutfreund, P.; Porcar, L.; Dattani, R.; Hermida-Merino, D.; et al. Shear Alignment of Bola-Amphiphilic Arginine-Coated Peptide Nanotubes. *Biomacromolecules* **2017**, *18* (1), 141–149.

(71) Silva, E. R. da; Alves, W. A.; Castelletto, V.; Reza, M.; Ruokolainen, J.; Hussaind, R.; Hamley, I. W. Self-Assembly Pathway of Peptide Nanotubes Formed by a Glutamatic Acid-Based Bolaamphiphile. *Chem Commun* **2015**, *51* (58), 11634–11637.

(72) Hill, T. A.; Shepherd, N. E.; Diness, F.; Fairlie, D. P. Constraining Cyclic Peptides to Mimic Protein Structure Motifs. *Angew. Chemie - Int. Ed.* **2014**, *53* (48), 13020–13041.

(73) Heinis, C.; Rutherford, T.; Freund, S.; Winter, G. Phage-Encoded Combinatorial Chemical Libraries Based on Bicyclic Peptides. *Nat. Chem. Biol.* **2009**, *5* (7), 502–507.

(74) Kirkham, S.; Castelletto, V.; Hamley, I. W.; Inoue, K.; Rambo, R.; Reza, M.; Ruokolainen, J. Self-Assembly of the Cyclic Lipopeptide Daptomycin: Spherical Micelle Formation Does Not Depend on the Presence of Calcium Chloride. *ChemPhysChem* **2016**, 2118–2122.

(75) Deres, K.; Rammensee, H.-G. In Vivo Priming of Virus-Specific Cytotoxic T Lymphocytes with Synthetic Lipopeptide Vaccine. *Nature* **1989**, *342*, 189–192.

(76) Krug, M.; Folkers, G.; Haas, B.; Hess, G.; Wiesmuller, K. H.; Freund, S.; Jung, G. Molecular Dynamics of the Alpha-Helical Epitope of a Novel Synthetic Lipopeptide Foot-and-Mouth Disease Virus Vaccine. *Biopolymers* **1989**, *28* (1), 499–512.

(77) Hamley, I. W.; Kirkham, S.; Dehsorkhi, A.; Castelletto, V.; Reza, M.; Ruokolainen, J. Toll-like Receptor Agonist Lipopeptides Self-Assemble into Distinct Nanostructures. *Chem. Commun.* **2014**, *50* (100), 15948–15951.

(78) Hamley, I. W. PEG-Peptide Conjugates. *Biomacromolecules* **2014**, *15* (5), 1543–1559.

(79) Swierczewska, M.; Lee, K. C.; Lee, S. What Is the Future of PEGylated Therapies? *Expert Opin.*

Emerg. Drugs **2015**, *20* (4), 531–536.

(80) Kolate, A.; Baradia, D.; Patil, S.; Vhora, I.; Kore, G.; Misra, A. PEG - A Versatile Conjugating Ligand for Drugs and Drug Delivery Systems. *J. Control. Release* **2014**, *192*, 67–81.

(81) Shechter, Y.; Tsubery, H.; Mironchik, M.; Rubinstein, M.; Fridkin, M. Reversible PEGylation of Peptide YY3-36 Prolongs Its Inhibition of Food Intake in Mice. *FEBS Lett.* **2005**, *579* (11), 2439–2444.

(82) Castelletto, V.; Hamley, I. W.; Seitsonen, J.; Ruokolainen, J.; Harris, G.; Bellmann-Sickert, K.; Beck-Sickinger, A. G. Conformation and Aggregation of Selectively PEGylated and Lipidated Gastric Peptide Hormone Human PYY 3-36. *Biomacromolecules* **2018**, *19* (11), 4320–4332.

(83) Hamley, I. W.; Cheng, G.; Castelletto, V. A Thermoresponsive Hydrogel Based on Telechelic PEG End-Capped with Hydrophobic Dipeptides. *Macromol. Biosci.* **2011**, *11* (8), 1068–1078.

(84) Kirkham, S.; Castelletto, V.; Hamley, I. W.; Reza, M.; Ruokolainen, J.; Hermida-Merino, D.; Bilalis, P.; Iatrou, H. Self-Assembly of Telechelic Tyrosine End-Capped PEO and Poly(Alanine) Polymers in Aqueous Solution. *Biomacromolecules* **2016**, *17* (3), 1186–1197.

(85) Jia, F.; Wang, J.; Peng, J.; Zhao, P.; Kong, Z.; Wang, K.; Yan, W.; Wang, R. D-Amino Acid Substitution Enhances the Stability of Antimicrobial Peptide Polybia-CP. *Acta Biochim. Biophys. Sin. (Shanghai).* **2017**, *49* (10), 916–925.

(86) Tugyi, R.; Uray, K.; Iván, D.; Fellinger, E.; Perkins, A.; Hudecz, F. Partial D-Amino Acid Substitution: Improved Enzymatic Stability and Preserved Ab Recognition of a MUC2 Epitope Peptide. *Proc. Natl. Acad. Sci. U. S. A.* **2005**, *102* (2), 413–418.

(87) Moradi, S. V.; Hussein, W. M.; Varamini, P.; Simerska, P.; Toth, I. Glycosylation, an Effective Synthetic Strategy to Improve the Bioavailability of Therapeutic Peptides. *Chem. Sci.* **2016**, *7* (4), 2492–2500.

(88) Feng, J.; Zhao, C.; Wang, L.; Qu, L.; Zhu, H.; Yang, Z.; An, G.; Tian, H.; Shou, C. Development of a Novel Albumin-Based and Maleimidopropionic Acid-Conjugated Peptide with Prolonged Half-Life and Increased in Vivo Anti-Tumor Efficacy. *Theranostics* **2018**, *8* (8), 2094–2106.

(89) Olsen, C. A.; Ziegler, H. L.; Nielsen, H. M.; Frimodt-Møller, N.; Jaroszewski, J. W.; Franzyk, H. Antimicrobial, Hemolytic, and Cytotoxic Activities of β-Peptoid- Peptide Hybrid Oligomers: Improved Properties Compared to Natural AMPs (ChemBioChem (2010) 11, (152-160)). *ChemBioChem* **2010**, *11* (12), 1630.

(90) Ahmed, E. M. Hydrogel: Preparation, Characterization, and Applications: A Review. *J. Adv. Res.* **2015**, *6* (2), 105–121.

(91) Singh, N.; Kumar, M.; Miravet, J. F.; Ulijn, R. V.; Escuder, B. Peptide-Based Molecular Hydrogels as Supramolecular Protein Mimics. *Chem. Eur. J.* **2017**, *23* (5), 981–993.

(92) Dasgupta, A.; Mondal, J. H.; Das, D. Peptide Hydrogels. *RSC Adv.* **2013**, *3* (24), 9117.

(93) Petka, W. A.; Harden, J. L.; Mcgrath, K. P.; Wirtz, D.; Tirrell, D. A. Reversible Hydrogels from Self-Assembling Artificial Proteins. *Science (80-.).* **1998**, *281* (5375), 389–392.

(94) Shen, W.; Zhang, K.; Kornfield, J. a; Tirrell, D. a. Tuning the Erosion Rate of Artificial Protein Hydrogels through Control of Network Topology. *Nat. Mater.* **2006**, *5* (2), 153–158.

(95) Stahl, P. J.; Romano, N. H.; Wirtz, D.; Yu, S. M. PEG-Based Hydrogels with Collagen Mimetic Peptide-Mediated and Tunable Physical Cross-Links. *Biomacromolecules* **2010**, *11* (9), 2336–2344.

(96) Jing, P.; Rudra, J. S.; Herr, A. B.; Collier, J. H. Self-Assembling Peptide-Polymer Hydrogels Designed from the Coiled Coil Region of Fibrin. *Biomacromolecules* **2008**, *9* (9), 2438–2446.

(97) Tzokova, N.; Fernyhough, C. M.; Butler, M. F.; Armes, S. P.; Ryan, A. J.; Topham, P. D.; Adams, D. J. The Effect of PEO Length on the Self-Assembly of Poly(Ethylene Oxide)-Tetrapeptide Conjugates Prepared by “Click” Chemistry. *Langmuir* **2009**, *25* (18), 11082–11089.

(98) Tzokova, N.; Fernyhough, C. M.; Topham, P. D.; Sandon, N.; Adams, D. J.; Butler, M. F.; Armes, S. P.; Ryan, A. J. Soft Hydrogels from Nanotubes of Poly(Ethylene Oxide)-Tetraphenylalanine Conjugates Prepared by Click Chemistry. *Langmuir* **2009**, *25* (4), 2479–2485.

(99) Lee, K. Y.; Mooney, D. J. Hydrogels for Tissue Engineering. *Chem. Rev.* **2001**, *101* (7), 1869–1879.

(100) Cheng, G.; Castelletto, V.; Jones, R. R.; Connon, C. J.; Hamley, I. W. Hydrogelation of Self-Assembling RGD-Based Peptides. *Soft Matter* **2011**, *7* (4), 1326–1333.

(101) Peppas, N. A.; Van Blarcom, D. S. Hydrogel-Based Biosensors and Sensing Devices for Drug Delivery. *J. Control. Release* **2016**, *240*, 142–150.

(102) Van Vlierberghe, S.; Dubruel, P.; Schacht, E. Biopolymer-Based Hydrogels as Scaffolds for Tissue Engineering Applications: A Review. *Biomacromolecules* **2011**, *12* (5), 1387–1408.

(103) DeForest, C. A.; Tirrell, D. A. A Photoreversible Protein-Patterning Approach for Guiding Stem Cell Fate in Three-Dimensional Gels. *Nat. Mater.* **2015**, *14* (5), 523–531.

(104) Slaughter, B. V; Khurshid, S. S.; Fisher, O. Z. Hydrogels in Regenerative Medicine. *Adv. Mater.* **2009**, *21* (0), 3307–3329.

(105) Yu, T. T.; Shoichet, M. S. Guided Cell Adhesion and Outgrowth in Peptide-Modified Channels for Neural Tissue Engineering. *Biomaterials* **2005**, *26* (13), 1507–1514.

(106) Murphy, W. L.; McDevitt, T. C.; Engler, A. J. Materials as Stem Cell Regulators. *Nat. Mater.* **2014**, *13* (6), 547–557.

(107) Thiele, J.; Ma, Y.; Bruekers, S. M. C.; Ma, S.; Huck, W. T. S. 25th Anniversary Article: Designer Hydrogels for Cell Cultures: A Materials Selection Guide. *Adv. Mater.* **2014**, *26* (1), 125–148.

(108) Miller, J. S.; Shen, C. J.; Legant, W. R.; Baranski, J. D.; Blakely, B. L.; Chen, C. S. Bioactive Hydrogels Made from Step-Growth Derived PEG-Peptide Macromers. *Biomaterials* **2010**, *31* (13), 3736–3743.

(109) Wilson, M. J.; Liliensiek, S. J.; Murphy, C. J.; Murphy, W. L.; Nealey, P. F. Hydrogels with Well-Defined Peptide-Hydrogel Spacing and Concentration: Impact on Epithelial Cell Behavior(). *Soft Matter* **2012**, *8* (2), 390–398.

(110) Liu, S. Q.; Tay, R.; Khan, M.; Rachel Ee, P. L.; Hedrick, J. L.; Yang, Y. Y. Synthetic Hydrogels for Controlled Stem Cell Differentiation. *Soft Matter* **2010**, *6* (1), 67.

(111) Hersel, U.; Dahmen, C.; Kessler, H. RGD Modified Polymers: Biomaterials for Stimulated Cell Adhesion and Beyond. *Biomaterials* **2003**, *24* (24), 4385–4415.

(112) Cooke, M. J.; Vulic, K.; Shoichet, M. S. Design of Biomaterials to Enhance Stem Cell Survival When Transplanted into the Damaged Central Nervous System. *Soft Matter* **2010**, *6* (20), 4988.

(113) Bae, Y.; Kataoka, K. Intelligent Polymeric Micelles from Functional Poly(Ethylene Glycol)-Poly(Amino Acid) Block Copolymers. *Adv. Drug Deliv. Rev.* **2009**, *61* (10), 768–784.

(114) Nishiyama, N.; Okazaki, S.; Cabral, H.; Miyamoto, M.; Kato, Y.; Sugiyama, Y.; Nishio, K.; Matsumura, Y.; Kataoka, K. Novel Cisplatin-Incorporated Polymeric Micelles Can Eradicate Solid Tumors in Mice. *Cancer Res.* **2003**, *63* (24), 8977–8983.

(115) Hu, F. Q.; Zhang, Y. Y.; You, J.; Yuan, H.; Du, Y. Z. PH Triggered Doxorubicin Delivery of

PEGylated Glycolipid Conjugate Micelles for Tumor Targeting Therapy. *Mol. Pharm.* **2012**, *9* (9), 2469–2478.

(116) Karakoti, A. S.; Das, S.; Thevuthasan, S.; Seal, S. Minireviews PEGylated Inorganic Nanoparticles. *Angew. Chem. Int. Ed.* **2011**, *50* (9), 1980–1994.

(117) Brown, S. D.; Nativo, P.; Smith, J. A.; Stirling, D.; Edwards, P. R.; Venugopal, B.; Flint, D. J.; Plumb, J. A.; Graham, D.; Wheate, N. J. Gold Nanoparticles for the Improved Anticancer Drug Delivery of the Active Component of Oxaliplatin. *J. Am. Chem. Soc.* **2010**, *132* (13), 4678–4684.

(118) Hartgerink, J. D.; Beniash, E.; Stupp, S. I. Self-Assembly and Mineralization of Peptide-Amphiphile Nanofibers. *Science (80-.).* **2001**, *294* (5547), 1684–1688.

(119) Spoerke, E. D.; Anthony, S. G.; Stupp, S. I. Enzyme Directed Templating of Artificial Bone Mineral. *Adv. Mater.* **2009**, *21* (4), 425–430.

(120) Cavalli, S.; Popescu, D. C.; Tellers, E. E.; Vos, M. R. J.; Pichon, B. P.; Overhand, M.; Rapaport, H.; Sommerdijk, N. A. J. M.; Kros, A. Self-Organizing ??-Sheet Lipopeptide Monolayers as Template for the Mineralization of CaCO3. *Angew. Chemie - Int. Ed.* **2006**, *45* (5), 739–744.

(121) Zhao, X.; Nagai, Y.; Reeves, P. J.; Kiley, P.; Khorana, H. G.; Zhang, S.; Buchanan, J. M. Designer Short Peptide Surfactants Stabilize G Protein-Coupled Receptor Bovine Rhodopsin. *Proc. Natl. Acad. Sci. U. S. A.* **2006**, *103* (47), 17707–17712.

(122) Matsumoto, K.; Vaughn, M.; Bruce, B. D.; Koutsopoulos, S.; Zhang, S. Designer Peptide Surfactants Stabilize Functional Photosystem-I Membrane Complex in Aqueous Solution for Extended Time. *J. Phys. Chem. B* **2009**, *113* (1), 75–83.

(123) Das, R.; Kiley, P. J.; Segal, M.; Norville, J.; Yu, A. A.; Wang, L.; Trammell, S. A.; Reddick, L. E.; Kumar, R.; Stellacci, F.; et al. Integration of Photosynthetic Protein Molecular Complexes in Solid-State Electronic Devices. *Nano Lett.* **2004**, *4* (6), 1079–1083.

(124) Kiley, P.; Zhao, X.; Vaughn, M.; Baldo, M. A.; Bruce, B. D.; Zhang, S. Self-Assembling Peptide Detergents Stabilize Isolated Photosystem I on a Dry Surface for an Extended Time. *PLoS Biol.* **2005**, *3* (7), 1180–1186.

(125) Boato, F.; Thomas, R. M.; Ghasparian, A.; Freund-Renard, A.; Moehle, K.; Robinson, J. A. Synthetic Virus-like Particles from Self-Assembling Coiled-Coil Lipopeptides and Their Use in Antigen Display to the Immune System. *Angew. Chemie - Int. Ed.* **2007**, *46* (47), 9015–9018.

(126) McGregor, C.-L.; Chen, L.; Pomroy, N. C.; Hwang, P.; Go, S.; Chakrabartty, A.; Privé, G. G. Lipopeptide Detergents Designed for the Structural Study of Membrane Proteins. *Nat. Biotechnol.* **2003**, *21* (2), 171–176.

(127) Hamley, I. W. Self-Assembly of Amphiphilic Peptides. *Soft Matter* **2011**, *7* (9), 4122–4138.

(128) Pakalns, T.; Haverstick, K. L.; Fields, G. B.; McCarthy, J. B.; Mooradian, D. L.; Tirrell, M. Cellular Recognition of Synthetic Peptide Amphiphiles in Self-Assembled Monolayer Films. *Biomaterials* **1999**, *20* (23–24), 2265–2279.

(129) Oku, N.; Koike, C.; Tokudome, Y.; Okada, S.; Nishikawa, N.; Tsukada, H.; Kiso, M.; Hasegawa, A.; Fujii, H.; Murata, J.; et al. Application of Liposomes for Cancer Metastasis. *Adv. Drug Deliv. Rev.* **1997**, *24* (2–3), 215–223.

(130) Silva, G. A.; Czeisler, C.; Niece, K. L.; Beniash, E.; Harrington, D. A.; Kessler, J. A.; Stupp, S. I. Selective Differentiation of Neural Progenitor Cells by High-Epitope Density Nanofibers. *Science (80-.).* **2004**, *303* (5662), 1352–1355.

(131) Tysseling-Mattiace, V. M.; Sahni, V.; Niece, K. L.; Birch, D.; Czeisler, C.; Fehlings, M. G.; Stupp, S. I.; Kessler, J. A. Self-Assembling Nanofibers Inhibit Glial Scar Formation and Promote Axon Elongation after Spinal Cord Injury. *J. Neurosci.* **2008**, *28* (14), 3814–3823.

(132) Dehsorkhi, A.; Castelletto, V.; Hamley, I. W.; Adamcik, J.; Mezzenga, R. The Effect of PH on the Self-Assembly of a Collagen Derived Peptide Amphiphile. *Soft Matter* **2013**, *9* (26), 6033.

(133) Miravet, J. F.; Escuder, B.; Segarra-Maset, M. D.; Tena-Solsona, M.; Hamley, I. W.; Dehsorkhi, A.; Castelletto, V. Self-Assembly of a Peptide Amphiphile: Transition from Nanotape Fibrils to Micelles. *Soft Matter* **2013**, *9* (13), 3558–3564.

(134) Leupold, E.; Nikolenko, H.; Beyermann, M.; Dathe, M. Insight into the Role of HSPG in the Cellular Uptake of Apolipoprotein E-Derived Peptide Micelles and Liposomes. *Biochim. Biophys. Acta* **2008**, *1778* (12), 2781–2789.

(135) Kim, J. K.; Anderson, J.; Jun, H. W.; Repka, M. A.; Jo, S. Self-Assembling Peptide Amphiphile-Based Nanofiber Gel for Bioresponsive Cisplatin Delivery. *Mol. Pharm.* **2009**, *6* (3), 978–985.

(136) Guo, X. D.; Tandiono, F.; Wiradharma, N.; Khor, D.; Tan, C. G.; Khan, M.; Qian, Y.; Yang, Y. Y. Cationic Micelles Self-Assembled from Cholesterol-Conjugated Oligopeptides as an Efficient Gene Delivery Vector. *Biomaterials* **2008**, *29* (36), 4838–4846.

(137) Wiradharma, N.; Khan, M.; Tong, Y. W.; Wang, S.; Yang, Y. Y. Self-Assembled Cationic Peptide Nanoparticles Capable of Inducing Efficient Gene Expression in Vitro. *Adv. Funct. Mater.* **2008**, *18* (6), 943–951.

(138) Wiradharma, N.; Tong, Y. W.; Yang, Y. Y. Self-Assembled Oligopeptide Nanostructures for Co-Delivery of Drug and Gene with Synergistic Therapeutic Effect. *Biomaterials* **2009**, *30* (17), 3100–3109.

(139) Missirlis, D.; Khant, H.; Tirrell, M. Mechanisms of Peptide Amphiphile Internalization by SJSA-1 Cells in Vitro. *Biochemistry* **2009**, *48* (15), 3304–3314.

(140) Hardie, D. G. Peptide Hormone Action: A Practical Approach; Hutton;, K. S. J. C., Ed.; Oxford University Press, 1991.

(141) Kahn, S. E.; Hull, R. L.; Utzschneider, K. M. Mechanisms Linking Obesity to Insulin Resistance and Type 2 Diabetes. *Nature* **2006**, *444* (7121), 840–846.

(142) Bergenstal, R. M.; Tamborlane, W. V.; Ahmann, A.; Buse, J. B.; Dailey, G.; Davis, S. N.; Joyce, C.; Peoples, T.; Perkins, B. A.; Welsh, J. B.; et al. Effectiveness of Sensor-Augmented Insulin-Pump Therapy in Type 1 Diabetes. *N. Engl. J. Med.* **2010**, *363* (4), 311–320.

(143) Striepens, N.; Kendrick, K. M.; Maier, W.; Hurlemann, R. Prosocial Effects of Oxytocin and Clinical Evidence for Its Therapeutic Potential. *Front. Neuroendocrinol.* **2011**, *32* (4), 426–450.

(144) Lintner, K.; Peschard, O. Biologically Active Peptides: From a Laboratory Bench Curiosity to a Functional Skin Care Product. *Int. J. Cosmet. Sci.* **2000**, *22* (3), 207–218.

(145) Su, L.-L.; Chong, Y.-S.; Samuel, M. Carbetocin for Preventing Postpartum Haemorrhage. *Cochrane Database Syst. Rev.* **2012**, *15* (2), CD005457.

(146) Ouberai, M. M.; Dos Santos, A. L. G.; Kinna, S.; Madalli, S.; Hornigold, D. C.; Baker, D.; Naylor, J.; Sheldrake, L.; Corkill, D. J.; Hood, J.; et al. Controlling the Bioactivity of a Peptide Hormone in Vivo by Reversible Self-Assembly. *Nat. Commun.* **2017**, *8* (1), 41467–017.

(147) Hutchinson, J. A., Burholt, S., Hamley, I. W., Lundback, A.-K., Uddin, S., Gomes dos Santos, A., Reza, M., Seitsonen, J. and Ruokolainen, J. The Effect of Lipidation on the Self- Assembly of the Gut-derived Peptide Hormone PYY3–36. *Chem. Bioconjugate* **2018**, *29* (7), 2296–2308.

(148) WHO Publishes List of Bacteria for Which New Antibiotics Are Urgently Needed. *Saudi Medical Journal*. 2017.

(149) Chan, D. I.; Prenner, E. J.; Vogel, H. J. Tryptophan- and Arginine-Rich Antimicrobial Peptides: Structures and Mechanisms of Action. *Biochim. Biophys. Acta - Biomembr.* **2006**, *1758* (9),

1184–1202.

(150) Park, A. J.; Okhovat, J. P.; Kim, J. Antimicrobial Peptides. *Pharmaceuticals* **2013**, *6*, 1542–1575.

(151) AB Naafs, M. The Antimicrobial Peptides: Ready for Clinical Trials? *Biomed. J. Sci. Tech. Res.* **2018**, *7* (4), 6038–6042.

(152) Mishra, A. K.; Choi, J.; Moon, E.; Baek, K. H. Tryptophan-Rich and Proline-Rich Antimicrobial Peptides. *Molecules* **2018**, *23* (4), 1–23.

(153) Band, V. I.; Weiss, D. S. Mechanisms of Antimicrobial Peptide Resistance in Gram-Negative Bacteria. *Antibiotics* **2014**, *4* (1), 18–41.

(154) Bahar., A. A.; Ren, D. Antimicrobial Peptides. *Pharmaceuticals* **2013**, *6* (12), 1543–1575.

(155) Fjell, C. D.; Hiss, J. A.; Hancock, R. E. W.; Schneider, G. Designing Antimicrobial Peptides: Form Follows Function. *Nat. Rev. Drug Discov.* **2012**, *11* (1), 37–51.

(156) Koo, H. B.; Seo, J. Antimicrobial Peptides under Clinical Investigation. *Pept. Sci.* **2019**, *111* (5), 1–15.

(157) Fernández-Vidal, M.; Jayasinghe, S.; Ladokhin, A. S.; White, S. H. Folding Amphipathic Helices Into Membranes: Amphiphilicity Trumps Hydrophobicity. *J. Mol. Biol.* **2007**, *370* (3), 459–470.

(158) Powers, J. P. S.; Hancock, R. E. W. The Relationship between Peptide Structure and Antibacterial Activity. *Peptides* **2003**, *24* (11), 1681–1691.

(159) Hancock, R. E. W.; Rozek, A. Role of Membranes in the Activities of Antimicrobial Cationic Peptides. *FEMS Microbiol. Lett.* **2002**, *206* (2), 143–149.

(160) E.W.Hancock, R. Peptide Antibiotics. *Lancet* **1997**, *349* (9049), 418–422.

(161) Mangoni, M. L.; Ludovica Marcellini, H. G.; Simmaco, M. Biological Characterization and Modes of Action of Temporins and Bombinins H, Multiple Forms of Short and Mildly Cationic Anti-Microbial Peptides from Amphibian Skin. *J. Pept. Sci.* **2007**, *13* (9), 603–613.

(162) Harris, F.; Dennison, S.; Phoenix, D. Anionic Antimicrobial Peptides from Eukaryotic Organisms. *Curr. Protein Pept. Sci.* **2009**, *10* (6), 585–606.

(163) Foletti, C.; Kramer, R. A.; Mauser, H.; Jenal, U.; Bleicher, K. H.; Wennemers, H. Functionalized Proline-Rich Peptides Bind the Bacterial Second Messenger c-Di-GMP. *Angew. Chemie - Int. Ed.* **2018**, *57* (26), 7729–7733.

(164) Grau-Campistany, A.; Manresa, Á.; Pujol, M.; Rabanal, F.; Cajal, Y. Tryptophan-Containing Lipopeptide Antibiotics Derived from Polymyxin B with Activity against Gram Positive and Gram Negative Bacteria. *Biochim. Biophys. Acta - Biomembr.* **2016**, *1858* (2), 333–343.

(165) Reddy, K. V. R.; Yedery, R. D.; Aranha, C. Antimicrobial Peptides: Premises and Promises. *Int. J. Antimicrob. Agents* **2004**, *24* (6), 536–547.

(166) Baumann, T.; Kämpfer, U.; Schürch, S.; Schaller, J.; Largiadèr, C.; Nentwig, W.; Kuhn-Nentwig, L. Ctenidins: Antimicrobial Glycine-Rich Peptides from the Hemocytes of the Spider Cupiennius Salei. *Cell. Mol. Life Sci.* **2010**, *67* (16), 2787–2798.

(167) Ilić, N.; Novković, M.; Guida, F.; Xhindoli, D.; Benincasa, M.; Tossi, A.; Juretić, D. Selective Antimicrobial Activity and Mode of Action of Adepantins, Glycine-Rich Peptide Antibiotics Based on Anuran Antimicrobial Peptide Sequences. *Biochim. Biophys. Acta - Biomembr.* **2013**, *1828* (3), 1004–1012.

(168) Oppenheim, F. G.; Xu, T.; McMillian, F. M.; Levitz, S. M.; Diamond, R. D.; Offner, G. D.; Troxler, R. F. Histatins, a Novel Family of Histidine-Rich Proteins in Human Parotid Secretion.

Isolation, Characterization, Primary Structure, and Fungistatic Effects on Candida Albicans. *J. Biol. Chem.* **1988**, *263* (16), 7427–7.

(169) Zasloff, M. Antimicrobial Peptides of Multicellular Organisms. *Nature* **2002**, *415* (6870), 389–395.

(170) Nguyen, L. T.; Haney, E. F.; Vogel, H. J. The Expanding Scope of Antimicrobial Peptide Structures and Their Modes of Action. *Trends Biotechnol.* **2011**, *29* (9), 464–472.

(171) Zasloff, M. Magainins, a Class of Antimicrobial Peptides from Xenopus Skin: Isolation, Characterization of Two Active Forms, and Partial CDNA Sequence of a Precursor. *Proc. Natl. Acad. Sci. U. S. A.* **1987**, *84* (15), 5449–5453.

(172) Selsted, M. E.; Novotny, M. J.; Morris, W. L.; Tang, Y. Q.; Smith, W.; Cullor, J. S. Indolicidin, a Novel Bactericidal Tridecapeptide Amide from Neutrophils. *J. Biol. Chem.* **1992**, *267* (7), 4292–4295.

(173) Neville, F.; Cahuzac, M.; Konovalov, O.; Ishitsuka, Y.; Lee, K. Y. C.; Kuzmenko, I.; Kale, G. M.; Gidalevitz, D. Lipid Headgroup Discrimination by Antimicrobial Peptide LL-37: Insight into Mechanism of Action. *Biophys. J.* **2006**, *90* (4), 1275–1287.

(174) Scott, M. G.; Davidson, D. J.; Gold, M. R.; Bowdish, D.; Hancock, R. E. W. The Human Antimicrobial Peptide LL-37 Is a Multifunctional Modulator of Innate Immune Responses. *J. Immunol.* **2002**, *169* (7), 3883–3891.

(175) Makovitzki, A.; Viterbo, A.; Brotman, Y.; Chet, I.; Shai, Y. Inhibition of Fungal and Bacterial Plant Pathogens in Vitro and in Planta with Ultrashort Cationic Lipopeptides. *Appl. Environ. Microbiol.* **2007**, *73* (20), 6629–6636.

(176) Hamley, I. W.; Dehsorkhi, A.; Jauregi, P.; Seitsonen, J.; Ruokolainen, J.; Coutte, F.; Chataigné, G.; Jacques, P. Self-Assembly of Three Bacterially-Derived Bioactive Lipopeptides. *Soft Matter* **2013**, *9* (40), 9572.

(177) Pouny, Y.; Rapaport, D.; Shai, Y.; Mor, A.; Nicolas, P. Interaction of Antimicrobial Dermaseptin and Its Fluorescently Labeled Analogs with Phospholipid Membranes. *Biochemistry* **1992**, *31* (49), 12416–12423.

(178) Bechinger, B. Detergent-like Properties of Magainin Antibiotic Peptides: A 31P Solid-State NMR Spectroscopy Study. *Biochim. Biophys. Acta - Biomembr.* **2005**, *1712* (1), 101–108.

(179) Bolintineanu, D. S.; Kaznessis, Y. N. Computational Studies of Protegrin Antimicrobial Peptides: A Review. *Peptides* **2011**, *32* (1), 188–201.

(180) Ludtke, S.; He, K.; Huang, H. Membrane Thinning Caused by Magainin 2+. *Biochemistry* **1995**, *34* (51), 16764–16769.

(181) Chen, F. Y.; Lee, M. T.; Huang, H. W. Evidence for Membrane Thinning Effect as the Mechanism for Peptide-Induced Pore Formation. *Biophys. J.* **2003**, *84* (6), 3751–3758.

(182) Matsuzaki, K. Magainins as Paradigm for the Mode of Action of Pore Forming Polypeptides. *Biochim. Biophys. Acta - Rev. Biomembr.* **1998**, *1376* (3), 391–400.

(183) Salay, L. C.; Ferreira, M.; Oliveira, O. N.; Nakaie, C. R.; Schreier, S. Headgroup Specificity for the Interaction of the Antimicrobial Peptide Tritrpticin with Phospholipid Langmuir Monolayers. *Colloids Surfaces B Biointerfaces* **2012**, *100*, 95–102.

(184) Wu, M.; Maier, E.; Benz, R.; Hancock, R. E. W. Mechanism of Interaction of Different Classes of Cationic Antimicrobial Peptides with Planar Bilayers and with the Cytoplasmic Membrane of Escherichia Coli. *Biochemistry* **1999**, *38* (22), 7235–7242.

(185) Zhang, L.; Rozek, A.; Hancock, R. E. W. Interaction of Cationic Antimicrobial Peptides with

Model Membranes. *J. Biol. Chem.* **2001**, *276* (38), 35714–35722.

(186) Ehrenstein, G.; Lecar, H. Electrically Gated Ionic Channels in Lipid Bilayers. *Q. Rev. Biophys.* **1977**, *10* (1), 1–34.

(187) Shimazaki, K.; Tazume, T.; Uji, K.; Tanaka, M.; Kumura, H.; Mikawa, K.; Shimo-Oka, T. Properties of a Heparin-Binding Peptide Derived from Bovine Lactoferrin. *J. Dairy Sci.* **1998**, *81* (11), 2841–2849.

(188) Taylor, S. D.; Palmer, M. The Action Mechanism of Daptomycin. *Bioorganic Med. Chem.* **2016**, *24* (24), 6253–6268.

(189) Debroah, O.; Mercer, D.; Duncan, V. Modified Antmicrobial Peptides, 2017.

(190) Boto, A.; De La Lastra, J. M. P.; González, C. C. The Road from Host-Defense Peptides to a New Generation of Antimicrobial Drugs. *Molecules* **2018**, *23* (2).

(191) Ballweber, L. M.; Jaynes, J. E.; Stamm, W. E.; Lampe, M. F. In Vitro Microbicidal Activities of Cecropin Peptides D2A21 and D4E1 and Gel Formulations Containing 0.1 to 2% D2A21 against Chlamydia Trachomatis. *Antimicrob. Agents Chemother.* **2002**, *46* (1), 34–41.

(192) Stevens, K. A.; Sheldon, B. W.; Klapes, N. A.; Klaenhammer, T. R. Effect of Treatment Conditions on Nisin Inactivation of Gram-Negative Bacteria. *J. Food Prot.* **1992**, *55* (10), 763–766.

(193) Prenner, E. J.; Lewis, R. N. A. H.; McElhaney, R. N. The Interaction of the Antimicrobial Peptide Gramicidin S with Lipid Bilayer Model and Biological Membranes. *Biochim. Biophys. Acta - Biomembr.* **1999**, *1462* ((1-2)), 201–221.

(194) Poirel, L.; Jayol, A.; Nordmanna, P. Polymyxins: Antibacterial Activity, Susceptibility Testing, and Resistance Mechanisms Encoded by Plasmids or Chromosomes. *Clin. Microbiol. Rev.* **2017**, *30* (2), 557–596.

(195) Steenbergen, J. N.; Alder, J.; Thorne, G. M.; Tally, F. P. Daptomycin: A Lipopeptide Antibiotic for the Treatment of Serious Gram-Positive Infections. *J. Antimicrob. Chemother.* **2005**, *55* (3), 283–288.

(196) Gottler, L. M.; Ramamoorthy, A. Structure, Membrane Orientation, Mechanism, and Function of Pexiganan - A Highly Potent Antimicrobial Peptide Designed from Magainin. *Biochim. Biophys. Acta - Biomembr.* **2009**, *1788* (8), 1680–1686.

(197) Alam, M. Z.; Wu, X.; Mascio, C.; Chesnel, L.; Hurdle, J. G. Mode of Action and Bactericidal Properties of Surotomycin against Growing and Nongrowing Clostridium Difficile. *Antimicrob. Agents Chemother.* **2015**, *59* (9), 5165–5170.

(198) Rew, Y.; Shin, D.; Hwang, I.; Boger, D. L. Total Synthesis and Examination of Three Key Analogues of Ramoplanin: A Lipoglycodepsipeptide with Potent Antibiotic Activity. *J. Am. Chem. Soc.* **2004**, *126* (4), 1041–1043.

(199) Kudrimoti, M.; Curtis, A.; Azawi, S.; Worden, F.; Katz, S.; Adkins, D.; Bonomi, M.; Elder, J.; Sonis, S. T.; Straube, R.; et al. Dusquetide: A Novel Innate Defense Regulator Demonstrating a Significant and Consistent Reduction in the Duration of Oral Mucositis in Preclinical Data and a Randomized, Placebo-Controlled Phase 2a Clinical Study. *J. Biotechnol.* **2016**, *239*, 115.

(200) Wiig, M. E.; Dahlin, L. B.; Fridén, J.; Hagberg, L.; Larsen, S. E.; Wiklund, K.; Mahlapuu, M. PXL01 in Sodium Hyaluronate for Improvement of Hand Recovery after Flexor Tendon Repair Surgery: Randomized Controlled Trial. *PLoS One* **2014**, *9* (10), e110735.

(201) Srinivas, N.; Jetter, P.; Ueberbacher, B. J.; Werneburg, M.; Zerbe, K.; Steinmann, J.; Van Der Meijden, B.; Bernardini, F.; Lederer, A.; Dias, R. L. A.; et al. Peptidomimetic Antibiotics Target Outer-Membrane Biogenesis in Pseudomonas Aeruginosa. *Science (80-.).* **2010**, *327* (5968),

1010–1013.

(202) Gueler, F.; Shushakova, N.; Mengel, M.; Hueper, K.; Chen, R.; Liu, X.; Park, J. K.; Haller, H.; Wensvoort, G.; Rong, S. A Novel Therapy to Attenuate Acute Kidney Injury and Ischemic Allograft Damage after Allogenic Kidney Transplantation in Mice. *PLoS One* **2015**, *10* (1), e0115709.

(203) Min, C.; Ohta, K.; Kajiya, M.; Zhu, T.; Sharma, K.; Shin, J.; Mawardi, H.; Howait, M.; Hirschfeld, J.; Bahammam, L.; et al. The Antimicrobial Activity of the Appetite Peptide Hormone Ghrelin. *Peptides* **2012**, *36* (2), 151.

(204) Kaplan, C. W.; Sim, J. H.; Shah, K. R.; Kolesnikova-Kaplan, A.; Shi, W.; Eckert, R. Selective Membrane Disruption: Mode of Action of C16G2, a Specifically Targeted Antimicrobial Peptide. *Antimicrob. Agents Chemother.* **2011**, *55* (7), 3446–3452.

(205) Teixeira, V.; Feio, M. J.; Bastos, M. Role of Lipids in the Interaction of Antimicrobial Peptides with Membranes. *Prog. Lipid Res.* **2012**, *51* (2), 149–177.

(206) Bojsen, R.; Torbensen, R.; Larsen, C. E.; Folkesson, A.; Regenberg, B. The Synthetic Amphipathic Peptidomimetic LTX109 Is a Potent Fungicide That Disturbs Plasma Membrane Integrity in a Sphingolipid Dependent Manner. *PLoS One* **2013**, *8* (7), e69483.

(207) van der Does, A. M.; Hensbergen, P. J.; Bogaards, S. J.; Cansoy, M.; Deelder, A. M.; van Leeuwen, H. C.; Drijfhout, J. W.; van Dissel, J. T.; Nibbering, P. H. The Human Lactoferrin-Derived Peptide HLF1-11 Exerts Immunomodulatory Effects by Specific Inhibition of Myeloperoxidase Activity. *J. Immunol.* **2012**, *118* (10), 5012–5019.

(208) Itoh, H.; Tokumoto, K.; Kaji, T.; Paudel, A.; Panthee, S.; Hamamoto, H.; Sekimizu, K.; Inoue, M. Total Synthesis and Biological Mode of Action of WAP-8294A2: A Menaquinone-Targeting Antibiotic. *J. Org. Chem.* **2018**, *83* (13), 6924–6935.

(209) Vertesy, L.; Ehlers, E.; Kogler, H.; Kurz, M.; Meiwes, J.; Seibert, G.; Vogel, M.; Hammann, P. Friulimicins: Novel Lipopeptide Antibiotics with Peptidoglycan Synthesis Inhibiting Activity from Actinoplanes Friuliensis Sp. Nov. II. Isolation and Structural Characterization. *J. Antibiot. (Tokyo).* **2000**, *53* (8), 816–827.

(210) Park, C.; Woo, E. R.; Lee, D. G. Antifungal Effect with Apoptotic Mechanism(s) of Styraxjaponoside C. *Biochem. Biophys. Res. Commun.* **2009**, *390* (4), 1256–1259.

(211) Chu-Kung, A. F.; Bozzelli, K. N.; Lockwood, N. A.; Haseman, J. R.; Mayo, K. H.; Tirrell, M. V. Promotion of Peptide Antimicrobial Activity by Fatty Acid Conjugation. *Bioconjug. Chem.* **2004**, *15* (3), 530–535.

(212) Sevcsik, E.; Pabst, G.; Jilek, A.; Lohner, K. How Lipids Influence the Mode of Action of Membrane-Active Peptides. *Biochim. Biophys. Acta - Biomembr.* **2007**, *1768* (10), 2586–2595.

(213) Wadia, J. S.; Stan, R. V; Dowdy, S. F. Transducible TAT-HA Fusogenic Peptide Enhances Escape of TAT-Fusion Proteins after Lipid Raft Macropinocytosis. *Nat Med* **2004**, *10* (3), 310–315.

(214) Fu, H.; Shi, K.; Hu, G.; Yang, Y.; Kuang, Q.; Lu, L.; Zhang, L.; Chen, W.; Dong, M.; Chen, Y.; et al. Tumor-Targeted Paclitaxel Delivery and Enhanced Penetration Using TAT-Decorated Liposomes Comprising Redox-Responsive Poly(Ethylene Glycol). *J. Pharm. Sci.* **2015**, *104* (3), 1160–1173.

(215) Liu, L.; Xu, K.; Wang, H.; Tan, P. K. J.; Fan, W.; Venkatraman, S. S.; Li, L.; Yang, Y.-Y. Self-Assembled Cationic Peptide Nanoparticles as an Efficient Antimicrobial Agent. *Nat. Nanotechnol.* **2009**, *4* (7), 457–463.

(216) Liu, Z.; Brady, A.; Young, A.; Rasimick, B.; Chen, K.; Zhou, C.; Kallenbach, N. R. Length

Effects in Antimicrobial Peptides of the (RW)n Series. *Antimicrob. Agents Chemother.* **2007**, *51* (2), 597–603.

(217) Gorter, E.; Grendel, F. On Bimolecular Layers of Lipoids on the Chromocytes of the Blood. *J. Exp. Med.* **1925**, *41* (4), 439.

(218) Kotyk, A.; Janacek, K.; Koryta, J. Biophysical Chemsitry of Membrane Functions, 1st ed.; John Wiley & Sons, 1988.

(219) Green, D. E. Membrane Structure. *Science (80-.).* **1971**, *174* (4011), 863–867.

(220) Wilkins, M. H. F.; Blaurock, A. E.; Engelman, D. M. Bilayer Structure in Membranes. *Nature* **1971**, *26* (138), 584–585.

(221) Alberts B, Johnson A, L. J. Molecular Biology of the Cell, 4th Editio.; Garland Science, 2002.

(222) Bretscher, M. S. Asymmetrical Lipid Bilayer Structure for Biological Membranes. *Nat. New Biol.* **1972**, *236*, 11–12.

(223) Van Meer, G.; Voelker, D. R.; Feigenson, G. W. Membrane Lipids: Where They Are and How They Behave. *Nature Reviews Molecular Cell Biology*. 2008.

(224) Korlach, J.; Schwille, P.; Webb, W. W.; Feigenson, G. W. Characterization of Lipid Bilayer Phases by Confocal Microscopy and Fluorescence Correlation Spectroscopy. *Proc. Natl. Acad. Sci. U. S. A.* **1999**, *96* (15), 8461–8466.

(225) Lindblom, G.; Rilfors, L. Cubic Phases and Isotropic Structures Formed by Membrane Lipids - Possible Biological Relevance. *BBA - Rev. Biomembr.* **1989**, *988* (2), 221–256.

(226) Simons, K.; Ikonen, E. Functional Rafts in Cell Membranes. *Nature*. 1997.

(227) Simons, K.; Sampaio, J. L. Membrane Organization and Lipid Rafts. *Cold Spring Harbor Perspectives in Biology*. 2011.

(228) Simons, K.; Vaz, W. L. C. Model Systems, Lipid Rafts, and Cell Membranes. *Annual Review of Biophysics and Biomolecular Structure*. 2004.

(229) Marsh, D. Structural and Thermodynamic Determinants of Chain-Melting Transition Temperatures for Phospholipid and Glycolipids Membranes. *Biochim. Biophys. Acta - Biomembr.* **2010**, *1798* (1), 40–51.

(230) Beattie, M. E.; Veatch, S. L.; Stottrup, B. L.; Keller, S. L. Sterol Structure Determines Miscibility versus Melting Transitions in Lipid Vesicles. *Biophys. J.* **2005**, *89* (3), 1760–1768.

(231) Lee, A. G. Lipid Phase Transitions and Phase Diagrams II. Mixtures Involving Lipids. *BBA - Rev. Biomembr.* **1977**, *472* (3–4), 285–344.

(232) Arouri, A.; Dathe, M.; Blume, A. Peptide Induced Demixing in PG / PE Lipid Mixtures : A Mechanism for the Speci Fi City of Antimicrobial Peptides towards Bacterial Membranes ? *Biochim. Biophys. Acta - Mol. Basis Dis.* **2009**, *1788* (3), 650–659.

(233) Nielsen, J. E.; Bjørnestad, V. A.; Lund, R. Resolving the Structural Interactions between Antimicrobial Peptides and Lipid Membranes Using Small-Angle Scattering Methods: The Case of Indolicidin. *Soft Matter* **2018**, *14* (43), 8750–8763.

(234) Malanovic, N.; Leber, R.; Schmuck, M.; Kriechbaum, M.; Cordfunke, R. A.; Drijfhout, J. W.; Breij, A. De; Nibbering, P. H.; Kolb, D.; Lohner, K. Phospholipid-Driven Differences Determine the Action of the Synthetic Antimicrobial Peptide OP-145 on Gram-Positive Bacterial and Mammalian Membrane Model Systems. *Biochim. Biophys. Acta - Biomembr.* **2015**, *1848* (10), 2437–2447.

(235) Ladokhin, A. S.; Wimley, W. C.; White, S. H. Leakage of Membrane Vesicle Contents:

Determination of Mechanism Using Fluorescence Requenching. *Biophys. J.* **1995**, *69* (5), 1964–1971.

(236) Hallett, F. R.; Watton, J.; Krygsman, P. Vesicle Sizing: Number Distributions by Dynamic Light Scattering. *Biophys. J.* **1991**, *59* (2), 357–362.

(237) Castelletto, V.; Barnes, R.; Karatzas, K.-A.; Edwards-Gayle, C. J. C.; Greco, F.; Hamley, I. W.; Seitsonen, J.; Ruokolainen, J. Restructuring of Lipid Membranes by an Arginine-Capped Peptide Bolaamphiphile. *Langmuir* **2018**, *35* (5), 1302–1311.

(238) Castelletto, V.; Barnes, R. H.; Karatzas, K. A.; Edwards-Gayle, C. J. C.; Greco, F.; Hamley, I. W.; Rambo, R.; Seitsonen, J.; Ruokolainen, J. Arginine-Containing Surfactant-Like Peptides: Interaction with Lipid Membranes and Antimicrobial Activity. *Biomacromolecules* **2018**, *19* (7), 2782–2794.

(239) Edwards-Gayle, C. J. C.; Castelletto, V.; Hamley, I. W.; Barrett, G.; Greco, F.; Hermida-Merino, D.; Rambo, R. P.; Seitsonen, J.; Ruokolainen, J. Self-Assembly, Antimicrobial Activity, and Membrane Interactions of Arginine-Capped Peptide Bola-Amphiphiles. *ACS Appl. Bio Mater.* **2019**, *2* (5), 2208–2218.

(240) Castelletto, V.; Edwards-Gayle, C. J. C.; Hamley, I. W.; Barrett, G.; Seitsonen, J.; Ruokolainen, J. Peptide-Stabilized Emulsions and Gels from an Arginine-Rich Surfactant-Like Peptide with Antimicrobial Activity. *ACS Appl. Mater. Interfaces* **2019**, *11* (10), 9893–9903.

(241) Costerton, J. W.; Ingram, J. M.; Cheng, K. J. Structure and Function of the Cell Envelope of Gram-Negative Bacteria. *Phys. Rev. A* **1974**, *38* (1), 87–110.

(242) Silhavy, T. J.; Kahne, D.; Walker, S. The Bacterial Cell Envelope. *Cold Spring Harb. Perspect. Biol.* **2010**, *2* (5), 1–17.

(243) Malanovic, N.; Lohner, K. Gram-Positive Bacterial Cell Envelopes: The Impact on the Activity of Antimicrobial Peptides. *Biochim. Biophys. Acta - Biomembr.* **2016**, *1858* (5), 936–946.

(244) Donlan, R. M. Biofilm Formation: A Clinically Relevant Microbiological Process. *Clin. Infect. Dis.* **2001**, *33* (8), 1387–1392.

(245) Jenal, U.; Reinders, A.; Lori, C. Cyclic Di-GMP: Second Messenger Extraordinaire. *Nat. Rev. Microbiol.* **2017**, *15* (5), 271–284.

(246) Ha, D.-G.; O'Toole, G. A. C-Di-GMP and Its Effects on Biofilm Formation and Dispersion: A Pseudomonas Aeruginosa Review. *Microbiol. Spectr.* **2015**, *3* (2), 1–12.

(247) Hengge, R. Principles of C-Di-GMP Signalling in Bacteria. *Nat. Rev. Microbiol.* **2009**, *7* (4), 263–273.

(248) Kaur, G.; Dufour, J. M. Cell Lines: Valuable Tools or Useless Artifacts. *Spermatogenesis* **2012**, *2* (1), 1–5.

Chapter 2.

Self-assembly and bioactivity of peptide bola-amphiphiles and surfactant-like peptides containing Alanine and Arginine

This work has, in part, been published by the author as several research articles titled: ***1.*** *Self-Assembly, Antimicrobial Activity, and Membrane Interactions of Arginine-Capped Peptide Bola-Amphiphiles Charlotte Edwards-Gayle, Valeria Castelletto, Ian W. Hamley, Glyn Barrett, Francesca Greco, Daniel Hermida Merino, Robert P. Rambo, Jani Seitsonen, Janne Ruokolainen. ACS Appl. Bio Mater. 2019, 25, 2208-2218.* ***2.*** *Peptide-Stabilized Emulsions and Gels from an Arginine-Rich Surfactant-Like Peptide with Antimicrobial Activity**.** Valeria Castelletto, Charlotte J. C. Edwards-Gayle, Ian W. Hamley**,** Glyn Barrett, Jani Seitsonen, Janne Ruokolainen ACS Appl. Mater. Interfaces. 2019,11(10), 9893-9903* ***3.*** *Restructuring of Lipid Membranes by an Arginine-Capped Peptide Bolaamphiphile Valeria Castelletto, Ruth Barnes, Kimon andreas Karatzas, Charlotte Edwards-Gayle, Francesca Greco, Ian W Hamley, Robert Rambo, Jani Seitsonen, Janne Ruokolainen. Langmuir. 2018, 35(5),1302-1311* ***4.*** *Arginine-Containing Surfactant-Like Peptides: Interaction with Lipid Membranes and Antimicrobial Activity. Valeria Castelletto, Ruth Barnes, Kimon andreas Karatzas, Charlotte Edwards-Gayle, Francesca Greco, Ian W Hamley, Robert Rambo, Jani Seitsonen, Janne Ruokolainen. Biomacromolecules. 2018, 19(7), 2782-2794.*

2.1 Introduction

Antibiotic resistance has led to a number of conventional medicines to become less effective. This leaves an urgent need to discover naturally occurring actives or to design novel therapeutics to combat this issue. One class of therapeutics that have been found to be effective are antimicrobial peptides. Antimicrobial peptides are attractive as they can be easily biofunctionalized and made biocompatible.[1–3] Many organisms, for example fungi, have naturally evolved host defence antimicrobial peptides, which can be used as an actives themselves or form the basis of designed synthetic materials. Antimicrobial peptides with the ability to self-assemble may be active without the need for carrier molecules.

A class of peptide with strong self-assembly properties are surfactant-like peptides (SLPs), initially developed by Zhang et al.[4–7] These peptides are short, consisting of a one or two charged residue head group, with a longer hydrophobic sequence as a tail group. Peptides with various cationic and anionic headgroups, and different hydrophobic amino acid tail groups (including alanine, glycine and valine repeat units) have been studied. Previously our group has studied the conformation and nanostructure of SLPs, including A_6H,[8] A_6K,[9], A_6RGD[10] and A_6D[11]. Self-assembly was observed for these peptides, above a critical aggregation concentration (*cac*), into variety of structures including nanosheets, helical ribbons, fibrils, vesicles, nanotubes and nanotapes, with a range of applications.

SLPs with cationic head groups have been shown to have potential antimicrobial activity. SLPs A_3K, A_6K and A_9K were shown to assemble into increasingly ordered structures with increased length of the alanine hydrophobic motif.[12] Interestingly, the antimicrobial activity of these peptides also increased with the length of the hydrophobic motif. The peptide A_3K had no antimicrobial activity whereas A_6K and A_9K showed activity against *E.coli* and *S.aureus*, which are Gram-negative and Gram-positive respectively.[12]

Peptide bola-amphiphiles are a class of surfactant-like peptides. These peptides incorporate a charged residue at either end of the molecule. The self-assembly behaviour of these SLPs has been investigated. The self-assembly of $I_2K_2I_2$ and KI_4K has been compared and it was reported that the former does not aggregate, whereas the latter aggregates into β-sheet nanotubes.[13,14] In another example, the self-assembly ability of arginine based bola-amphiphile RFL_4FR was investigated and found to form nanosheets through lateral association of the backbone and dried films were compatible with human corneal stromal fibroblast cells.[15]

This chapter focuses on the self-assembly and bioactivity of a group of alanine-arginine SLPs and peptide bola-amphiphiles (Scheme 2.1 and 2.2). The self-assembly and lipid interactions of A_6R, CapA_6R, A_9R and RA_3R has been studied by Dr Valeria Castelletto (University of Reading).

A_6R assembles into thin sheets.[16] Peptide capA_6R (CONH-AAAAAAR-NH_2) assembled into fibres and had a lower *cac* value than A_6R due to increased hydrophobicity.[17] Interactions with zwitterionic membrane models (POPC/DOPC) [POPC: 1,2-dioleoyl-sn-glycero-3-phosphocholine, DOPC: 2-oleoyl-1-palmitoyl-sn-glycero-3-phosphocholine] and mixtures (POPG/POPE) [POPG: 2-oleoyl-1-palmitoyl-sn-glycero-3-phospho-rac-(1-glycerol) sodium salt, POPE: 2-oleoyl-1-palmitoyl-sn-glycero-3-phosphoethanolamine] containing the anionic POPG lipid were studied by SAXS and circular dichroism spectroscopy.[17] CapA_6R was found to incorporate into the anionic membrane in a β-sheet conformation, in contrast to the uncapped peptide A_6R (NH_2-AAAAAAR-OH). CapA_6R was found to have a strong selective antimicrobial activity against *Listeria monocytogenes*, compared to A_6R which shows non-selective activity against *E.coli*, *S.aureus* and *L.monocytogenes*. A_9R was found to assemble into β-sheet fibrils and induce bilayer correlations for the POPE/POPG vesicles, but not insert into the POPC mammalian membrane model.

The self-assembly, antimicrobial activity and membrane interaction of a short bola-amphiphile, RA_3R, was examined.[18] RA_3R formed a polyproline II (collagen-like) secondary structure but did not assemble in water, probably due the solubility imparted by the R residues. RA_3R was found to induce strong correlation between anionic lipid bilayers through electrostatic interactions with POPG. The peptide demonstrated strong activity against the Gram-positive foodborne pathogen *L. monocytogenes*.

Here, the self-assembly of three bola-amphiphiles, RA_6R, RA_9R, $RA_{12}R$ and one SLP $A_{12}R_2$, is examined. The interactions of these peptides with lipid vesicle membrane models consisting of DPPG and DPPE at different ratios in water are measured. DPPG (1,2-dipalmitoyl-sn-glycero-3-phosphoglycerol), is anionic and DPPE (1,2-dipalmitoyl-sn-glycero-3-phosphoethanolamine) is zwitterionic. Phosphatidylglycerol (PG) and phosphatidylethanolamine (PE) lipids are commonly found in bacterial cell walls, and have been used previously as model systems.[12,19–21] The lipids DPPG/DPPE were selected for the present study as they have accessible melting temperatures (in contrast to POPG used in previous studies which has Tm = -2 °C). After this, the cytocompatibility of all the peptides in Scheme 2.1 and 2.2 is examined using MTT assays. Finally, the antimicrobial activity of the peptide bola-amphiphiles, RA_6R, RA_9R, $RA_{12}R$, and SLP's A_9R and $A_{12}R_2$ are assessed against one gram positive strain, *S.aureus*, and gram-negative strains *E.coli*, *P.aeruginosa* and *P.syringae*.

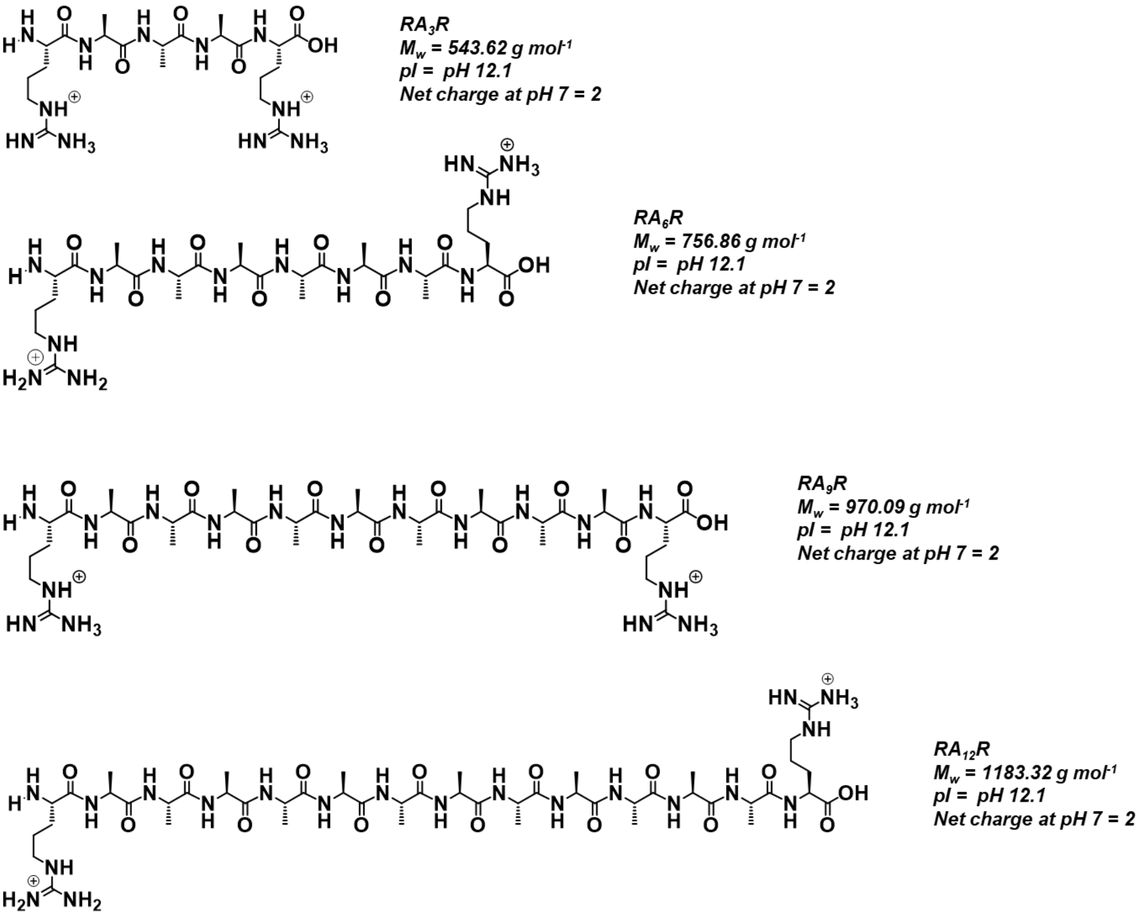

RA$_3$R
M_w = 543.62 g mol^{-1}
pI = pH 12.1
Net charge at pH 7 = 2

RA$_6$R
M_w = 756.86 g mol^{-1}
pI = pH 12.1
Net charge at pH 7 = 2

RA$_9$R
M_w = 970.09 g mol^{-1}
pI = pH 12.1
Net charge at pH 7 = 2

RA$_{12}$R
M_w = 1183.32 g mol^{-1}
pI = pH 12.1
Net charge at pH 7 = 2

***Scheme 2.1**. Structure of peptide bola-amphiphiles discussed in this chapter*

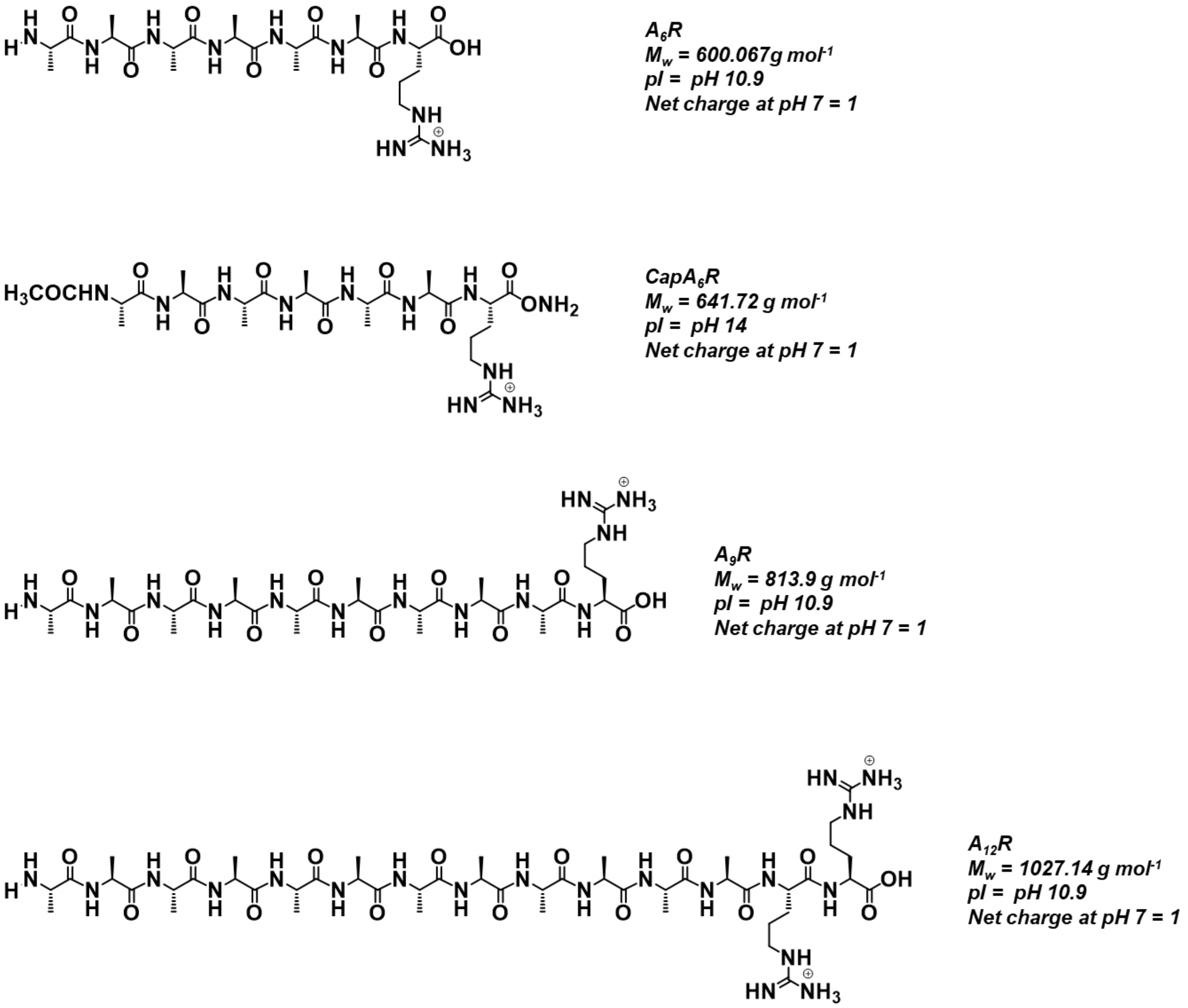

Scheme 2.2. *Structure of surfactant like peptides (SLP’s) discussed in this chapter.*

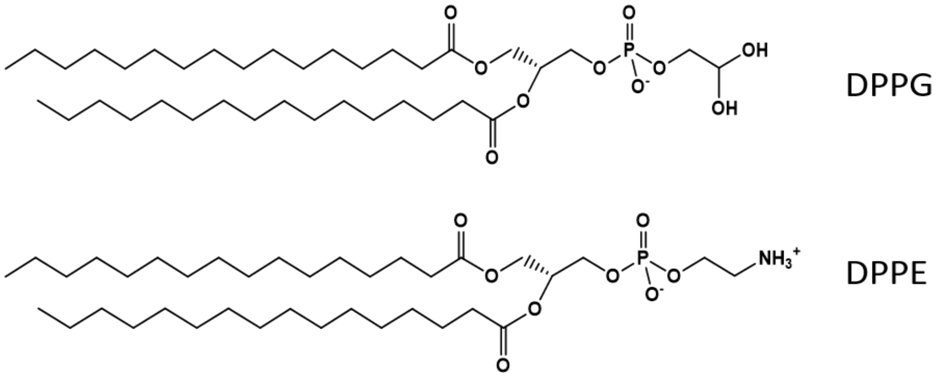

Scheme 2.3. *Structure of Lipids used to model bacterial membranes*

2.2 Results and Discussion

2.2.1 Self-assembly

2.2.1.1 RA_6R

A fluorescence assays using 8-Anilinonaphthalene-1-sulfonic acid (ANS), was performed to determine the critical aggregation concentration (*cac*) for RA_6R in water Figure 2.1. The fluorescence intensity of ANS increases when bound to a hydrophobic environment, which occurs through peptide aggregating.[22] ANS assays provided no evidence of peptide aggregation up to 1 wt% RA_6R, since there were no discontinuities in the fluorescence spectra for either fluorescence probe (Figure 2.1). In fact, CD, FTIR, XRD and SAXS experiments, performed to study the secondary structure of RA_6R in water, indicate the formation of oligomeric aggregates.

The CD spectra for (0.5-1) wt% RA_6R are characterised by a broad positive maximum at ~220 nm and a deep negative band around 190 nm (Figure 2.1b) and can be assigned to a polyproline II (PPII) conformation.[18,23–27] The FTIR spectrum for a 1 wt% sample (Figure 2.1c) shows bands at 1672 cm^{-1}, 1608 cm^{-1} and 1587 cm^{-1}, the former of which can be assigned to TFA counter-ions in solution,[28,29] while the latter two can be assigned to arginine side chain vibrations.[30,31] A small peak at 1675 cm^{-1} is observed for 2 wt% RA_6R, which is characteristic of short peptides with a poly-proline II structure, in agreement with the CD spectrum (Figure 2.1b).[32,33] The XRD profile (Figure 2.1d) shows a peak at 4.6 Å corresponding to a disordered side-to-side packing of the RA_6R molecules.[34]

SAXS data for RA_6R (Figure 2.1e) shows the features of peptide monomers. The SAXS curves were fitted to a generalised Gaussian coil model, corresponding to coil-like molecules in solution with different degrees of solvation. The parameters fitted using the generalised Gaussian coil model where the radius of gyration of the peptide R_g and the Flory exponent, ν. Fittings of the SAXS data (Table 2.1) provided R_g= 7.0 Å for all concentrations and a ν= 0.64, 0.24, 0.20 for 1 wt%, 5 wt% and 15 wt% RA_6R respectively. This set of parameters implies that RA_6R is in a swollen conformation at 1 wt% and a relatively folded conformation at 5 wt% and 16 wt%. Cryo-TEM images of RA_6R solutions show the formation of clustered monomers (Figure 2.1f).

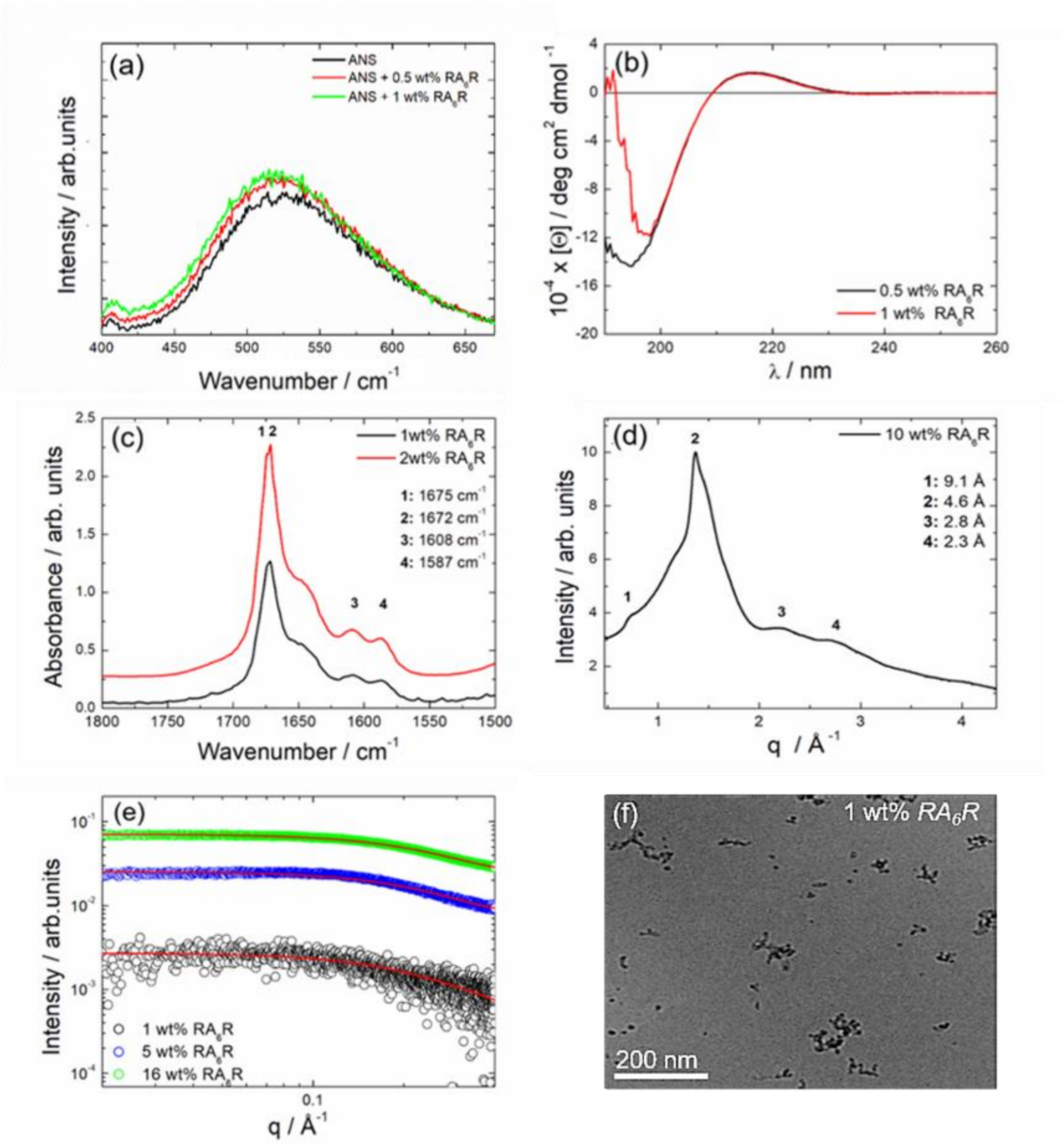

Figure 2.1. *Conformational and structural characterization of RA$_6$R in solution a) ANS binding, b) CD and c) FTIR spectra, d) XRD profile, e) SAXS profiles, with fits in red (see table 2.1) and f) cryo-TEM.*

Table 2.1. *Parameters extracted from the fitting of the SAXS curve in Figure 2.1e*

	1 wt% RA$_6$R	**5 wt% RA$_6$R**	**16 wt% RA$_6$R**
R_g / (Å)	7.0	7.0	7.0
ν	0.6	0.2	0.2
I(0)	0.02	0.04	0.02
N	0.12	0.50	0.57
BG	9.09 x 10^{-6}	7.20 x 10^{-6}	0.5

Where N denotes scaling parameter, v is the Flory exponent, I(0) is the forward scattering intensity, Rg is the radius of gyration and BG is the background.

2.2.1.2. RA_9R

The self-assembly of RA_9R in water was examined. Results from Thioflavin T (ThT) assay (Figure 2.2a) shows that RA_9R aggregates in amyloid fibres[35] above a *cac* = (0.18 ± 0.03) wt%. CD shows that the structure of the fibres is predominantly PP-II like (Figure 2.2b). This is an unexpected finding since fibril structures are generally associated with β-sheet structures. The secondary structure remains predominantly PPII like upon heating (Figure 2.2c), but changes into a β-sheet conformation, characterised by the minimum near 216 nm, upon drying the sample (Figure 2.2d). The FTIR spectrum for 1 wt% RA_9R (Figure 2.2e) shows peaks at 1672 cm^{-1}, 1647 cm^{-1},1608 cm^{-1} and 1587 cm^{-1} which are respectively assigned to modes associated with TFA counter ions,[28,29] disordered structure or arginine vibrations[30,31] as stated above. Upon increasing concentration to 5 wt%, additional peaks appear at 1675 cm^{-1} which can be assigned to PP-II structure and 1667 cm^{-1} which indicates a β-turn secondary structure.[31,36]

The XRD profile of RA_9R (Figure 2.2f) shows a 5.32 Å reflection which can be assigned to the packing of polyalanine β-sheets,[17] with inter-strand and intra-strand spacings of 4.32 Å, 3.72 Å, 2.83 Å, 2.39 Å and 2.26 Å. Interestingly, we observed that RA_9R has the ability to form a weak gel at a concentration of 5 wt%, which could be driven by the change in secondary structure from PP-II to β-sheet.

SAXS data, measured for 1 wt% RA_9R, was modelled using the form factor of a long cylindrical shell (Figure 2.2g; fitting parameters listed in Table 2.2). The parameters of the model are the core radius R (with polydispersity ΔR), the shell thickness D_r and the scattering length density of the core, shell and solvent D_{core}, D_{shell} and D_{solv}. The extracted parameters $R \pm \Delta R$ = (15±10) Å and D_r = 3 Å, indicate that the cylinder core radius is smaller than the length of the oligoalanine A_9 sequence= 28.8 Å (spacing per residue in a parallel β-sheet is 3.2 Å), while the external shell has a thickness very similar to one arginine unit. This result shows that there is an overlapping of the alanine chains within the core of the fibers, with the arginine residue exposed at the surface of the fibres. Cryo-TEM confirms the presence of fibres with an average diameter of 7.6 nm thick (Figure 2.2h). RA_9R forms a self-standing gel at 10 wt% and 15 wt%.

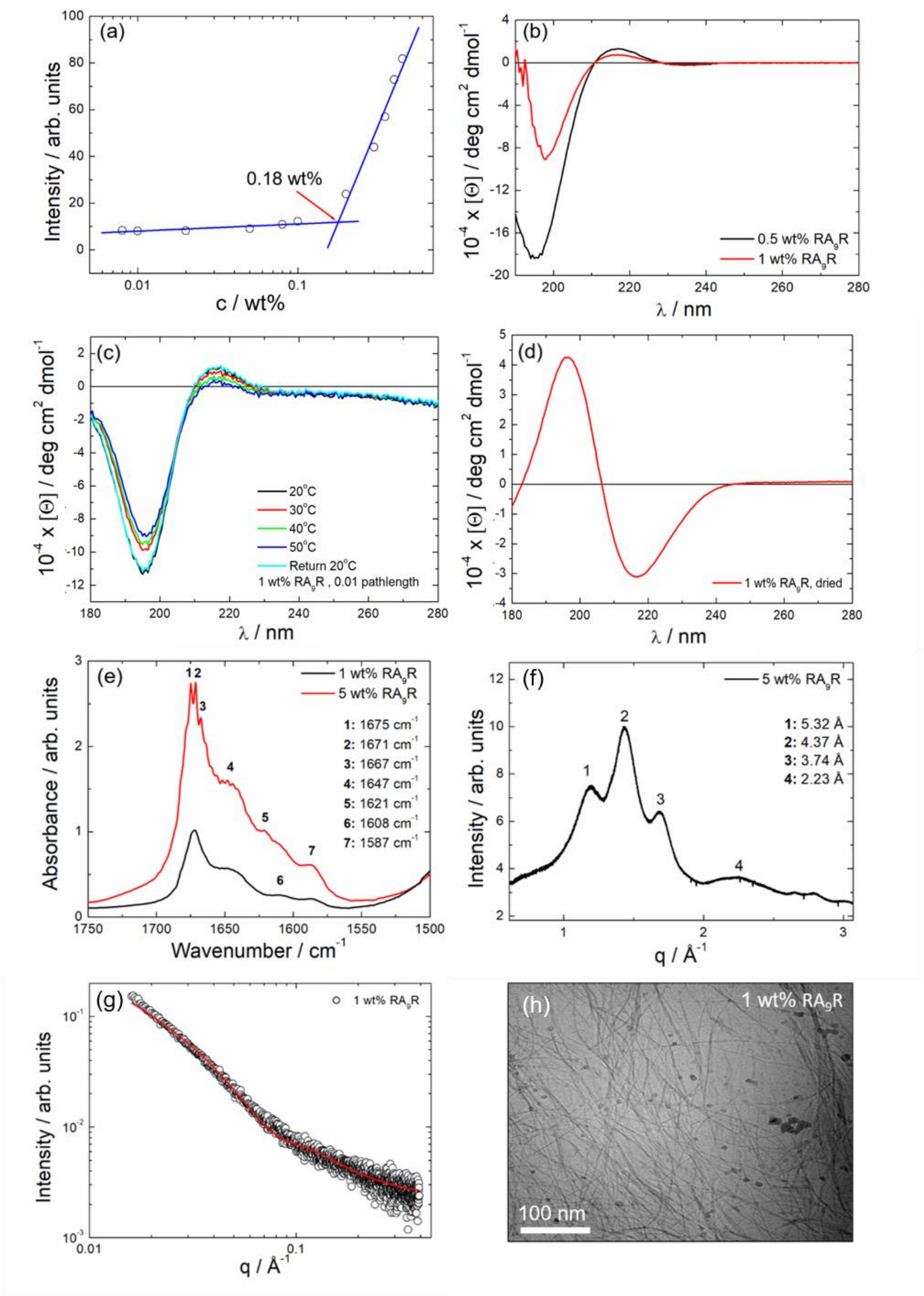

Figure 2.2. *RA_9R self-assembly in water: a) concentration dependence of ThT fluorescence intensity at λ_{em}= 520 nm, b)c) and d) CD data, e) FTIR spectra; f) XRD data, g) SAXS profiles h) cryo-TEM image for samples above the cac. The concentration of the solutions is indicated in the plot. The red line in e) correspond to the fitting of the SAXS data as described in the text. 1wt% solution.*

Table 2.2. *Parameters extracted from the fitting of the SAXS curve in Figure 2.2g: core radius R, shell thickness D_r and scattering length density of the core, shell and solvent η_{core}, η_{shell} and η_{core} and background BG.*

	1 wt% RA_9R
$R \pm \Delta R$ (Å)	15 ± 10
D_r (Å)	3
η_{core} (a.u.)	$4\text{x}10^{-9}$
η_{shell} (a.u.)	$1.5\text{x}10^{-6}$
η_{solv} (a.u.)	$1.1\text{x}10^{-7}$
BG	$2.3\text{x}10^{-3}$

2.2.1.3 $RA_{12}R$

ANS was used to determine the critical aggregation concentration of $RA_{12}R$ (Figure 2.3a). Results from ANS show a critical aggregation concentration of 0.007 wt%. This is lower than reported for RA_6R and RA_9R, however a different probe was used. ThT, which binds to amyloid fibrils, [22,37] was also used to determine the *cac* (data not shown), however, there was no clear increase in fluorescence intensity.

To examine the secondary structure, CD and FTIR was used (Figure 2.3c,d). The circular dichroism spectrum at 1 wt% is characterised by a minimum at 218 nm, corresponding to a β-sheet secondary structure.[26] CD spectra of 5 wt% and 10 wt% $RA_{12}R$ gel show reduced molar ellipticity. FTIR was used to further probe the secondary structure. FTIR showed peaks in the amide-I region at 1619 cm^{-1}, 1624 cm^{-1} which confirm the β-sheet secondary structure.[31,36,38,39] The 1673 cm^{-1} peak can be assigned to TFA counterions,[28,29] and 1586 cm^{-1} as stated previously is assigned to arginine vibrations.[30,31]

SAXS data, measured for 1 and 2 wt% $RA_{12}R$, was modelled using the form factor of a long cylindrical shell.[40] (Figure 2.3e. Fitting parameters listed in Table 2.3) . The extracted parameters $R \pm \Delta R$ = (23 ± 11) Å for 1 wt%, which is similar for the 2 wt%, and D_r = 15 Å and 17.3 Å. The high polydispersity is confirmed by cryo-TEM which shows a small population of micelles. This implies the cylinder core radius is smaller than the length of the oligoalanine A_{12} sequence= 38.4 Å, while the external shell has a thickness very similar to 7 arginine units. This result shows that there is an overlapping of the alanine chains within the core of the fibres, with the arginine residue exposed at the surface of the fibres. $RA_{12}R$ forms a standing gel between at 10 wt%, the SAXS data for which is included in figure 2.3e. This is slightly higher than the concentration at which RA_9R forms a stand-alone gel.

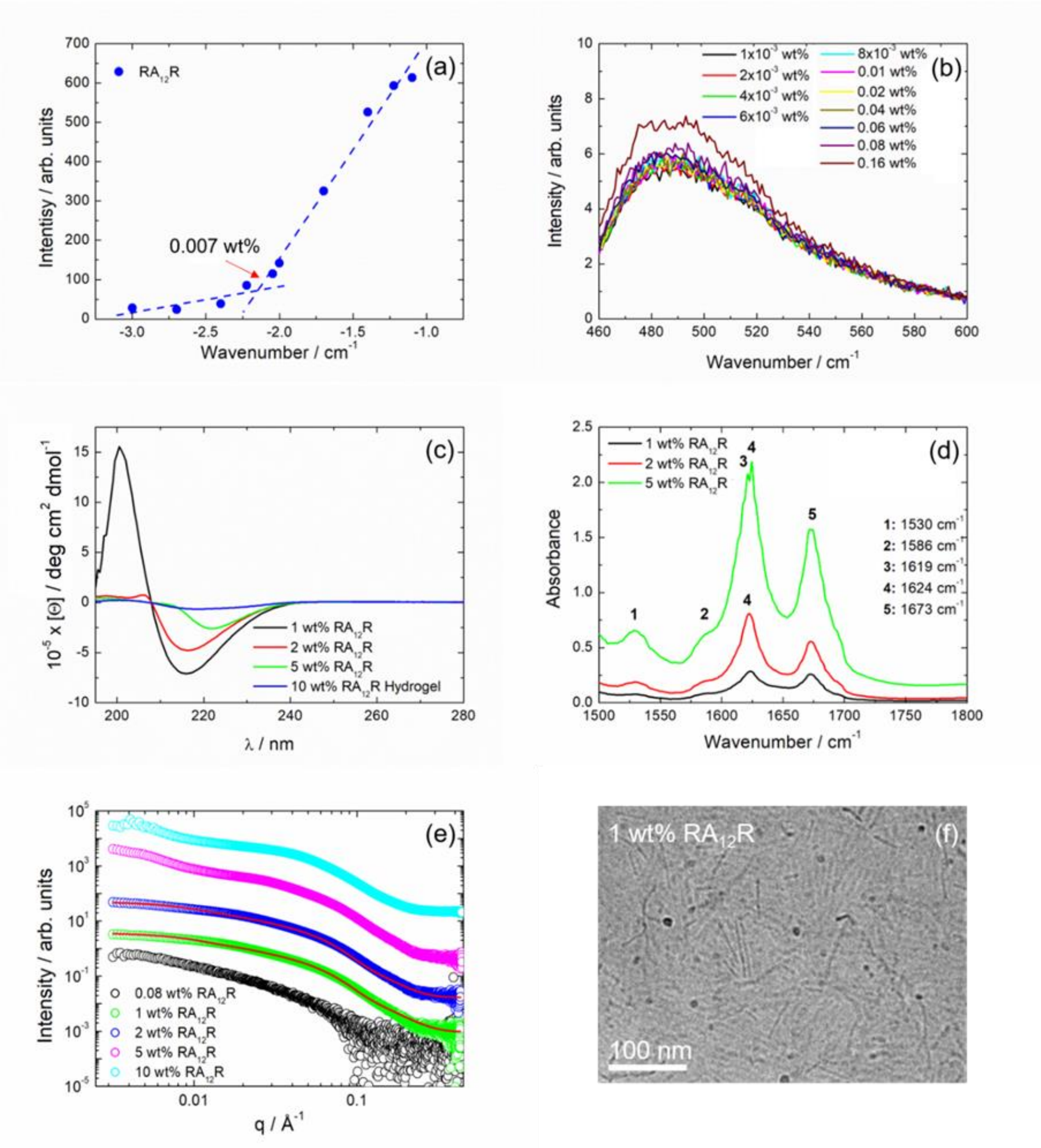

Figure 2.3. *Self-assembly of $RA_{12}R$. a) b) critical aggregation concentration using ANS, c) circular dichroism d) FTIR, e) SAXS data of $RA_{12}R$ at different concentrations with fits in Red and f) cryo-TEM image*

Table 2.3. *Parameters extracted from the fitting of the SAXS curves in Figure 2.3e: core radius R, shell thickness* D_r *and scattering length density of the core, shell and solvent* η_{core}, η_{shell} *and* η_{core} *and background BG.*

	1 wt% RA$_{12}$R	**2 wt% RA$_{12}$R**
$R \pm \Delta R$ **(Å)**	23 ± *11*	23 ± *11*
D_r **(Å)**	14.5	17.3
η_{core} **(a.u.)**	3.00×10^{-6}	3.38×10^{-6}
η_{shell} **(a.u.)**	-6.33×10^{-7}	-5.13×10^{-7}
η_{solv} **(a.u.)**	0	0
BG	9.31×10^{-4}	1.65×10^{-3}

2.2.1.4 A$_{12}$R$_2$

$A_{12}R_2$ was studied previously.[41] It was re-examined here for comparison with the other SLP's and instead of $A_{12}R$ which is not soluble in water as it is too hydrophobic. To determine the cac, ANS and ThT were used (Figure 2.4a,b). Results from ANS show a critical aggregation concentration of 0.007 wt%. ThT which binds to amyloid fibrils, was also used to determine the cac, however, there was no clear increase in fluorescence intensity.[22,35,37] This is similar to $RA_{12}R$.

To examine the secondary structure, CD and FTIR was used (Figure 2.4c,d). The circular dichroism spectrum at 1 wt% is characterised by a minimum at 221 nm, corresponding to a β-sheet secondary structure.[26,42] FTIR was used to further probe the secondary structure. FTIR showed peaks in the amide-I region at 1624 cm^{-1} which confirm the β-sheet secondary structure.[31,36,38] The 1673 cm^{-1} peak can be assigned to TFA counterions,[28,29] and 1586 cm^{-1} as stated previously is assigned to arginine vibrations.[30,31] The 1698 cm^{-1} shoulder can be assigned to anti-parallel β-sheet.[38]

SAXS data, measured for 1 and 2 wt% $A_{12}R_2$ (Figure 2.4e), was modelled using the form factor of a long cylindrical shell[40] (Figure 2.4e. Fitting parameters listed in Table 2.4. The extracted parameters for 1wt% $R \pm \Delta R$ = (23 ±15) Å, with the same radius for 2wt% but with less polydispersity. The polydispersity is confirmed by cryo-TEM which shows a mixture of fibres and spherical micelles. The shell radius, D_r = 25.5 Å, indicate that the cylinder core radius is smaller than the length of the oligoalanine A_{12} sequence= 38.4 Å, while the external shell has a thickness very similar to 8 arginine units. For 2 wt% this decreases significantly to 5 alanine amino acids, which could be due to increased ordering, as Cryo-TEM (Figure 2.4f) at 1 wt% shows clustered fibres as well as individual fibres, which explains somewhat the high polydispersity in the SAXS fits. This result shows that there is an overlapping of the alanine chains within the core of the fibers, with the arginine residue exposed at the surface of the fibres. $A_{12}R_2$ forms a standing gel at 5 wt% which is lower than the concentration at which $RA_{12}R$ forms a gel.

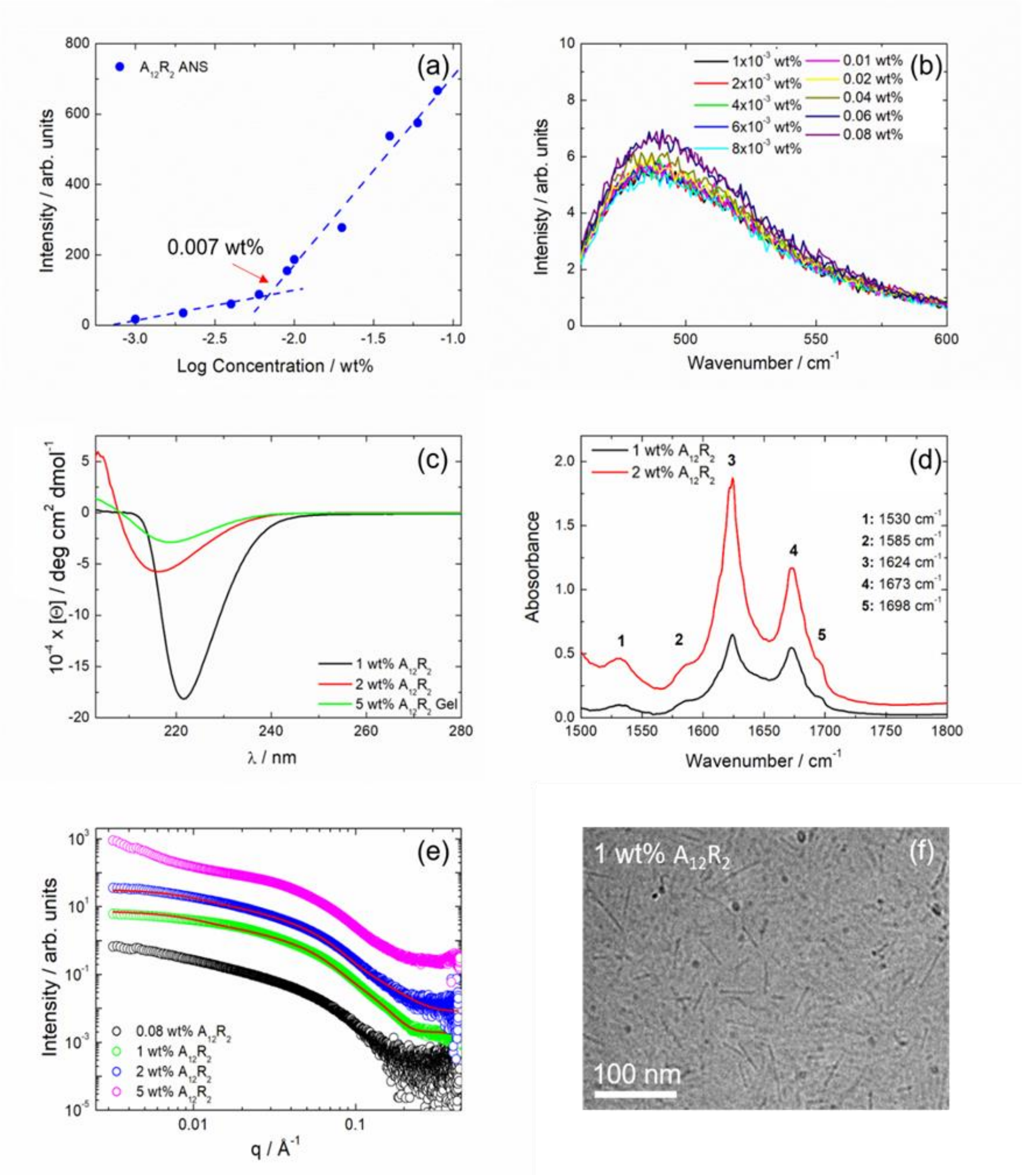

Figure 2.4. Self-assembly of $A_{12}R_2$ a) b) critical aggregation concentration using ANS, c) circular dichroism d) FTIR e) SAXS data of $A_{12}R_2$ at different concentrations with fits in Red and f) cryo-TEM of 1 wt% $A_{12}R_2$

Table 2.4. *Parameters extracted from the fitting of the SAXS curve in Figure 2.4e: core radius R, shell thickness D_r and scattering length density of the core, shell and solvent η_{core}, η_{shell} and η_{core} and background BG.*

	1 wt% $A_{12}R_2$	**2 wt% $A_{12}R_2$**
$R \pm \Delta R$ (Å)	22.6 ± *15*	22.6 ± *12*
D_r (Å)	25.7	15.5
η_{core} (a.u.)	3.55×10^{-6}	2.53×10^{-6}
η_{shell} (a.u.)	-6.52×10^{-7}	-5.50×10^{-7}
η_{solv} (a.u.)	0	0
BG	1.61×10^{-3}	8.05×10^{-4}

2.2.1.5 Comparison of Self-Assembly

A_6R was previously shown to assembly into ultrathin nanosheets at relatively dilute solutions, and ordered nanotubes at high concentration, with a critical aggregation concentration of 1.4 wt%.[16] Adding cap to the C-terminus promotes the assembly of long fibres, lowering the *cac* to 0.4 wt%. A_9R was reported to have a *cac* of 0.05 wt% and assemble into β-sheet amyloid fibres.[17] $A_{12}R_2$ as reported above assembles into β-sheet amyloid fibres, with a cac of 0.007 wt%. The tend for the *cac* to decrease with the length of the A_n chain length is consistent with increased hydrophobicity.

A similar effect is observed for the bola amphiphiles. RA_3R and RA_6R do not self-assemble into regular structures in water. It is likely that the flexibility of the PP II helical structure together with the solubility of the arginine residues does not favour RA_3R and RA_6R assembly. Increasing the length of the hydrophobic central block decreases the solubility of the molecule and allows for the self-assembly of RA_9R and $RA_{12}R$ into β-sheet fibrils. RA_9R forms long amyloid fibres, and interestingly $RA_{12}R$ forms shorter comparative fibres (as can be seen by the SAXS and Cryo-TEM.)

Generally, the aggregation concentration is lower for the SLP's than for their corresponding bola amphiphile, which is probably linked to the bola amphiphiles (except for $RA_{12}R$ and $A_{12}R_2$ which have the same *cac*) being more soluble due to the additional arginine residue. Across both groups, the alanine chain length increases, the increased amphilicity causes lower aggregation concentrations, more ordered structures, and generally lower concentrations for which hydrogelation is observed.

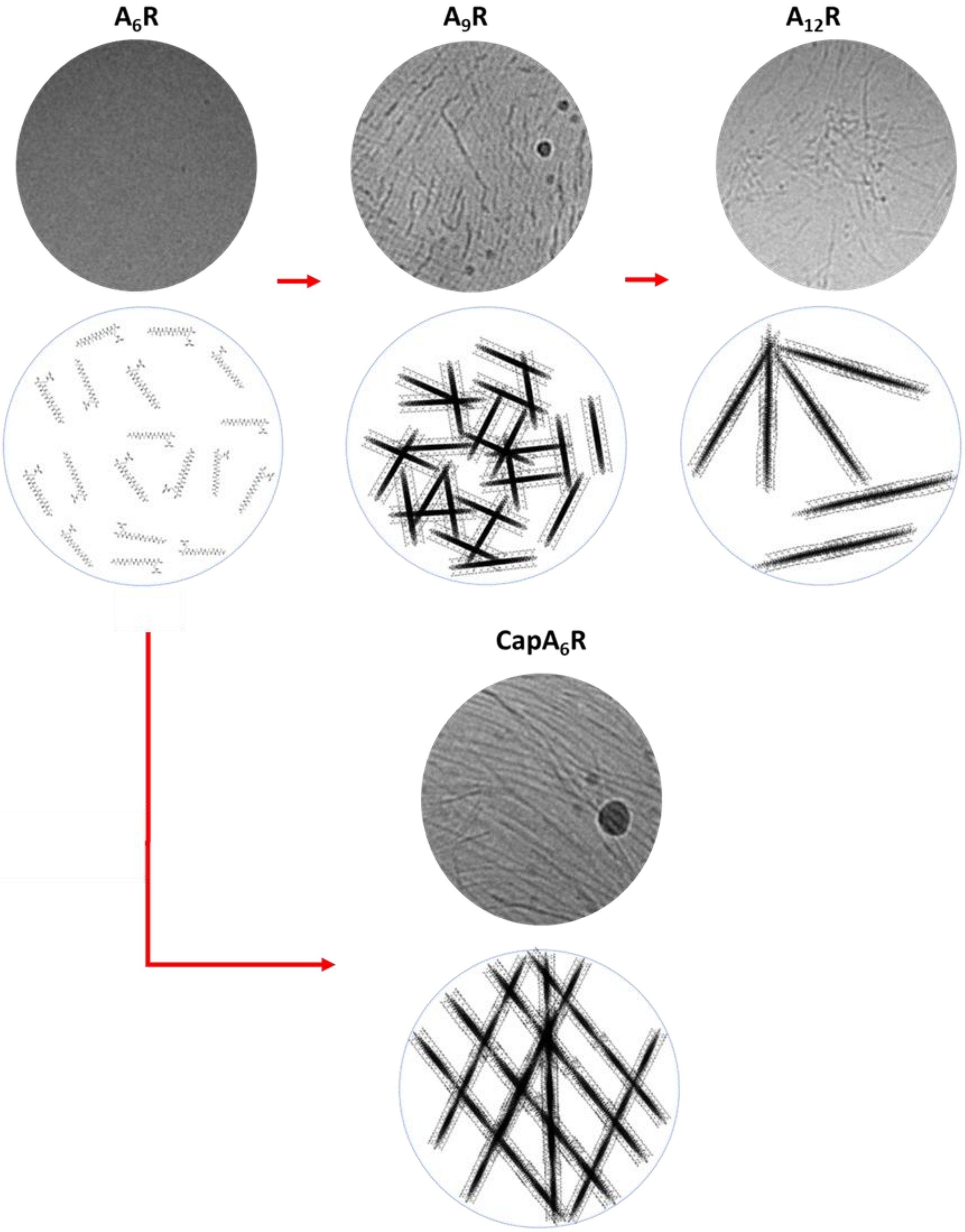

Scheme 2.4. *Schematic representation of the self-assembly of the surfactant-like peptides (SLPs) s at 1 wt%*

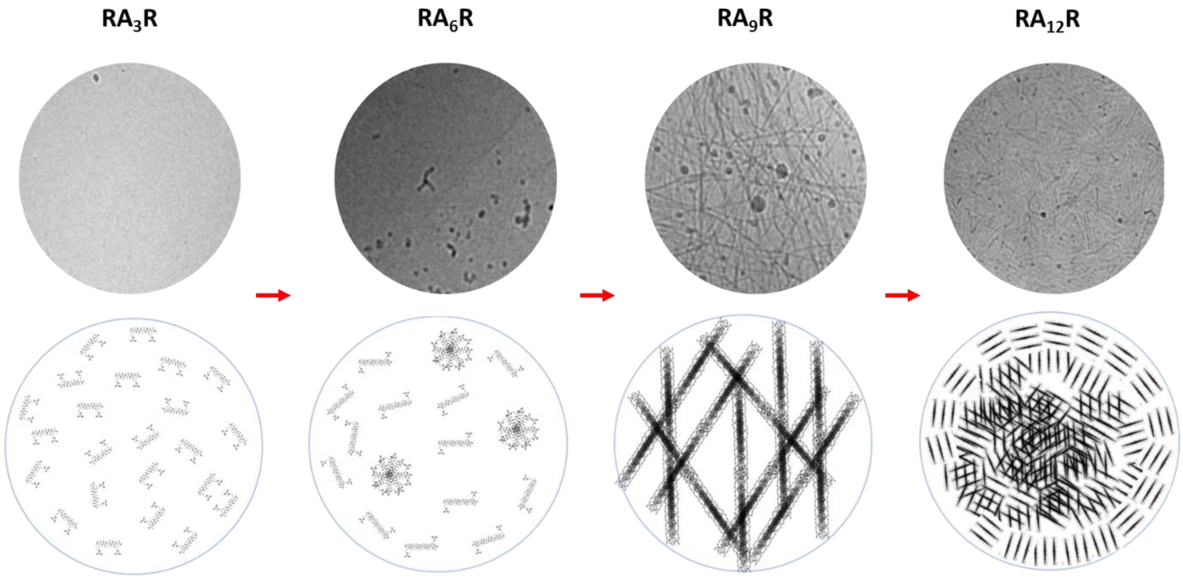

Scheme 2.5. *Schematic representation of the self-assembly of the bola-amphiphiles at 1 wt%*

2.2.2 Cytocompatibility of RAnR's and AnR's

To assess the cytocompatibility of the peptides, an MTT assay using human skin fibroblast cells was performed on all of the RA_nR and A_nR peptides (Figure 2.5). The IC_{50} values can be seen in Table 2.5. This was examined to assess whether increased alanine chain, and the architecture of the bola-amphiphile or the SLP affects the toxicity. Previously it has been reported that increased size of antimicrobial peptides (AMP's),[43] as well as increased catonic charge and increased hydrophobic motifs can increase toxicity.

For the bola-amphiphiles, there is no clear relationship between the length of the peptide and the cytotoxicity. In order of compatibility, the most compatible is RA_6R, followed by $RA_{12}R$ and RA_3R, with the least compatible being RA_9R. The peptide RA_6R is much more strongly tolerated by the cells than the other peptides in the group. The least compatible peptide, RA_9R, is significantly less compatible, particularly when looking at the molar concentrations, which reveals it is around 5 times less compatible than the second most toxic peptide RA_3R.

Although we can establish there is not a strong link between the self-assembled structure of these peptides, and toxicity, it does imply that toxicity may arise through different mechanisms. RA_3R was reported to interact with lipid membranes in the form of unassociated molecules due to interactions between the arginine residues and anionic or lipid head groups.[20] The mechanism of toxicity for RA_6R could be similar to this. The cytotoxicity of RA_9R and $RA_{12}R$ is higher than that of RA_6R at a given concentration, likely in some part due to the self-assembly of the fibrils, in which the arginine motif is presented at high density on the fibril surface.

One theory for increased toxicity between the group may be due to the sizes of the peptides. Although passive diffusion across cell membranes is generally thought to occur for small polar molecules (e.g. CO_2 and O_2), there are reports of some peptides passively diffusing across membranes, for example, cyclosporin A.[44] RA_3R is relatively small and is a monomer, enabling it to potentially be more permeable to the human cell membrane than RA_6R, which also forms some clustered aggregates which may also be too large to cross. Thus, RA_3R may diffuse into the membrane more easily than RA_6R. The increased molecular weight and perhaps self-assembly into larger aggregates displayed by RA_9R and the $RA_{12}R$ may prevent the from being able to diffuse across the membrane. However, the self-assembled overall structure, which presents cationic charge at high density may be more disruptive to the membrane, thus the increased toxicity. This could imply there is an optimum length of alanine chain, where there is less toxicity when there is less permeability at longer peptide lengths, but not too amphiphilic where it presents positive charge at high density. Further cytotoxicity data of bola-amphiphiles with alanine lengths of 4, 5, 7 and 8 would be needed to examine this further.

The majority of the SLP's did not have an IC_{50} concentration within in the studied range (above 0.5 wt%). $A_{12}R_2$ did have an IC_{50} within this range, which could either be to do with increased size of the hydrophobic motif, the increased amphilicity or the additional arginine residue.

The cytotoxicity of both RA_6R and A_6R, are within the same error of each other across the concentration range (Figure 2.6a). RA_9R is significantly more toxic that A_9R (Figure 2.6b). $A_{12}R_2$ is more toxic than $RA_{12}R$ (Figure 2.6C).

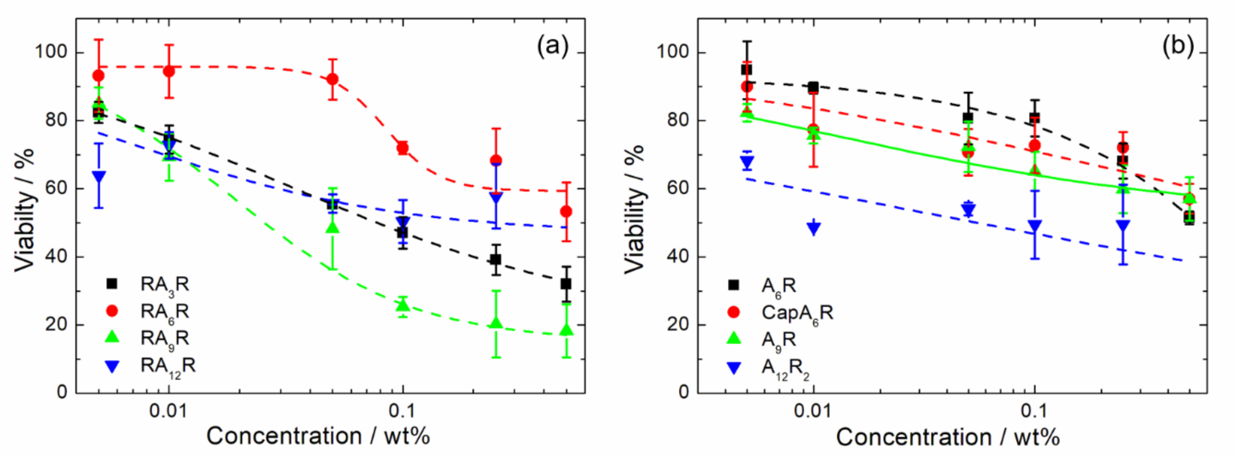

Figure 2.5. *Cytocompatibility of peptides using MTT assay, a) peptide bolaamphiphiles and b) SLPs with sigmoidal fits as a guide to the eye.*

Table 2.5. *List of IC50 values for the A$_n$R and RA$_n$R peptides.*

Peptide	***IC50***	
	wt%	*mM*
RA$_3$R	0.077 ± 0.03	1.4
RA$_6$R	>0.5	>6.61
RA$_9$R	0.026 ± 0.008	0.27
RA$_{12}$R	0.18 ± 0.1	1.56
A$_6$R	>0.5	>8.32
CapA$_6$R	>0.5	>7.79
A$_9$R	>0.5	>6.14
A$_{12}$R$_2$	0.05 ± 0.02	0.48

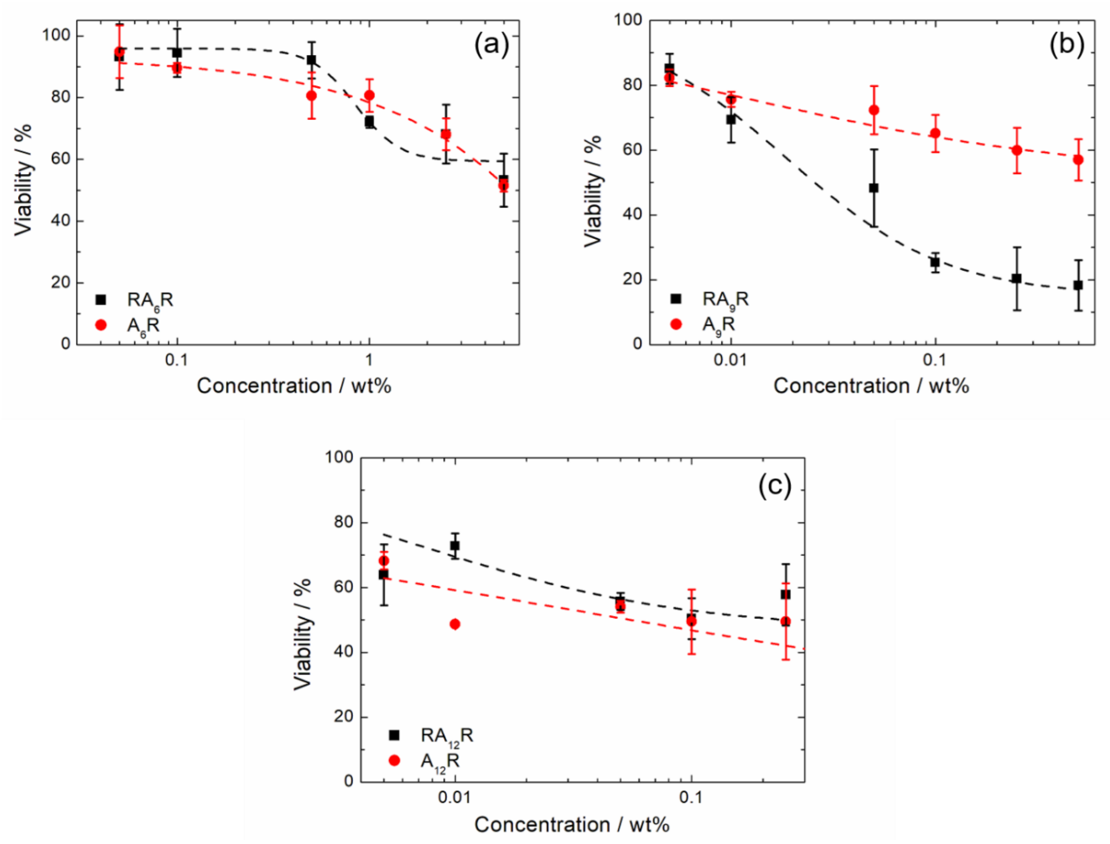

Figure 2.6. *MTT assays of bolaamphiphiles compared to the same alanine-chain length surfactant-like peptides. Sigmoidal fits are used as a guide to the eye.*

2.2.3 Antimicrobial Activity of RANR's and AnR's

To investigate the potential antimicrobial activity of the peptides, a range of common Gram-negative and Gram-positive bacteria were selected for initial screens, using straightforward bacterial kill (counts of colony-forming units, CFUs) assays. The Gram-positive microbe selected was *S.aureus*, which is commonly found as part of the human microbiota, and is an opportunist pathogen which can cause a range of infections including food poisoning, skin infections and respiratory tract infections. The Gram-negative strains selected included *E.coli*, which is a widely studied bacteria which often causes food borne infection, and *P. aeruginosa*, which is an opportunist pathogen causing serious infections in cystic fibrosis. We also examined *P.syringae*, a Gram-negative plant pathogen

Antimicrobial assays were conducted against these species to assess the survival of *E.coli*, *S.aureus*, *P.syringae* and *P.aeruginosa* in the presence of either control (water), RA_3R, RA_6R,

RA_9R, $RA_{12}R$, A_9R or $A_{12}R_2$. The concentration used and corresponding viability are reported in Table 2.6.

2.2.3.1 Antimicrobial activity of the bolaamphiphiles.

RA_6R at lower concentration showed a small reduction in bacterial colony counts for *E.coli* and *P. aeruginosa* after 24 hours (Figure 2.7). For RA_6R acting against both *E. coli*, *P.aeruginosa* and *P.syringae* the main reduction in the number of CFUs occurs in the first 2 hours after treatment with the peptide. At 0.1 wt% RA_6R there is a more significant effect against *P. aeruginosa* (Figure 2.7c), denoted by a 5 log reduction in CFU after 24 hrs. There is a small increase in the effect of 0.1 wt% RA_6R on *E. coli* or *S. aureus* (Figure 2.7a,b). Interestingly, RA_6R is also strongly active against *P.syringae* with a log 4.5 reduction in CFU after 24 hrs (Figure 2.7d), suggesting that RA_6R is more active against *pseudomonas* bacterium.

There was no reduction in the bacterial colony count of *P.aeruginosa* or *E.coli* below the IC_{50} concentration of RA_9R (Figure 2.f,g). There is a small reduction of 1.4 log for *S.aureus* (Figure 2.7e). When increasing the concentration to 0.05 wt%, there was a 0.6 log CFU reduction for *E.coli* after 24 hours. For *S.aureus* there was a similar reduction of 1.4 log CFU after 2 hours and 1.3 log CFU after 24 hours (Figure 2.7e). For *P.aeruginosa* and *P.syringae* there is no effect (Figure 7g,h). When increasing the concentration to 0.1 wt% peptide, there is a small, statistically insignificant reduction of 1.3 log of *E. coli* numbers when exposed to RA_9R. Interestingly, the reduction in colony forming units (CFU) after 24 hrs are 2.6, 3.3 and 4.0 orders of magnitude for *S. aureus, P. aeruginosa* and *P. syringae* respectively. From this we can conclude RA_9R has no effect in the cytocompatible range, but has a small effect of E.coli, a slightly larger effect on *S.aureus*, *P.aeruginosa* and *P.syringae* above this range. As *S.aureus* is gram positive and *P.aeruginosa* and *P.syringae* are Gram-negative, this shows a broader range effect.

Antimicrobial activities of RA_3R was previously measured at 0.25 wt%.[18] This concentration has low human cell viability, but showed a large effect against food pathogen *L.Monocytogenes*. In order to compare the peptide length with activity, RA_3R and $RA_{12}R$ were screened at 0.1 wt% (Figure 2.8). $RA_{12}R$ has more activity against all species than RA_3R. Interestingly, when the length of the alanine chain is plotted, against the reduction in colony forming units, there seems to not be any correlation between length of the peptide chain with activity (Figure 2.8d).

Table 2.6. *Reported and measured antimicrobial activity of the SLP's and bola-amphiphiles after 24 hours.*

Peptide	**Conc / wt%**		**Reduction / Log CFU mL^{-1}**			
		Viability	***S.aureus***	***P.aeruginosa***	***E.coli***	***L.monocytogenes***
RA$_3$R	0.25[18]	39.1 (±4.2)	2.6	N/A	3.5	5.6
	0.1	47.1 (±4.6)	0.68	3.69	1.18	N/A
A$_6$R	0.5[16,17]	51.5 (±1.8)	~6	N/A	~4	~6
CapA$_6$R	0.25[17]	72.0 (±4.6)	1.2	N/A	1.8	4.7
RA$_6$R	0.05	92.1 (±3.4)	0	1.36	0.68	N/A
	0.1	72.2 (±1.8)	0.64	4.98	1.01	N/A
A$_9$R	0.05	72.3 (±7.4)	0.12	4.16	1.22	N/A
RA$_9$R	0.01	69.3 (±6.3)	1.4	0.011	0	N/A
	0.05	48.2 (±12)	1.4	0.096	0.62	N/A
	0.1	25.3 (±2.9)	2.64	3.32	1.29	N/A
A$_{12}$R$_2$	0.1	49.5 (±9.9	0.41	4.0	1.7	N/A
RA$_{12}$R	0.1	55.7 (±2.9)	1.32	4.44	2.81	N/A

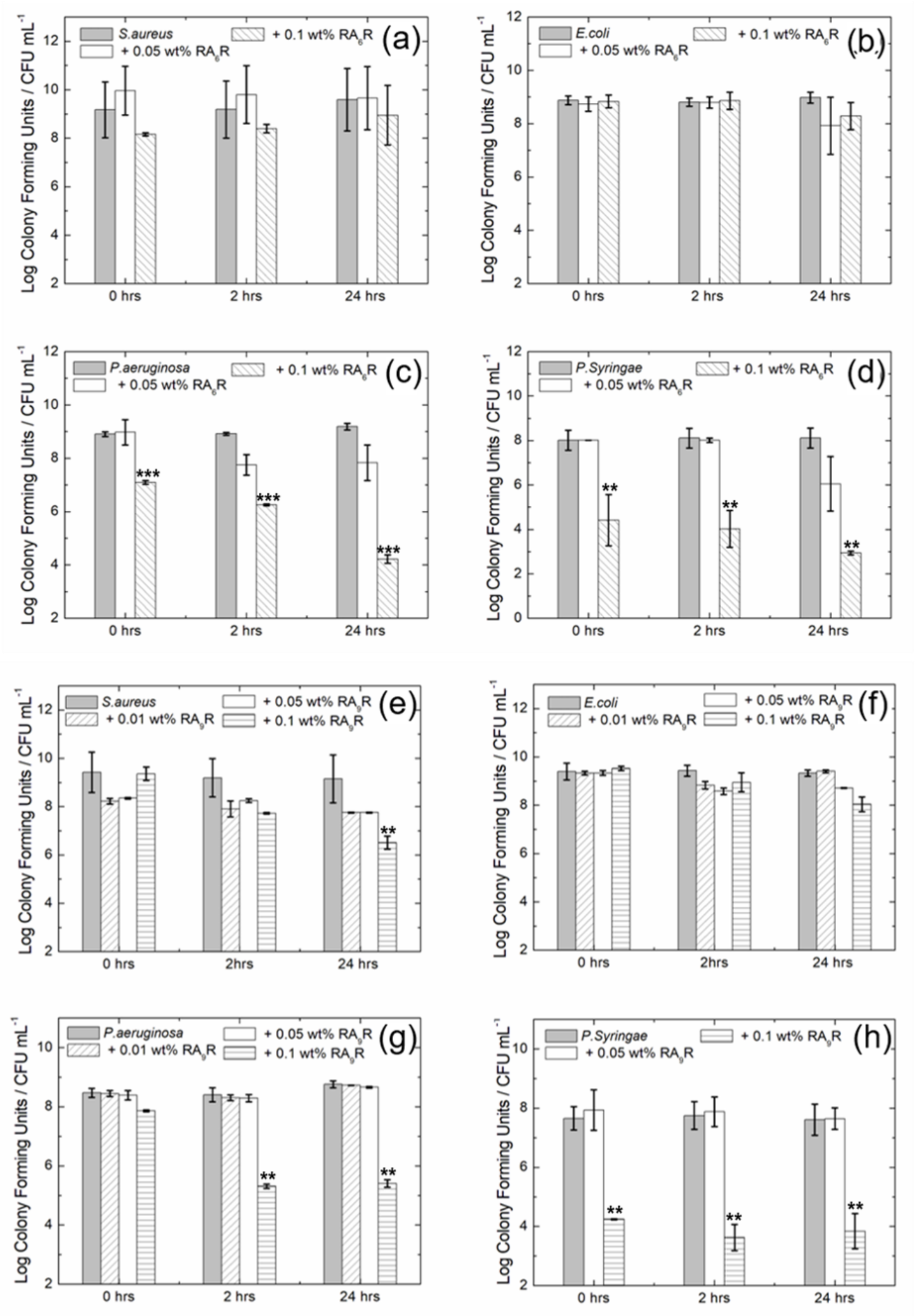

Figure 2.7. *Antimicrobial screen of RA_6R with a) S.aureus, b) E.coli, c) P.aeruginosa d) P.syringae and RA_9R with e) S.aureus, f) E.coli, g) P.aeruginosa and h) P.syringae*

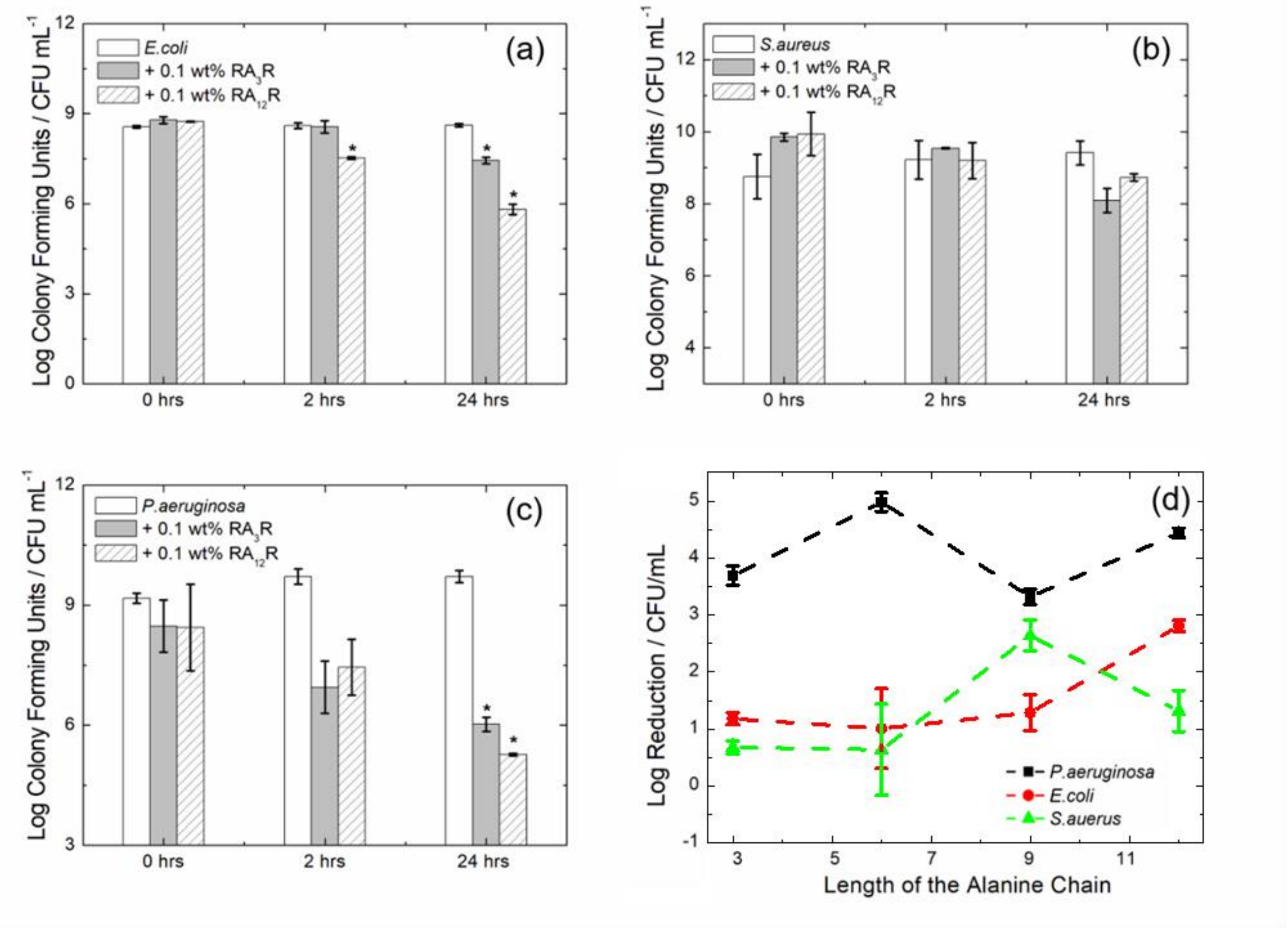

Figure 2.8. *Antimicrobial screen of $A_{12}R_2$ and $RA_{12}R$ with a) S.aureus, b) E.coli, and c) P.aeruginosa and d) Antimicrobial activity vs length for alanine chain length of the bola-amphiphiles compared at 0.1 wt% after 24 hours.*

2.2.3.2 Surfactant like peptides

The antimicrobial activity of A_6R and CapA_6R was discussed previously elsewhere.[16,17] In summary, all of these peptides showed strong activity against *L.monocytogenes* a food borne pathogen (Table 2.6). A_6R had a much larger effect against *S.aureus* than CapA_6R, although this may be due to the concentration difference used in the study.

Peptide A_9R (Figure 2.9) assayed at 0.05 wt% had a statistically significant decrease in the numbers of *E.coli* and *P.aeruginosa* after 24 hours. The latter particularly, with a reduction of 4 log CFU mL^{-1}. As A_9R reduced the number of the two Gram-negative bacteria, if may be that it is selective for Gram negative bacteria, although a larger group of gram-negative bacteria species would be needed to examine this further. A_9R does have significantly higher activity against *P.aeruginosa* than bola-amphiphile RA_9R, being more active by 4 log units at the corresponding concentration of 0.05 wt%, and by 0.8 log units when the concentration of RA_9R is doubled (Figure 2.7g, 2.9c, Table 2.6). RA_9R does display some activity at against *S.aureus*, (Figure 2.7e) but A_9R demonstrates a negligible activity at the corresponding concentration(Figure 2.9b).

$A_{12}R_{2}$, similar to the other peptides displays activity against *P.aeruginosa* (Figure 2.9f , and log 4.0 reduction in cFU mL^{-1}). Despite being measured at a higher concentration than A_9R, it still displays less activity against *P.aeruginosa*. Similarly to $RA_{12}R$, (Table 2.6) there is activity against *E.coli* (Figure 2.9d, log 1.7 reduction) but little activity against *S.aureus* (Figure 2.9e, 0.4 log reduction).

Overall, both the SLP's and bola-amphiphiles display some antimicrobial activity. It can be seen that RA_9R displays little antimicrobial activity under these conditions. Interestingly RA_6R and A_9R display strong activity against *P. aeruginosa* at a concentration where the cytocompatibility (to fibroblasts) is acceptable. The concentrations used for A_6R and $CapA_6R$ measured in previous studies[16,17] are significantly higher than those in the present study, meaning further testing would be required in order to compare the effectiveness of these peptides with the rest of the group.

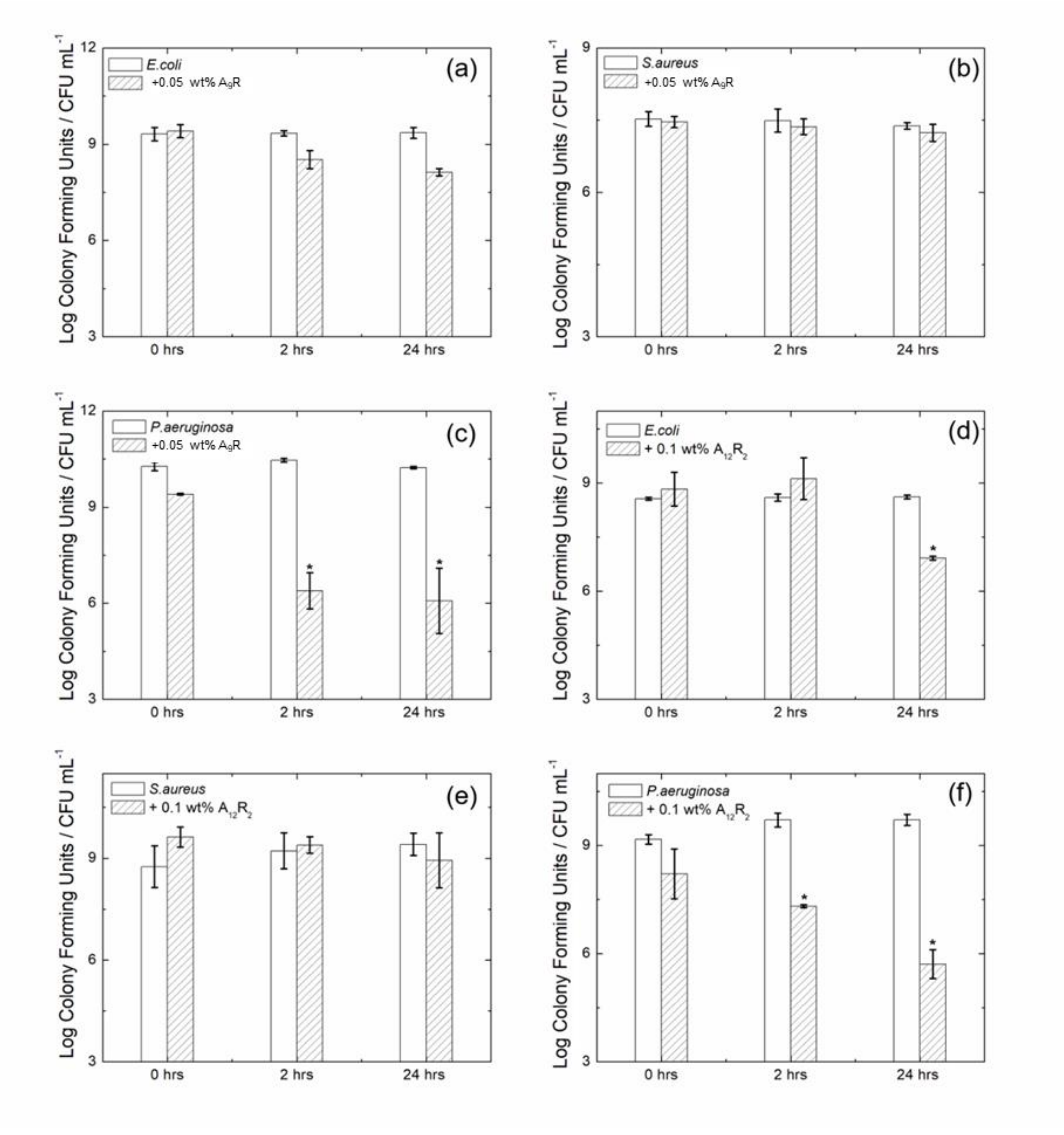

Figure 2.9. Antimicrobial screening of A_9R *a) E.coli b) S.aureus and c) P.aeruginosa and* $A_{12}R_2$ *with d) E.coli e) S.aureus and f) P.aeruginosa*

2.2.3 Interactions with liposomes.

In order to understand further the way in which these cationic peptides interact with bacterial membrane models, RA_6R, RA_9R, $RA_{12}R$ and $A_{12}R_2$ were examined with combinations of simple membrane models.

Previously Dr Castelletto examined the interactions of A_6R, capA_6R, RA_3R and A_9R with DOPC/POPC zwitterionic membranes and POPG/POPE anionic lipid vesicles. Mammalian cells contain PC and PG lipids, whereas bacterial cells contain PG and PE (Table 2.7). Therefore, these lipids were used as a simplified system to model peptide interactions. RA_3R was shown to decorrelate the bilayers of DOPC/POPC vesicles, and change the structure of POPG/POPE vesicles depending on composition of the latter.[18] A_6R was reported to have a thinning effect on DOPC/POPC vesicles through interacting at the surface, and a minimal effect on anionic vesicles POPG/POPE.[17] A_9R has a similar mechanism for interacting with the zwitterionic vesicles, however, inserts into the POPG/POPE bilayers, causing increased bilayer distances and correlation.[45] CapA_6R was reported to cause structuring of the POPG/POPE bilayers due to incorporation of the peptide with the lipid membrane in a β-sheet conformation, and tubulation of the zwitteironic vesicles at certain compositions.[17]

For this study, three ratios of DPPG/DPPE, 1:3 DPPG/DPPE (which is similar to *P.aeruginosa*), 1:1 which has a similar ratio to *B.cereus*, 3:1 DPPG/DPPE and DPPG only which are more similar to *S.aureus* membranes which contain no PE lipid. The rationale for the change of model system from previously the POPG/POPE system to DPPG/DPPE system was due to transition temperatures. POPG and POPE have T_m values of -18 °C and 25 °C, whereas DPPG/DPPE have T_ms of 41 °C and 63 °C respectively.[46] These T_m values are more accessible for measurement (for example nanoDSC, which has a minimum temperature of 0 °C), and these lipids have well defined phase diagrams.

Table 2.7. *Content of different species bacteria membranes*.[47]

Species	% PG	% PE
Gram Negative		
Escherichia coli	15	80
Pseudomonas aeruginosa	21	60
Gram Positive		
Staphylococcus aureus	58	0
Bacillus cereus	40	43

2.2.3.1 Circular Dichroism

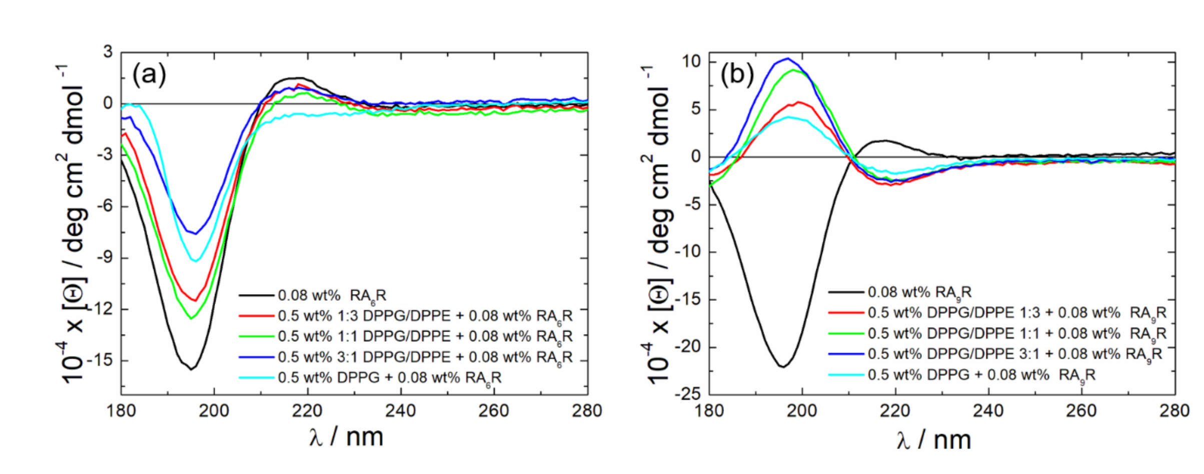

Figure 2.10. *CD spectra for (a) RA$_6$R and (b) RA$_9$R peptides on their own or mixed with lipids at the concentrations indicated.*

CD was used to examine whether interactions of the peptide with DPPG/DPPE membranes influenced the peptide secondary structure. Figure 2.10 shows the CD spectra of the RA$_6$R and RA$_9$R with 0.08 wt% peptide concentration compared to those in the presence of DPPG/DPPE lipid mixtures. RA$_6$R appears to remain as a PP II helix in the presence of lipids. The decreased molar ellipticity implies slight loss of structure. The molar ellipticity decreases with higher ratios of DPPG:DPPE, and a disordered structure is observed for the solution of RA$_6$R with DPPG, which is characterised by a 190 nm minimum and the loss of the 220 nm broad peak. This is perhaps due to the strong binding between the ionic head group of the DPPG and the peptide inhibiting secondary structure formation.

Remarkably, the PP-II helix secondary structure measured for pure RA$_9$R in solution, changes into a β-sheet structure in the presence of lipid (Figure 2.10b). This shows that the DPPG/DPPE lipid membrane orders the peptide into a β-sheet secondary structure at a concentration of RA$_9$R below its *cac* (Figure 2.10b). A similar effect has previously been reported by us for capA$_6$R.[17] The population of RA$_9$R-induced β-sheets increases with increasing DPPG (Figure 2.10b), showing that RA$_9$R binds more strongly to DPPG than to DPPE.

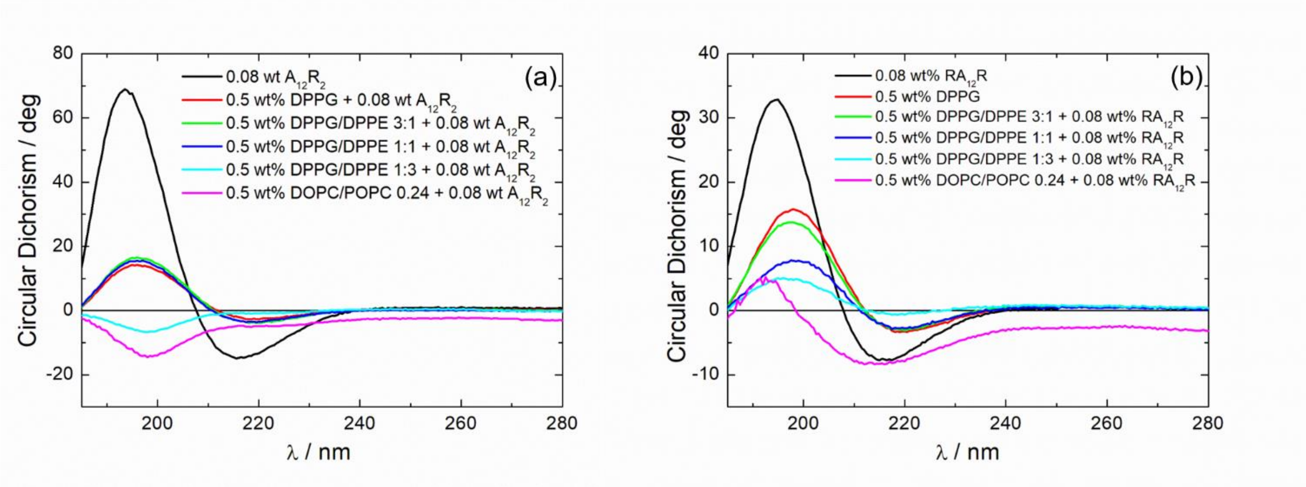

Figure 2.11. *CD spectra for (a) $RA_{12}R$ and (b) $A_{12}R_2$ peptides on their own and mixed with lipids at the concentrations indicated.*

For both $A_{12}R_2$ (Figure 2.11a) and $RA_{12}R$ (Figure 2.11b), the concentration of 0.08 wt% is above the aggregation concentration for which the peptides form fibres. CD with lipid mixtures (Figure 2.11) shows that β-sheet formation is already observed at these low concentrations. For both peptides, addition of the lipid mixtures causes reduced molar ellipticity, decreasing the order of the structure. $RA_{12}R$ has decreased molar ellipticity when interacting with liposome mixtures, which decreases more when there is increased PE content, and blue shifted β-sheet structure when compared to DOPC/POPC mammalian membrane model (Figure 2.11b). Interestingly, $A_{12}R_2$ becomes disordered when mixed with high PE ratios, is disordered when mixed with DOPC/POPC human membrane models. This is interesting as $A_{12}R_2$ has more activity against bacteria with high PE cell wall content (Table 2.7, *E.coli* and *P.aeruginosa*) which could in turn be linked to the change in conformation of the peptide at the surface.

2.2.3.2 SAXS and Cryo-TEM

SAXS was also used to examine the interactions of lipids with the peptides. SAXS data for lipids and peptides shown in Figure 2.12 was collected at 20 ^{o}C, which is in the gel L_{β} phase for all lipid mixtures.[21] For the pure lipids, a broad peak positioned at approximately q = 0.15 Å^{-1} corresponds to unilamellar vesicles. SAXS data from temperature ramps in the range 20 – 50 ^{o}C for the peptides mixed with DPPG at two concentrations (Figure 2.13) shows particularly enhanced lipid bilayer correlations on heating at the higher peptide concentration studies (0.25 wt%).

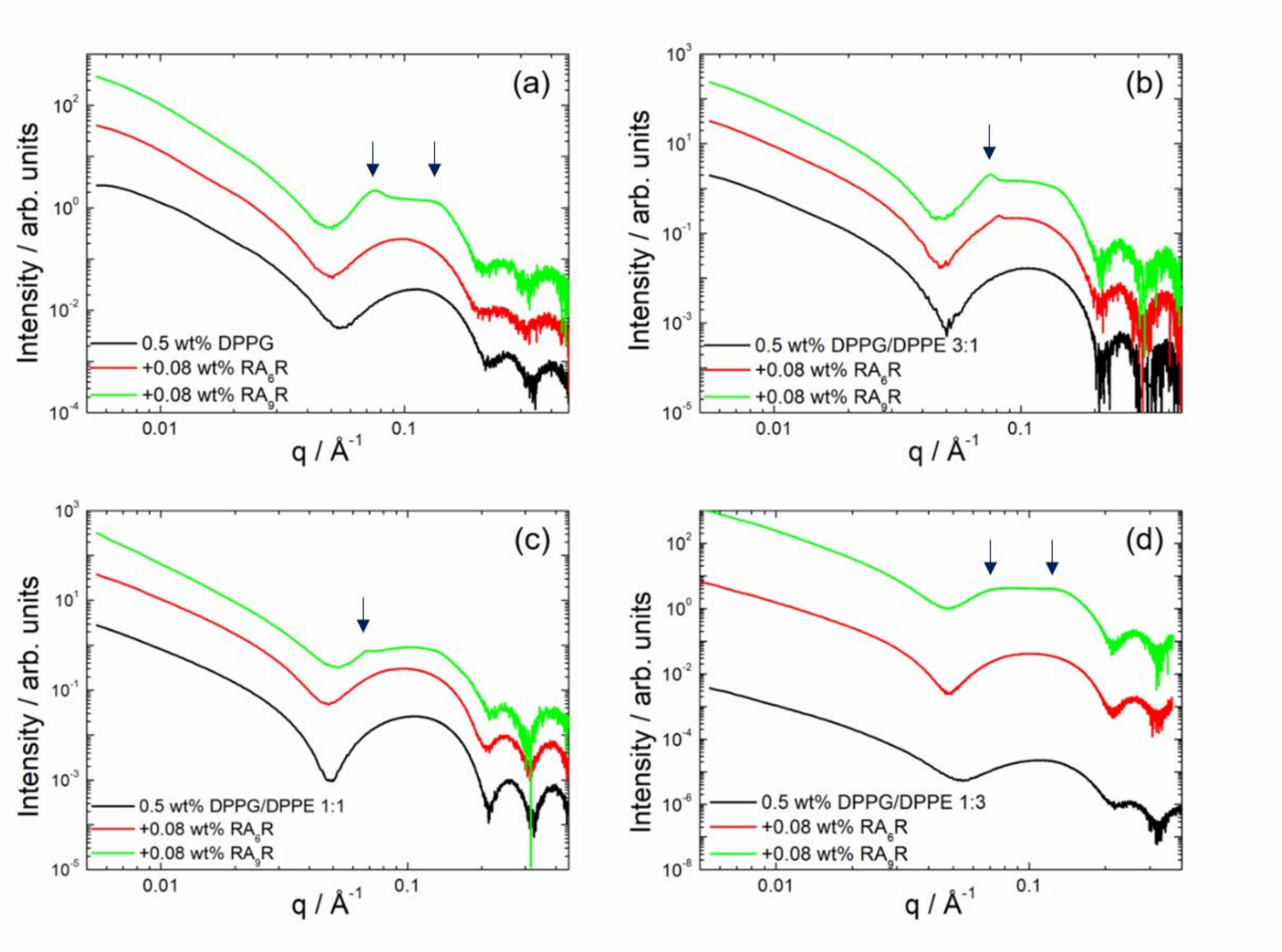

Figure 2.12. *SAXS profiles for mixtures of lipids (total 0.5 wt%) and 0.08 wt% peptide.*

Upon addition of RA$_9$R, the SAXS data in Figure 2.12 shows that some correlation between bilayers is induced, as indicated by the presence of small Bragg peaks. In contrast, RA$_6$R only causes a shift to lower *q* of the form factor minimum, i.e. there is a slight increase in the bilayer spacing. This implies that RA$_9$R causes membrane correlations due to the formation of β-sheet structure as concluded from CD results above. However, RA$_6$R does not change membrane correlations, but it does restructure the membranes, possibly due to interaction between the arginine residues and the charged DPPG head groups. In the DPPG/RA$_9$R, mixture the peptide induces two Bragg peaks with *d*-spacing values of 83.1 Å and 44.8 Å ($d= 2\pi/q_0$; q_0: coordinate for the peak maxima), consistent with a lamellar structure. Cryo-TEM images of peptides in the presence of the lipid mixtures are shown in Figure 2.14. These images show the presence of some fibrils of RA_9R coexisting with vesicles, however the SAXS signal is dominated by the contribution from the vesicles, as shown by the data in Figure 2.12.

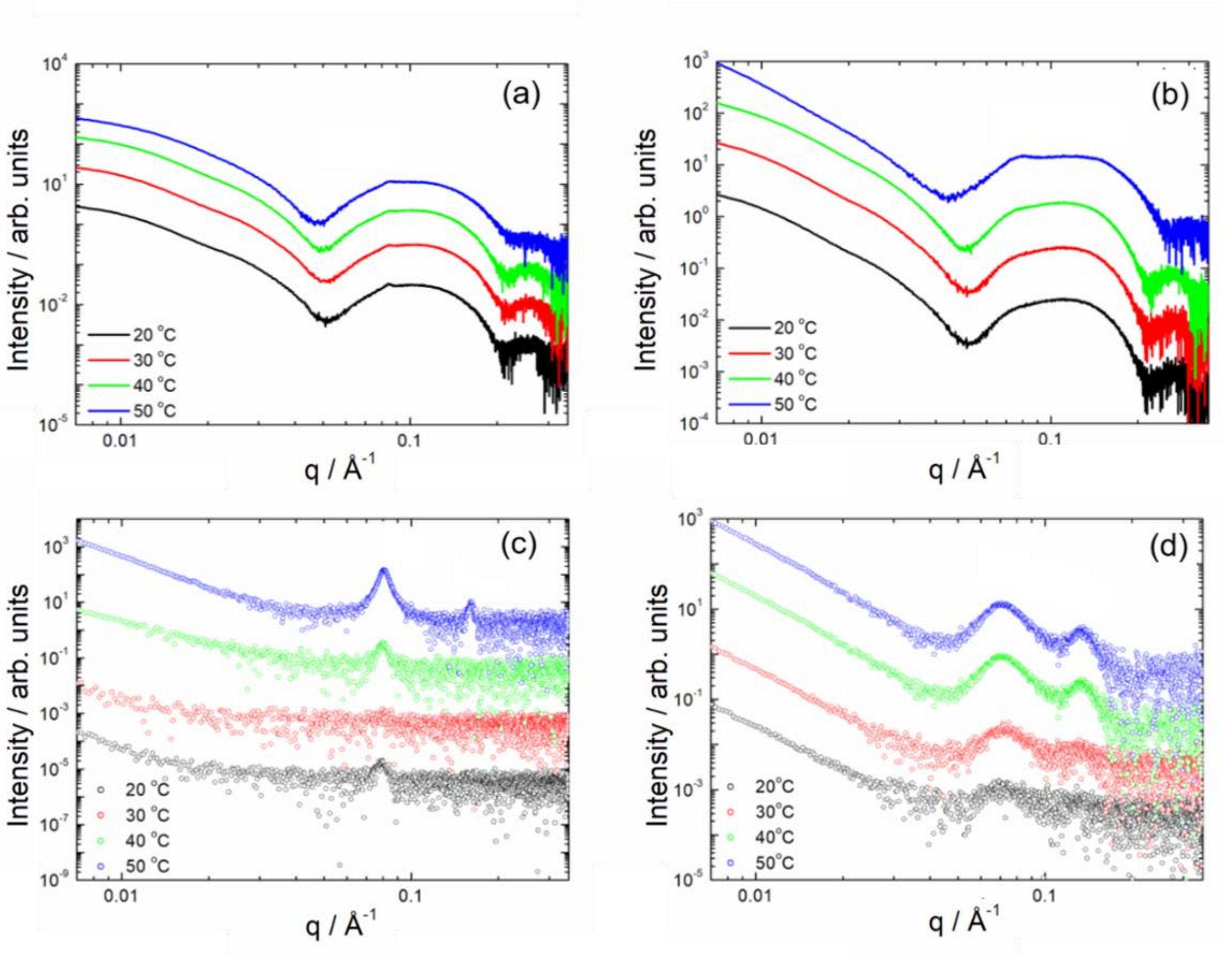

Figure 2.13. *Temperature-ramp SAXS data for a) 0.5 wt% DPPG, 0.08 wt%* RA_6R *b) 0.5 wt% DPPG, 0.08 wt %* RA_9R *c) 0.5 wt% DPPG, 0.25 wt%* RA_6R *and d) 0.5 wt% DPPG, 0.25 wt%* RA_9R

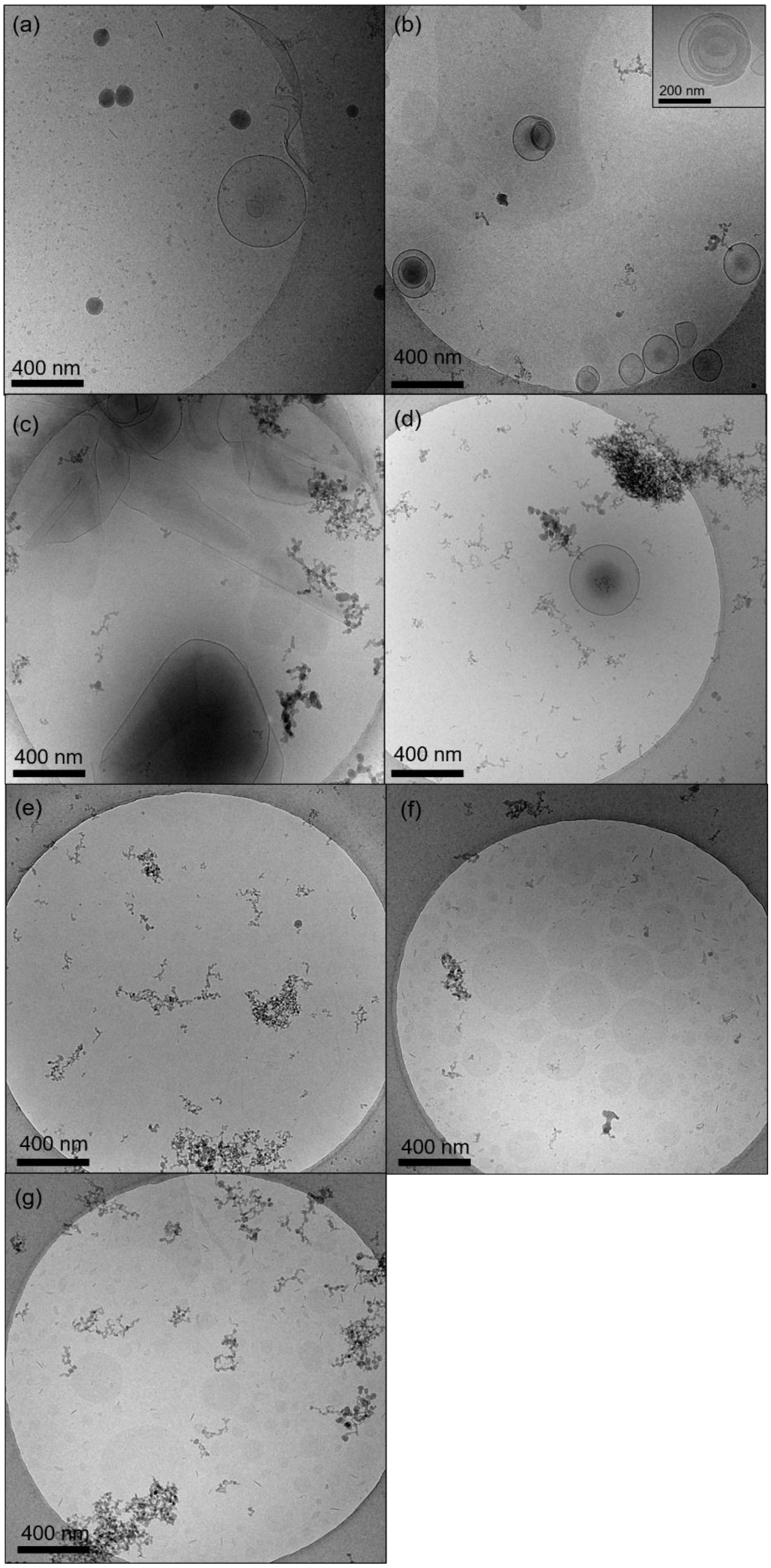

***Figure 2.14**. Cryo-TEM images of a) 0.5 wt% DPPG/DPPE 1:3, b) 0.5 wt% DPPG/DPPE + 0.08 wt% RA_6R and c) 0.5 wt% DPPG/DPPE + 0.08 wt% RA_9R , d) 0.08 wt% RA_6R + 0.5 wt% DPPG/DPPE 1:1 e) 0.08 wt% RA_9R + 0.5 wt% DPPG/DPPE 1:1 f) 0.08 wt% RA_6R + 0.5 wt% DPPG/DPPE 3:1 g) 0.08 wt% RA_9R + 0.5 wt% DPPG/DPPE 3:1*

Comparing the SAXS data of $RA_{12}R$ and $A_{12}R_2$ with different mixtures of liposomes, across the liposome ratios there is some correlation between the bilayers, similar to RA_6R and RA_9R, indicated by the presence of small Bragg peaks. For DPPG alone, $A_{12}R_2$ causes a shift in the central peak q = 0.1 $Å^{-1}$ peak to 0.123 $Å^{-1}$, whereas for $RA_{12}R$ there is a Bragg peak with d spacing value 86.9 Å. For DPPG/DPPE 3:1 mixture, Bragg peaks at d spacing values 88.38 Å for both $A_{12}R_2$ and $RA_{12}R$ are seen. There is a second Bragg peak at 57.1 Å for $A_{12}R_2$ and 47.0 Å for $RA_{12}R$ respectively. In the 1:1 DPPG/DPPE, $RA_{12}R$ mixture, there are 2 d-spacing values of 85.8 Å and 47.1 Å for $RA_{12}R$, which is a 1.82 ratio, similar to the 3:1 ratio. Mixtures of $A_{12}R_2$ with the 1:1 DPPG/DPPE also have similar d-spacing values to the 3:1 DPPG/DPPE, with d-spacings of 85.8 Å and 50.7 Å respectively. These peaks can be explained by coexisting lamellar phases.

For DPPG/DPPE 1:3 mixtures with both peptides, there is a complete loss of form factor features, which is different for the peptide alone assembled fibres. This shows that the peptides disrupt liposome formation. This is consistent with the circular dichroism data which suggests a loss of secondary structure of the peptide.

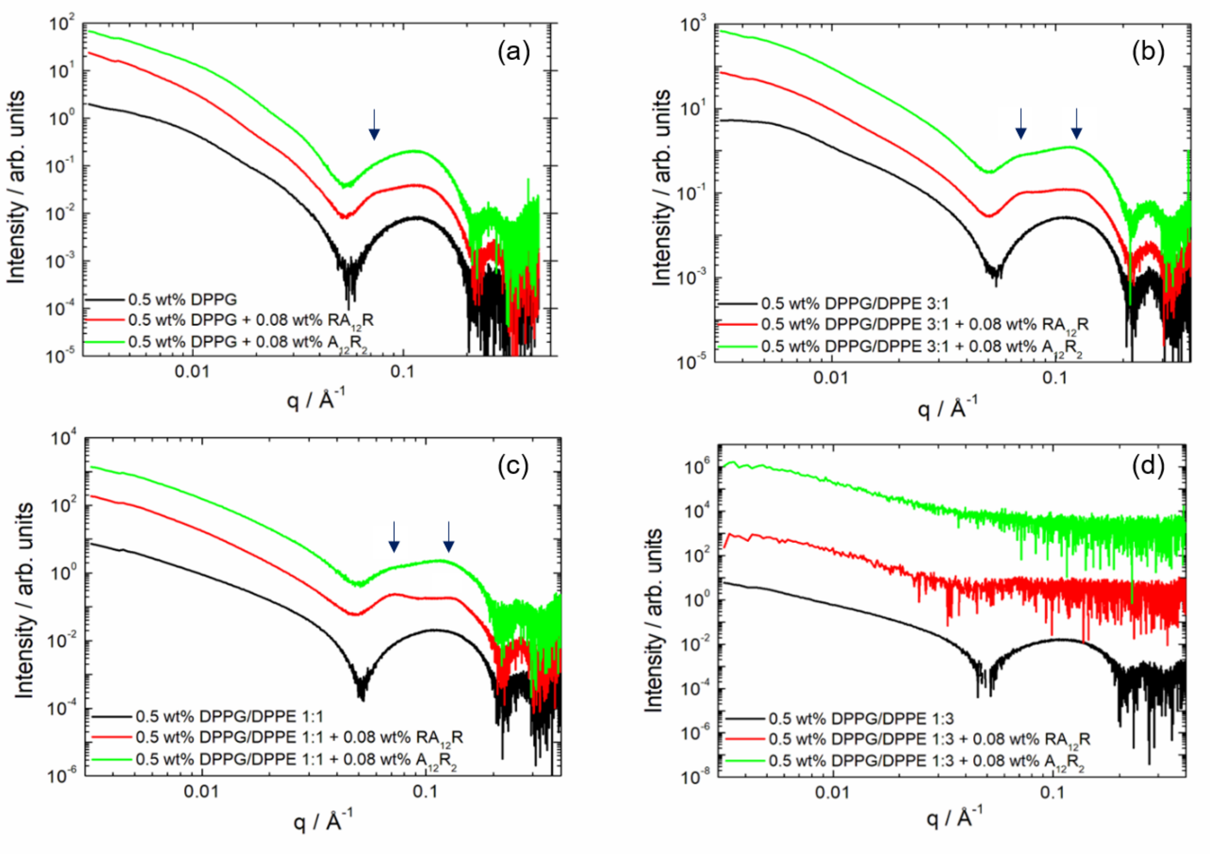

Figure 2.15. *SAXS profiles of 0.08 wt% $RA_{12}R$ and 0.08 wt% $A_{12}R_2$ with different liposome ratios at 0.5 wt% peptide concentration.*

2.2.3.1 DSC

Next, differential scanning calorimetry (DSC) was used to examined the interactions of RA_6R and RA_9R with a model bacterial lipid membranes, represented by DPPG/DPPE vesicles. DPPG is an anionic lipid, whereas DPPE is zwitterionic and both are commonly found in bacterial membranes.[12,21] We selected DPPG and DPPE because the melting temperatures (T_m), are accessible by conventional instruments being 41 °C (DPPG) and 63 °C (DPPE).[21] We examined 0.5 wt% DPPG/DPPE vesicles with ratios 3:1, 1:1 or 1:3, loaded only with 0.08 wt% peptide. While 0.08 wt% peptide is in the range of concentrations used for the antimicrobial assays discussed previously, higher concentrations of peptide led to DPPG/DPPE peptide sample precipitation and therefore were excluded from this study. DSC has previously been used to investigate lipid de-mixing in binary lipid membranes, driven by the membrane interaction with charged peptides.[12,21] The results of this study are displayed in Figure 2.16, with T_m and ΔH values being reported in Table 2.8.

DSC thermograms for the lipids alone (Figure 2.16) present well-defined peaks in the second heating ramps, as observed previously[21,48] (with the exception of the data DPPG which shows a broad transition for reasons discussed below). To compare the influence of RA_6R and RA_9R on the thermotropic phase behaviour of the DPPG/DPPE mixtures, the thermodynamic parameters, namely the main transition temperature (T_m) and the transition enthalpy ΔH were calculated as an indication of the transition cooperativity. For DPPE, the T_m stays within 0.1 °C of the lipid transition alone indicating little peptide binding, however there is a decrease in ΔH by 23.2 kJ mol^{-1} and 27.8 kJ mol^{-1} upon addition of RA_6R and RA_9R respectively. This indicates that there may be some interaction between the peptides and DPPE which promotes a lowering of the energy needed for DPPE to undergo the phase transition from the L_β to the L_α phase.

DPPG alone shows a pre-transition to the P_β ripple phase at about 35 °C and a main chain melting temperature (to fluid state, L_α phase) of 40.5 °C in good agreement with previous measurements for DPPG.[19,49] In the presence of RA_6R, there is a shift in the melting temperature T_m to 47 °C as expected from peptide binding to anionic lipid.[19] RA_9R also causes transition a slight increase in the main T_m. A similar lowering of energy is observed for DPPG where ΔH is reduced by 8.9 kJ mol^{-1} and 14.93 kJ mol^{-1} for RA_6R and RA_9R respectively. Interestingly there is an increase in main transition temperature by 11.9 °C for RA_6R and 14.0 °C for RA_9R. This increase in main transition temperature is likely caused by the charged arginine residues strongly binding to the anionic DPPG group causing an increase in the main transition temperature. Moreover, the peaks for DPPG with added peptide are asymmetric in shape, with RA_9R having a small second peak at 50.1 ^oC which could be due to DPPG transitioning in steps into the L_β phase based on how much peptide is bound.

The DPPG/DPPE 3:1 mixture shows an increase in main chain transition temperature by 5.5 ^oC and 10.8 ^oC respectively for RA_6R and RA_9R, which places T_m for RA_6R at a similar value to that observed in the mixture with DPPG alone, suggesting some de-mixing could be occurring. RA_9R has a higher main transition temperature than that of DPPG alone. There is an increase in ΔH for the transition temperature, when mixed with both RA_6R (9.27 kJ mol^{-1}) and RA_9R (2.88 kJ mol^{-1}) showing that the peptide is stabilising the L_β phase. At a ratio of 1:1 DPPG/DPPE, there are no large changes in main transition temperature (~1^{o}C), however RA_6R shows a small secondary peak at 60 ^oC showing evidence of DPPE-rich regions, which shows de-mixing may be occurring. Finally, in the mixture with 1:3 ratio of DPPG/DPPE, RA_9R has an asymmetric peak with a T_m of 61.5 ^oC which is comparable to that when only DPPE is present, suggesting de-mixing. RA_6R has a decreased transition temperature from 60.8 ^oC to 56.2 ^oC (4.6 ^oC reduction) suggesting formation of DPPE depleted domains compared to the control lipid mixture.

Overall, the DSC shows that the both peptides stabilise the L_β phase of DPPG, seen through increased transition temperature. This could be due to the peptides being cationic, therefore binding to anionic DPPG. When the peptides are mixed with DPPE, the temperature of transition remains the same, however the peptides reduce enthalpy requirement for transition to L_α phase, thus the peptides destabilise the L_β phase. Thermograms of the mixtures with peptide imply the peptides are causing some de-mixing of the lipids.

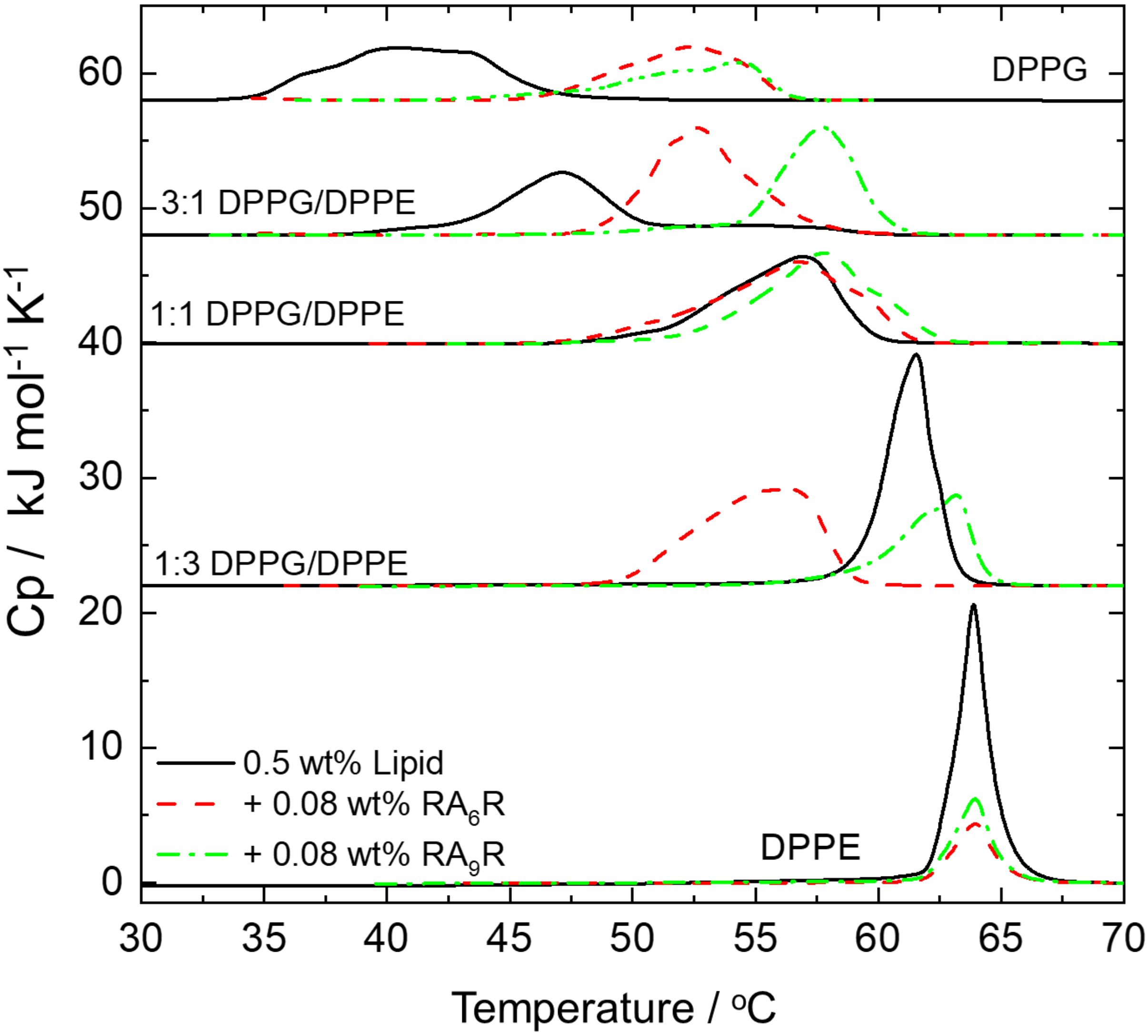

Figure 2.16. *DSC scans showing second heating of DPPG/DPPE lipid mixtures with or without peptide. Scans for peptides mixed with lipids are plotted as dashed lines, and data for the lipid mixtures (without peptide) by the solid lines. The corresponding sample compositions are indicated in the graph.*

***Table 2.8**. The maximum transition temperature, T_m and enthalpy ΔH of phase changes determined from the data plotted in Figure 3.*

Mixture	**T_m (°C)**	**ΔH (kJ mol^{-1})**
DPPE	63.9	37.1
DPPE +RA_6R	63.9	13.9
DPPE + RA_9R	64.0	9.3
0.5 wt% DPPG/DPPE 3:1	47.1	29.4
0.5 wt% DPPG/DPPE 3:1 + 0.08 RA_6R	53.6	38.6
0.5 wt% DPPG/DPPE 3:1 + 0.08 RA_9R	57.7	32.2
0.5 wt% DPPG/DPPE 1:1	56.9	30.8
0.5 wt% DPPG/DPPE 1:1 + 0.08 RA_6R	56.8	34.6
0.5 wt% DPPG/DPPE 1:1 + 0.08 RA_9R	57.8	36.9
0.5 wt% DPPG/DPPE 1:3	60.8	37.5
0.5 wt% DPPG/DPPE 1:3 + 0.08 RA_6R	56.2	43.0
0.5 wt% DPPG/DPPE 1:3 + 0.08 RA_9R	61.5	37.5
DPPG	40.5	32.4
DPPG + RA_6R	52.4	23.5
DPPG + RA_9R	54.5	17.5

2.3 Conclusions

The self-assembly of peptide bola-amphiphiles and SLPs containing arginine and alanine have been examined. Peptide RA_6R does not form self-assembled nanostructures, similar to RA_3R, and in contrast to RA_9R and $RA_{12}R$ which form fibrils above a critical aggregation concentration. Interestingly, RA_9R binds amyloid specific dye ThT, although CD and FTIR spectroscopy show no evidence of β-sheet conformation. $RA_{12}R$ does not bind ThT although there is evidence of β-sheet structures in CD and FTIR. $A_{12}R_2$ has a similar aggregation propensity to $RA_{12}R$ and similar self-assembly into clustered fibres. Hydrogelation occurs at lower concentrations as the length of the alanine chain is increased across the series of bola-amphiphiles, however SLP $A_{12}R_2$ gels at a lower concentration than corresponding bola-amphiphile $RA_{12}R$.

The cytotoxicity data reveals that generally (with the exception of $A_{12}R_2$ and $RA_{12}R$) that the SLPs are less toxic that their corresponding bola-amphiphile, which is perhaps due to the lower cationic charge. Increase in toxicity for the bola-amphiphiles is not directly linked to increased molecular weight but perhaps is linked to a mixture of membrane permeability and the presentation of cationic charge at high density from the larger self-assembled bola-amphiphiles which can cause membrane disruption.

The initial antimicrobial screening study (and corresponding assay showing low cytotoxicity at the corresponding peptide concentration) shows that A_9R and RA_6R are promising antibacterial agents active against *P. aeruginosa*, strains of which (including those that have evolved antimicrobial resistance) can cause serious infections. The strong activity of these two peptides is within the cytocompatible range. There is no correlation between the size of the alanine hydrophobic block and antimicrobial activity. Peptides $A_{12}R_2$, $RA_{12}R$ and RA_3R also have activity against *P.aeruginosa* but near the concentrations for which they are toxic.

Lastly, concerning the interaction of the peptides with model DPPG/DPPE lipid membranes. DSC shows evidence for peptide-induced lipid de-mixing, especially in the DPPG rich mixtures, consistent with electrostatic interactions between this anionic lipid and the cationic arginine units in the peptides. Circular dichroism spectra indicate no change of peptide conformation for RA_6R in the presence of lipids (PPII conformation retained) whereas unexpectedly RA_9R undergoes a transition to a β-sheet conformation in the presence of the lipids. Peptides $A_{12}R_2$ and $RA_{12}R$ show potential reordering of the bacterial bilayer models, with $A_{12}R_2$ becoming disordered on associating with membranes with high PE content.

These arginine-rich peptide bola-amphiphiles show activity towards lipid membranes, which is presumed to be the origin of their antimicrobial activities.

2.4. Methods

2.4.1. Materials

Peptides RA_3R, RA_6R, RA_9R, $RA_{12}R$, A_6R, $CapA_6R$, A_9R and $A_{12}R_2$ were supplied by Biomatik (Cambridge, Ontario, Canada). The purity values were as follows: RA_3R 96.85%, RA_6R 98.86 %, RA_9R was 96.56%, $RA_{12}R$ was 97.15%, A_6R was 96.64 %, $CapA_6R$ was 95.87%, A_9R was 98.73% and $A_{12}R_2$ was 97.51%, determined by HPLC using an Inertsil ODS-SP column with an actetonitrile/water gradient with 0.1% TFA.

The molar mass of each peptide determined by ESI-MS was : RA_3R was 543.63 $gmol^{-1}$, RA_6R was 757.45 $gmol^{-1}$ RA_9R was 970.65 $gmol^{-1}$, $RA_{12}R$ was 1183.32 $gmol^{-1}$, A_6R was 600.68 $gmol^{-1}$ and $CapA_6R$ was 641.73 $gmol^{-1}$, A_9R was 814.90 g mol^{-1} and $A_{12}R_2$ was 1183 $gmol^{-1}$.

Solutions containing pure peptide in water were made by dissolving weighed amounts of peptide in water and leaving to equilibrate for 3 hrs. Lipids DPPG and DPPE were obtained from Sigma-Aldrich. Details of multi-lamellar lipid vesicles preparation are given below.

2.4.2. Fluorescence Assays

The presence of any critical aggregation concentration (*cac*) was assayed using fluorescence probes, measuring spectra for a series of peptide concentrations. Fluorescence spectra were recorded with a Varian Cary Eclipse fluorescence spectrometer with samples in 4 mm inner width quartz cuvettes. ThT was used to determine the *cac* of RA_9R, $RA_{12}R$ and $A_{12}R_2$, as it is sensitive to the formation of amyloid fibrils at the *cac*.[35,37,50–52] ThT assays were performed using 5.0 x 10^{-3} wt% solution to solubilise the peptide. Spectra were recorded between 460-600 (λ_{ex} = 440 nm). ANS (8-anilinonaphthalene-1-sulfonic acid) was further used to examine whether there is a *cac* for RA_6R, , $RA_{12}R$ and $A_{12}R_2$. ANS is a fluorescent probe used to determine the formation of molecular hydrophobic environments in solution,[22,53] and can be used to determine the *cac* independently of self-assembly into amyloid fibres. Peptides were dissolved in a 66.8 µM ANS solution, and spectra were recorded between 400-650 nm (λ_{ex}= 356 nm)

2.4.3. Circular Dichroism (CD) Spectroscopy

CD spectra were recorded using a Chirascan spectropolarimeter (Applied Photophysics, UK) in the wavelength range 180 – 260 nm. Samples containing 1 wt% RA_6R, RA_9R, , $RA_{12}R$ and $A_{12}R_2$ in pure H_2O at were pipetted into 0.1 mm pathlength quartz cuvettes. Mixtures of liposomes in ratios with 0.08 wt% peptide were also loaded in the same way. Data with absorbance less than 2 at any point only are reported. Measurements were recorded with a 0.5 nm bandwidth, 1 nm step and 1 s collection time per point. The CD signal for the background solution was subtracted from the CD signal of the sample, and molar ellipticity was calculated.

2.4.4. Fourier Transform Infrared (FTIR) Spectroscopy

Spectra were recorded using a Thermo Scientific Nicolet IS5 instrument equipped with a DTGS detector, with a PEARL liquid cell (sample contained between fixed CaF_2 plates). Aliquots containing 80 µL of (1-5) wt% RA_6R, RA_9R, , $RA_{12}R$ and $A_{12}R_2$ in D_2O were prepared and added to a PEARL liquid cell. Spectra were scanned 128 times over the range of 900 − 4000 cm^{-1}. The peptide signal was background corrected with the FTIR spectra of D_2O.

2.4.5. Cryogenic Transmission Electron Microscopy (cryo-TEM)

Cryo-TEM was kindly performed by Jani Seitsonen, Aalto University, Finland. Vitrified specimens were prepared using an automated FEI Vitrobot device using Quantifoil 3.5/1 holey carbon copper grids with a hole size of 3.5 µm. Prior to use, grids were plasma cleaned using a Gatan Solarus 9500 plasma cleaner and then transferred into the environmental chamber of a FEI Vitrobot at room temperature and 100% humidity. After this, sample solutions were applied onto a grid, and were blotted twice for 5 s and then vitrified in a 1/1 mixture of liquid ethane and propane at a temperature of −180 °C. The grids with vitrified sample solution were maintained at liquid nitrogen temperature and then cryo-transferred to the microscope. Imaging was carried out using a field emission cryo-electron microscope (JEOL JEM-3200FSC) operating at 200 kV. Images were taken in bright field mode and using zero loss energy filtering (Ω type) with a slit width of 20 eV. Micrographs were recorded using a Gatan Ultrascan 4000 CCD camera. The specimen temperature was maintained at −187 °C during the imaging.

2.4.6. Liposome preparation

Liposome vesicles were prepared using the thin-layer hydration method. Weighed quantities of DPPG and DPPE were dissolved in chloroform, and thin lipid films were prepared by evaporating the chloroform under a stream of nitrogen. Lipid films were then placed under vacuum for 2 hrs to remove any remaining organic solvent. After this, lipids were re-suspended in water at 0.5 wt% lipid at 65^{o}C heated above their lipid melting temperature, T_m, and vortexed for 5 minutes. Liposome mixtures were then left to equilibrate for 3 hrs before experiments. DPPG/DPPE vesicles were prepared using this method at different molar ratios of 1:3, 1:1, 3:1 and 1:0 DPPG:DPPE. Peptide/lipid mixtures were made by adding enough peptide powder to re-suspend lipids and obtain a final concentration of either 0.08 wt% or 0.25 wt% peptide. Peptide/lipid samples were then heated above the T_m and vortexed for 5 minutes, and finally left to equilibrate for 3 hrs before experiments. Dynamic light scatter (DLS) (data not shown) was measured to check the size of the liposomes using a Zetasizer instrument.

2.4.7. Nano Differential Scanning Calorimetry (nano-DSC)

Differential scanning calorimetry measurements were carried out using a nanoDSC, DSC TA-Q200 instrument. 600 µl of lipid mixtures at 0.5 wt% with and without 0.08 wt% peptide were degassed for 10 minutes before being 600 µL pipetted into the DSC sample cell. 600 µL of water was pipetted into the reference cell. The temperature range measured was 20 ^{o}C to 80 ^{o}C for DPPG/DPPE mixtures and 20^{o}C to 60^{o}C for DPPG alone. The scan rate was 1 ^{o}C per minute at pressure of 3 bar. Background subtraction, main phase transition temperature, and the transition enthalpy ΔH, were calculated using nanoanalyse software.

2.4.8. Small-angle X-ray scattering (SAXS)

Data from solutions was collected on the bioSAXS beamlines B21 (Diamond Light Source, UK) and ID02 (ESRF, Grenoble). At the former, liposome and peptide samples were loaded into PCR tubes in an automated sample changer, then 30 μL was delivered into a temperature-controlled quartz capillary and 30 frames (1 s each) of SAXS data were acquired at 20 ^{o}C. The temperature was then increased, measurements being taken each 10 ^{o}C. The camera length was 3.9 m, and the X-ray wavelength was λ= 1.02 Å. Data was collected using a Dectris PILATUS 2M detector and processed using ScÅtter,[54]and is presented as a function of $q = 4\pi \sin\theta/\lambda$. At the ESRF (ID02), 200 μL of sample was manually loaded into a glass capillary with a 2 mm internal radius. The beamline operated with a flux of 2.19 x 10^{12} photon s^{-1} (100 mA) and an 12.46 keV energy. The sample-detector distance was 1474.2 mm. The 2D data was collected using a Rayonix MX170 detector, with a 2x2 binning, and processed using SAXSUtilities software. The SAXS data was fitted using model form factors using the software SASfit.[40] SAXS from hydrogels was collected on beamline BM26B (DUBBLE) at the ESRF. On BM26B, hydrogels were placed in DSC pans modified with mica windows to enable transmission of the X-ray beam. The sample to SAXS detector distance was 3.16 m using a wavelength of 1.033 Å. A Dectris PILATUS 1M detector was used to acquire the 2D SAXS scattering patterns. Standard corrections for sample absorption and background subtraction were performed. The data were normalized to the intensity of the incident beam (in order to correct for primary beam intensity fluctuations) and were corrected for absorption, background scattering. The diffraction spectra from silver behenate were used to calibrate the wavevector scale of the scattering curve.

2.4.9 Cell Viability assays

In vitro cell culture was conducted using 161Br (European Collection of Authenticated Cell Cultures, ECACC) cells, a human skin fibroblast cell line. Cells were maintained in a humidified atmosphere at 37 ^{o}C, 5% CO_2, and cultured in EMEM (Eagle’s minimum essential medium), with 2 mM glutamine, enriched with 15% fetal bovine serum (FBS) and 1% non-essential amino acids (NEAA).

Potential cytotoxicity effects of RA3R, RA_6R, RA_9R, $RA_{12}R$, A_6R, CapA_6R, A_9R and $A_{12}R_2$ were examined using an MTT (3-(4,5-dimethylthiazol-2-yl)-2,5-diphenyltetrazolium bromide) assay. Cells were seeded into a 96-well plate at $4x10^4$ cells/mL and allowed to adhere for 24 hrs in 100 µL complete medium. This seeding density was selected through growth curve assays (Appendix Figure A1.) After this, peptides were dissolved in complete medium, and 100 µL of either complete media and/or peptide solution was added, to give either control solution (complete medium only) or peptide solutions with concentrations in the range (0.05-5) mg/mL

Cells were incubated for 67 hours. Following this, 20 µL MTT (5 mg/mL, in PBS) was pipetted into each well plate and allowed to incubate for 5 hrs. After a further 5 hrs (corresponding to a total of 72 hrs treatment) the solution was removed from the wells and replaced with 100 µL DMSO per well, in order to dissolve the formazan crystals. Plates were incubated for 30 mins, and then analysed using the UV microplate reader (λ = 570 nm). Results are reported as a % cell viability compared to control (untreated) values, and fitted to a sigmoidal function as a guide to the eye.

2.4.10 Antimicrobial Assays

The antimicrobial assays were performed with four species of bacteria, *Escherichia coli* (K12),[55] *Staphylococcus aureus*[56], *Pseudomonas aeruginosa*[57] and *P.syringae*. Stock cultures were stored in -80 ^oC in 7% (v/v) DMSO. Prior to experiments all three strains were streaked out onto Lysogeny Broth (LB) agar and grown overnight at 37^oC.

From these plates, one colony was then transferred into 5 mL LB, and grown at 37 ^oC under agitation at 150 rev/min, on an orbital shaker overnight and these cultures were used for ongoing experiments. Cultures were then transferred into a 15 ml Falcon tube and cells were harvested by centrifugation at 9000 rpm and 4^oC for 10 minutes. The supernatant was discarded and the pellet was resuspended in 1.5 mL ice chilled PBS (phosphate buffered saline).

After this, 30 µL of this solution was transferred into 300 µL of 0.1, 0.5 or 1 mg/mL (or 0.01,0.05 or 0.1 wt%) of RA_3R, RA_6R, RA_9R, $RA_{12}R$, A_9R and $A_{12}R_2$ in sterile water, or control solutions of 300 µL of sterile water. Solutions were then vortexed for 5 seconds and 3 x 20µL aliquots were taken at times 0, 30, 60, 120 and 1440 mins. These samples were then serially diluted in PBS, and 10 µL of each dilution was plated onto LB agar and incubated at 37 ^oC overnight before colony counting.

2.5 References

(1) Dehsorkhi, A.; Castelletto, V.; Hamley, I. W. Self-Assembling Amphiphilic Peptides. *J. Pept. Sci.* **2014**, *20* (7), 453–467.

(2) Edwards-Gayle, C. J. C.; Hamley, I. W. Self-Assembly of Bioactive Peptides, Peptide Conjugates, and Peptide Mimetic Materials. *Org. Biomol. Chem.* **2017**, *15* (28), 5867–5876.

(3) Hamley, I. W. Self-Assembly of Amphiphilic Peptides. *Soft Matter* **2011**, *7*, 4122–4138.

(4) Santoso, S.; Hwang, W.; Hartman, H.; Zhang, S. Self-Assembly of Surfactant-like Peptides with Variable Glycine Tails to Form Nanotubes and Nanovesicles. *Nano Lett.* **2002**, *2* (7), 687–691.

(5) Von Maltzahn, G.; Vauthey, S.; Santoso, S.; Zhang, S. Positively Charged Surfactant-like Peptides Self-Assemble into Nanostructures. *Langmuir* **2003**, *19* (10), 4332–4337.

(6) Hauser, C. A. E.; Zhang, S. Designer Self-Assembling Peptide Nanofiber Biological Materials. *Chem. Soc. Rev.* **2010**, *39* (8), 2780–2790.

(7) Vauthey, S. Molecular Self-Assembly of Surfactant-like Peptides to Form Nanotubes and Nanovesicles. *Proc. Natl. Acad. Sci.* **2002**, *99* (8), 5355–5360.

(8) Castelletto, V.; Hamley, I. W.; Segarra-Maset, M. D.; Berdugo Gumbau, C.; Miravet, J. F.; Escuder, B.; Seitsonen, J.; Ruokolainen, J. Tuning Chelation by the Surfactant-like Peptide A6H Using Predetermined PH Values. *Biomacromolecules* **2014**, *15* (2), 591–598.

(9) Castelletto, V.; Nutt, D. R.; Hamley, I. W.; Bucak, S.; Cenker, C.; Olsson, U. Structure of Single-Wall Peptide Nanotubes: In Situ Flow Aligning X-Ray Diffraction. *Chem Commun* **2010**, *46* (34), 6270–6272.

(10) Castelletto, V.; Gouveia, R. M.; Connon, C. J.; Hamley, I. W.; Seitsonen, J.; Nykänen, A.; Ruokolainen, J. Alanine-Rich Amphiphilic Peptide Containing the RGD Cell Adhesion Motif: A Coating Material for Human Fibroblast Attachment and Culture. *Biomater. Sci.* **2014**, *2*, 362–369.

(11) Hamley, I. W.; Hutchinson, J.; Kirkham, S.; Castelletto, V.; Kaur, A.; Reza, M.; Ruokolainen, J. Nanosheet Formation by an Anionic Surfactant-like Peptide and Modulation of Self-Assembly through Ionic Complexation. *Langmuir* **2016**, *32* (40), 10387–10393.

(12) Chen, C.; Pan, F.; Zhang, S.; Hu, J.; Cao, M.; Wang, J.; Xu, H.; Zhao, X.; Lu, J. R. Antibacterial Activities of Short Designer Peptides: A Link between Propensity for Nanostructuring and Capacity for Membrane Destabilization. *Biomacromolecules* **2010**, *11* (2), 402–411.

(13) Zhao, Y.; Deng, L.; Yang, W.; Wang, D.; Pambou, E.; Lu, Z. Tuning One-Dimensional Nanostructures of Bola-Like Peptide Amphiphiles by Varying the Hydrophilic Amino Acids. *Chem. - A Eur. J.* **2016**, *22* (32), 11394–11404.

(14) Zhao, Y.; Wang, J.; Deng, L.; Zhou, P.; Wang, S.; Wang, Y.; Xu, H.; Lu, J. R. Tuning the Self-Assembly of Short Peptides via Sequence Variations. *Langmuir* **2013**, *29* (44), 13457–13464.

(15) Rodrigo, E.; Nathaniel, M.; Walter, M.; Reza, M.; Castelletto, V.; Ruokolainen, J.; Connon, C. J.; Alves, W. A.; Hamley, I. W. Self-Assembled Arginine-Capped Peptide Bolaamphiphile Nanosheets for Cell Culture and Controlled Wettability Surfaces. *Biomacromolecules* **2015**, *16*

(10), 3180–3190.

(16) Dehsorkhi, A.; Castelletto, V.; Hamley, I. W.; Seitsonen, J.; Ruokolainen, J. Interaction between a Cationic Surfactant-like Peptide and Lipid Vesicles and Its Relationship to Antimicrobial Activity. *Langmuir* **2013**, *29* (46), 14246–14253.

(17) Castelletto, V.; Barnes, R. H.; Karatzas, K. A.; Edwards-Gayle, C. J. C.; Greco, F.; Hamley, I. W.; Rambo, R.; Seitsonen, J.; Ruokolainen, J. Arginine-Containing Surfactant-Like Peptides: Interaction with Lipid Membranes and Antimicrobial Activity. *Biomacromolecules* **2018**, *19* (7), 2782–2794.

(18) Castelletto, V.; Barnes, R.; Karatzas, K.-A.; Edwards-Gayle, C. J. C.; Greco, F.; Hamley, I. W.; Seitsonen, J.; Ruokolainen, J. Restructuring of Lipid Membranes by an Arginine-Capped Peptide Bolaamphiphile. *Langmuir* **2018**, *35* (5), 1302–1311.

(19) Malanovic, N.; Leber, R.; Schmuck, M.; Kriechbaum, M.; Cordfunke, R. A.; Drijfhout, J. W.; Breij, A. De; Nibbering, P. H.; Kolb, D.; Lohner, K. Phospholipid-Driven Differences Determine the Action of the Synthetic Antimicrobial Peptide OP-145 on Gram-Positive Bacterial and Mammalian Membrane Model Systems. *Biochim. Biophys. Acta - Biomembr.* **2015**, *1848* (10), 2437–2447.

(20) Pimthon, J.; Willumeit, R.; Lendleina, A.; Hofmann, D. Membrane Association and Selectivity of the Antimicrobial Peptide NK-2: A Molecular Dynamics Simulation Study. *J. Pept. Sci.* **2009**, *15* (10), 654–657.

(21) Arouri, A.; Dathe, M.; Blume, A. Peptide Induced Demixing in PG / PE Lipid Mixtures : A Mechanism for the Speci Fi City of Antimicrobial Peptides towards Bacterial Membranes ? *Biochim. Biophys. Acta - Mol. Basis Dis.* **2009**, *1788* (3), 650–659.

(22) Gasymov, O. K.; Glasgow, B. J. ANS Fluorescence: Potential to Augment the Identification of the External Binding Sites of Proteins. *Biochim. Biophys. Acta - Proteins Proteomics* **2007**, *1774* (3), 403–411.

(23) Chen, K.; Liu, Z.; Kallenbach, N. R. The Polyproline II Conformation in Short Alanine Peptides Is Noncooperative. *Proc. Natl. Acad. Sci. U. S. A.* **2004**, *101* (43), 15352–15357.

(24) Bochicchio, B.; Tamburro, A. M. Polyproline II Structure in Proteins : Identification by Chiroptical Spectroscopies , Stability , and Functions. *Chirality* **2002**, *14* (10), 782–792.

(25) Hirst, J. D.; Colella, K.; Gilbert, A. T. B. Electronic Circular Dichroism of Proteins from First-Principles Calculations. *J. Phys. Chem. B* **2003**, *107* (42), 11813–11819.

(26) Woody, R. W. Circular Dichroism Spectrum of Peptides in the Poly (Pro) II Conformation. *J. Am. Chem. Soc.* **2009**, *131* (23), 8234–8245.

(27) Schweitzer-stenner, R.; Measey, T.; Hagarman, A.; Eker, F.; Griebenow, K. Salmon Calcitonin and Amyloid : Two Peptides with Amyloidogenic Capacity Adopt Different Conformational Manifolds in Their Unfolded States. *Biochemistry* **2006**, *45* (9), 2810–2819.

(28) Pelton, J. T.; Mclean, L. R. Spectroscopic Methods for Analysis of Protein Secondary Structure. *Anal. Biochem.* **2000**, *227* (2), 167–176.

(29) Lavoie, M. C.; Subirade, M. Replacement of Trifluoroacetic Acid with HCl in the Hydrophobic Purification Steps of Pediocin PA-1 : A Structural Effect. *Appl. Environ. Microbiol.* **2002**, *68*

(10), 4803–4808.

(30) Ghosh, A.; Tucker, M. J.; Hochstrasser, R. M. Identification of Arginine Residues in Peptides by 2D-IR Echo Spectroscopy. *J. Phys. Chem. A* **2011**, *115* (34), 9731–9738.

(31) Barth, A. The Infrared Absorption of Amino Acid Side Chains. *Prog. Biophys. Mol. Biol.* **2000**, *74* (3–5), 141–173.

(32) Eker, F.; Cao, X.; Nafie, L.; Huang, Q.; Schweitzer-stenner, R. The Structure of Alanine Based Tripeptides in Water and Dimethyl Sulfoxide Probed by Vibrational Spectroscopy. *J. Phys. Chem. A* **2003**, *107* (1), 358–365.

(33) Schweitzer-stenner, R. Dihedral Angles of Tripeptides in Solution Directly Determined by Polarized Raman and FTIR Spectroscopy. *Biophys. J.* **2002**, *83* (1), 523–532.

(34) Hamley, I. W.; Dehsorkhi, A.; Castelletto, V. Self-Assembled Arginine-Coated Peptide Nanosheets in Water. *Chem. Commun.* **2013**, *49* (18), 1850–1852.

(35) LeVine, H. Quantification of β-Sheet Amyloid Fibril Structures with Thioflavin T. *Methods Enzymol.* **1999**, *309*, 274–284.

(36) Chimie, R. R. De. Rapid Characterization of Peptide Secondary Structure by FT-IR Spectroscopy. *Rev. Roum. Chim.* **2011**, *56* (8), 783–791.

(37) Levine, H. Thioflavine T Interaction with Synthetic Alzheimer's Disease B-amyloid Peptides: Detection of Amyloid Aggregation in Solution. *Protein Sci.* **1993**, *2* (3), 404–410.

(38) Barth, A. Infrared Spectroscopy of Proteins. *Biochim. Biophys. Acta* **2007**, *1767* (9), 1073–1101.

(39) Barth, A.; Zscherp, C. What Vibrations Tell Us about Proteins. *Q. Rev. Biophys.* **2002**, *35* (4), 369–430.

(40) Breßler, I.; Kohlbrecher, J.; Thünemann, A. F. *SASfit* : A Tool for Small-Angle Scattering Data Analysis Using a Library of Analytical Expressions. *J. Appl. Crystallogr.* **2015**, *48* (5), 1587–1598.

(41) Hamley, I. W.; Dehsorkhi, A.; Castelletto, V.; Seitsonen, J.; Ruokolainen, J.; Iatrou, H. Self-Assembly of a Model Amphiphilic Oligopeptide Incorporating an Arginine Headgroup. *Soft Matter* **2013**, *9*, 4794–4801.

(42) Castelletto, V.; Hamley, I. W. Methods to Characterize the Nanostructure and Molecular Organization of Amphiphilic Peptide Assemblies. In *Peptide Self-Assembly: Methods and Protocols*; Nilsson, B. L., Doran, T. M., Eds.; Springer New York: New York, NY, 2018; pp 3–21.

(43) Park, A. J.; Okhovat, J. P.; Kim, J. Antimicrobial Peptides. *Pharmaceuticals* **2013**, *6*, 1542–1575.

(44) Yang, N. J.; Hinner, M. J. Getting Across the Cell Membrane: An Overview for Small Molecules, Peptides, and Proteins. *Methods Mol Bio* **2016**, *1266*, 29–53.

(45) Castelletto, V.; Edwards-Gayle, C. J. C.; Hamley, I. W.; Barrett, G.; Seitsonen, J.; Ruokolainen, J. Peptide-Stabilized Emulsions and Gels from an Arginine-Rich Surfactant-Like Peptide with Antimicrobial Activity. *ACS Appl. Mater. Interfaces* **2019**, *11* (10), 9893–9903.

(46) Ishitsuka, Y.; Pham, D. S.; Waring, A. J.; Lehrer, R. I.; Lee, K. Y. C. Insertion Selectivity of Antimicrobial Peptide Protegrin-1 into Lipid Monolayers: Effect of Head Group Electrostatics and Tail Group Packing. *Biochim. Biophys. Acta - Biomembr.* **2006**, *1758* (9), 1450–1460.

(47) Epand, R. M.; Epand, R. F. Bacterial Membrane Lipids in the Action of Antimicrobial Agents. *J. Pept. Sci.* **2011**, *17* (5), 298–305.

(48) Garidel, A. P.; Blume, A. Miscibility of Phosphatidylethanolamine-Phosphatidylglycerol Mixtures as a Function of PH and Acyl Chain Length. *Eur. Biophys. J.* **2000**, *28* (8), 629–638.

(49) Sevcsik, E.; Pabst, G.; Jilek, A.; Lohner, K. How Lipids Influence the Mode of Action of Membrane-Active Peptides. *Biochim. Biophys. Acta - Biomembr.* **2007**, *1768* (10), 2586–2595.

(50) Khurana, R.; Coleman, C.; Ionescu-Zanetti, C.; Carter, S. A.; Krishna, V.; Grover, R. K.; Roy, R.; Singh, S. Mechanism of Thioflavin T Binding to Amyloid Fibrils. *J. Struct. Biol.* **2005**, *151* (3), 229–238.

(51) Krebs, M. R. H.; Bromley, E. H. C.; Donald, A. M. The Binding of Thioflavin-T to Amyloid Fibrils: Localisation and Implications. *J. Struct. Biol.* **2005**, *149* (1), 30–37.

(52) Lindgren, M.; Sörgjerd, K.; Hammarström, P. Detection and Characterization of Aggregates, Prefibrillar Amyloidogenic Oligomers, and Protofibrils Using Fluorescence Spectroscopy. *Biophys. J.* **2005**, *88* (6), 4200–4212.

(53) Hawe, A.; Sutter, M.; Jiskoot, W. Extrinsic Fluorescent Dyes as Tools for Protein Characterization. *Pharm. Res.* **2008**, *25* (7), 1487–1499.

(54) Rambo, R. P. Http://Www.Bioisis.Net/.

(55) Blattner, F. R.; Plunkett, G.; Bloch, C. A.; Perna, N. T.; Burland, V.; Riley, M.; Collado-vides, J.; Glasner, J. D.; Rode, C. K.; Mayhew, G. F.; et al. The Complete Genome Sequence of Escherichia Coli K-12. *Science (80-.).* **1997**, *277* (5331), 1453–1462.

(56) Horsburgh, M. J.; Aish, J. L.; White, I. J.; Shaw, L.; Lithgow, J. K.; Foster, S. J.; England, S. ΣB Modulates Virulence Determinant Expression and Stress Resistance : Characterization of a Functional RsbU Strain Derived from Staphylococcus Aureus 8325-4. *J. Bacteriol.* **2002**, *184* (19), 5457–5467.

(57) Holloway, B. Y. B. W. Genetic Recombination in Pseudomonas Aeruginosa. *J. Gen. Microbiol.* **1955**, *13* (3), 572–581.

Chapter 3.

Selective Antibacterial Activity and Lipid Membrane Interactions of Arginine-Rich Amphiphilic Peptides

This chapter has been submitted by the author as a research article entitled "Selective antibacterial activity and lipid membrane interactions of arginine-rich amphiphilic peptides" C.J.C. Edwards-Gayle, G. Barrett, S. Roy, , F. Greco, J. Seitsonen, J. Ruokolainen, R. P. Rambo, I.W. Hamley .

3.1 Introduction

The increase in prevalence of multi antibiotic-resistant pathogens is of great concern and has been listed by the World Health Organisation (WHO) as one of the biggest threats to modern day healthcare, food security and development. There is great interest in the development of new therapeutics in order to overcome this. Peptides, especially those containing cationic residues and/or tryptophan, have been shown to have great potential in this regard.[1,2] Many antimicrobial peptides have evolved naturally in species of plants and animals, providing a strong basis to produce biocompatible therapeutics.

Antimicrobial peptides are thought to interact with the cell membranes of bacteria through different mechanisms.[2] It has been proposed that some peptides induce pore formation where the pore is lined with peptide (the barrel-stave model), or with a mixture of peptide and lipid (the toroidal pore model).[3] Another mechanism involves peptide deposition on the membrane surface (the carpet model) which is followed by a detergent-like action that leads to pore formation.[3] Cationic peptides are able to associate with the membrane and cause an electrical potential difference across the membrane, inducing electroporation (the molecular electroporation model).[4–6]

An important class of antimicrobial peptide are those containing L-arginine.[2] L-arginine is commonly found as an active site residue in proteins,[7] and is common in many cell-penetrating peptides. The antimicrobial activity of L-arginine is due the cationic charge of this amino acid which interacts with anionic or zwitterionic lipid membranes and can lead to pore formation.[8,9]

Surfactant-like peptides (SLPs) are a group of peptides with promising applications as antimicrobials. Structurally, SLPs have a head group of a small sequence of charged residues and a longer hydrophobic tail which gives them good self-assembling properties.[10–19] Recently, the self-assembly of three SLPs, A_3K, A_6K and A_9K, was examined and distinct morphologies were observed for the three peptides.[20] The antimicrobial properties were found to be dependent on the length of the hydrophobic chain, with A_9K being most active against *E. coli* and *S. aureus*. Peptide A_6K strongly disrupted the structure of anionic vesicle DPPG,[20] used as a model system for bacterial cell membranes. Our group has studied the self-assembling properties and antimicrobial activities of several SLPs and bola amphiphiles containing one or two arginine groups, discussed in more detail in Chapter 2.

Recently, Silva et al examined the self-assembly of peptides consisting of alternating RF motifs. The short oligopeptide $[RF]_4$ was found to assemble into highly ordered amyloid-like fibrils above a critical aggregation concentration.[21] Further studies of $[RF]_n$, where n is between 1 and 5, showed an increased structural order and cytotoxicity with increasing n.[22] In another example, Fojan *et al.* studied the self-assembly of RFFFR which was shown to self-assemble into fibres stabilised by π-stacking interactions, which further assembled into solid spheres. [23]

This chapter focuses on the self-assembly behaviour and antimicrobial activity of two SLPs (Scheme 3.1) with sequences RRRFFF (R_3F_3) and RRRRFFFF (R_4F_4). These peptides comprise a hydrophobic phenylalanine block and a block of cationic L-arginine residues. They were designed as novel arginine-rich SLPs containing aromatic hydrophobic blocks, incorporated to drive self-assembly via π-stacking interactions. The two peptides we investigate, R_3F_3 and R_4F_4, are architecturally different from these previously studied RF-containing peptides and surfactant-like peptides, as they contain symmetric charged and hydrophobic blocks. These can be considered oligomeric block co-polypeptides, although the blocks are much shorter than those studied by Deming *et al*,[24,25] such as $R_{60}L_{20}$, which were prepared by ring-opening polymerization methods and showed cell penetrating properties.

The self-assembly and conformation of R_3F_3 and R_4F_4 is examined, as well as interactions with bacterial membrane models DPPG and DPPE. DPPG (1,2-dipalmitoyl-*sn*-glycero-3-phosphoglycerol) is anionic, whereas DPPE (1,2-dipalmyitoyl-*sn*-glycero-3-phosphoethanolamine) is zwitterionic. Cationic peptides may have the ability to distinguish between human cell membranes, which mainly contain lipids based on phosphocholine (PC), as opposed to bacterial cell membranes, which contain significant quantities of PG (Phosphatidylglycerol) and PE (Phosphatidylethanolamines) lipids.[26–29] Examining the interactions of the two peptides with these bacterial membrane models enables greater understanding on the mechanisms by which these peptides interact with specific membrane constituents of bacteria. Typically, more PG lipids are found in Gram positive bacteria, whereas PE lipids are more abundant in Gram negative bacteria.[30,31] Here, the interaction of the two designed peptides with model lipid (Scheme 3.1.) membranes are examined better understand antimicrobial activity. Specifically, the interactions of the peptides with mixed liposomes comprising ratios PG:PE and 3:1, 1:1, 1:3 and 1:0, in line with a previous study, was examined.[29] The combination of DPPG/DPPE was chosen due to the accessible melting temperature T_m values, which are well separated for the two lipids, being reported to be 41°C and 63°C respectively.[32]

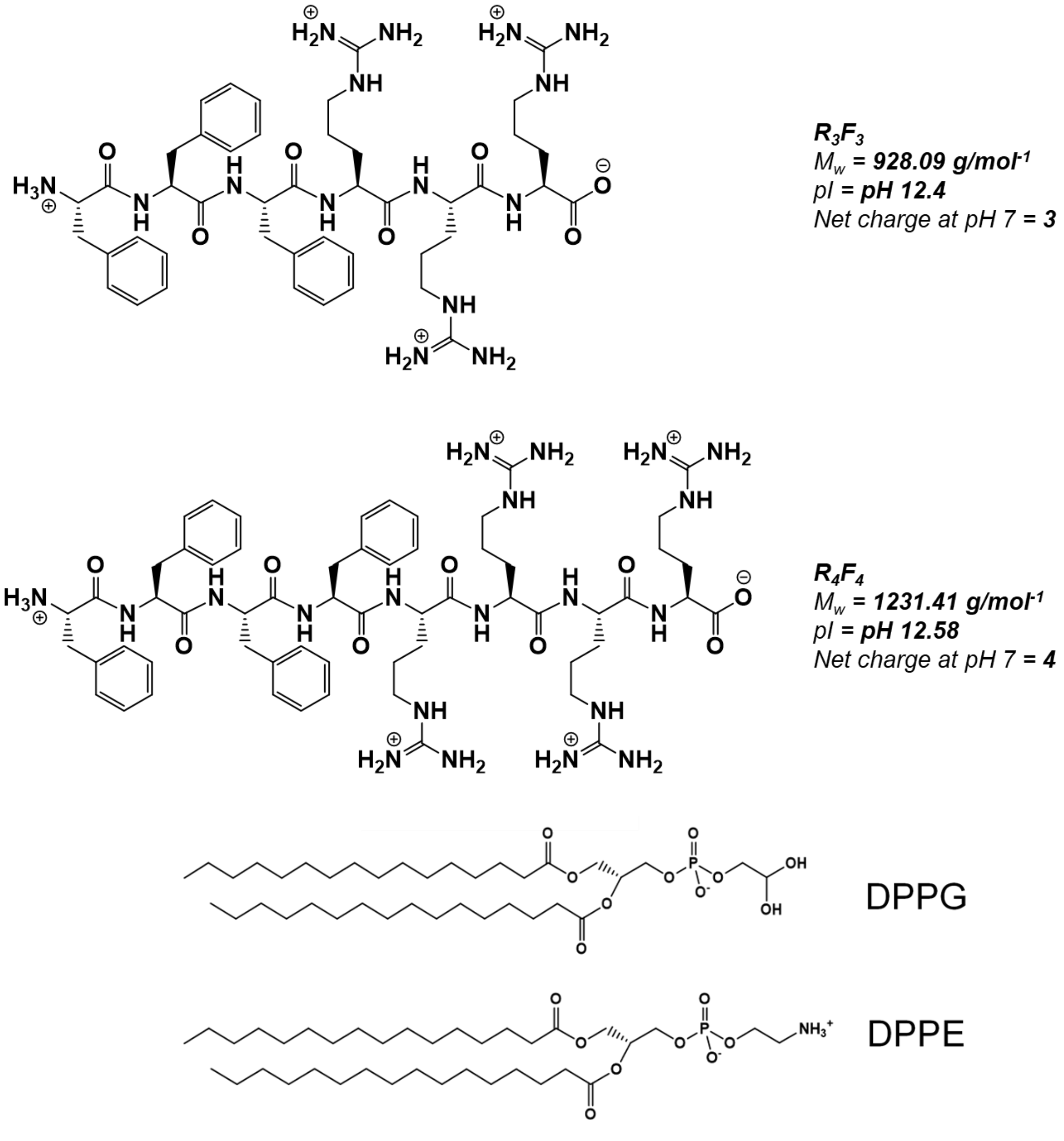

Scheme 3.1. *Structures of peptides RRRFFF (R_3F_3), RRRRFFFF (R_4F_4) and the two lipids used in model membranes, 1,2-dipalmitoyl-sn-glycero-3-phosphoglycerol (DPPG) and 1,2-dipalmitoyl-sn-glycero-3-phosphoethanolamine (DPPE).*

Finally the antibacterial activity of these peptides against five strains of human pathogenic bacteria, *E.coli*, *S. aureus*, and *P.aeruginosa and S.typhi* was measured. Further to this, plant microbes from the *pseudomonas* family were screened with the peptides. Since minimal toxicity to human cells is an essential requirement of an effective peptide therapeutic, the cytocompatibility of these peptides is measured using a human skin fibroblast model.

3.2 Results

3.2.1 Self-Assembly

The critical aggregation concentration (*cac*) for both R_3F_3 and R_4F_4 was determined using 8-anilinonaphthalene-1-sulfonic acid (ANS) which is used because the fluorescence changes within a hydrophobic environment. The *cac* values for R_3F_3 (Figure 3.1a) and R_4F_4 (Figure 3.2a) were found to be (0.32± 0.02) wt% and (0.22 ± 0.03) wt% respectively. There is a significant difference in *cac* values between the two peptides, with the *cac* being lower for R_4F_4 than for R_3F_3. This suggests that the *cac* depends not only on the balance of hydrophobic and charged residues but is also influenced by the number of charged residues. To further assess the critical aggregation concentration, thioflavin T (ThT) was used. ThT is a fluorescent probe used to detect amyloid fibril formation.[33,34] Interestingly, only R_3F_3 was found to bind significantly to ThT indicating that it forms amyloid like fibres (Figure 3.1c). As shown in Figure 3.1a, the *cac* of R_3F_3 determined by ThT was found to be (0.27± 0.03) wt%, which is consistent within uncertainty with that detected by ANS.[35] This suggests that hydrophobic collapse occurs at the same concentration as the formation of amyloid structures for R_3F_3.

To examine the secondary structure of R_3F_3 and R_4F_4, circular dichroism (CD) and Fourier transform infrared spectroscopy (FTIR) were conducted at concentrations above the *cac*. The CD spectrum (Figure 3.1b and 3.2b) is dominated by electronic transitions associated with the phenylalanine side chain. The main feature for all spectra is the peak at 220 nm which is due to phenylalanine π-stacking electronic transitions.[36] The molar ellipticity increases when R_3F_3 and R_4F_4 are adjusted to pH 7. This indicates an increase in content of chiral secondary structure. FTIR (figure 3.1c and 3.2c) was used to further probe secondary structure. The data shows a peak at 1673 cm^{-1} which can be assigned to vibrations of the TFA counter-ions bound to the peptide.[37,38] The peak at 1645 cm^{-1}, characteristic of a disordered secondary structure, is present only at native pH for both peptides. All spectra show a peak at 1608 cm^{-1} which is characteristic of arginine side chains.[27,39–42] The peak at 1588 cm^{-1} can be assigned to the arginine side chain guanidinium group vibrating symmetrically. The 1456 cm^{-1} peak can be ascribed to -CH$_2$ bond vibrations.[43] Considering the data from both CD and FTIR spectroscopy, we conclude that at native pH R$_3$F$_3$ and R$_4$F$_4$ have a disordered secondary structure.

Transmission Electron Microscopy was used to image the self-assembled structure of R$_3$F$_3$ and R$_4$F$_4$ (Figure 3.1e,f and 3.2e,f). Self-assembled structures were observed for both peptides, with R$_3$F$_3$ forming a population of twisted nanotapes that are several microns long, with a width between 50 nm-120 nm. The presence of nanotapes agrees with the binding of fluorescent probe ThT. R$_4$F$_4$ was found to assemble into a population of large nanosheets of differing sizes with widths between 342 nm to 1.7 μM. These non-amyloid structures are not expected to bind ThT, consistent with the fluorescence binding assays.

To further probe the self-assembled structures, SAXS measurements were performed (Figure 3.1d and 3.2d) in dilute solutions order to provide form factors. These are analysed to provide information on the shape and dimensions of self-assembled nanostructures. Data from peptide solutions at pH 7 show initial intensity decays with q^{-2} which indicates planar structures. The data was fitted to a bilayer Gaussian form factor model (previously used by our group to describe the density profile across a bilayer)[44,45] and a generalised Gaussian coil form factor to account for any monomers remaining in the solution using the software SASfit.[46] The parameters for these fits are presented in Table 3.1 and 3.2. This model fits the data very well. An estimate of the length of the peptide (assuming an antiparallel β-sheet structure) is the number of residues multiplied by 3.4 Å. The approximate lengths of R$_3$F$_3$ and R$_4$F$_4$ are 20 Å and 27 Å respectively. The bilayer thickness obtained from the SAXS fit corresponds approximately to these values implying that the nanosheets and twisted tapes are one molecule thick. This suggests an antiparallel arrangement leading to arginine-coated nanotapes/nanosheets (a nanosheet structure with this configuration was proposed for A$_6$R).[17] From these measurements, it can be seen that the peptides primarily remain as monomers in solution at pH 2 and pH 7 with a population of bilayer structures, as seen by TEM and SAXS. Adjustment to pH 7 increases the population of these structures.

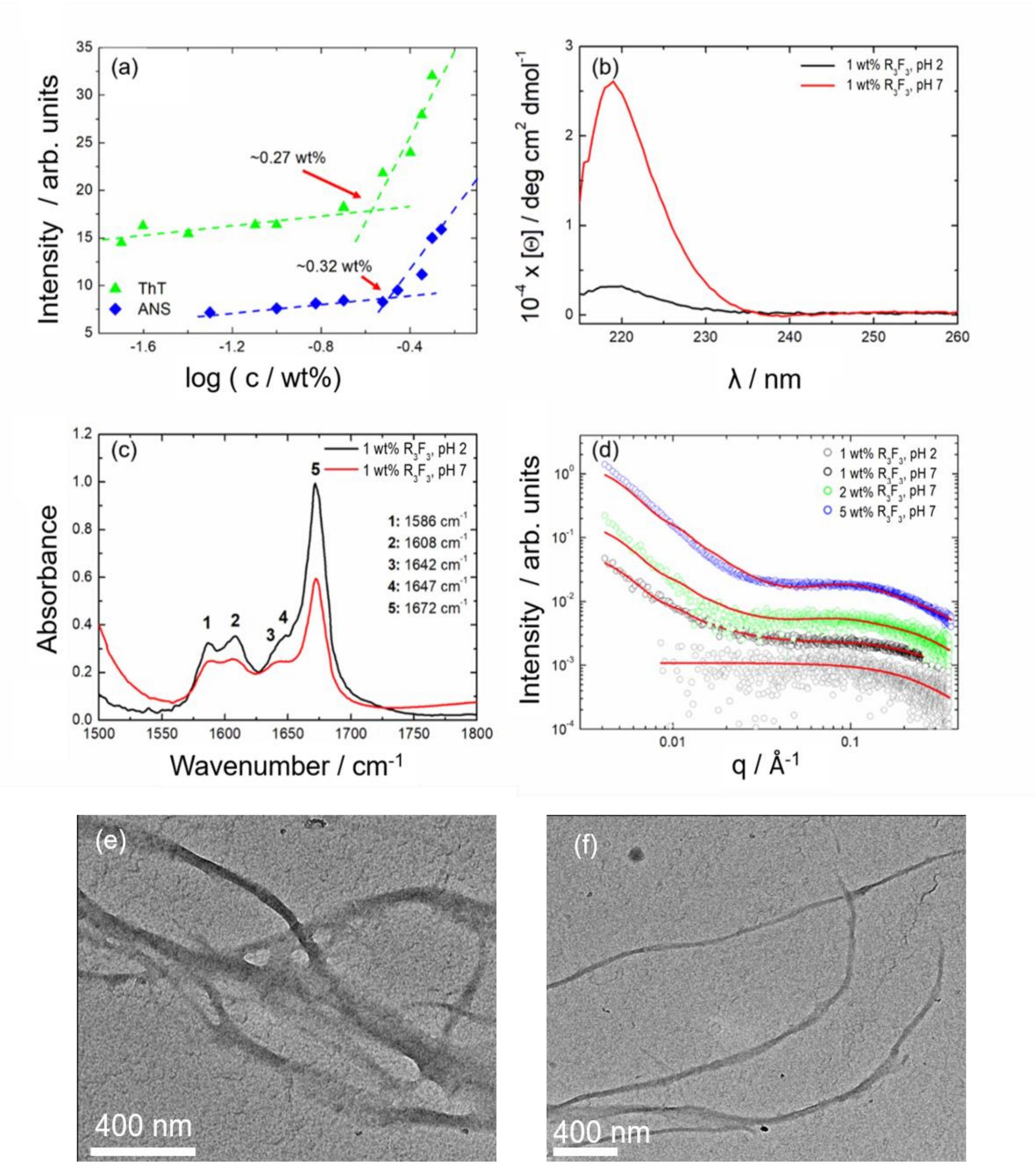

Figure 3.1. *Conformation and self-assembly of R_3F_3 a) cac fluorescence assay using ANS and ThT at native pH (pH 2) b) CD spectra at pH values indicated c) FTIR spectra at pH values indicated d) SAXS data with fitted form factors in red, and e)f) TEM images of 1 wt% R_3F_3*

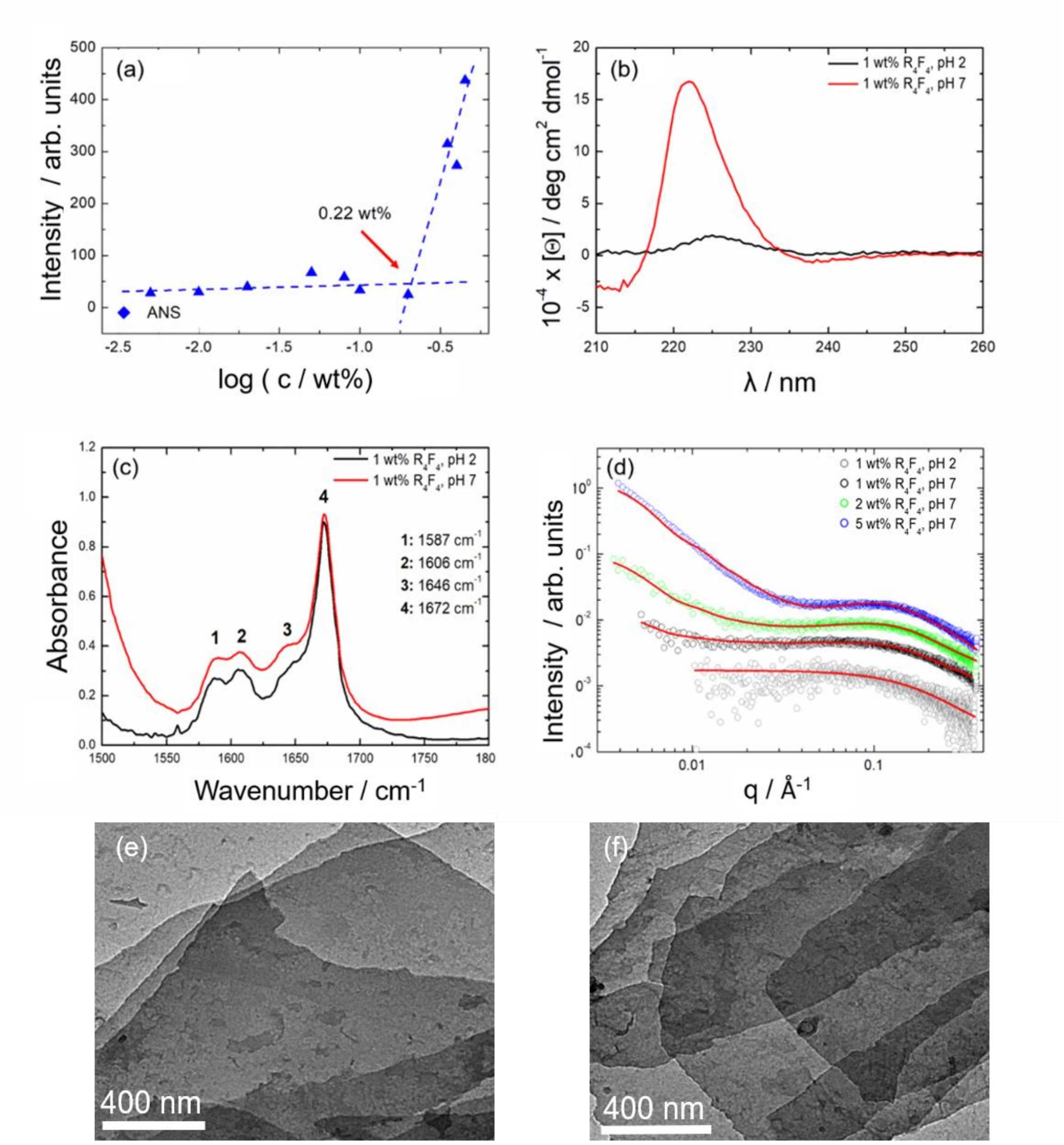

Figure 3.2. *Conformation and self-assembly of R_4F_4 a) cac fluorescence assay using ANS at native pH (pH 2) b) CD spectra at pH values indicated c) FTIR spectra at pH values indicated d) SAXS data with fitted form factors in red, and e)f) TEM images of 1 wt% R_4F_4*

***Table 3.1**. Parameters from SAXS fits for R4F4 and R3F3 at pH 7. Fits were performed using SASfit*

	1 wt% R_3F_3	2 wt% R_3F_3	5 wt% R_3F_3	1 wt% R_4F_4	2 wt% R_4F_4	5 wt% R_4F_4
			Bilayer Gaussian			
N_A	1.31×10^{-3}	1.69×10^{-4}	1.13×10^{-2}	2.07×10^{-3}	5.46×10^{-3}	1.34×10^{-2}
T / Å	21.9	44.1	20.0	27.3	25.0	25.1
Δt / Å	10.3	13.3	13.7	10.7	13.5	13.7
σ_{out}	3.54	7.36	6.61	3.48	3.47	4.88
b_{out}	2.41×10^{-6}	2.60×10^{-6}	1.87×10^{-6}	2.56×10^{-6}	2.32×10^{-6}	1.94×10^{-6}
σ_{core}	9.86	6.79	4.94	9.91	5.86	5.45
b_{core}	-2.12×10^{-6}	-2.80×10^{-6}	-3.68×10^{-6}	-1.93×10^{-6}	-2.36×10^{-6}	-2.47×10^{-6}
D / Å	1000	1000	1000	1000	1000	1000
			Generalised Gaussian Coil			
N_B	0.03	0.03	0.30	0.03	0.03	0.45
R_g / Å	5.09	5.72	6.77	7.66	7.78	6.11
N	0.52	0.31	0.52	0.59	0.43	0.39
I(0)	0.07	0.22	0.04	0.13	0.27	0.02
			Background			
BG	2.26×10^{-4}	1.63×10^{-4}	1.89×10^{-3}	3.12×10^{-4}	1.11×10^{-3}	4.12×10^{-4}

N_A and N_B are relative weights of the bilayer Gaussian and generalized Gaussian coil terms summed in the model form factor fits. For a Bilayer Gaussian form factor,[47] t = bilayer thickness, Δt = associated polydispersity. σ_{out} = Scattering density of outer Gaussians. b_{out} = width of outer Gaussians. σ_{core} = scattering density of inner Gaussian. b_{core} = width of inner Gaussians, D = diameter of disc (fixed parameter)

Generalized Gaussian coil model, the radius of gyration of the chain is defined as $\boldsymbol{R_g^2 = an^{2v}/(2v+1)(2v+2)}$ where a is the segment length, n is the chain length and v is the Flory exponent. I_0 = forward scattering

Table 3.2. *Parameters from SAXS fits for R_4F_4 and R_3F_3 at native pH*

	1 wt% R_3F_3	**1 wt% R_4F_4**
Generalised Gaussian Coil		
N_B	0.48	0.30
R_g / Å	6.99	9.35
N	0.28	0.46
I(0)	0.005	0.004
Background		
BG	3.36×10^{-4}	2.14×10^{-4}

Generalized Gaussian coil model, the radius of gyration of the chain is defined as $\boldsymbol{R_g^2 = an^{2v}/(2v+1)(2v+2)}$ where *a* is the segment length, *n* is the chain length and *v* is the Flory exponent. I_0 = forward scattering

3.2.2 Cytocompatibility

Before investigating the potential antimicrobial activity of R_3F_3 and R_4F_4, it is good practice to assay cytocompatibility, to determine the concentration range of peptides over which viability of human cells is retained. Therefore, cytotoxicity assessments were performed using the MTT assay on *161BR* human skin fibroblasts (Figure 3.3). The IC_{50} of R_4F_4 was calculated to be 2.15 mM (or 2.64 mg/ml or 0.264 wt%). Interestingly, this is in the error range of the *cac* value determined for R_4F_4 (Figure 3.2a) implying that the self-assembly into nanosheet structures correlates to the onset of increased toxicity. The IC_{50} of R_4F_4 is higher than previously studied $[RF]_4$ peptide which has an IC_{50} value of less than 1 mM, meaning that R_4F_4 is less cytotoxic. Clearly, sequence has a significant effect on the cytotoxicity of these compositionally identical peptides. The IC_{50} of R_3F_3 was found to be 4.31 mM, the maximum concentration used in the concentration series and above the *cac* of this peptide. The finding that an increased number of residues leads to increased toxicity agrees with studies conducted with [RF] repeating peptides,[22] although R_4F_4 is significantly less cytotoxic than its compositional homologue RFRFRFRF.

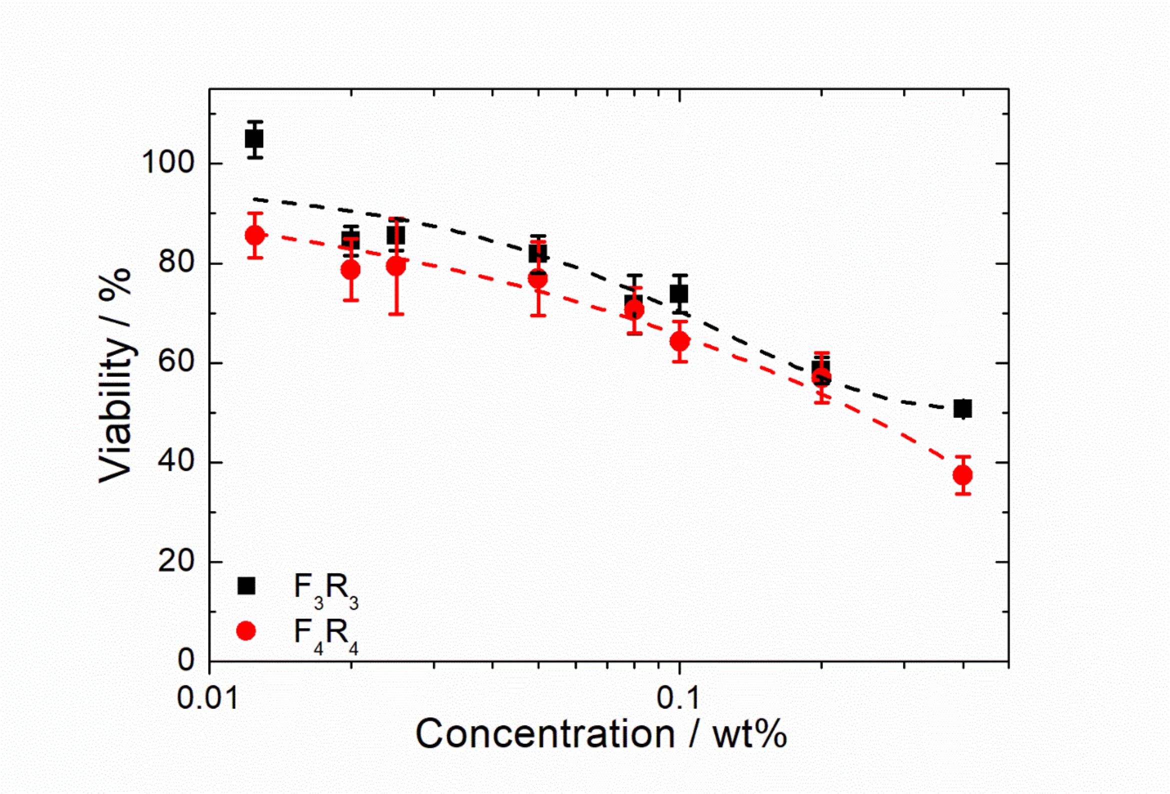

Figure 3.3. *Cytotoxicity profiles from MTT assays. a) R_3F_3 and b) R_4F_4. IC50 values (vertical blue dashed lines) were calculated in Origin using sigmoidal fits to the viability data (dashed red lines shown). Where, n=3, error bars = standard deviation,*

3.2.3 Initial Antimicrobial screening

Having determined conditions where viability of human fibroblasts in the presence of these peptides is acceptable, we then studied their antimicrobial activity in planktonic form. Compounds that are active against bacteria have either inhibitory or bacteriocidal properties. Inhibitory compounds are less likely to cause bacterial resistance but are more vulnerable to the innate immune system and antibiotics. Bacteriocidal compounds are useful for fighting bacterial infections, but can increase the resistance of bacteria. Both activities are valuable for different purposes.[48] To examine whether R_3F_3 and R_4F_4 are bacteriocidal, the two peptides were inoculated with several strains of bacteria for 24 hours. Figure 3.4 shows the antimicrobial activity of these peptides against Gram positive *S. aureus* and three Gram-negative bacteria, one strain of *P. aeruginosa* (PA01) and one of *E. coli* (K12), and *S,typhi.* A concentration of 0.05 wt% was selected based upon the viability of human skin fibroblasts at this concentration which was shown to be 77% and 81% for R_3F_3 and R_4F_4 respectively

(Figure 3.3). The data indicate that R_3F_3 has no effect on *E.coli*, *S.typhi* and *S.aureus*. The peptide R_4F_4 causes a small, but not statistically significant reduction of one order of magnitude in colony forming units/millilitre (CFU/mL) of *E. coli* (K12) after 24 h. This effect however, is not seen for the clinically relevant *E. coli* (0157) strain (Figure 3.4b). Neither peptide showed activity against *S.typhi* or *S. aureus*, the latter in contrast to previously studied arginine-rich peptides,[27,49] although this could be due to the lower concentrations used. Interestingly, both peptides showed a strong antimicrobial effect against *P. aeruginosa* (Figure 3.4e), with a 3.2 log reduction in CFU/mL upon addition of R_3F_3, and complete death of the strain after 2 hours on exposure to 0.05 wt% R_4F_4 (Figure 3.4e). To investigate this further, a series of concentrations of R_3F_3 (Figure 3.4g) and R_4F_4 (Figure 3.4f) were examined to locate any MIC. The data indicate that R_3F_3 does not have an MIC below 0.1 wt% and R_4F_4 has a MIC value between 0.045 wt% and 0.05 wt% for *P. aeruginosa*.

To further understand the specificity of these peptides against *Pseudomonas* bacteria, the antibacterial activity of the peptides against four other species was examined (Figure 7). Since R_4F_4 is particularly active against *Pseudomonas* species, data were obtained for an additional three species. Data for *P. putida, P. agarici* and *P. fluorescens* are shown in Figure 3.5 which shows that all bacteria displayed an initial die off when exposed to R_4F_4. However, interestingly *P. fluorescens* has some recovery in bacterial colony counts after 24 hours, which may be due to the bacteria being able to metabolise the peptide, however further studies would be needed to understand this effect. There is also a significant (log 2.6) reduction in CFU/mL of plant pathogen *P. syringae* when exposed to R_3F_3 and a complete bacterial death when exposed to R_4F_4, similar to the effects seen with *P. aeruginosa* after 2 hours of exposure. The MIC concentration is ~0.001 wt% R_4F_4 for *P. syringae,* which is approximately 50x lower than that for *P. aeruginosa*. Our data suggests that R_4F_4 is selectively active against specific *Pseudomonas* species.

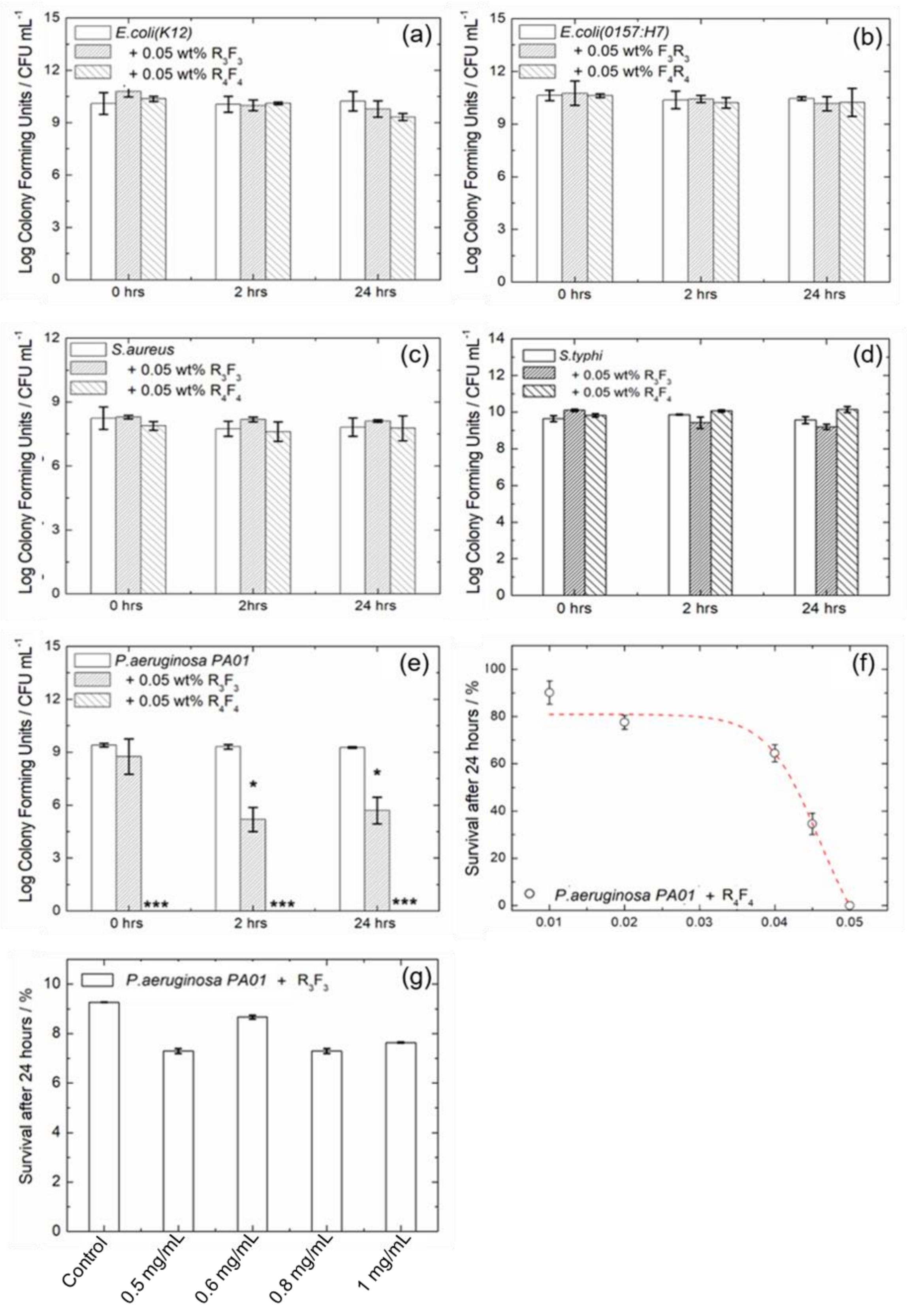

Figure 3.4. *Activity of R_3F_3 and R_4F_4 against several strains of human bacterial pathogens. Where, n=3, error bars = standard deviation, *= p<0.05, **=p<0.01 and ***= p<0.001.*

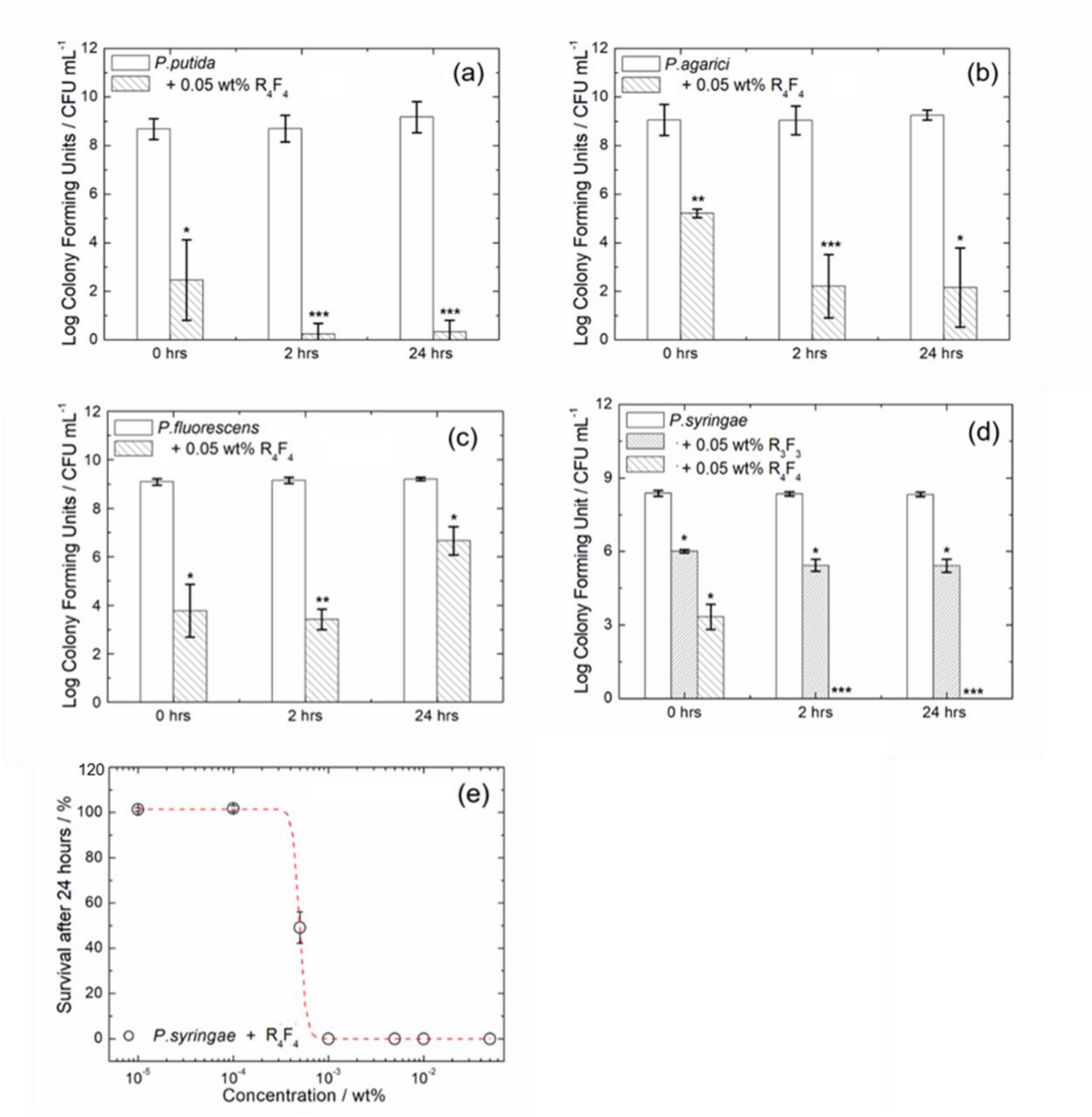

***Figure 3.5**. Survival assays of R_4F_4 and R_3F_3 against other species of Pseudomonas. Where, n=3, error bars = standard deviation, *= $p<0.05$, **=$p<0.01$ and ***= $p<0.001$.*

3.2.4 Interaction with Lipid Vesicles

To understand the antimicrobial activity of R_3F_3 and R_4F_4 discussed in the previous section, the interaction between the peptides and the model lipid membrane models composed of DPPG and DPPE mixtures was examined. The lipids DPPG and DPPE are commonly used as a bacterial membrane models. [20,29] SAXS was used to probe structure changes resulting from interaction of peptides with lipid membranes. We examined the ratios 1:0, 1:3, 1:1 and 3:1 of DPPG/DPPE. In accordance with the phase diagrams recorded previously,[29,50] the samples with mixtures 1:0, 1:1 and 3:1 DPPG/DPPE are expected to be in the disordered liquid crystal phase at 20 °C, L_α whereas 1:3 DPPG/DPPE is expected to be in the L_α/ L_β coexistence region at 20 °C (where L_β is the ordered gel phase). PE alone is not studied as the shape of the lipid means it forms inverted micelles with hexagonal symmetry.[27] The 1:3 DPPG/DPPE has similar PE content to the amount found in the *P.aeruginosa*, whereas DPPG alone more resembles the *S.aureus* membrane which has no PE.

Figure 3.6 shows SAXS intensity profiles obtained with ratios 1:0, 1:3, 1:1 and 3:1 of DPPG/DPPE at 0.5 wt% with and without R_3F_3 and R_4F_4. For all ratios, the lipids alone displayed a broad scattering pattern with a peak centred at q ~ 0.1 Å^{-1}, which is associated with unilamellar vesicles.[26] Figure 3.6 also contains the SAXS data for samples containing the peptides. A concentration of 0.08 wt% peptide was used (data being shown for an additional concentration of 0.25 wt% for R_4F_4 with DPPG), since addition of 0.25 wt% peptide caused precipitation in many samples, as seen with previously studied peptides.[26,27]

In the SAXS data for 1:0 DPPG:DPPE, 0.08 wt% R_3F_3, there is a small Bragg peak with a corresponding domain spacing d= 45.9 Å and a distortion of the broad peak shape. This indicates some correlation between bilayers, i.e. restructuring of a proportion of vesicles into multilamellar vesicles. Adding 0.08 wt% R_4F_4 to DPPG leads to a change in the shape of the SAXS profile (broadening of the form factor extrema), and when the concentration of R_4F_4 is increased 0.25 wt%, two Bragg peaks with d= 43.4 Å and 14.6 Å are present. These peaks correspond to the first and third order reflections of a multi-lamellar structure. This shows restructuring of most liposomes into multilamellar vesicles in the presence of R_4F_4 indicating peptide-induced lipid restructuring. R_3F_3 was not examined at this concentration due to precipitation of the sample.

For the lipid mixture 3:1 DPPG:DPPE, no Bragg peak was observed in the SAXS profiles in the presence of either peptide. Indeed, the form factor resembles that for the corresponding mixed liposome, with again only some broadening of form factor features (and a shift to higher q), particularly in the presence of R_4F_4. For R_3F_3 combined with 1:1 DPPG:DPPE, there is again a broadening in the features in the SAXS curve. However, for R_4F_4, two Bragg peaks are noted with corresponding spacings d = 96.0 Å and d = 68.2 Å which is approximately a 1 : √2 ratio, suggesting cubic symmetry,[51] although the presence of two coexisting lamellar structures cannot be excluded in the absence of higher order Bragg reflections.

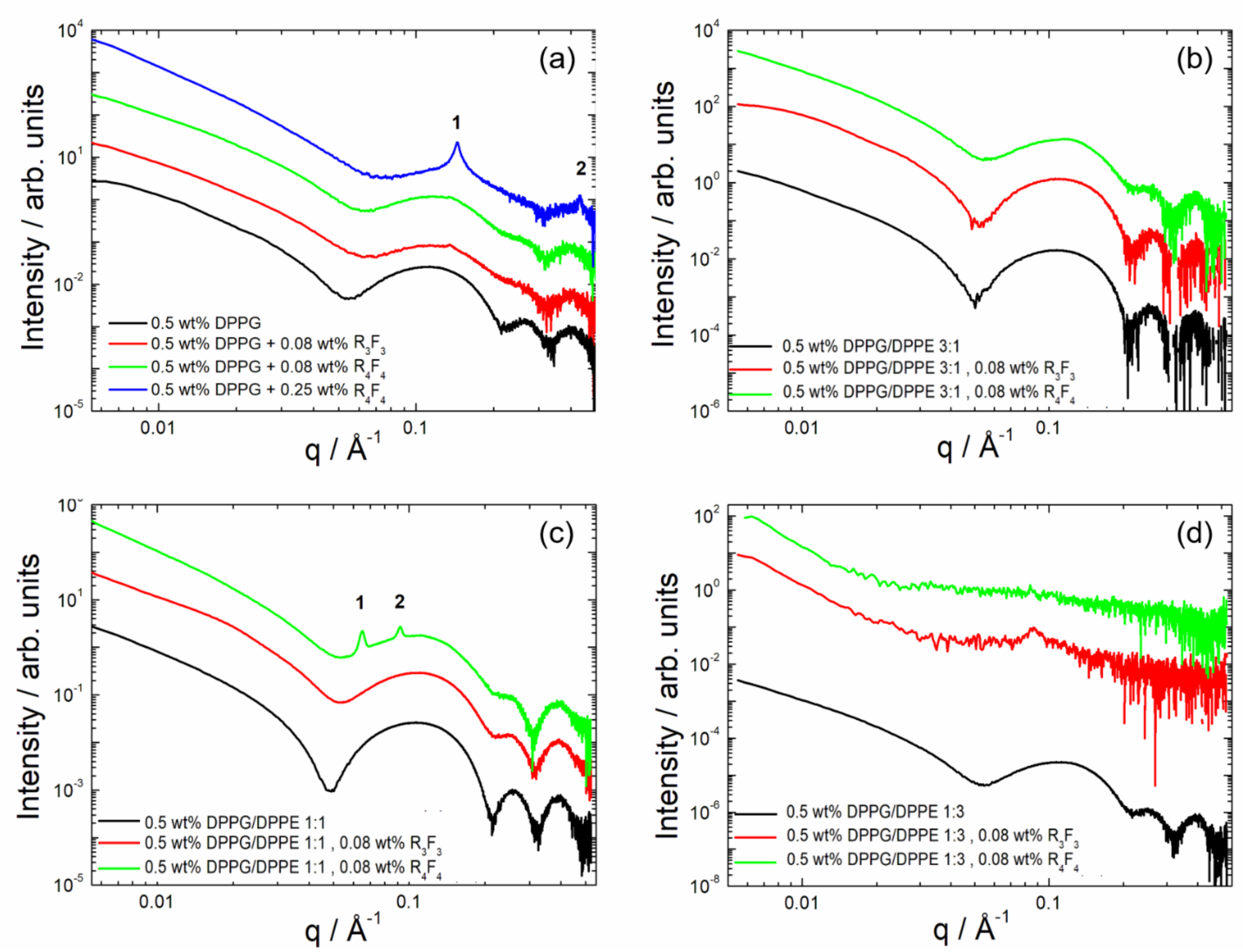

***Figure 3.6** SAXS profiles for different ratios of DPPG:DPPE in the presence of R_3F_3 or R_4F_4 at the concentrations indicated.*

Considering the SAXS data for the samples containing the most DPPE (1:3 DPPG:DPPE), the liposome form factor is lost upon addition of either peptide, thus being replaced with form factor profiles with a similar shape to those for the peptides alone (Fig.3.1d, Fig.3.2d), especially for R_4F_4. Though there is a Bragg peak for R_3F_3 showing some multilamellar vesicles are still present. Cryo-TEM images of samples prepared with lipids at this ratio show that R_3F_3 causes a change in morphology of liposomes, seen by the appearance of rougher looking surfaces (Figure 3.7d,e). Cryo-TEM images of samples with this lipid composition in the presence of R_4F_4 show that the peptide induces complete disruption of liposome formation, in agreement with conclusions from the SAXS data (Figure 3.7d,f). The Cryo-TEM image for vesicles of DPPG (Figure 3.7a), shows that vesicles are generally larger when exposed to R_3F_3 (Figure 3.7b) with some fibres (presumably peptide) also present. For mixtures of DPPG with R_4F_4 (Figure 3.7c) the vesicles are more swollen, and moreover are much more angular in shape and have a multilamellar structure. This is consistent with the SAXS data.

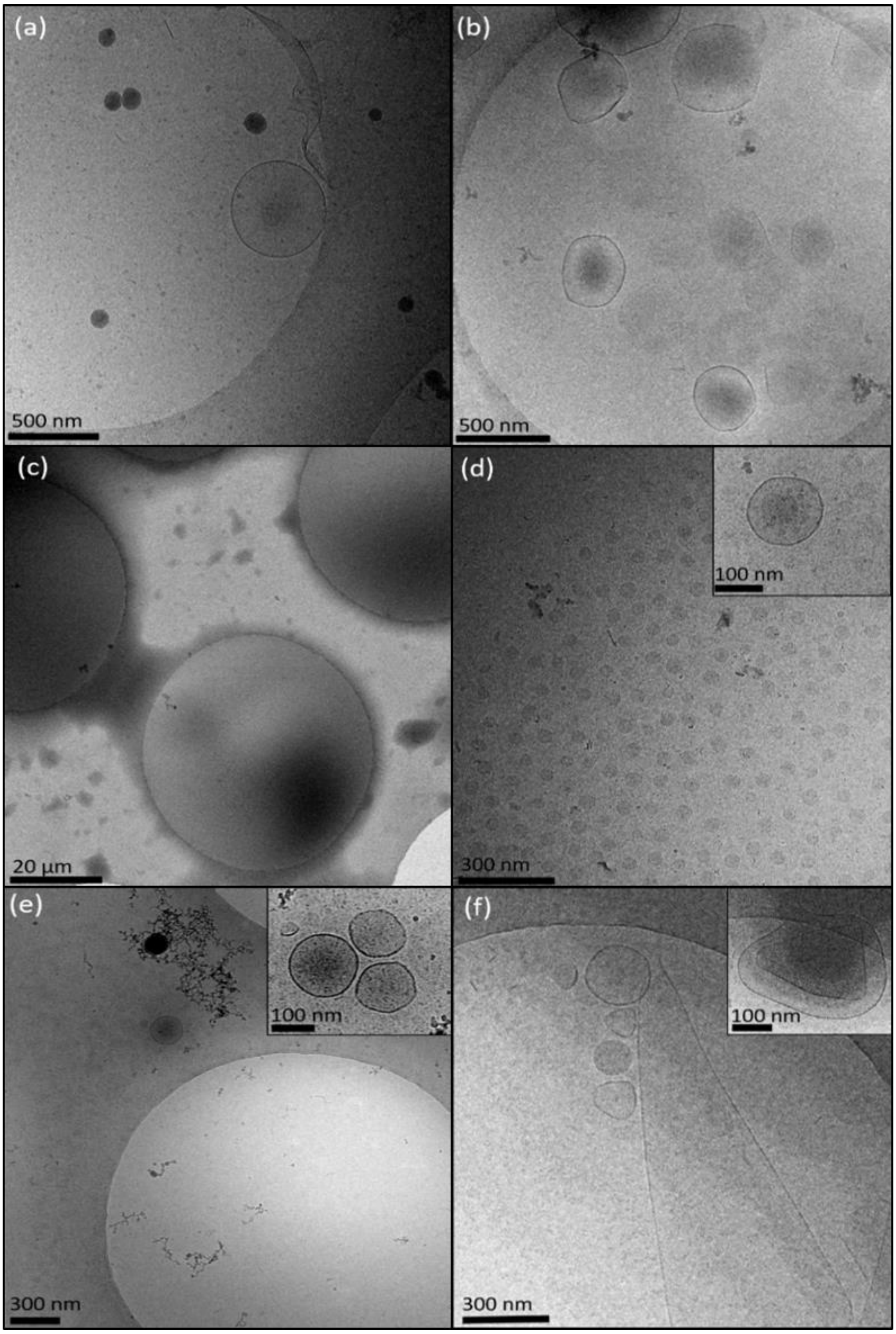

Figure 3.7. *Cryo-TEM images of vesicles with and without peptide. a) 0.5 wt% DPPG/DPPE 1:3 b) 0.5 wt% DPPG/DPPE 1:3 + 0.08 wt%* R_3F_3 *c) 0.5 wt% DPPG/DPPE 1:3 + 0.08 wt%* R_4F_4 *d) 0.5 wt% DPPG e) 0.5 wt% DPPG + 0.08 wt%* R_3F_3 *f) 0.5 wt% DPPG + 0.08 wt%* R_4F_4*. Cryo-TEM captured by Janne Rukolanien, University of Aalto, Finland.*

Circular dichroism spectroscopy is often also used to examine the interactions of lipid membranes with peptides.[26,27,50] In some instances, peptide secondary structure is shown to be influenced in the presence of lipid membranes, inducing the formation of a more ordered secondary structure. This gives information about whether the peptide interacts with the lipid as a monomer or as a self-assembled structure. Figure 3.8 shows the circular dichroism spectra for the mixtures of the two peptides with different composition lipid mixtures. Due to the presence of a broad maximum around 220 nm in the spectra, it is concluded that the peptides interact with the lipids in a monomeric form.

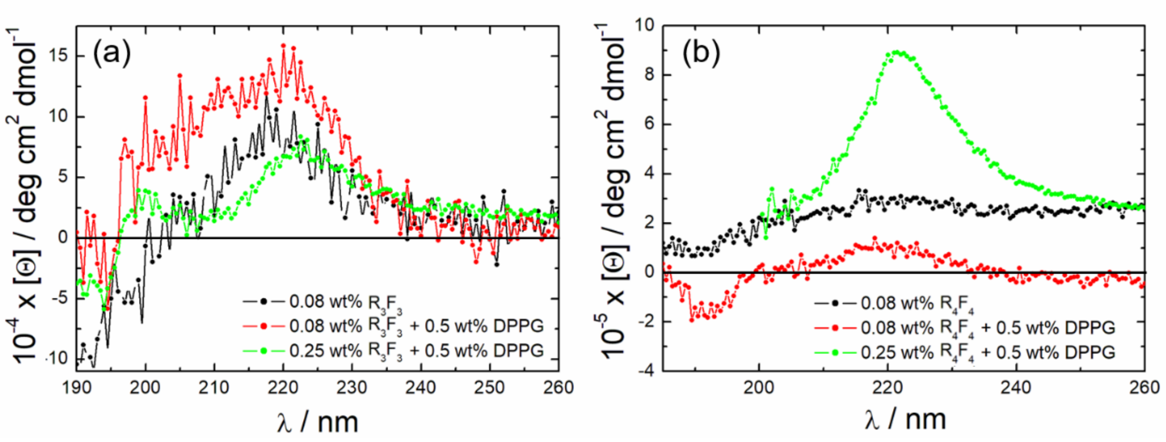

Figure 3.8 *CD data for a) R_3F_3 and b) R_4F_4 with DPPG (concentrations indicated).*

Differential scanning calorimetry (DSC) is a valuable technique to detect phase transitions in lipid systems and has also been used to probe the interactions of peptides with lipid membranes. In particular, to investigate phase separation in lipid membranes induced by antimicrobial peptides.[28,29,52] We examined the interaction of the two peptides with DPPG using this technique. The thermograms are shown in Figure 3.9 and the determined transition temperatures and enthalpies are listed in Table 3.1. Lipid DPPG alone shows a pre-transition to the P_β phase at 37.2 ^{o}C and a main chain melting temperature to the L_α phase at 40.4^{o}C in the second heating scan. This is in agreement with published data.[28,29] First heat scans of peptide and DPPG differ from subsequent scans due to non-equilibrium effects. Figure 3.9 shows the DSC thermograms from the second heating scans of DPPG with 0.08 wt% R_3F_3 and R_4F_4. The data show that upon addition of R_3F_3 a shouldered peak is observed, with a main transition at 38 ^{o}C and a shoulder at 40 ^{o}C. On the other hand, R_4F_4 shows a double peak with maxima at 37 °C and at 44 °C. The presence of double peaks/shoulder peaks suggests phase separation of the peptide-rich and peptide-depleted regions in the sample. If there is electrostatic binding to the PG head group, an increase in T_m would be expected.[28] However, if the peptide is interacting with the hydrophobic region of the membranes, this can lead to perturbation of the lipid chain packing and a reduction in transition temperature.[28] Therefore, the data suggests that R_3F_3 interacts with the hydrophobic region of DPPG due to the decrease in T_m of 1.5 °C. In contrast, R_4F_4 causes enhanced coexistence of L_α and P_β phases, possibly indicating the formation of phase separated domains (rafts).

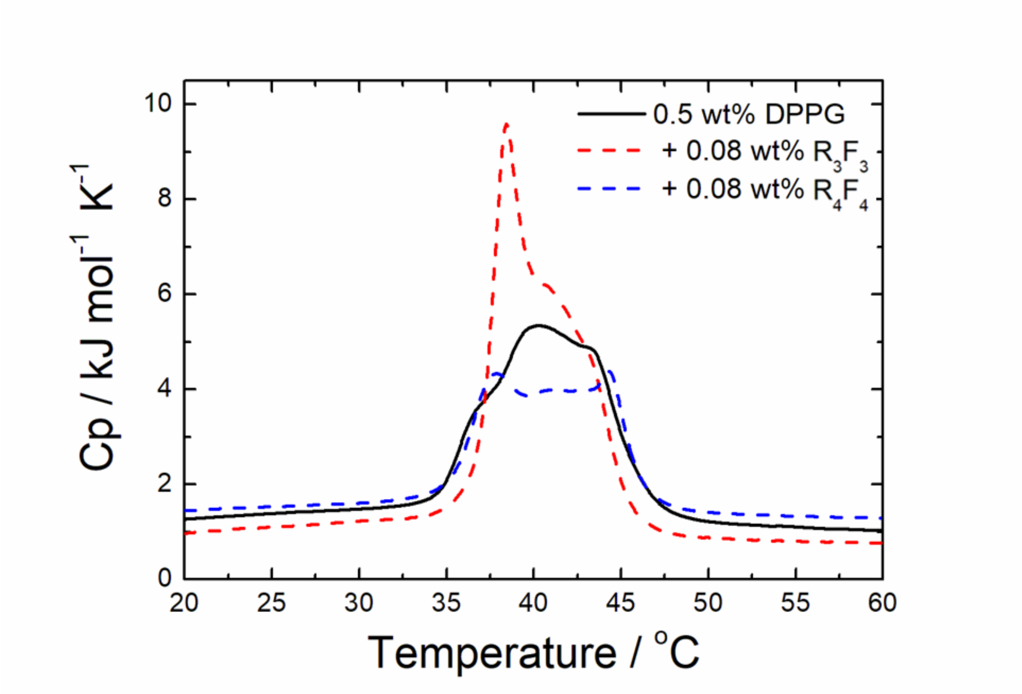

***Figure 3.9** Differential scanning calorimetry thermograms of DPPG with and without peptides. Scans displayed are second heat scans.*

***Table 3.3.** Transition peaks, energy of transition and HWHM calculated from Figure 3.9. DSC data, of 0.5 wt% DPPG with and without peptide.*

Sample	T_1 / °C	T_2 / °C	ΔH / kJ mol^{-1}	HWHM
0.5 wt% DPPG	37.2	40.4	29.8	28.0
0.5 wt% DPPG, 0.08 wt% R_3F_3	38.5	40.9	37.8	48.5
0.5 wt% DPPG, 0.08 wt% R_4F_4	37.8	44.4	25.3	15.1

T_1 = Transition temperature 1, T_2 = Transition temperature 2, ΔH = change in enthalpy across the peaks and HWHM = half width half maximum of the overall peak

In the mixture of 1:3 DPPG/DPPE with R_4F_4, there is a small increase in the transition temperature compared with lipid alone by 2.17 °C. The transition temperature of 62.94 °C is similar to the transition temperature of DPPE which is 63 °C, showing evidence of DPPE-rich regions, which shows de-mixing may be occurring. There is also a decrease in the ΔH, showing that the peptide is destabilising the L_β phase, enabling transition to the liquid phase with a lower energy requirement.

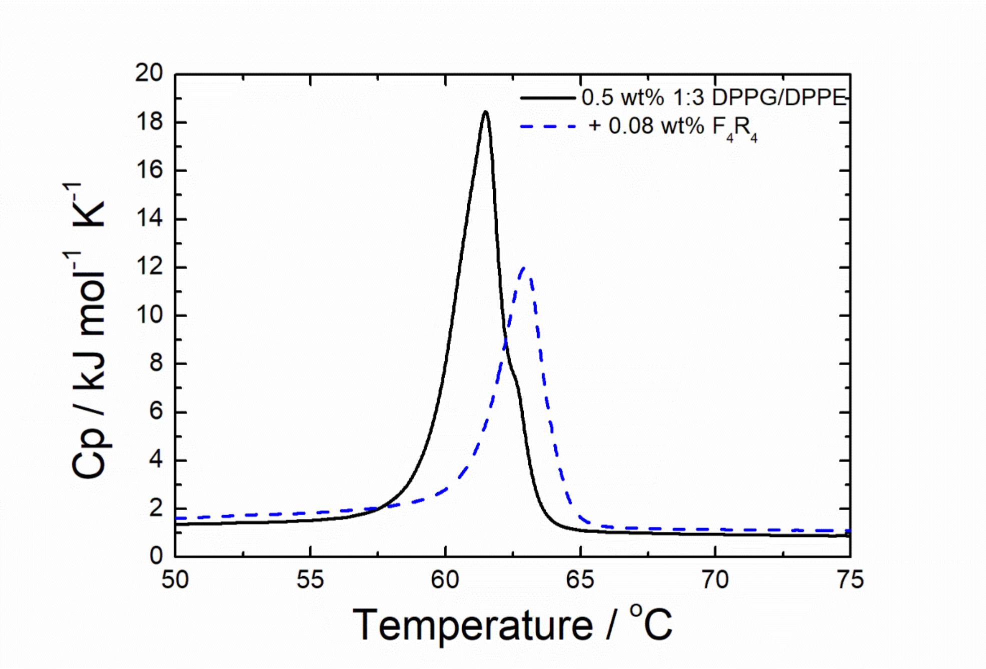

***Figure 3.10.** DSC thermograms for 1:3 DPPG/DPPE with R_4F_4.*

***Table 3.2**. Transition peaks, energy of transition and HWHM calculated from Figure 3.10. DSC data, of 0.5 wt% 1:3 DPPG/DPPE with and without peptide.*

Sample	T_1 / °C	ΔH / kJ mol^{-1}	HWHM
0.5 wt% 1:3 DPPG/DPPE	60.77	37.5	52.03
0.5 wt% 1:3 DPPG, 0.08 wt% R_4F_4	62.94	34.1	25

T_1 = Transition temperature 1, T_2 = Transition temperature 2, ΔH = change in enthalpy across the peaks and HWHM = half width half maximum of the overall peak

3.2.5 Biofilm disruption and interactions with ci-d-GMP

P. aeruginosa has the ability to form biofilms, which is a major problem in infections, in particular those of the respiratory tract. An important regulator of biofilm formation in *P. aeruginosa* is the second messenger signalling molecule cyclic di-GMP (c-di-GMP).[53–55] High levels of c-di-GMP in *P. aeruginosa* are associated with the formation of biofilms, which leads to virulence and persistence of bacteria in hosts.[54,56] Compounds that can reduce and prevent biofilm formation by targeting c-di-GMP are therefore attracting attention. We first examined whether R_3F_3 and R_4F_4 inhibit biofilm growth formation and then examined interactions of these peptides with c-di-GMP. Crystal violet was used to assay biofilm formation, this cationic dye binding to anionic polysaccharides in the biofilm.[57,58] The assay shows that R_4F_4 causes a reduction of biofilm formation in two strains of *P. aeruginosa*, PA01 and ATCC-12600. At a concentration 0.05 wt% of R_3F_3, we observe 84% survivability of the PA01 biofilm (Figure 3.11a) whereas R_4F_4 significantly reduces biofilm viability to 37% of *P. aeruginosa strain* PA01 and 33% for strain ATCC-12600 (Figure 3.11b)

A series of biophysical techniques to observe the interaction of both peptides with ci-d-GMP were used, which included SAXS, CD and TEM. At concentrations of 100 μM or more, c-di-GMP exists in equilibrium with its homodimer.[48] Interestingly, the CD spectra of R_4F_4 and R_3F_3 show that c-di-GMP causes a strong increase in molar ellipticity (Figure 3.12a) at a 255 nm maximum for R_3F_3 and a slight red shifted maximum of R_4F_4 of 259 nm. There is also an increase in negative ellipticity at the minimum at 281 nm for R_3F_3 and 284 nm for R_4F_4, which corresponds to the stacking of the four guanine rings present in dimers of c-di-GMP. This shows that the addition of the peptides stabilises the homodimer.[48] The red-shifted peak positions for R_4F_4 are evidence of altered π-stacking in the complex between c-di-GMP and R_4F_4, which is not observed for the c-di-GMP complex with R_3F_3.

TEM images for c-di-GMP with R_3F_3 show the formation of nanosheets (Figure 3.12c). In contrast, the TEM image for c-di-GMP with R_4F_4 shows the formation of a fibrous network structure (Figure 3.12e). Differences in structure also change the slope of the SAXS profiles in the low q region (Figure 12.b), $I \sim q^{-n}$. The slope of the low q intensity for c-di-GMP alone is $n = 0.8$ consistent with locally extended structures. Upon addition of R_3F_3, the slope changes to $n = 1.8$ which suggests the formation of layered structure, such as bilayers as seen in the TEM images. The peptide alone shows n = 3.5. For R_4F_4 (Figure 3.12d), the slope changes to n = 4.2, suggesting the presence of compact globular structures.

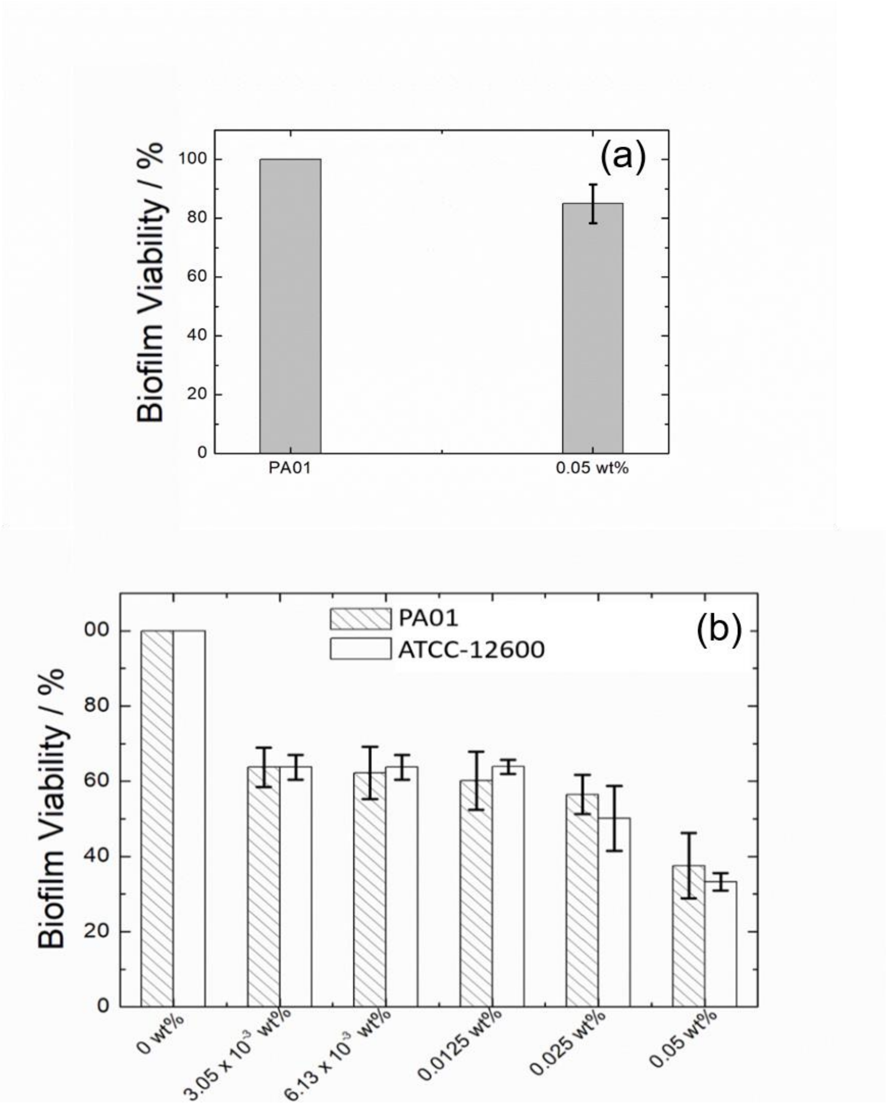

***Figure 3.11**. Biofilm viability of P.aeruginosa determined through crystal violet assays when exposed to a) R_3F_3 and b) R_4F_4. where error bars = standard deviation, n= 3.*

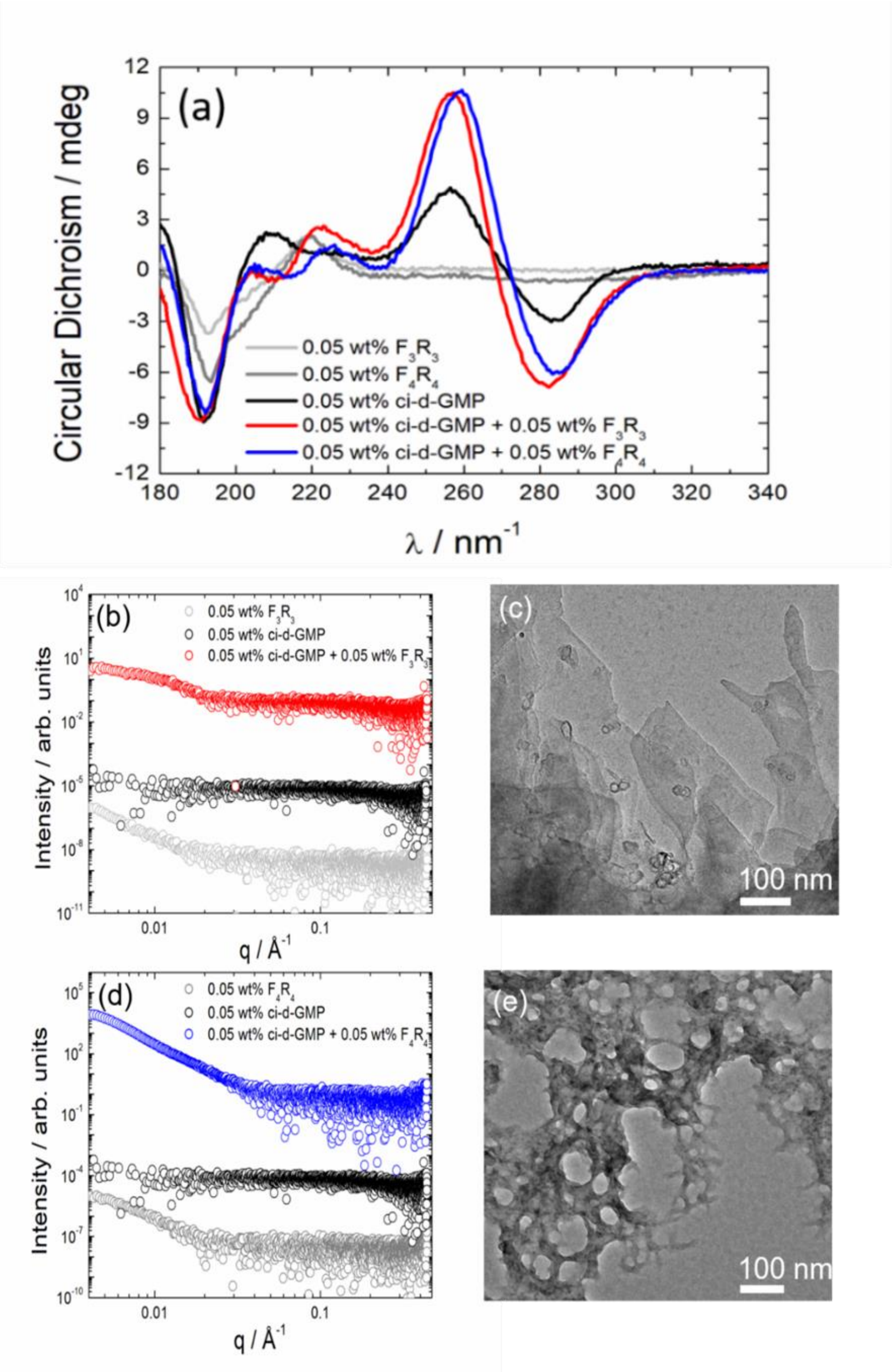

***Figure 3.12**. Interactions of R_3F_3 and R_4F_4 with ci-d-GMP, a) Circular Dichroism, b) and d) are SAXS profiles c) TEM of R_3F_3 with ci-d-GMP and e) TEM of R_4F_4 with ci-d-GMP.*

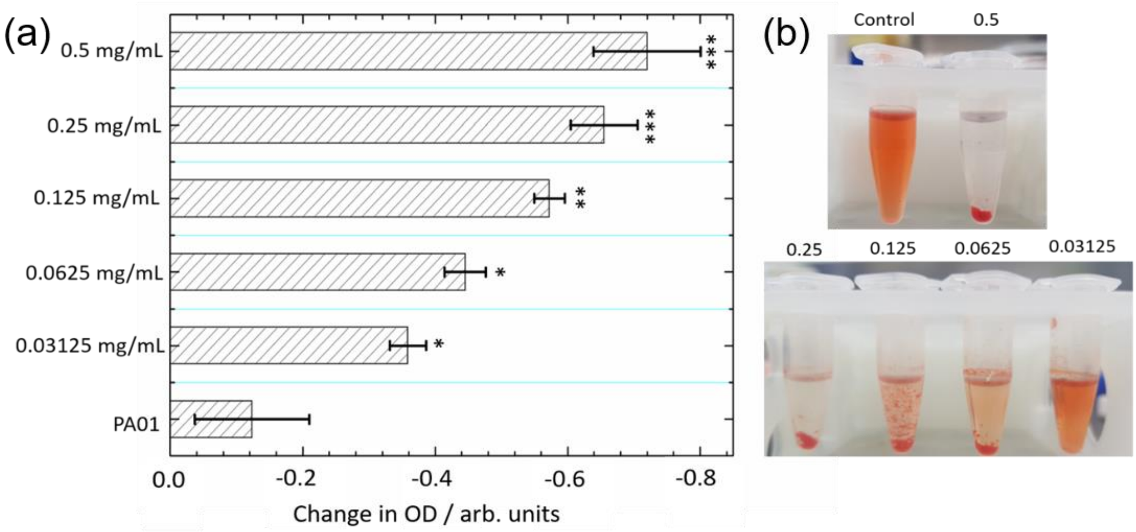

Figure 3.13. *Indirect measurements of ci-d-GMP a) Congo red assay measuring amount of polysaccharide produced by bacteria, at the peptide concentrations indicated and b) Congo red staining vials showing flocculation of the bacteria to the bottom of the tube as opposed to the sides where there is growth. Where, n=3, error bars = standard deviation, *= $p<0.05$, **=$p<0.01$ and ***= $p<0.001$.*

Congo red staining can be used to quantify the amount of polysaccharides produced by bacteria.[59] Congo red binds to fibrous material, and bacteria produce polysaccharides in response to either stress or high levels of c-di-GMP, which lead to biofilm formation. This has been used as an indirect measurement of c-di-GMP levels since these are correlated to polysaccharide expression.[59] Congo red binds to polysaccharides resulting in a decreased optical density (OD) when polysaccharide matrices are formed by the bacteria.[59] When adding R_4F_4 to *P. aeruginosa*, we observe a decrease in optical density of the supernatant (Figure 3.13b). This indicates enhanced biofilm growth. However, it was observed that from 0.0625 mg/mL to 0.25 mg/mL there was a precipitate at the bottom of the tube, and some film growth occurred at the interface of the tube between the air and the solution. *P. aeruginosa* is a motile organism, therefore is expected to form a biofilm at the interface.[60] At 0.5 mg/mL (0.05 wt%), a concentration that is the above the MIC in water, and for which 37% biofilm viability is observed (Figure 3.12b), there is no biomass on the side of the tube, but a deposit on the bottom of the tube. *P. aeruginosa* has a mucoidal phenotype, which means it can form a polysaccharide capsule around itself in response to stressed conditions.[61]

Therefore we conclude that the reduction in the OD is due to stressed bacteria producing polysaccharides as part of the stress response.

3.3 Conclusions

The two SLP peptides R_3F_3 and R_4F_4 both self-assemble above a critical aggregation concentration obtained by fluorescence probe assays. Overall, their propensity for aggregation is weak, displayed by the higher *cac* values obtained compared to many other SLP's, SAXS intensity profiles above the *cac* which suggest significant amounts of monomer still present, and CD and FTIR analysis of secondary structure which is not well defined.

Moreover, the "blocky" nature of R_4F_4 and R_3F_3 leads to changes in morphology of self-assembly compared to their homologues. In comparison to previously studied alternate hydrophilic-hydrophobic peptides, $[RF]_3$ forming globules, compared to R_3F_3 forming twisted nanotapes, and $[RF]_4$ forming nanofibers, compared to R_4F_4 which forms nanosheets.

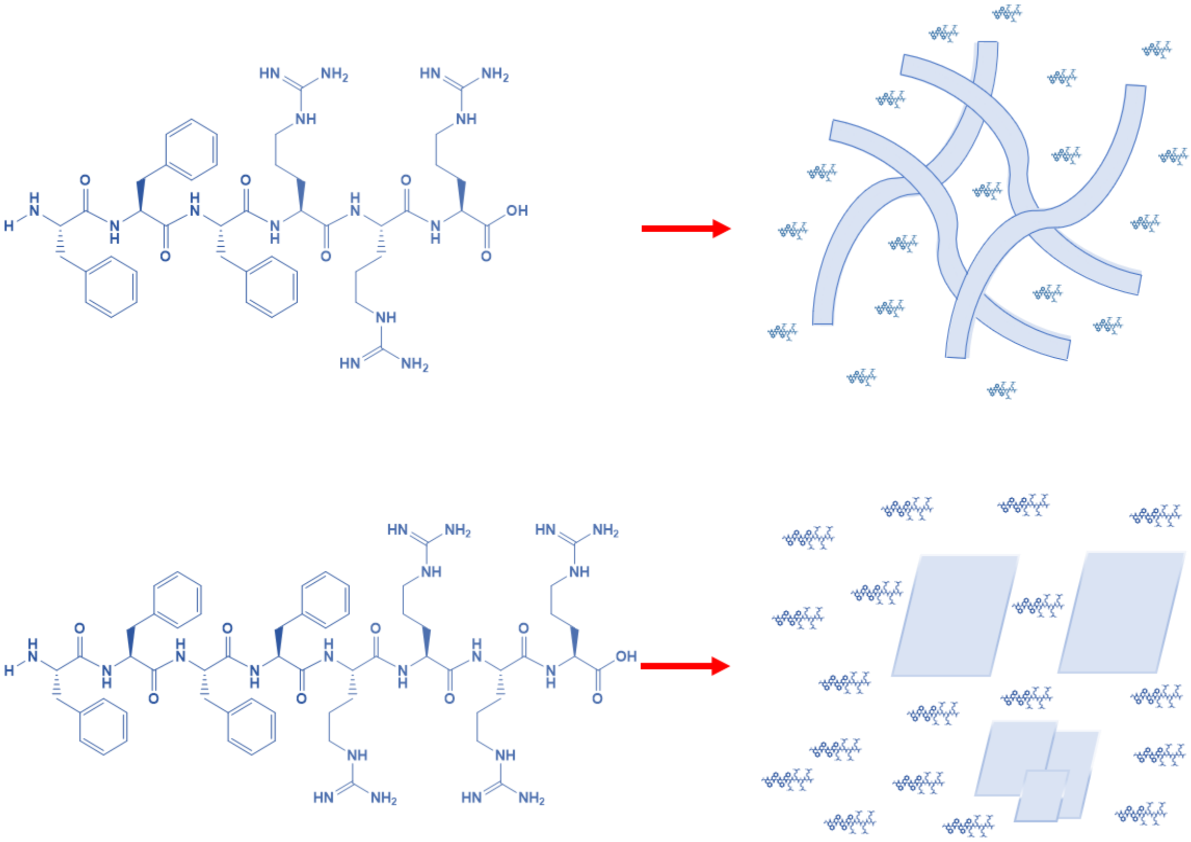

Scheme 3.2. *Overall Self-assembly of a) R_3F_3 and b) R_4F_4*

Both R_3F_3 and R_4F_4 have strong antimicrobial activity against the *pseudomonas* species, within the range of human cell viability. The latter is particularly active against pseudomonas species, including, *P.aeruginosa* in the planktonic form, as well as plant pathogen *P.syringae*. Activity in this planktonic form may be in part due to the interactions with the bacterial lipid membrane, which in *pseudomonas* contains ca. 21 % PG and 60% PE. The ratio of 1:3 DPPG/DPPE best represents this composition, which when measured by SAXS and cryo-TEM with peptide mixtures shows disruption of the membranes.

Further to this, the activity of R_3F_3 and R_4F_4 against *P.aeruginosa* in biofilms was examined. The former displayed small activity against biofilm formation, whereas for the latter there was a significant reduction in biofilm formation at 0.05 wt% to 37%, although not complete death which was observed in the planktonic form. Since c-di-GMP is known to be an important signalling molecule involved in *pseudomonas* biofilm formation, the interactions between the two peptides and ci-d-GMP was examined. CD confirmed that there was an interaction with the peptides which stabilised the homodimer form of c-di-GMP. In the case of R_4F_4, modification of the π-stacking interactions was observed. This points to a potential mechanism for the inhibition of biofilm formation. The guanidinium group in the arginine is known to bind c-di-GMP through H-bonding and electrostatic interactions.[48,62] To further examine this, Congo red staining of polysaccharides, which were overexpressed by bacteria exposed to the antimicrobial activity of R_4F_4.

3.4 Experimental Section

3.4.1 Materials

R_3F_3 and R_4F_4 were synthesised by Peptide Synthetics (Fareham, UK). Purity was determined by HPLC, and for R_3F_3 was found to be 97.83%, the molar mass from ESI-MS was M_w = 928.089 g mol^{-1}. The purity of R_4F_4 was 97.98%, and the molar mass from ESI-MS was M_w= 1231.452 g mol^{-1}.

3.4.2 Sample Preparation

Samples of R_3F_3 and R_4F_4 were dissolved in water. The native pH was found to be 2.22 and 2.28 respectively. Adjustment of pH to pH 7.0 was done using 0.5 M NaOH.

3.4.3 Fluorescence assays

The critical aggregation concentrations (*cac*) of R_3F_3 and R_4F_4 were determined using fluorescence spectroscopy. Fluorescence spectra were recorded with a Varian Cary Eclipse fluorescence spectrometer with samples in 4 mm inner width quartz cuvettes. ANS (8-anilinonaphthalene-1-sulfonic acid) was used to probe the aggregation as a probe that is sensitive to hydrophobic environments making it suitable to locate the *cac*.[44,63–66] ANS assays were performed using a 66.8 µM ANS solution to solubilise R_3F_3 and R_4F_4. Fluorescence spectra were recorded between 400-650 nm (λ_{ex} = 356nm). Additionally, ThT was used to determine the *cac* of R_3F_3, as it is sensitive to the formation of amyloid fibrils at the *cac*.[33,34,65,67,68] ThT assays were performed using 5.0 x 10^{-3} wt% solution to solubilise the peptide. Spectra were recorded between 460-600 nm (λ_{ex} = 440 nm).

3.4.4 Circular Dichroism (CD)

CD spectra were recorded using a Chirascan spectropolarimeter (Applied Photophysics, UK) in the wavelength range 180 – 260 nm. Samples 1 wt% of R_3F_3 and R_4F_4 in pure H_2O at native pH and pH 7 were pipetted into a quartz plate cell with 0.1 mm path length. Data with absorbance less than 2 only are reported. Measurements were recorded with a 0.5 nm bandwidth, 1 mm step and 1 second collection time per point. The CD signal for the background solution was subtracted from the CD signal of the sample, and molar ellipticity was calculated.

3.4.5 Fourier Transform Infrared Spectroscopy (FTIR)

Spectra were recorded using a Thermo Scientific Nicolet iS5 equipped with a DTGS detector, with a Specac Pearl liquid cell (sample contained between fixed CaF_2 plates).

Aliquots 80 µl of 1 wt% R_3F_3 and R_4F_4 at native and pH 12 dissolved in D_2O were prepared and added into the liquid cell. Spectra were scanned 128 times over the range 900 − 4000 cm^{-1}

3.4.6 Transmission Electron Microscopy (TEM)

TEM imaging was performed using a JEOL 2100 Plus TEM microscope operated at 200 kV. Droplets of sample were placed on Cu grids coated with a carbon film (Agar Scientific, UK), stained with uranyl acetate (0.5 wt %) (Sigma-Aldrich, UK) and dried. Specimens were then loaded into the microscope.

3.4.7 Cryo-TEM

Cryo-TEM was kindly done by Jani Seitsonen, Aalto University, Finland. Vitrified specimens were prepared using an automated FEI Vitrobot device using Quantifoil 3.5/1 holey carbon copper grids with a hole size of 3.5 µm. Prior to use, grids were plasma cleaned using a Gatan Solarus 9500 plasma cleaner and then transferred into the environmental chamber of a FEI Vitrobot at room temperature and 100% humidity. Thereafter sample solution was applied onto the grid, and it was blotted twice for 5 s and then vitrified in a 1/1 mixture of liquid ethane and propane at a temperature of −180 °C. The grids with vitrified sample solution were maintained at liquid nitrogen temperature and then cryo-transferred to the microscope. Imaging was carried out using a field emission cryo-electron microscope (JEOL JEM-3200FSC) operating at 200 kV. Images were taken in bright field mode and using zero loss energy filtering (Ω type) with a slit width of 20 eV. Micrographs were recorded using a Gatan Ultrascan 4000 CCD camera. Specimen temperature was maintained at −187 °C during the imaging.

3.4.8 Liposome preparation

Liposomes were prepared using the thin-layer hydration method. Weighed quantities of DPPG and DPPE were prepared by dissolution in chloroform, and thin lipid films were prepared by drying the lipids under a stream of nitrogen gas. Films were then placed under vacuum for 2 hours to remove any remaining organic solvent. After this, lipids were resuspended in water to a final concentration of 0.5 wt% lipid, heated above their T_m and vortexed for 5 minutes. Liposome mixtures were then left to equilibrate before experiments. DPPG/DPPE vesicles were prepared using this method at different molar ratios of 1:3, 1:1, 3:1 and 1:0 DPPG:DPPE. To obtain peptide/ lipid mixtures, resuspended lipids were added to peptide powders to make up a 0.08 wt% concentration of peptide, heated above the T_m and vortexed for 5 minutes, then left to equilibrate. Dynamic light scattering (DLS) was measured to check the size of the liposomes using a Zetasizer instrument (data not shown).

3.4.9 Small-angle X-ray scattering

Solution small-angle X-ray scattering (SAXS) data was collected on the bioSAXS beamline B21, at Diamond Light Source, Harwell, United Kingdom and beamline ID02 of the European Synchrotron Radiation Facility (ESRF), Grenoble France. On beamline B21, samples of 1 wt% R_3F_3 and 1 wt% R_4F_4 were loaded into PCR tubes in an automated sample changer. The samples were then delivered into a temperature-controlled quartz capillary and exposed for 1s, acquiring 30 frames at 20 ^oC. Data was collected using a Pilatus Dectris 2M detector with a 3.9 m sample-detector distance and X-ray wavelength $\lambda = 1.0$ Å. Background was manually subtracted using ScÅtter. Form factor modelling was done using SASfit.

At ID02, samples were loaded into a glass capillary (internal radius = 2 mm) using a syringe. The beamline operated with an X-ray wavelength $\lambda = 1.0$ Å. 2D data was collected using a Rayonix MX170 detector, with a 1.474 m sample-detector distance.

3.4.10 Differential Scanning Calorimetry

Differential scanning calorimetry measurements were carried out using a nanoDSC, DSC TA-Q200 instrument. Aliquots 600 µL of lipid mixtures at 0.5 wt% with and without 0.08 wt% peptide were degassed for 10 minutes before being 600 µL pipetted into the DSC. Data were acquired from 20 ^oC to 60 ^oC. The scan rate was 1 ^oC per minute at a pressure of 3 bar. Solvent background, Enthalpy (ΔH) and specific heat capacity was calculated in NanoAnalyze.

3.4.11 Cell Viability assays

The cytotoxicity of both R_3F_3 and R_4F_4 was examined. In vitro cell culture was conducted using 161Br (European Collection of Authenticated Cell Cultures, ECACC) cells, a human skin fibroblast cell line. Cells were cultured in EMEM (Eagle's minimum essential medium), with 2 mM glutamine, enriched with 15% fetal bovine serum (FBS) and 1% non-essential amino acids (NEAA). Cells were maintained in a humidified atmosphere of 37 ^{o}C, 5% CO_2.

Potential cytotoxicity effects were examined using the MTT (3-(4,5-dimethylthiazol-2-yl)-2,5-diphenyltetrazolium bromide) assay. The peptides were dissolved in complete media. Cells were seeded into a 96-well plate at $4x10^4$ cells/mL and allowed to adhere for 24 hours in 100 µL complete medium. After this, 100 µL of either complete media and/or peptide solution was added, to give either control solution, or solutions of peptide between the concentrations of

0.0625 mg/mL to 4 mg/mL.

Cells were incubated for 67 hours. After this, 20 µL MTT (5 mg/ mL, in PBS) was added to each well plate and allowed to incubate for 5 hours. After a further 5 hours (72 hours total) the solution was removed from the wells and replaced with 100 µL DMSO per well, which dissolves the formazan crystals. Plates were incubated for 30 minutes, and then analysed using a UV microplate reader (λ=570 nm). Results are reported as a percentage cell viability compared to control (untreated) values, and fitted to a sigmoidal function using Origin Lab as a guide to the eye.

3.4.12 Antimicrobial Studies

The antimicrobial assays were performed with three types of bacteria which cause disease in humans, two being Gram-negative *Escherichia coli* (K12),[69] and *Pseudomonas aeruginosa (PA01)* ,[70] and one being Gram-positive *Staphylococcus aureus* (8325-4).[71] Plant bacterial strains *P.syringae, P.putida*, *P.agarici* and *P.fluorescens* were also used to examine specificity against *pseudomonas*. Stock cultures were stored in -80 ^{o}C in 7% (v/v) DMSO. Prior to experiments, samples of all human bacteria were streaked out onto LB (Lysogeny Broth) agar and grown overnight at 37^{o}C, whereas the plant bacteria were grown overnight at 27^{o}C

3.4.12.1 Bacterial survival assays

In order to examine whether the peptides were bacteriocidal, one colony from streaked plates was transferred into 7 mL sterile lysogeny broth (LB), and grown overnight at 37 ^{o}C under agitation at 150 rev / min, on an orbital shaker, and these cultures were used for ongoing experiments. Cultures were then transferred into a 15 ml Falcon tube and cells were harvested by centrifugation at 9000 rpm at 4 ^{o}C for 10 minutes. The supernatant was discarded and the pellet was resuspended in 1.5 mL ice-chilled PBS (phosphate buffered saline).

After this, 30 µL of this solution was transferred into 300 µL of 0.5 mg/mL (or 0.05 wt%) of R3F3 or R4F4, in sterile water, or control solutions of 300 µL of sterile water. Solutions were then vortexed for 5 seconds and 3 x 20µL were taken at times 0, 120 and 1440 minutes. These samples were then serially diluted in PBS, and 10 µL of each dilution was platted onto LB agar and incubated at 37 ^{o}C overnight before colony counting.

3.4.13.2 Biofilm assays

To form a biofilm, *Pseudomonas aeruginosa* PA01 and ATCC2363 strains were grown overnight in LB media. Following this, the culture was diluted 1:100 in M63 minimal medium supplemented with arginine and magnesium sulphate, with and without R_3F_3 or R_4F_4, with four technical replicates. After this the plate was incubated for 4-24 hrs.

Following incubation, the supernatant was discarded and then gently washed in water several times to decrease background staining. After this, 125 µL of 0.1 wt% Crystal violet solution was added to each well of the microtiter plate and incubated for 10 minutes. Following this, the plate was washed several times and left to dry overnight.

After this, 125 µL of 30% acetic acid in water was added, to solubilise the biofilm, and the plate was incubated for further 10 minutes to allow solubilisation. Absorbance was measured using a plate reader at 550 nm. Anova and Tukey were used to assess statistical significance.

3.4.14.3 Indirect measurements of c-di-GMP using Congo Red

Pseudomonas aeruginosa PA01 was grown overnight in LB media. After this, the culture was diluted 1:100 in 1 ml of M63 minimal medium supplemented with 0.4 % L-arginine and 1 mM magnesium sulphate, with 40 µg/mL Congo red with and without R_4F_4. Control solutions were also prepared using the described medium above with no bacterial cells present. Congo red provides an indirect measure of c-di-GMP levels as it binds to the matrix of the biofilm, production of which is correlated to c-di-GMP levels.[59] Samples were shaken at 200 RPM overnight in a shaking incubator. After this, 200 uL of supernatant was added in triplicate to a 96 well place, and measured using a plate reader at 490 nm. Results are reported as (Control solution OD– Bacteria containing solution OD). t-tests were used to assess significance.

3.5 References

(1) Falla, T. J.; Nedra Karunaratne, D.; Hancock, R. E. W. Mode of Action of the Antimicrobial Peptide Indolicidin. *J. Biol. Chem.* **1996**, *271* (31), 19298–203.

(2) Chan, D. I.; Prenner, E. J.; Vogel, H. J. Tryptophan- and Arginine-Rich Antimicrobial Peptides: Structures and Mechanisms of Action. *Biochim. Biophys. Acta - Biomembr.* **2006**, *1758* (9), 1184–1202.

(3) Brogden, K. A. Antimicrobial Peptides: Pore Formers or Metabolic Inhibitors in Bacteria? *Nat. Rev. Microbiol.* **2005**, *3* (3), 238–250.

(4) Miteva, M.; Andersson, M.; Karshikoff, A.; Otting, G. Molecular Electroporation: A Unifying Concept for the Description of Membrane Pore Formation by Antibacterial Peptides, Exemplified with NK-Lysin. *FEBS Lett.* **1999**, *462* (1–2), 155–158.

(5) Tieleman, D. P. The Molecular Basis of Electroporation. *BMC Biochem.* **2004**, *5* (10), 1–12.

(6) Pokorny, A.; Almeida, P. F. F. Permeabilization of Raft-Containing Lipid Vesicles by δ-Lysin: A Mechanism for Cell Sensitivity to Cytotoxic Peptides. *Biochemistry* **2005**, *44* (27), 9538–9544.

(7) Betts, M. J.; Russell, R. B. Amino-Acid Properties and Consequences of Substitutions. In *Bioinformatics for Geneticists: A Bioinformatics Primer for the Analysis of Genetic Data: Second Edition*; 2007; pp 291–316.

(8) Hamley, I. W. Small Bioactive Peptides for Biomaterials Design and Therapeutics. *Chem. Rev.* **2017**, *117* (24), 14015–14041.

(9) Schmidt, N.; Mishra, A.; Lai, G. H.; Wong, G. C. L. Arginine-Rich Cell-Penetrating Peptides. *FEBS Lett.* **2010**, *584* (9), 1806–1813.

(10) Hauser, C. A. E.; Zhang, S. Designer Self-Assembling Peptide Nanofiber Biological Materials. *Chem. Soc. Rev.* **2010**, *39* (8), 2780–2790.

(11) Santoso, S. S.; Vauthey, S.; Zhang, S. Structures, Function and Application of Amphiphilic Peptides. *Curr. Opin. Colloid Interface Sci.* **2002**, *7* (5–6), 262–266.

(12) Hamley, I. W. Self-Assembly of Amphiphilic Peptides. *Soft Matter* **2011**, *7*, 4122–4138.

(13) Dehsorkhi, A.; Castelletto, V.; Hamley, I. W. Self-Assembling Amphiphilic Peptides. *J. Pept. Sci.* **2014**, *20* (7), 453–467.

(14) Castelletto, V.; Nutt, D. R.; Hamley, I. W.; Bucak, S.; Cenker, C.; Olsson, U. Structure of Single-Wall Peptide Nanotubes: In Situ Flow Aligning X-Ray Diffraction. *Chem Commun* **2010**, *46* (34), 6270–6272.

(15) Middleton, D. A.; Madine, J.; Castelletto, V.; Hamley, I. W. Insights into the Molecular Architecture of a Peptide Nanotube Using FTIR and Solid-State NMR Spectroscopic Measurements on an Aligned Sample. *Angew. Chemie* **2013**, *52* (40), 10537–10540.

(16) Castelletto, V.; Hamley, I. W.; Segarra-Maset, M. D.; Berdugo Gumbau, C.; Miravet, J. F.; Escuder, B.; Seitsonen, J.; Ruokolainen, J. Tuning Chelation by the Surfactant-like Peptide A6H Using Predetermined PH Values. *Biomacromolecules* **2014**, *15* (2), 591–598.

(17) Hamley, I. W.; Dehsorkhi, A.; Castelletto, V. Self-Assembled Arginine-Coated Peptide Nanosheets in Water. *Chem. Commun.* **2013**, *49* (18), 1850–1852.

(18) Hamley, I. W.; Hutchinson, J.; Kirkham, S.; Castelletto, V.; Kaur, A.; Reza, M.; Ruokolainen, J. Nanosheet Formation by an Anionic Surfactant-like Peptide and

Modulation of Self-Assembly through Ionic Complexation. *Langmuir* **2016**, *32* (40), 10387–10393.

(19) Castelletto, V.; Gouveia, R. M.; Connon, C. J.; Hamley, I. W.; Seitsonen, J.; Nykänen, A.; Ruokolainen, J. Alanine-Rich Amphiphilic Peptide Containing the RGD Cell Adhesion Motif: A Coating Material for Human Fibroblast Attachment and Culture. *Biomater. Sci.* **2014**, *2* (3), 362–369.

(20) Chen, C.; Pan, F.; Zhang, S.; Hu, J.; Cao, M.; Wang, J.; Xu, H.; Zhao, X.; Lu, J. R. Antibacterial Activities of Short Designer Peptides: A Link between Propensity for Nanostructuring and Capacity for Membrane Destabilization. *Biomacromolecules* **2010**, *11* (2), 402–411.

(21) Decandio, C. C.; Silva, E. R.; Hamley, I. W.; Castelletto, V.; Liberato, M. S.; Oliveira, V. X.; Oliveira, C. L. P.; Alves, W. A. Self-Assembly of a Designed Alternating Arginine/Phenylalanine Oligopeptide. *Langmuir* **2015**, *31* (15), 4513–4523.

(22) Silva, E. R.; Listik, E.; Han, S. W.; Alves, W. A.; Soares, B. M.; Reza, M.; Ruokolainen, J.; Hamley, I. W. Sequence Length Dependence in Arginine/Phenylalanine Oligopeptides: Implications for Self-Assembly and Cytotoxicity. *Biophys. Chem.* **2018**, *233*, 1–12.

(23) Slyngborg, M.; Nielsen, D. A.; Fojan, P. The Physical Properties and Self-Assembly Potential of the RFFFR Peptide. *ChemBioChem* **2016**, *17* (21), 2083–2092.

(24) Holowka, E. P.; Sun, V. Z.; Kamei, D. T.; Deming, T. J. Polyarginine Segments in Block Copolypeptides Drive Both Vesicular Assembly and Intracellular Delivery. *Nat. Mater.* **2007**, *6* (1), 52–57.

(25) Sun, V. Z.; Li, Z.; Deming, T. J.; Kamei, D. T. Intracellular Fates of Cell-Penetrating Block Copolypeptide Vesicles. *Biomacromolecules* **2011**, *12* (1), 10–13.

(26) Castelletto, V.; Barnes, R. H.; Karatzas, K. A.; Edwards-Gayle, C. J. C.; Greco, F.; Hamley, I. W.; Rambo, R.; Seitsonen, J.; Ruokolainen, J. Arginine-Containing Surfactant-Like Peptides: Interaction with Lipid Membranes and Antimicrobial Activity. *Biomacromolecules* **2018**, *19* (7), 2782–2794.

(27) Castelletto, V.; Barnes, R.; Karatzas, K.-A.; Edwards-Gayle, C. J. C.; Greco, F.; Hamley, I. W.; Seitsonen, J.; Ruokolainen, J. Restructuring of Lipid Membranes by an Arginine-Capped Peptide Bolaamphiphile. *Langmuir* **2018**, *35* (5), 1302–1311.

(28) Malanovic, N.; Leber, R.; Schmuck, M.; Kriechbaum, M.; Cordfunke, R. A.; Drijfhout, J. W.; Breij, A. De; Nibbering, P. H.; Kolb, D.; Lohner, K. Phospholipid-Driven Differences Determine the Action of the Synthetic Antimicrobial Peptide OP-145 on Gram-Positive Bacterial and Mammalian Membrane Model Systems. *Biochim. Biophys. Acta - Biomembr.* **2015**, *1848* (10), 2437–2447.

(29) Arouri, A.; Dathe, M.; Blume, A. Peptide Induced Demixing in PG / PE Lipid Mixtures : A Mechanism for the Speci Fi City of Antimicrobial Peptides towards Bacterial Membranes ? *Biochim. Biophys. Acta - Mol. Basis Dis.* **2009**, *1788* (3), 650–659.

(30) Grau-Campistany, A.; Manresa, Á.; Pujol, M.; Rabanal, F.; Cajal, Y. Tryptophan-Containing Lipopeptide Antibiotics Derived from Polymyxin B with Activity against Gram Positive and Gram Negative Bacteria. *Biochim. Biophys. Acta - Biomembr.* **2016**, *1858* (2), 333–343.

(31) Epand, R. M.; Rotem, S.; Mor, A.; Berno, B.; Epand, R. F. Bacterial Membranes as Predictors of Antimicrobial Potency. *J. Am. Chem. Soc.* **2008**, *130* (43), 14346–14352.

(32) Li, J.; Wang, X.; Zhang, T.; Wang, C.; Huang, Z.; Luo, X.; Deng, Y. A Review on Phospholipids and Their Main Applications in Drug Delivery Systems. *Asian J. Pharm. Sci.*

2014, *10* (2), 81–89.

(33) LeVine, H. Quantification of β-Sheet Amyloid Fibril Structures with Thioflavin T. *Methods Enzymol.* **1999**, *309*, 274–284.

(34) Levine, H. Thioflavine T Interaction with Synthetic Alzheimer’s Disease B-amyloid Peptides: Detection of Amyloid Aggregation in Solution. *Protein Sci.* **1993**, *2* (3), 404–410.

(35) Barth, A.; Haris, P. I. Biological and Biomedical Infrared Spectroscopy; IOS Press, 2009; Vol. 2.

(36) Krysmann, M. J.; Castelletto, V.; Hamley, I. W. Fibrillisation of Hydrophobically Modified Amyloid Peptide Fragments in an Organic Solvent. *Soft Matter* **2007**, *3* (11), 1401–1406.

(37) Pelton, J. T.; Mclean, L. R. Spectroscopic Methods for Analysis of Protein Secondary Structure. *Anal. Biochem.* **2000**, *227* (2), 167–176.

(38) Lavoie, M. C.; Subirade, M. Replacement of Trifluoroacetic Acid with HCl in the Hydrophobic Purification Steps of Pediocin PA-1 : A Structural Effect. *Appl. Environ. Microbiol.* **2002**, *68* (10), 4803–4808.

(39) Barth, A.; Zscherp, C. What Vibrations Tell Us about Proteins. *Q. Rev. Biophys.* **2002**, *35* (4), 369–430.

(40) Barth, A. Infrared Spectroscopy of Proteins. *Biochim. Biophys. Acta* **2007**, *1767* (9), 1073–1101.

(41) Ghosh, A.; Tucker, M. J.; Hochstrasser, R. M. Identification of Arginine Residues in Peptides by 2D-IR Echo Spectroscopy. *J. Phys. Chem. A* **2011**, *115* (34), 9731–9738.

(42) Hamley, I. W.; Dehsorkhi, A.; Castelletto, V.; Seitsonen, J.; Ruokolainen, J.; Iatrou, H. Self-Assembly of a Model Amphiphilic Oligopeptide Incorporating an Arginine Headgroup. *Soft Matter* **2013**, *9*, 4794–4801.

(43) Barth, A. The Infrared Absorption of Amino Acid Side Chains. *Prog. Biophys. Mol. Biol.* **2001**, *74* (2000), 141–173.

(44) Castelletto, V.; Gouveia, R. M.; Connon, C. J.; Hamley, I. W. New RGD-Peptide Amphiphile Mixtures Containing a Negatively Charged Diluent. *Faraday Discuss.* **2013**, *166*, 381–397.

(45) Castelletto, V.; Hamley, I. W. Methods to Characterize the Nanostructure and Molecular Organization of Amphiphilic Peptide Assemblies. In *Peptide Self-Assembly: Methods and Protocols*; Nilsson, B. L., Doran, T. M., Eds.; Springer New York: New York, NY, 2018; pp 3–21.

(46) Breßler, I.; Kohlbrecher, J.; Thünemann, A. F. *SASfit* : A Tool for Small-Angle Scattering Data Analysis Using a Library of Analytical Expressions. *J. Appl. Crystallogr.* **2015**, *48* (5), 1587–1598.

(47) Pabst, G.; Rappolt, M.; Amenitsch, H.; Laggner, P. Structural Information from Multilamellar Liposomes at Full Hydration : Full q-Range Fitting with High Quality X-Ray Data. *Phys. Rev. E - Stat. Nonlinear, Soft Matter Phys.* **1999**, *62* (3), 4000–4009.

(48) Foletti, C.; Kramer, R. A.; Mauser, H.; Jenal, U.; Bleicher, K. H.; Wennemers, H. Functionalized Proline-Rich Peptides Bind the Bacterial Second Messenger c-Di-GMP. *Angew. Chemie - Int. Ed.* **2018**, *57* (26), 7729–7733.

(49) Dehsorkhi, A.; Castelletto, V.; Hamley, I. W.; Seitsonen, J.; Ruokolainen, J. Interaction between a Cationic Surfactant-like Peptide and Lipid Vesicles and Its Relationship to Antimicrobial Activity. *Langmuir* **2013**, *29* (46), 14246–14253.

(50) Edwards-Gayle, C. J. C.; Castelletto, V.; Hamley, I. W.; Barrett, G.; Greco, F.; Hermida-Merino, D.; Rambo, R. P.; Seitsonen, J.; Ruokolainen, J. Self-Assembly, Antimicrobial Activity, and Membrane Interactions of Arginine-Capped Peptide Bola-Amphiphiles. *ACS Appl. Bio Mater.* **2019**, *2* (5), 2208–2218.

(51) Hamley, I. W. Introduction to Soft Matter: Synthetic and Biological Self-Assembling Materials, Revised Edition; 2007.

(52) Nielsen, J. E.; Bjørnestad, V. A.; Lund, R. Resolving the Structural Interactions between Antimicrobial Peptides and Lipid Membranes Using Small-Angle Scattering Methods: The Case of Indolicidin. *Soft Matter* **2018**, *14* (43), 8750–8763.

(53) Kulasekara, B. R.; Christen, M.; Miller, S. I.; Kulasekara, H. D.; Christen, B.; Hoffman, L. R. Asymmetrical Distribution of the Second Messenger C-Di-GMP upon Bacterial Cell Division. *Science (80-.).* **2010**, *328* (5983), 1295–1297.

(54) Ha, D.-G.; O'Toole, G. A. C-Di-GMP and Its Effects on Biofilm Formation and Dispersion: A Pseudomonas Aeruginosa Review. *Microbiol. Spectr.* **2015**, *3* (2), 1–12.

(55) Jenal, U.; Reinders, A.; Lori, C. Cyclic Di-GMP: Second Messenger Extraordinaire. *Nat. Rev. Microbiol.* **2017**, *15* (5), 271–284.

(56) Hengge, R. Principles of C-Di-GMP Signalling in Bacteria. *Nat. Rev. Microbiol.* **2009**, *7* (4), 263–273.

(57) Christensen, G. D.; Simpson, W. A.; Bisno, A. L.; Beachey, E. H.; Younger, J. J.; Baddour, L. M.; Barrett, F. F.; Melton, D. M. Adherence of Slime-Producing Strains of Staphylococcus Epidermidis to Smooth Surfaces\rAdherence of Coagulase-Negative Staphylococci to Plastic Tissue Culture Plates: A Quantitative Model for the Adherence of Staphylococci to Medical Devices. *Infect Immun* **1982**, *37* (1), 318–326.

(58) Peeters, E.; Nelis, H. J.; Coenye, T. Comparison of Multiple Methods for Quantification of Microbial Biofilms Grown in Microtiter Plates. *J. Microbiol. Methods* **2008**, *72* (2), 157–165.

(59) Jones, C. J.; Wozniak, D. J. Congo Red Stain Identifies Matrix Overproduction and Is an Indirect Measurement for C-Di-GMP in Many Species of Bacteria. In: Sauer K. (Eds) c-Di-GMP Signaling. Methods in Molecular Biology; Sauer, K., Ed.; Human Press, 2017.

(60) O'Toole, G. A. Microtiter Dish Biofilm Formation Assay. *J. Vis. Exp.* **2011**, No. 47, 10–11.

(61) Kim, E.-J.; Sabra, W.; Zeng, A.-P. Physiological Responses of Pseudomonas Aeruginosa PAO1 to Oxidative Stress in Controlled Microaerobic and Aerobic Cultures. *Microbiology* **2015**, *148* (10), 3195–3202.

(62) Habazettl, J.; Allan, M. G.; Jenal, U.; Grzesiek, S. Solution Structure of the PilZ Domain Protein PA4608 Complex with Cyclic Di-GMP Identifies Charge Clustering as Molecular Readout. *J. Biol. Chem.* **2011**, *286* (16), 14304–14314.

(63) Gasymov, O. K.; Glasgow, B. J. ANS Fluorescence: Potential to Augment the Identification of the External Binding Sites of Proteins. *Biochim. Biophys. Acta - Proteins Proteomics* **2007**, *1774* (3), 403–411.

(64) Hawe, A.; Sutter, M.; Jiskoot, W. Extrinsic Fluorescent Dyes as Tools for Protein Characterization. *Pharm. Res.* **2008**, *25* (7), 1487–1499.

(65) Lindgren, M.; Sörgjerd, K.; Hammarström, P. Detection and Characterization of Aggregates, Prefibrillar Amyloidogenic Oligomers, and Protofibrils Using Fluorescence Spectroscopy. *Biophys. J.* **2005**, *88* (6), 4200–4212.

(66) Castelletto, V.; Kirkham, S.; Hamley, I. W.; Kowalczyk, R.; Rabe, M.; Reza, M.;

Ruokolainen, J. Self-Assembly of the Toll-Like Receptor Agonist Macrophage-Activating Lipopeptide MALP-2 and of Its Constituent Peptide. *Biomacromolecules* **2016**, *17* (2), 631–640.

(67) Khurana, R.; Coleman, C.; Ionescu-Zanetti, C.; Carter, S. A.; Krishna, V.; Grover, R. K.; Roy, R.; Singh, S. Mechanism of Thioflavin T Binding to Amyloid Fibrils. *J. Struct. Biol.* **2005**, *151* (3), 229–238.

(68) Krebs, M. R. H.; Bromley, E. H. C.; Donald, A. M. The Binding of Thioflavin-T to Amyloid Fibrils: Localisation and Implications. *J. Struct. Biol.* **2005**, *149* (1), 30–37.

(69) Blattner, F. R.; Plunkett, G.; Bloch, C. A.; Perna, N. T.; Burland, V.; Riley, M.; Collado-vides, J.; Glasner, J. D.; Rode, C. K.; Mayhew, G. F.; et al. The Complete Genome Sequence of Escherichia Coli K-12. *Science (80-.).* **1997**, *277* (5331), 1453–1462.

(70) Holloway, B. Y. B. W. Genetic Recombination in Pseudomonas Aeruginosa. *J. Gen. Microbiol.* **1955**, *13* (3), 572–581.

(71) Horsburgh, M. J.; Aish, J. L.; White, I. J.; Shaw, L.; Lithgow, J. K.; Foster, S. J.; England, S. ΣB Modulates Virulence Determinant Expression and Stress Resistance : Characterization of a Functional RsbU Strain Derived from Staphylococcus Aureus 8325-4. *J. Bacteriol.* **2002**, *184* (19), 5457–5467.

Chapter 4.

Self-assembly of Telechelic Tyrosine End-Capped PEO Star polymers in Aqueous Solution

This chapter has, in part, been published by the author as a research article entitled "Self-assembly of Telechelic Tyrosine End-Capped PEO Star polymers in Aqueous Solution' C. J. C. Edwards-Gayle, F. Greco, I. W. Hamley, R .P .Rambo, M. Reza, J. Ruokolainen, D. Skoulas and H. Iatrou. Biomacromolecules. 2018, 19, 167-177"

4.1 Introduction

An established method for developing novel peptide-based biomaterials is to conjugate them to other molecules. Conjugation of peptides with other materials can enhance amphiphilicity, biocompatibility and functionality by increasing stability and half-life. Peptide conjugation to polymers is particular interest, especially with polymers that can be synthesised inexpensively, and this can lead to biomaterials with a diverse range of applications.[1–8] This can change the behaviour of the polymers, which is influenced by the size and nature of the incorporated peptide, and the positioning of attachment. Therefore, it is possible to generate a large range of novel materials, which include peptide-functionalized polymer hydrogels,[9–14] which have important applications including but not limited to, slow release drug delivery systems[15–20] and supports and matrices for cells with applications in tissue engineering.[21–32]

Capping polymers that are hydrophilic with hydrophobic end groups creates telechelic polymers. Telechelic polymers exhibit useful rheological behaviours due to their noncovalent end group associations, which is exploited in associative polymers, [33,34] which are used as thickeners. Additionally, this is exploited in polyethylene glycol (PEG)-based polymers. Examples are Pluronics, which are polymeric surfactants, with the ability to form hydrogels at high concentrations in aqueous solution. Pluronics have a linear triblock polymer architecture. Tetronics are analogous to pluronics but with a four-arm architecture. [35] PEG or PEO-(poly ethylene oxide) based polymers have been previously reported to have low toxicity and high biocompatibility. They have been proposed act as inert spacers within peptide sequences to improve stability and circulation time of actives, for applications such as cell signalling, [36] drug delivery[20] and gene delivery. [37]

There have been few studies on the self-assembling properties of telechelic peptide-polymer conjugates. Heise and co-workers reported that PEG-oligotyrosine diblock copolymers examining a range of different molecular weights of PEG conjugated to varying length of oligotyrosine repeating units. [38] They observed an optimum composition of PEG2000-Tyr6 (where Tyr6 denotes 6 tyrosine residues) which was found to undergo thermo-responsive gelation at 0.25 – 0.3 wt % between 25 °C and 50 °C. These conjugates form β-sheet fibrils, which had better packing upon increased temperature, confirmed by circular dichroism. Moreover, this hydrogel was found to be cytocompatibile and biodegradable.

Hamley and co-workers reported on the gel-sol transition of PEO conjugates with hydrophobic dipeptides, including dityrosine and diphenylalanine.[11] These conjugates were synthesised by coupling dipeptides to bis-aminopropyl PEO with a molar mass of 1500 g mol^{-1}. The Fmoc protecting group, which was used in synthesis, was retained in some of the prepared conjugates, at either one or both termini. This influenced the hydrophile-lipophile balance, resulting in a significant impact on self-assembling behaviour. One conjugate with a di-tyrosine cap and a C-terminal Fmoc protecting group was found to undergo a gel-sol transition period near body temperature, driven by loss of β-sheet structure associated with extended fibril formation.[11] The self-assembly of three conjugates, Tyr5-PEO2K-Tyr5, Tyr5-PEO6K-Tyr5 and Tyr3-PAla-Tyr3 [PAla = poly(L-alanine), PEO2K and PEO6K are PEO with M_w = 2000 g mol^{-1} and 6000 mg mol^{-1} respectively], was examined.[39] These polymers were synthesised by living NCA (N-carboxy anhydride) polymerization techniques which allows control of polymer chain length. Tyr5-PEO2K-Tyr5 and Tyr3-PAla-Tyr3 were shown to have poor solubility in water until adjusted to pH 12, whereas Tyr5-PEO6K-Tyr5 showed good solubility. All three polymer conjugates were shown to assemble into β-sheet fibrillar structures probed by cryo-TEM. Interestingly, hydrogel formation was not observed for any samples up to 20 wt%.[39]

The Lendlein group also worked with similar telechelic conjugates of DAT (desaminotyrosine) or DATT (desaminotyrosyl-tyrosine), with a linear PEG (3000 g mol^{-1}) midblock and also four arm-PEG conjugates, which were shown to self-assemble at high concentration.[40] The same group investigated star-shaped and linear oligo-ethylene glycol/ DATT conjugates.[40] Moreover, the structure, self-assembled conformation and rheological properties of gelatine (which has collagen-based helical structure) functionalised with either DAT or DATT at lysine residues was examined[41,42]. Fibrillar hydrogels have also been reported for PAla-PGlu-PAla, [PGlu: poly(L-glutamic acid)] in aqueous buffer.[43]

This chapter examines the self-assembly in aqueous solution of telechelic PEO star-shaped polymers capped with short tyrosine sequences synthesised by Dimitrios Skoulas and Hermis

Iatrou.[44] The creation of tyrosine-functionalised conjugates is of interest in the development of biomaterials. The central core PEO star molecular mass is either 10 kg mol^{-1} or 20 kg mol^{-1}. Tyrosine is considered to be hydrophobic according to the majority of hydrophobicity scales[45,46] (excluding the Kyte-Doolittle scale[47]), and is capable of undergoing π-π stacking (aromatic) interactions. Tyrosine is involved in biological interactions including cell signalling, where it is responsive to a large number of tyrosine kinase and phosphatase enzymes, which have the ability to phosphorylate or dephosphorylate tyrosine residues. These interactions are vital for a large number of signalling cascades, and are of clinical interest because dysregulation is highly linked to a number of cancers.[48,49] Therefore, this material could be of interest for development of enzyme responsive materials. The self-assembly is examined using a number of spectroscopic techniques including fluorescence, FTIR, CD, SAXS, Cryo-TEM and finally cell viability assays to assess cytocompatibility.

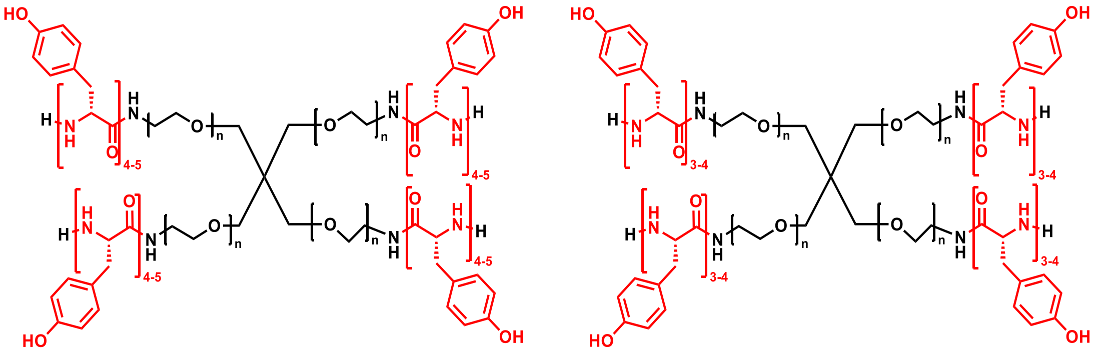

Scheme 4.1. *The peptide-polymer conjugates, on the left is [poly(L-tyrosine$_{4\text{-}5}$)-b-(PEO 2.5k)]$_4$ and on the right hand side is [poly(L-tyrosine$_{3\text{-}4}$)-b-(PEO 5k)]$_4$*

4.2 Results and Discussions

To examine whether there is a critical concentration for aggregation of the telechelic polymers, a fluorescence assay using 8-anilinonaphthalene-1-sulfonic acid (ANS) was performed. ANS is sensitive to hydrophobic environments[50–54] which gives information on copolymer aggregation. Figure 4.1 shows fluorescence intensity against concentration. The *cac* for [poly(L-tyrosine$_{4\text{-}5}$)-*b*-(PEO 2.5k)]$_4$ was found to be 0.0035 wt% and for [poly(L-tyrosine$_{3\text{-}4}$)-*b*-(PEO 5k)]$_4$ it was found to be considerably higher at 0.019 wt%. This could be explained by [poly(L-tyrosine$_{4-5}$)-*b*-(PEO 2.5k)]$_4$ having a higher ratio of hydrophobic segments to hydrophilic units compared to [poly(L-tyrosine$_{3-4}$)-*b*-(PEO 5k)]$_4$ as the PEO chain is shorter.

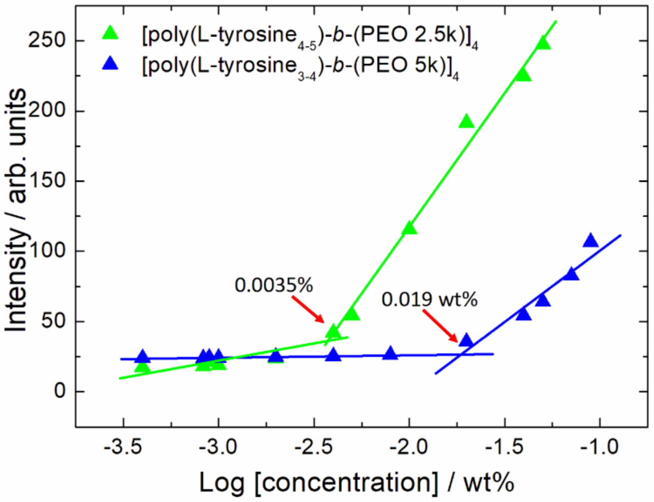

Figure 4.1. *Critical aggregation concentrations measured using ANS fluorescence measurements*

The secondary structure of the peptide end blocks was examined at a concentration above the *cac* using a combination of circular dichroism (CD), FTIR and XRD. Figure 4.2a and b shows the CD spectra for the conjugates. For [poly(L-tyrosine$_{4-5}$)-*b*-(PEO 2.5k)]$_4$, at native pH (pH 7.88), the spectra (Figure 4.2) show minima at 195 nm and 218 nm, which may be evidence of some β-sheet structure, and a maximum at 228 nm. When adjusted to pH 12 (Figure 4.2b), there is reduced molar ellipticity indicating a loss of structure, although there is similarity in shape of those measured at native pH. For [poly(L-tyrosine$_{3-4}$)-*b*-(PEO 5k)]$_4$ at native pH, the spectra have maxima at 205 nm. Both conjugates at native pH show a 228 nm peak, which is due to tyrosine absorbance.[11,39] Similar features having been observed for Tyr$_5$-PEO6k-Tyr$_5$ and Tyr$_2$-PEO1.5k-Tyr$_2$.[39] When adjusted to pH 12 (Figure 4.2b), [poly(L-tyrosine$_{3-4}$)-*b*-(PEO 5k)]$_4$ shows reduced molar ellipticity implying loss of secondary structure. The temperature dependence of the CD data was examined in the range of 10-70 ^{o}C (Figure 4.3) and there were no significant changes in molar ellipticity upon heating for either [poly(L-tyrosine$_{4-5}$)-*b*-(PEO 2.5k)]$_4$ or [poly(L-tyrosine$_{3-4}$)-*b*-(PEO 5k)]$_4$ at native and pH 12.

In order to confirm that pH adjustment does not cause irreversible change and peptide degradation, CD spectra were measured. The conjugate solutions were measured at native pH, adjusted to pH 12 using NaOH and measured, and then adjusted back to native pH using HCl and remeasured. The data is shown in Figure 4.4. The reversibility of the CD spectra shows that the peptide does not decompose at high pH but rather unfolds and refolds.

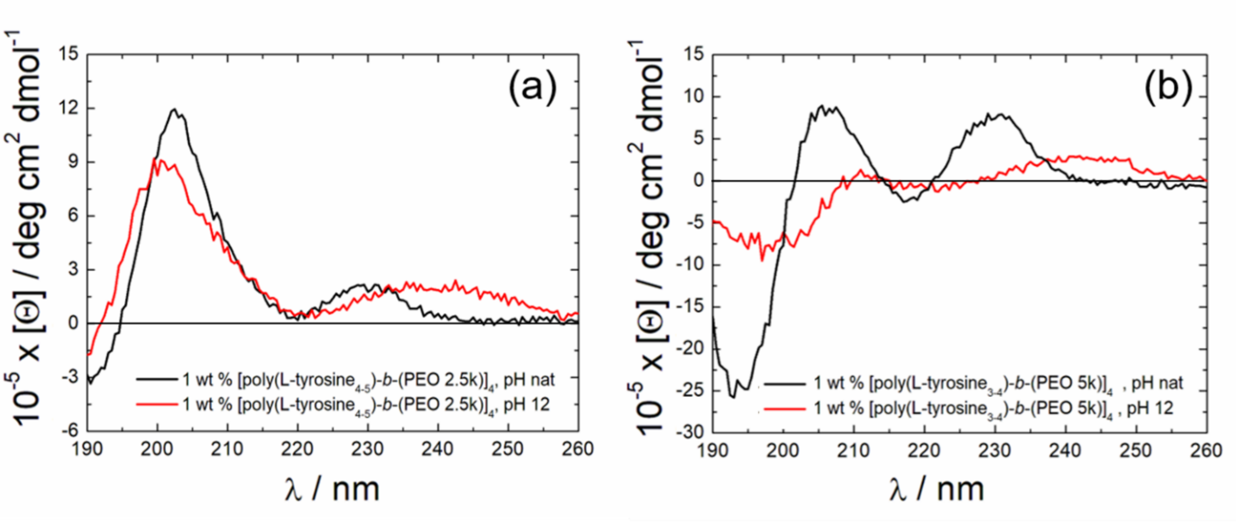

Figure 4.2. *CD spectra for both conjugates at 1 wt%*

The FTIR spectra measured for the two polymers at native pH (but not pH 12), shown in figure 4.5 shows a strong peak at 1515 cm^{-1} which is assigned to the Tyr-OH side chain residue.[55] The amide I' region provides information about C=O deformation modes, meaning secondary structure can be determined. Due to complexities in the spectra, the FTIR spectra of the precursor molecules, (PEO 2.5k)$_4$ and (PEO 5k)$_4$ star polymers were also collected. The spectra for [poly(L-tyrosine$_{4-5}$)-*b*-(PEO 2.5k)]$_4$ at native pH shows a peak at 1626 cm^{-1}, indicating the presence of β-sheet structure.[55,56] This peak is less defined for [poly(L-tyrosine$_{3-4}$)-*b*-(PEO 5k)]$_4$. There is also a small peak at 1612 cm^{-1} which can be associated with tyrosine.[57] At pH 12, [poly(L-tyrosine$_{4-5}$)-*b*-(PEO 2.5k)]$_4$ has a slight shifted peak value of 1630 cm^{-1}. The FTIR spectra measured for [poly(L-tyrosine$_{3-4}$)-*b*-(PEO 5k)]$_4$ has no defined peak across the amide I' region. At pH 12, [poly(L-tyrosine$_{3-4}$)-*b*-(PEO 5k)]$_4$ shows a small peak at 1653 cm^{-1} indicating it is disordered.[58] Both samples at native pH show a peak near 3400 cm^{-1} which is consistent with –OH stretch deformations of hydrogen bonded carbonyl groups in PEO.[59,60] All samples show peaks around 1455 cm^{-1} and 1474 cm^{-1} which are assigned to backbone –CH$_2$ deformation PEO modes.[59,60]

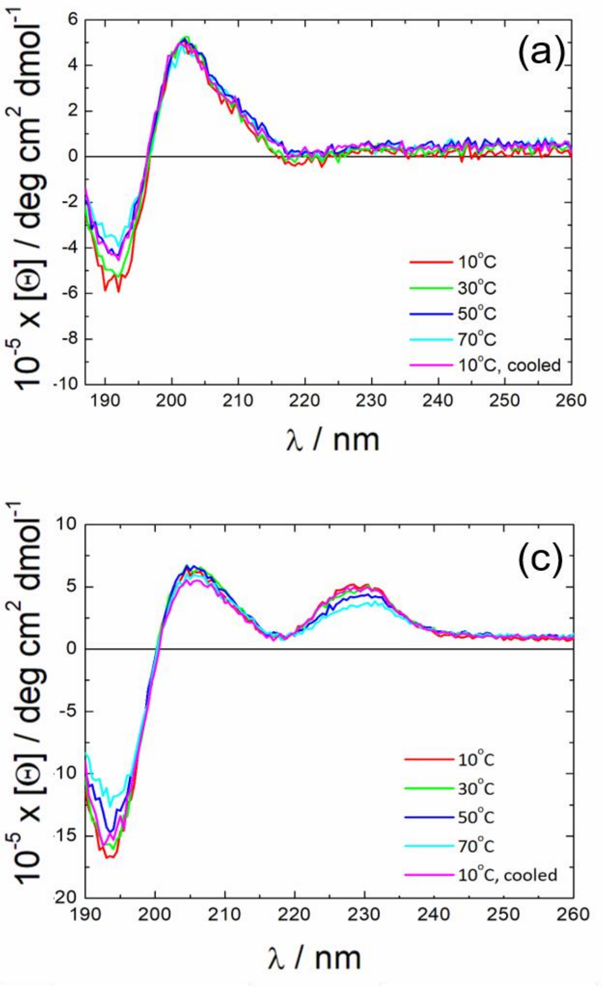

Figure 4.3. *Temperature-dependent CD spectra. a) 0.025% [poly(L-tyrosine$_{4\text{-}5}$)-b-(PEO 2.5k)]$_4$, native pH 7.8, b) 0.025% [poly(L-tyrosine$_{4\text{-}5}$)-b-(PEO 2.5k)]$_4$, pH 12, c) 0.025% [poly(L-tyrosine$_{3\text{-}4}$)-b-(PEO 5k)]$_4$, native pH 6.9, d) 0.025% [poly(L-tyrosine$_{3\text{-}4}$)-b-(PEO 5k)]$_4$. 1 mm pathlength.*

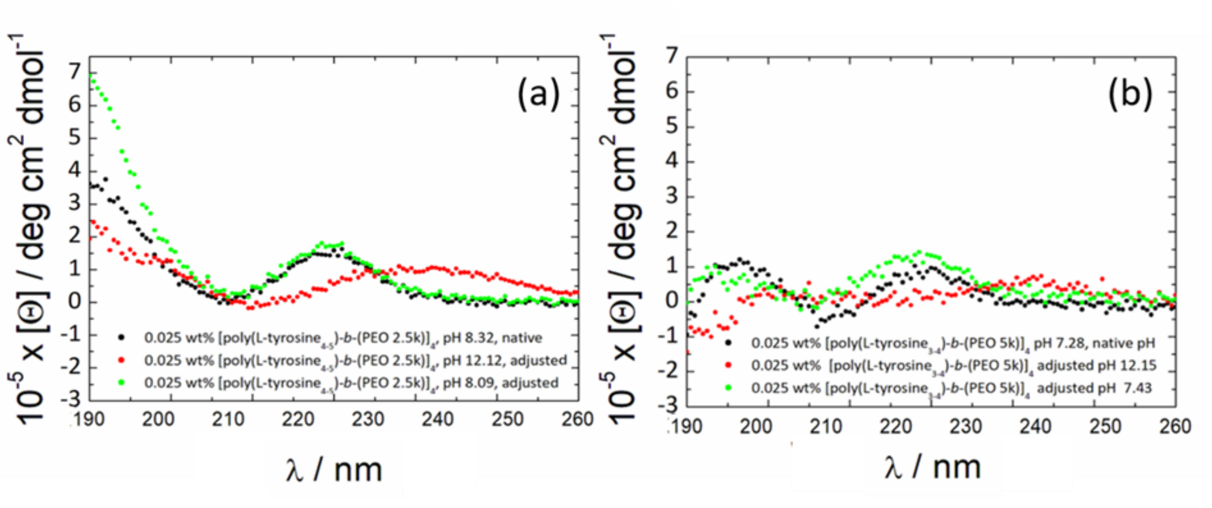

Figure 4.4 *CD spectra showing the reversibility of pH-induced conformational transitions*

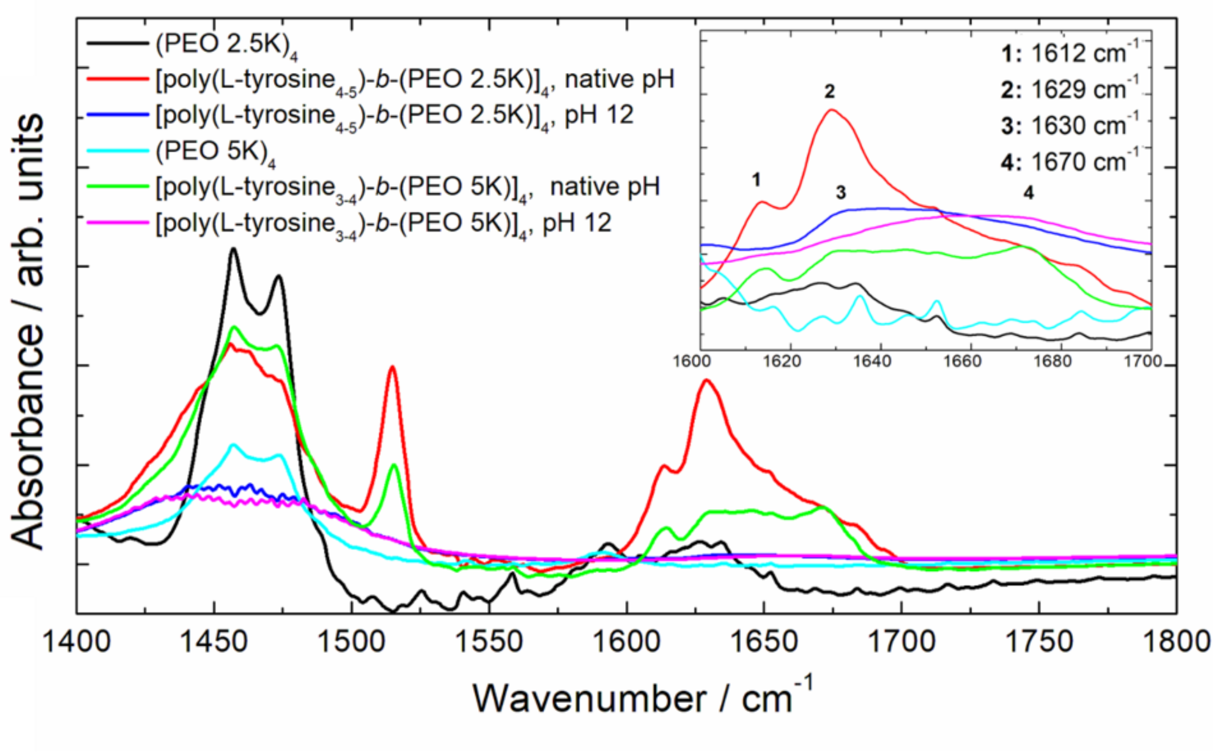

Figure 4.5. *FTIR spectra for 1 wt % samples. Spectra are normalised to the absorbance at 1900 cm^{-1}.*

X-ray fibre diffraction was used to investigate the structure (Figure 4.6). The fibre X-ray diffraction patterns were isotropic and were reduced to one-dimensional form. All the samples show broad peaks at around 4.6 and 3.8 Å consistent with a high degree of PEO crystallinity.[39] These peaks overlap with those from β-sheet structures and it is therefore not possible to deconvolute PEO crystallinity and β-sheet formation in these samples.[11,39] The assignment of these peaks to PEO crystallinity was confirmed through measurement of the PEO star precursor molecules. Previously, tyrosine end groups have been shown to affect PEO unit cell dimensions for example, in the case of Tyr$_5$-PEO6K-Tyr$_5$.[39] For the star polymers there is a decrease in crystallinity between [poly(L-tyrosine$_{4-5}$)-*b*-(PEO 2.5k)]$_4$ at native pH and pH 12. A slight decrease in crystallinity is observed in the X-ray diffraction patterns obtained for [poly(L-tyrosine$_{3-4}$)-*b*-(PEO 5k)]$_4$ comparing data at pH 12 and native pH.

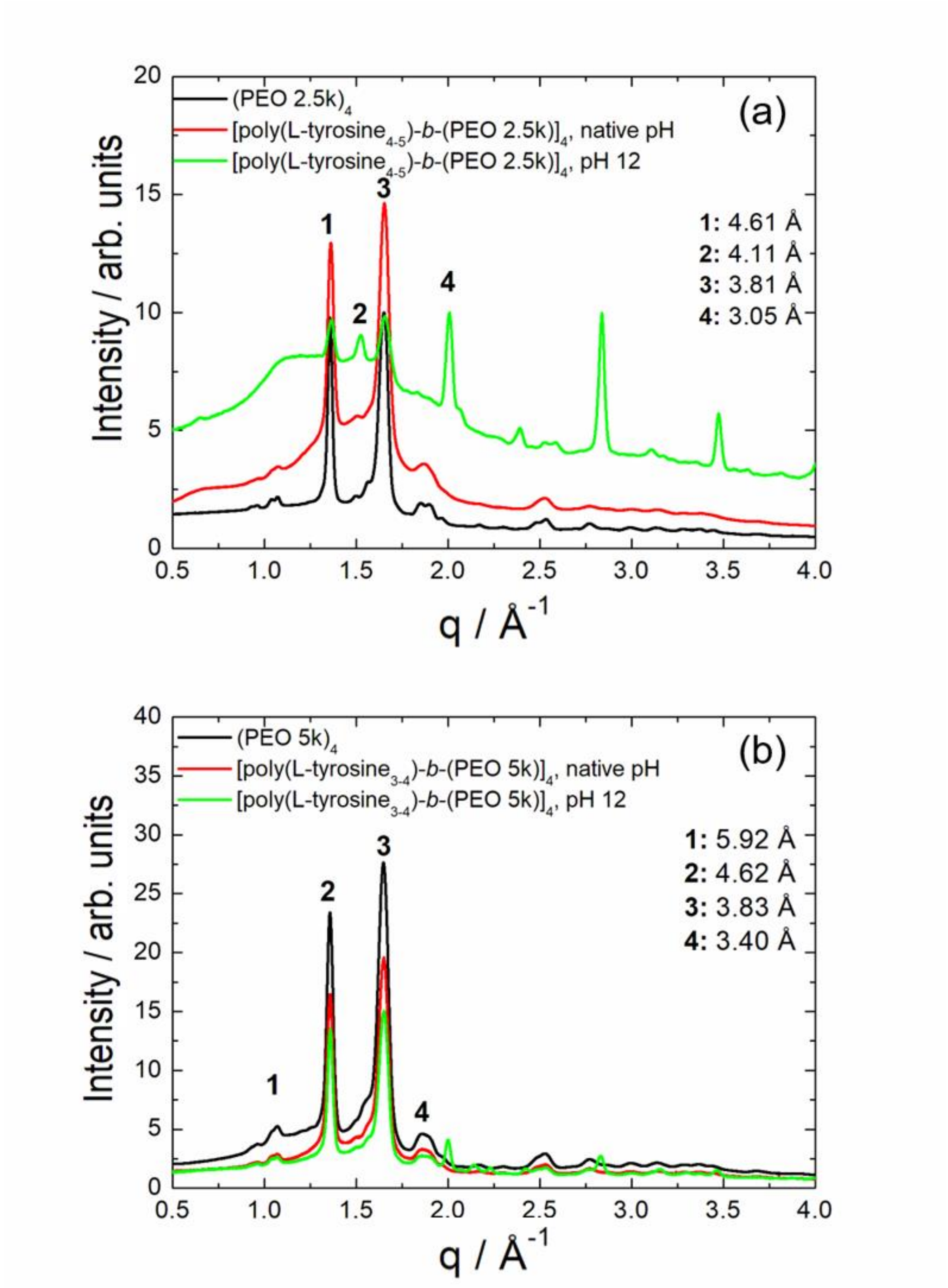

Figure 4.6. *X-ray fibre diffraction. Data obtained from dried stalks made from 3 wt% solutions of, a) [poly(L-tyrosine$_{4-5}$)-b-(PEO 2.5K)]$_4$ and precursor molecule (PEO 2.5K)$_4$, and, b) [poly(L-tyrosine$_{3-4}$)-b-(PEO 5k)]$_4$ and precursor molecule (PEO 5k)$_4$*

In order to observe the possibility of dityrosine formation under alkaline condition at pH 12, fluorescence spectroscopy was performed. Dityrosine links can be a means of stabilising self-assembled structures, and this has previously been reported to play a role in the nucleation of fibril formation.[61] Figure 4.7a,b shows the emission spectra obtained at λ_{ex} = 320 nm. A peak close to 400 nm is associated with dityrosine formation.[61–63] At pH 12, spectra for both [poly(L-tyrosine$_{4-5}$)-*b*-(PEO 2.5k)]$_4$ and for [poly(L-tyrosine$_{3-4}$)-*b*-(PEO 5k)]$_4$ show a peak at approximately 400 nm. At native pH of 7.8 and 6.9 respectively, this peak is absent. This is expected due to the fact that the tyrosine hydroxyl unit is present at native pH as opposed to the phenolate form present at high pH.[61–63]

The excitation spectra (Figure 4.7c,d) for both poly(L-tyrosine$_{4-5}$)-*b*-(PEO 2.5k)]$_4$ and for [poly(L-tyrosine$_{3-4}$)-*b*-(PEO 5k)]$_4$ show a red shift of the 280 nm peak at native pH to 320 nm at pH 12, also consistent with dityrosine formation.[61,63] Contrary to other reports, the intensity in the excitation spectrum is lower at pH 12 than at the native pH.[61]

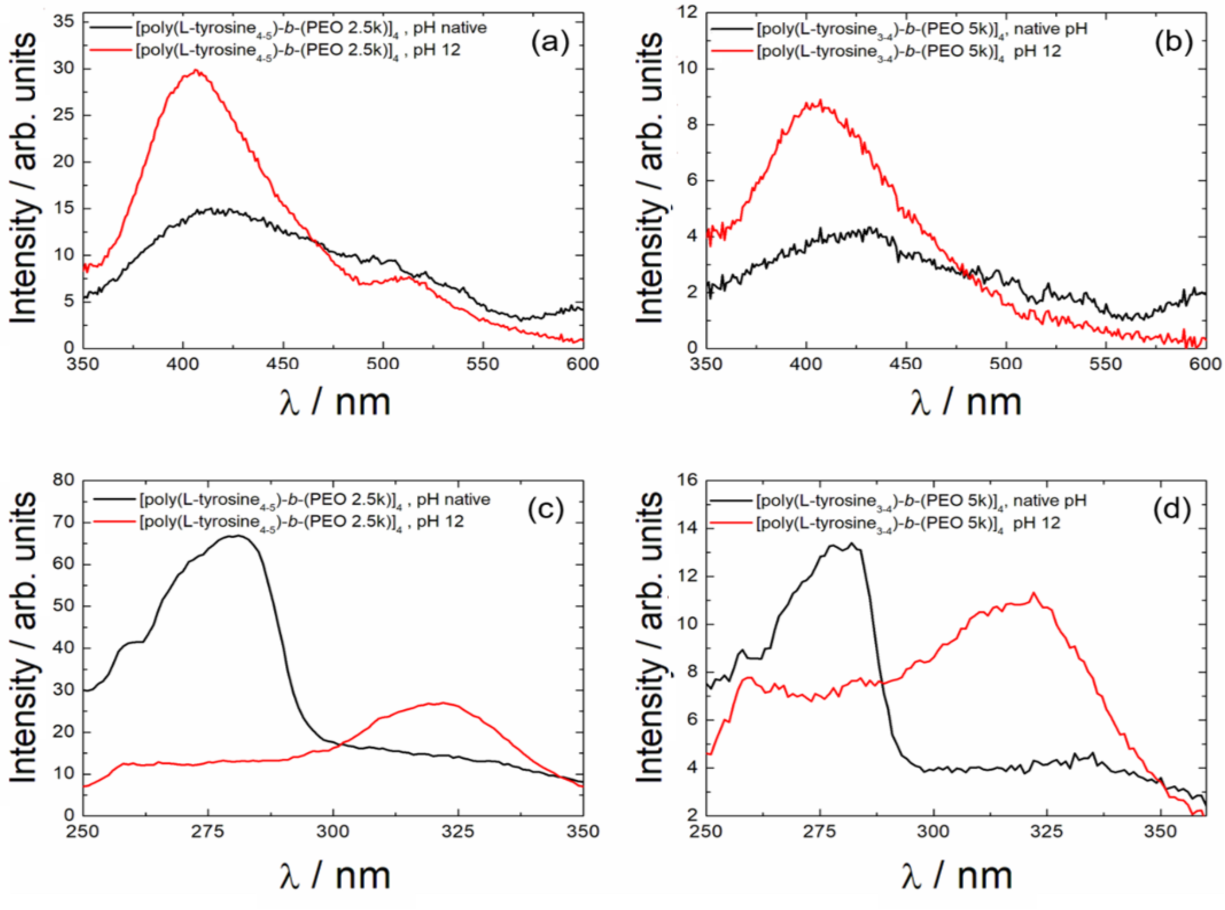

Figure 4.7. *a and b) Fluorescence emission spectra of 0.1 wt% Conjugates (λ_{ex}=320) and c) and d) Fluorescence excitation spectrum of 0.1 wtp% conjugates (λ_{em}=410).*

Cryo-TEM (Figure 4.8) was used to image the self-assembled nanostructures. The ANS fluorescence assays confirm that aggregation occurs above a critical concentration for the conjugates. For comparison, Cryo-TEM images for the precursor molecules (PEO 2.5k)$_4$ and (PEO 5k)$_4$ were also examined. For [poly(L-tyrosine$_{4-5}$)-*b*-(PEO 2.5k)]$_4$ at native pH (Figure 4.8a), there was a mixture of large spherical nanostructures of an average size of 31 nm and short clusters of fibres. Interestingly, cryo-TEM for the same conjugate in a pH 12 solution (Figure 4.8b) shows very little assembly, showing that adjusting the pH disrupts the self-assembly of [poly(L-tyrosine$_{4-5}$)-*b*-(PEO 2.5k)]$_{4.}$ There are occasional spherical structures. The cryo-TEM images for the precursor molecule (PEO 2.5k)$_4$ show very little self-assembly with occasional aggregates (Figure 4.8c).. The [poly(L-tyrosine$_{3-4}$)-*b*-(PEO 5k)]$_4$ sample at native pH (Figure 4.8d) shows a mixture of fibrillar structures and small spherical structures. At pH 12 (Figure 4.8e) the self-assembled nanostructure is a mixture of long straight fibrils and smaller spherical nanostructures with an average diameter of 15 nm. Straight fibres have been previously observed with linear conjugates of aromatic peptides with linear PEG (PEO), for example, Phe$_4$-PEO5k[64] and Tyr$_5$-PEO6K-Tyr$_5$.[39] The precursor molecule (PEO 5k)$_4$ show very little self-assembly (Figure 4.8f). Figure 4.9 shows additional cryo-TEM images from other areas of the TEM grids, with less frequently observed assembles.

To further probe the self-assembled structures of the PEO conjugates, small-angle X-ray scattering measurements were performed. The measured data and corresponding fits are shown in Figure 4.10. Both the pH adjusted, and native pH polymers were fitted to a general mass fractal Gaussian model to describe the aggregated structures and a Gaussian coil form factor, to account for the presence of monomers in solution. This model describes the data very well. The SAXS data for the precursor polymers was fitted to a general Gaussian coil model. The parameters of the fits are listed in Table 1 and 2.

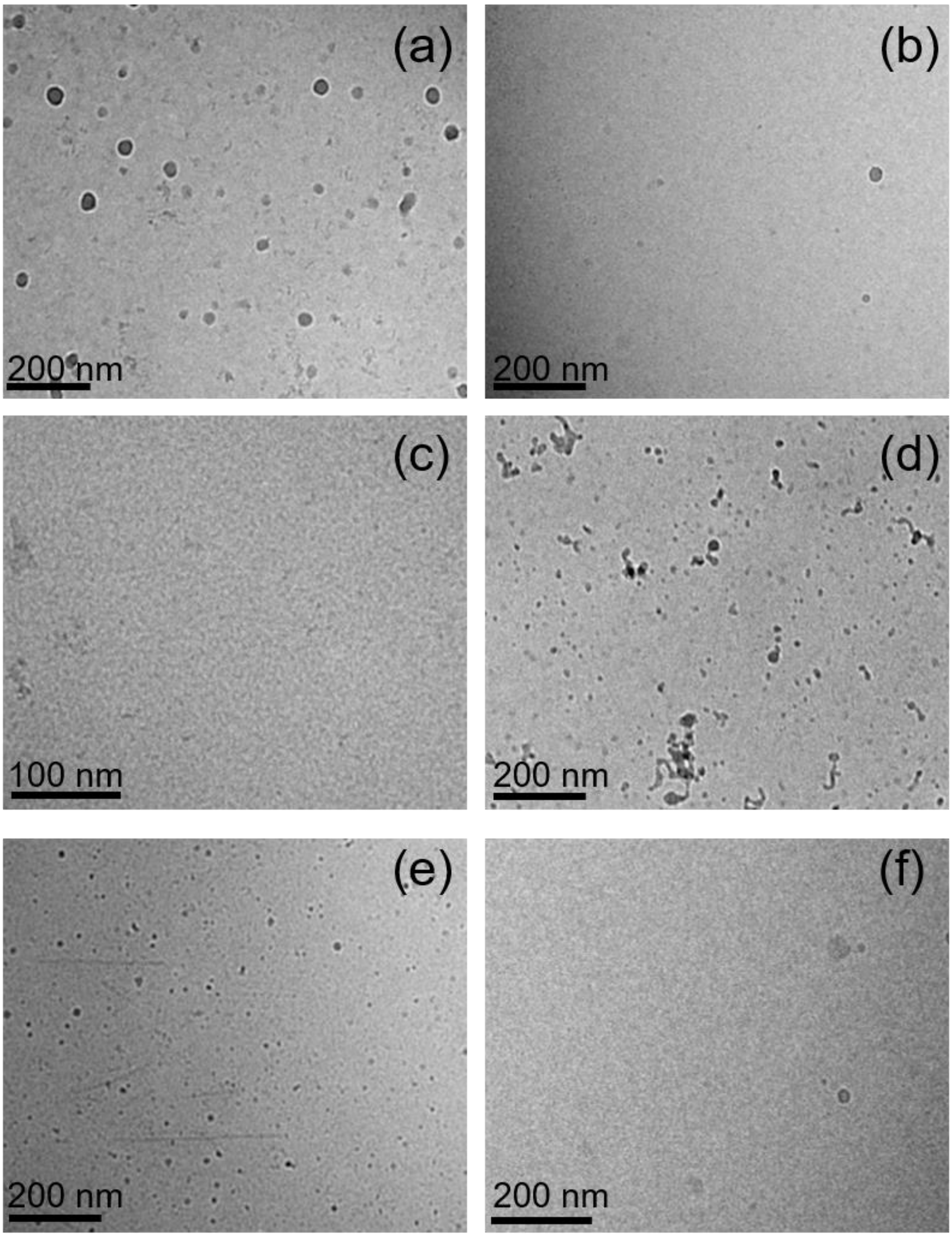

Figure 4.8. *Cryo-TEM images of 1 wt % conjugates. (a) [poly(L-tyrosine$_{4\text{-}5}$)-b-(PEO 2.5k)]$_4$ (native pH). (b) [poly(L-tyrosine$_{4\text{-}5}$)-b-(PEO 2.5k)]$_4$ (pH 12) (c) (PEO 2.5k)$_4$ (d) [poly(L-tyrosine$_{3\text{-}4}$)-b-(PEO 5k)]$_4$ (native pH) (e) [poly(L-tyrosine$_{3\text{-}4}$)-b-(PEO 5k)]$_4$ (pH 12), (f) (PEO 5k)$_4$*

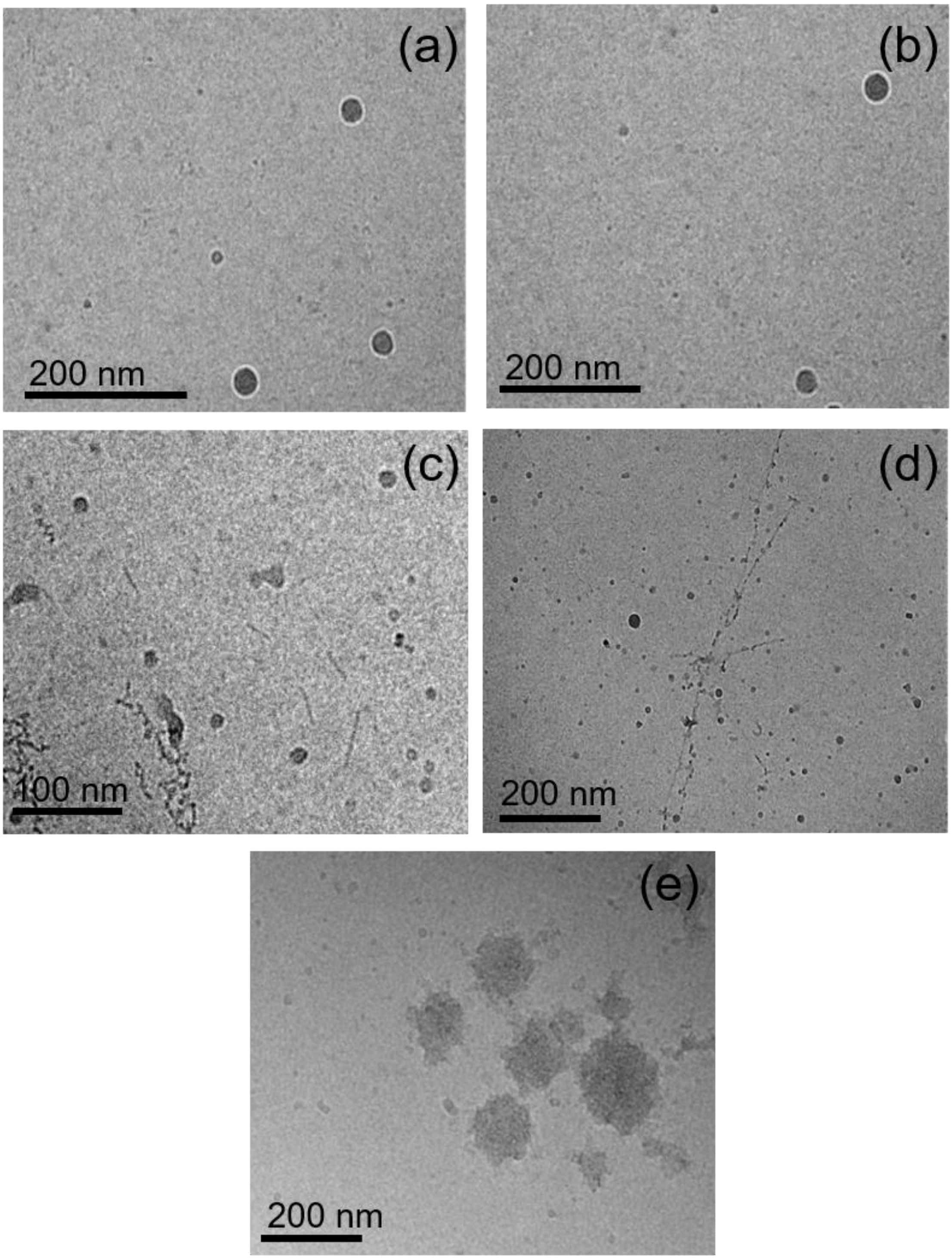

Figure 4.9. *Rare self-assembled structures observed by Cryo-TEM for the conjugates. (a) [poly(L-tyrosine$_{4-5}$)-b-(PEO 2.5k)]$_4$ pH 12 shows occasional spherical structures. (b) (PEO 2.5k)$_4$ shows occasional spherical clusters. (c) [poly(L-tyrosine$_4$)-b-(PEO 5k)]$_4$ pH 7 shows occasional short straight fibres and longer fibres. (d) [poly(L-tyrosine$_4$)-b-(PEO 5k)]$_4$ shows occasional very long fibers, (e) (PE0 5k)$_4$ shows occasional large clusters.*

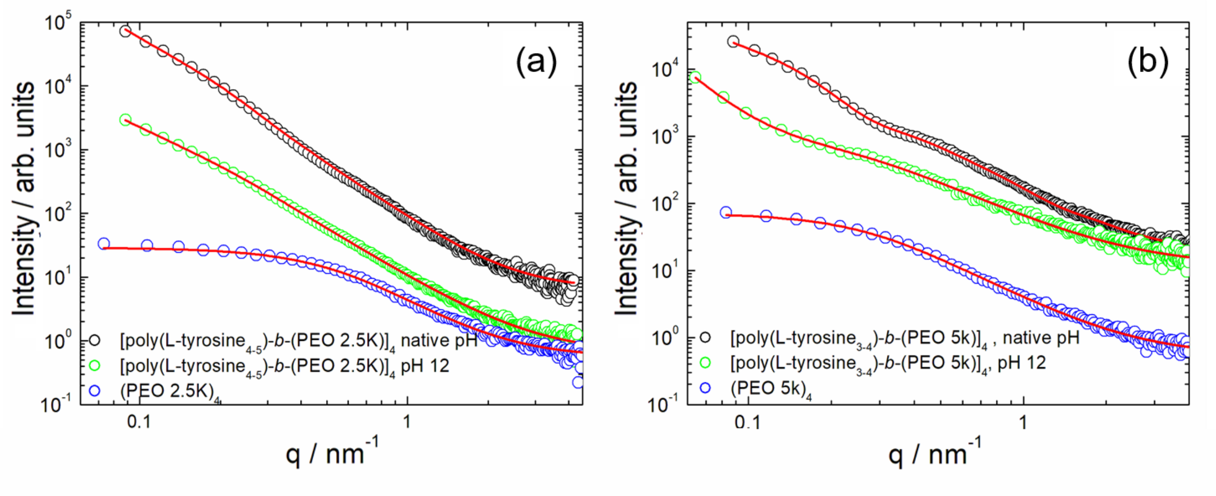

Figure 4.10. *SAXS Profiles for 1 wt% conjugates dissolved in water. a) SAXS profiles for [poly(L-tyrosine$_{4-5}$)-b-(PEO 2.5k)]$_4$ and b) SAXS profiles for [poly(L-tyrosine$_{3-4}$)-b-(PEO 5k)]$_4$. Scattering profiled are multiplied by factors of 10 and only every third data point is shown.*

Table 4.1. *Parameters of SAXS fits for [poly(L-tyrosine$_{4-5}$)-b-(PEO 2.5k)]$_4$ and [poly(L-tyrosine$_{3-4}$)-b-(PEO 5K)]$_4$ at native and adjusted pH. Fitting to a generalised Gaussian coil and mass fractal Gaussian model using SASFIT. Here Rg is the radius of gyration, D is the dimension fractal, I(0) is the forward scattering, v is the Flory exponent, N is the scaling factor and BG is the background.*

	Generalised Gaussian coil				**BG**
	R_g / nm	***v***	**I(0)**	**N**	
(PEO 2.5)$_4$	3.25	0.40	5.60	5.07	0.56
(PEO 5K)$_4$	5.80	0.47	13.2	5.43	0.54

***Table 4.2.** Parameters of SAXS fits for [poly(L-tyrosine$_{4-5}$)-b-(PEO 2.5K)]$_4$ and [poly(L-tyrosine$_{3-4}$)-b-(PEO 5k)]$_4$ at pH 12. Fitting to a generalised Gaussian coil model using SASFIT. Where Rg is the radius of gyration, nu is the flory exponent, I0 is forward scattering, N is the scaling factor and BG is the background.*

	Mass fractal Gaussian			**Generalised Gaussian Coil**				**BG**
	R_g / nm	**D**	**I(0)**	**R_g / nm**	***v***	**I(0)**	**N**	
[poly(L-tyrosine$_{4-5}$)-*b*-(PEO 2.5k)]$_4$ pH 7.89 (native)	28.3	2.4	26.1	13.9	0.23	3.70	1.3	$3.54\text{x}10^{-4}$
[poly(L-tyrosine$_{4-5}$)-*b*-(PEO 2.5k)]$_4$ pH 12	26.4	2.2	9.34	11.5	0.34	1.7	0.7	$6.56\text{x}10^{-4}$
[poly(L-tyrosine$_{3-4}$)-*b*-(PEO 5k)]$_4$ pH 6.93 (native)	29.2	1.9	4.7	15.8	0.29	0.5	0.4	$3.00\text{x}10^{-5}$
[poly(L-tyrosine$_{3-4}$)-*b*-(PEO 5k)]$_4$ pH 12	34.4	2.5	2.8	5.59	0.54	0.5	0.1	$1.15\text{x}10^{-3}$

The radius of gyration (R_g) of the star polymers was calculated using the equation[65]:

$$Rg_2 = \frac{N}{f}\frac{B^2}{6}\left(3 - \frac{2}{6}\right).$$

The R_g for (PEO 2.5k)$_4$ and (PEO 5k)$_4$ was calculated to be 1.36 and 1.93 nm respectively. The fits show a radius of gyration of 3.25 nm and 5.80 nm respectively which indicates significant swelling. Interestingly, only the pH adjusted [poly(L-tyrosine$_{4-5}$)-*b*-(PEO 2.5k)]$_4$ shows the signature of monomers with a component of scattering from Gaussian coils with R_g=5.59 nm.

Kratky plots (figure 4.11) were used to further visualize the data for the precursor molecules. It can be seen that the precursor molecules have a typical shape of unfolded molecules having branched conformations. The Kratky plots for the conjugates behaviour are not consistent with this, this probably due to the fact that the Kratky approximation assumes globular like structures.

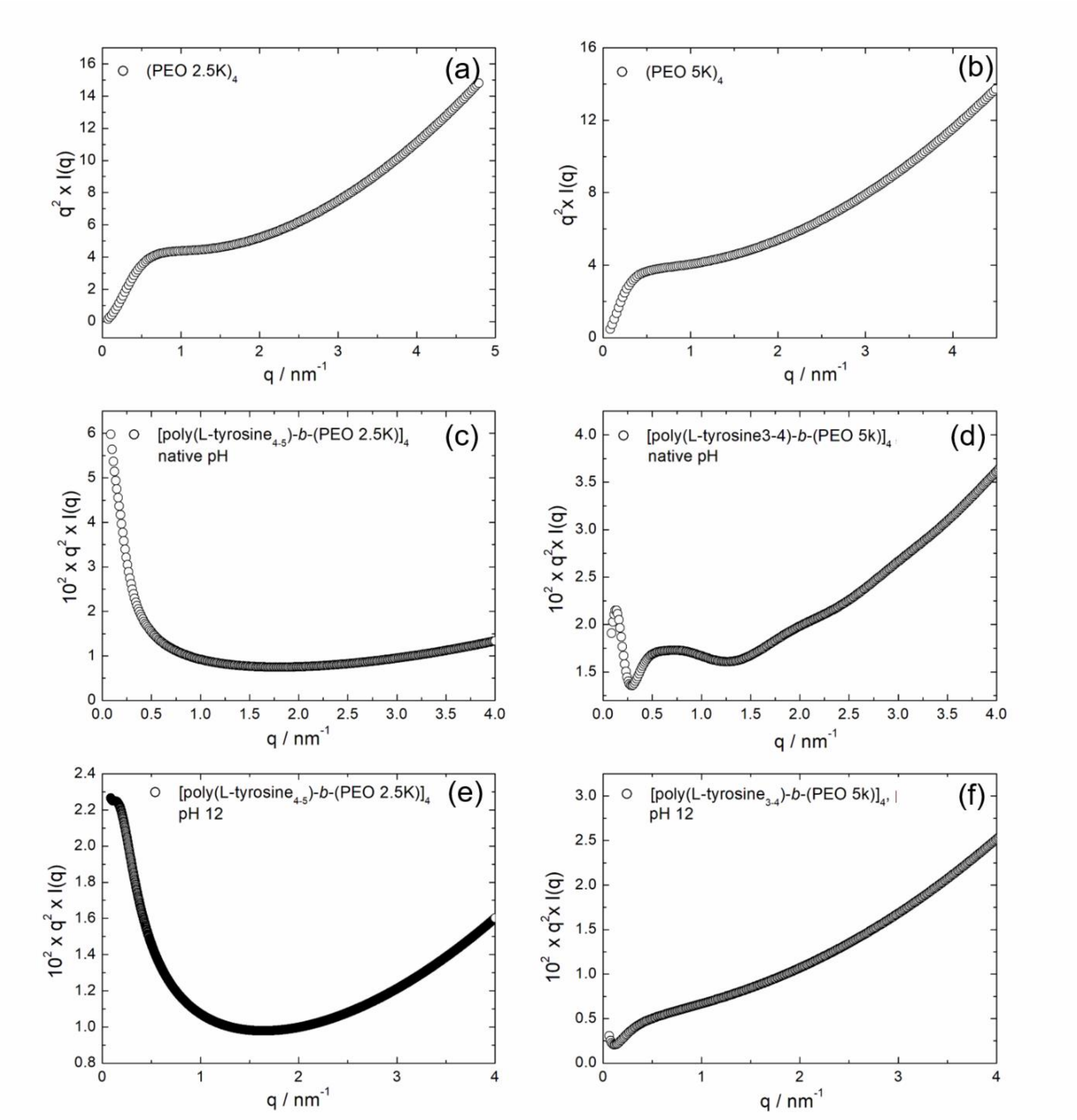

Figure 4.11. *Kratky plots to show unfolded conformation of precursor molecules. Kratky plots of the SAXS data for precursor molecules, consistent with branched conformation.*

In order to examine the cytocompatibility of the conjugates, the viability of [poly(L-tyrosine$_{4-5}$)-*b*-(PEO 2.5k)]$_4$ and [poly(L-tyrosine$_{3-4}$)-*b*-(PEO 5k)]$_4$ was tested using 161Br skin fibroblast cells using an 3-[4,5-dimethylthiazole-2-yl]-2,5-diphenyltetrazolium bromide (MTT) assay (Figure 4.12). [poly(L-tyrosine$_{4-5}$)-*b*-(PEO 2.5k)]$_4$ and [poly(L-tyrosine$_{3-4}$)-*b*-(PEO 5k)]$_4$ were shown to be tolerated by the cells up to a concentration of 0.05 wt% (above >83% viability, with no statistical significant difference between the concentrations and the negative control.) Above this concentration there is significant decrease in cell proliferation. The cell viability in solution containing the precursor molecules was examined. It was found that there was decreased cell viability at high concentrations for (PEO 5K)$_4$, which displayed a significant reduction in viability at 0.5 wt% whereas (PEO 2.5K)$_4$ showed a slight decrease in viability. This indicates that the decreased viability could be due to the PEO molar mass, as (PEO 5k)$_4$ has a greater effect on cell viability than the (PEO 2.5k)$_4$. This is in agreement with previous work, where high molecular mass PEG at high concentrations have been shown to display some toxicity.[66] The precursor molecules have less effect on viability than the [poly(L-tyrosine$_{4-5}$)-*b*-(PEO 2.5k)]$_4$ and [poly(L-tyrosine$_{3-4}$)-*b*-(PEO 5k)]$_4$, showing that the presence of the tyrosine does slightly reduce viability at higher concentrations. The concentrations tolerated by the cells are significantly higher than the critical aggregation point.

The cell viability of tyrosine alone was measured. Concentrations were chosen based on the tyrosine content in each of the precursor molecules. The highest concentration of tyrosine, present in 0.5 wt% of the [poly(L-tyrosine$_{4-5}$)-b-(PEO 2.5k)]$_4$ could not be tested with the MTT assay due to tyrosine solubility, the limit of which is 0.045 wt% in water. Interestingly, the concentrations of tyrosine alone present in the precursor molecules (Figure 4.12) does not show to have an effect on viability, suggesting that is due to the oligo-tyrosine block.

We examined possible gel formation for the telechelic star polymers. Gel formation in water was not observed up to concentrations where the conjugates became insoluble. This is in agreement with previous work based on linear Tyr$_5$-PEO6k-Tyr$_5$ previously investigated by our group, in which gelation was not observed even with 20 wt% polymer in aqueous solution.[11] As an alternative means to produce gels, we used the widely available and readily gelled polysaccharide sodium alginate. Therefore, peptide functionalized gels (Figure 4.13) were made using 1 wt % sodium alginate, 0.1 wt% $CaCl_2$, and either 0.1, 1 or 5 wt% of conjugate (apart from [poly(L-tyrosine$_{4-5}$)-*b*-(PEO 2.5k)]$_4$ which is not soluble at 5 wt% concentration). $CaCl_2$ at 0.1 wt% and sodium alginate have previously been shown to be non-toxic, and indeed are shown to be able to support and encapsulate cells.[67]

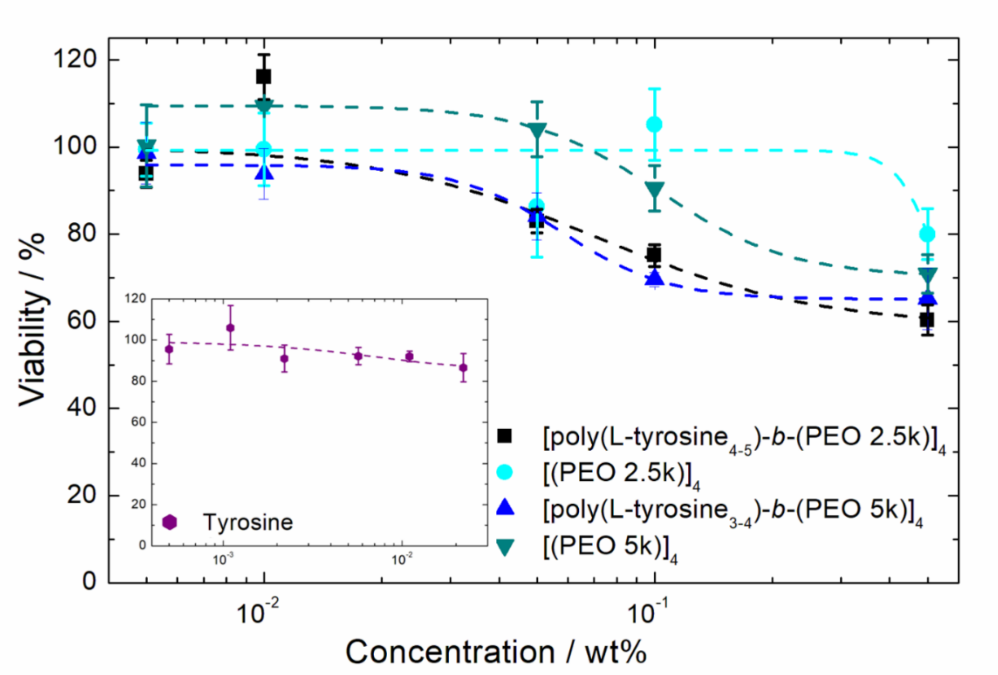

***Figure 4.12**. Cell Viability profile for [poly(L-tyrosine$_{4-5}$)-b-(PEO 2.5K)]$_4$ and [poly(L-tyrosine$_{3-4}$)-b-(PEO 5K)]$_4$ error bars =SEM (where n=3). *= $p<0.05$, **=$p<0.01$, ***=$p<0.001$..*

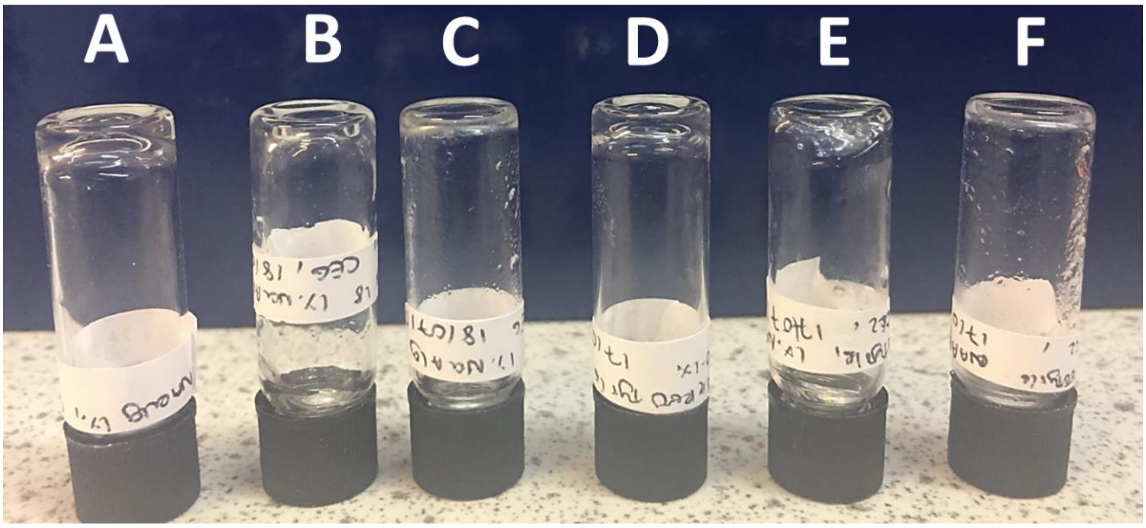

***Figure 4.13.** Image of formed hydrogels. a) 0.1 wt% $CaCl_2$, 1 wt% NaAlg, b) 1 wt% [poly(L-tyrosine$_{4-5}$)-b-(PEO 2.5k)]$_4$, 0.1 wt% $CaCl_2$, 1 wt% NaAlg. c) 0.1 wt% [poly(L-tyrosine$_{4-5}$)-b-(PEO 2.5k)]$_4$, 0.1 wt% $CaCl_2$, 1 wt% NaAlg d) 5 wt% [poly(L-tyrosine$_{3-4}$)-b-(PEO 5k)]$_4$, , 0.1 wt% $CaCl_2$, 1 wt% NaAlg e) 1 wt% [poly(L-tyrosine$_{3-4}$)-b-(PEO 5k)]$_4$, , 0.1 wt% $CaCl_2$, 1 wt% NaAlg f) 0.1 wt% [poly(L-tyrosine$_{3-4}$)-b-(PEO 5k)]$_4$, , 0.1 wt% $CaCl_2$, 1 wt% NaAlg.*

To probe the structure of the gels and to examine whether the peptide caused structural changes, SAXS measurements were performed. SAXS measurements were performed on hydrogels comprising of 0.1 wt% and 1 wt% of [poly(L-tyrosine$_{4-5}$)-*b*-(PEO 2.5k)]$_4$ and 0.1 wt%, 1 wt% and 5 wt% of [poly(L-tyrosine$_{3-4}$)-*b*-(PEO 5k)]$_4$ with 0.1 wt% CaCl$_2$ and 1 wt% sodium alginate was conducted. The measured fits and corresponding data are shown in Figures 4.14. SAXS profiles were also measured on the unfunctionalized alginate gel. This was fitted to a broad peak fit model. The parameters of the fit are listed in table 4.3. From the SAXS data it can be seen that the gel structure is not significantly influenced by addition of 0.1 wt% star polymer, but there is a significant change with addition of 1 wt% polymer. This is manifested by a significant change in scattering at low q (development of a broad peak) and a change in slope at high q.

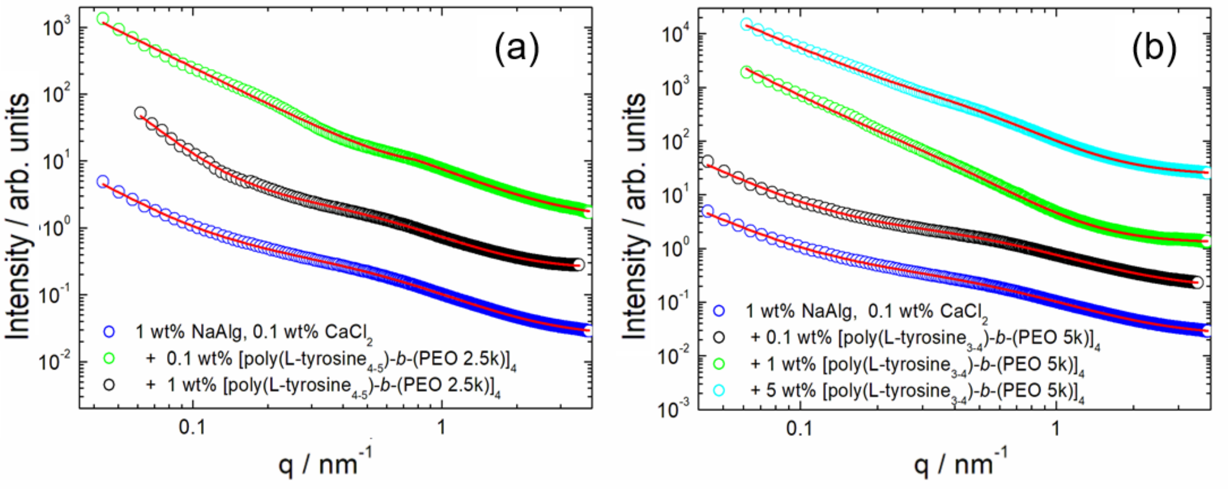

Figure 4.14. *SAXS of peptide functionalized gels. a) [poly(L-tyrosine$_{4-5}$)-b-(PEO 2.5K)]$_4$ functionalized gels. b) [poly(L-tyrosine$_{3-4}$)-b-(PEO 5k)]$_4$ functionalized gels. Scattering profiles is multiplied by multiples of 10 and only every third data point is shown for clarity. Corresponding fits and parameters are listed in table 4.3*

Table 4.3. *Parameters of SAXS fits for [poly(L-tyrosine$_{4-5}$)-b-(PEO 2.5k)]$_4$ and [poly(L-tyrosine$_{3-4}$)-b-(PEO 5k)]$_4$ functionalised hydrogels.* ***.*** *Fitting to a broad peak model with a sloping background using SASFIT. Where I(0) is the forward scattering, ξ is the correlation length, q_0 is the peak position which is related to d-spacing (q_0= 2π/d). m and p are exponentials. Sloping background is based on the equation BG = $c_0 + c_1^q + c_4q^{-x}$*

	Broad Peak					**Background**		
	I(0)	ξ	**q_0**	**m**	**p**	**c_0**	**c_4**	**α**
0.1 wt% $CaCl_2$, 1 wt% NaAlg	0.32	14.3	0.01	1.37	1.70	0.02	4.79×10^{-5}	2.09
0.1 wt% [poly(L-tyrosine$_{4-5}$)-*b*-(PEO 2.5k)]$_4$ 0.1 wt% $CaCl_2$, 1 wt% NaAlg	0.20	12.96	0.02	1.35	1.96	0.02	1.93×10^{-6}	2.88
1 wt% [poly(L-tyrosine$_{4-5}$)-*b*-(PEO 2.5k)]$_4$ 0.1 wt% $CaCl_2$, 1 wt% NaAlg	0.04	8.98	0.08	1.15	1.80	0.01	4.98×10^{-4}	1.85
0.1 wt% [poly(L-tyrosine$_{3-4}$)-b-(PEO 5k)]$_4$ 0.1 wt% $CaCl_2$, 1 wt% NaAlg	0.20	16.2	0.01	1.65	1.22	0.02	2.08×10^{-5}	2.21
1 wt% [poly(L-tyrosine$_{3-4}$)-b-(PEO 5k)]$_4$ 0.1 wt% $CaCl_2$, 1 wt% NaAlg	0.08	10.1	0.01	1.32	2.49	0.004	3.40×10^{-5}	2.10
5 wt% [poly(L-tyrosine$_{3-4}$)-b-(PEO 5k)]$_4$ 0.1 wt% $CaCl_2$, 1 wt% NaAlg	0.40	18.8	0.004	2.05	1.62	0.02	3.5×10^{-4}	2.07

4.3 Summary and Conclusions

The novel conjugates [poly(L-tyrosine$_{4-5}$)-*b*-(PEO 2.5k)]$_4$ and [poly(L-tyrosine$_{3-4}$)-*b*-(PEO 5k)]$_4$ have been shown to self-assemble with a disordered conformation, forming highly polydisperse mixtures of globules and fibres through a combination of microscopy, scattering and spectroscopic techniques.

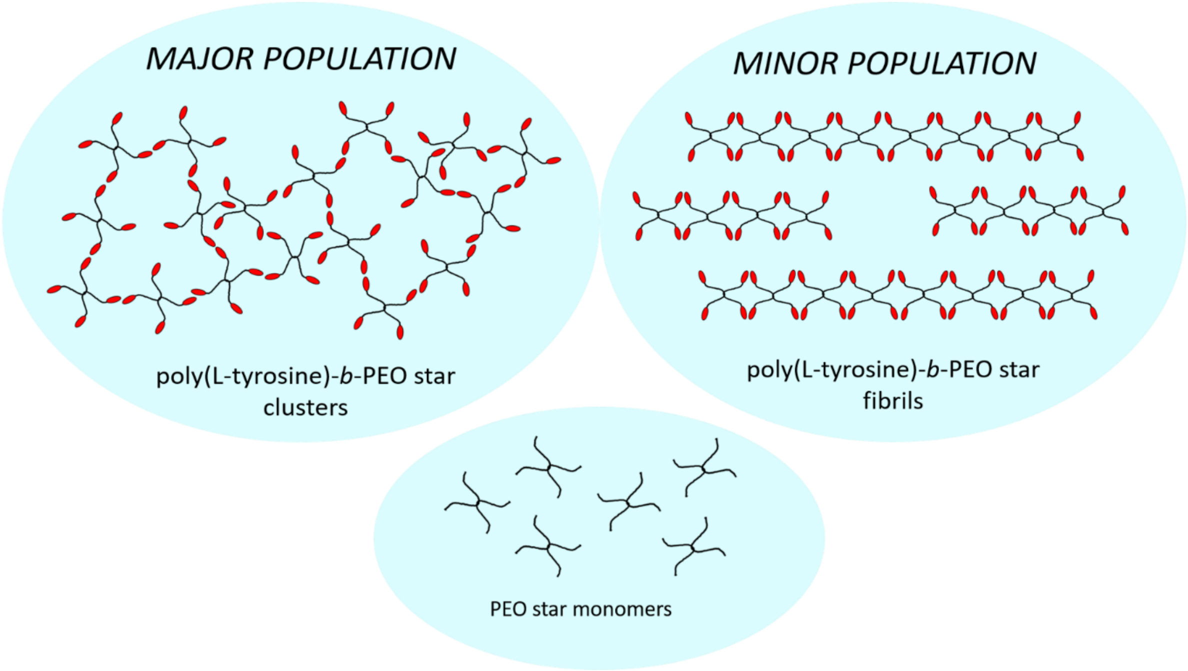

Scheme 4.2. Schematic of proposed aggregation of the PEO conjugates**.**

Adjustment of pH of [poly(L-tyrosine$_{4-5}$)-*b*-(PEO 2.5k)]$_4$ to pH 12 causes a loss in secondary structure, and disruption of self-assembly, whereas [poly(L-tyrosine$_{3-4}$)-*b*-(PEO 5k)]$_4$ shows change in self-assembly from fibrillar worm-like globules to long very straight fibres and small globules. This straight fibre formation is consistent with other work,[39] where pH adjusted tyrosine end capped linear telechelic PEO was examined. The increased polydispersity of self-assembly comparative to linear PEO molecules previously studied may be due to the star-shape of the PEO which gives conformational restrictions, leading to irregular packing and interactions. The XRD patterns show that PEO crystallinity occurs through drying.

Interestingly, [poly(L-tyrosine$_{4-5}$)-*b*-(PEO 2.5k)]$_4$ and [poly(L-tyrosine$_{3-4}$)-*b*-(PEO 5k)]$_4$ cause decreased cell viability at higher concentrations (above 0.05 wt%). From the precursor molecules, it can be seen that this in part may be due to the branched nature of the PEO molecules, where size is clearly causing decreased cell proliferation in this case. Tyrosine is an important amino acid in many cell signalling cascades, being the site of phosphorylation targeted by a specific set of protein kinases named tyrosine-kinases. The presence of several tyrosine residues enhances the lack of proliferation. Self-assembly occurs well below the concentrations of some of the tolerated concentrations showing that self-assembly itself is not linked to or causative of cytotoxicity. Future work could focus on the bioactivity of these conjugates, such as tyrosine phosphorylation using kinases.

4.4 Experimental Section

4.4.1 Materials

The two conjugates, of [poly(L-tyrosine$_{4\text{-}5}$)-*b*-(PEO 2.5k)]$_4$ and [poly(L-tyrosine$_{3\text{-}4}$)-*b*-(PEO 5k)]$_4$ were custom synthesized by Dmitros Skulous and Hermis Iatrou, using NCA-polymerization techniques reported elsewhere.[68]

4.4.2 Sample Preparation

The conjugate [poly(L-tyrosine$_{3\text{-}4}$)-*b*-(PEO 5k)]$_4$ was found to have greater solubility than [poly(L-tyrosine$_{4\text{-}5}$)-*b*-(PEO 2.5k)]$_4$ in water and in D_2O. Samples were studied at native pH and pH 12. The native pH values of [poly(L-tyrosine$_{4\text{-}5}$)-*b*-(PEO 2.5k)]$_4$ and [poly(L-tyrosine$_{3\text{-}4}$)-*b*-(PEO 5k)]$_4$ were 7.74 and 6.90 respectively. For the alkaline solutions, pH was adjusted to 12 using 1M NaOH solution.

4.4.3 Fluorescence assays

Fluorescence spectroscopy was used to determine the critical aggregation concentrations (*cac*) of [poly(L-tyrosine$_{4\text{-}5}$)-*b*-(PEO 2.5k)]$_4$ and [poly(L-tyrosine$_{3\text{-}4}$)-*b*-(PEO 5k)]$_4$. Fluorescence spectra were recorded with a Varian Cary Eclipse fluorescence spectrometer with samples in 4 mm inner width quartz cuvettes. 8-anilinonaphthalene-1-sulfonic acid (ANS) was used to probe the aggregation as probe that is sensitive to hydrophobic environments making it suitable to locate the *cac*.[50–54] ANS assays were performed using 66.8µM ANS (0.002 wt%) solution to solubilise the telechelic conjugates. Fluorescence spectra were recorded between 400-650 nm (λ_{ex} = 356 nm).

The possibility of dityrosine formation for [poly(L-tyrosine$_{4-5}$)-*b*-(PEO 2.5k)]$_4$ and [poly(L-tyrosine$_{3-4}$)-*b*-(PEO 5k)]$_4$ at native and alkaline pH was measured using a Varian Cary Eclipse fluorescence spectrophotometer. The fluorescence was measured for water and for 0.1 wt% of [poly(L-tyrosine$_{4-5}$)-*b*-(PEO 2.5k)]$_4$ and [poly(L-tyrosine$_{3-4}$)-*b*-(PEO 5k)]$_4$ at native pH and pH 12. Samples were measured in 4 mm inner width quartz cuvettes, and the slit width was 5 nm. Emission spectra were recorded at λ_{ex}=320 nm from 340 to 600 nm. A total of 5 averages were taken, and the background was subtracted. Excitation spectra were also measured at λ_{ex}=410 nm, from 250 nm to 410 nm. A total of 5 averages were taken, and the background was subtracted.

4.4.4 Circular Dichroism (CD)

CD spectra were recorded using a Chirascan spectropolarimeter (Applied Photophysics, UK) in the wavelength range 180 – 260 nm. The samples, 0.025 wt% in D_2O were pipetted into a 1 mm path length bottle, with absorbance less than 2 at any point being reported. Measurements were recorded with a 0.5 nm bandwidth, 1 mm step and 1 second collection time per point. Data was collected at 10°C intervals between 10-70 °C were measured, with samples being allowed to adjust at each temperature for 5 minutes. The CD signal for the background was subtracted from the CD signal of the sample, and molar ellipticity was calculated.

4.4.5 Fourier Transform Infrared Spectroscopy (FTIR) Studies of Self-Assembly

Spectra were recorded using a Thermo Scientific Nicolet IS5 equipped with a DTGS detector, with a PEARL liquid cell (sample was contained between fixed CaF_2 plates). 80 µl of 1 wt% sample dissolved in D_2O were prepared and added to a PEARL liquid cell. Spectra were scanned 128 times over the range of 900 − 4000 cm^{-1}

4.4.6 Cryogenic Transmission Electronic Microscopy (Cryo-TEM)

Cryo-TEM was performed by M.Reza at Aalto University, Finland. Vitrified specimens were prepared using an automated FEI Vitrobot device using Quantifoil 3.5/1 holey carbon copper grids with a hole size of 3.5 µm. Prior to use, grids were plasma cleaned using a Gatan Solarus 9500 plasma cleaner and then transferred into an environmental chamber of a FEI Vitrobot at room temperature and 100% humidity. Thereafter sample solution was applied onto the grid, and it was blotted twice for 5 s and then vitrified in a 1/1 mixture of liquid ethane and propane at a temperature of −180 °C. The grids with vitrified sample solution were maintained at liquid nitrogen temperature and then cryotransferred to the microscope. Imaging was carried out using a field emission cryo-electron microscope (JEOL JEM-3200FSC) operating at 200 kV. Images were taken in bright field mode and using zero loss energy filtering (Ω type) with a slit width of 20 eV. Micrographs were recorded using a Gatan Ultrascan 4000 CCD camera. Specimen temperature was maintained at −187 °C during the imaging.

4.4.7 X-ray diffraction (XRD)

Measurements were performed on a stalk prepared by suspending a 3 wt% solution of conjugate between two wax coated capillaries. After drying, wax capillaries were separated leaving the stalk on the end of one capillary. Diffraction was measured using the Oxford Diffraction Gemini Ultra instrument at the University of Reading. Stalks were mounted vertically onto the four axis goniometer. The sample-detector distance was 44 mm, and the X-ray wavelength was λ=1.5418 Å. The wavenumber scale ($q = 4\pi \sin \theta/\lambda$ where 2θ is the scattering angle) was geometrically calculated. The detector was a Sapphire CCD.

4.4.8 Small-angle X-ray scattering

Collection of solution small-angle X-ray scattering (SAXS) data was performed on the bioSAXS beamline B21, at Diamond Light Source, United Kingdom and BM29, ESRF, Grenoble, France. Solutions of 1 wt% [poly(L-tyrosine$_{4-5}$)-*b*-(PEO 2.5k)]$_4$ and [poly(L-tyrosine$_{3-4}$)-*b*-(PEO 5K)]$_4$ at native pH and pH 12 were loaded in PCR tubes in an automated sample changer. Samples (30 µl) were then delivered into a temperature controlled quartz cell capillary and exposed for 15 s, collecting 18 frames at 20 ^{o}C. Data was collected using a Pilatus Dectris 2M detector. Background was manually subtracted using ScÅtter.[69] Form factor modelling was done using SASfit.[70]

At the ESRF, solutions of (PEO 2.5k)$_4$ and (PEO 5k)$_4$ at native pH were loaded into PCR tubes in an automated sample changer. Samples of 30 ul were then delivered in a temperature controlled quartz cell capillary and exposed for 3 s, collecting 10 frames at 20 °C. Data was collected using a Pilatus Dectris 1M detector. The sample detector distance was 2.89 m. Form factor modelling was done using SASfit.[70]

SAXS for Gels was also performed on Diamond beamline B21, with a custom-designed gel cell with kapton windows. Samples were manually loaded, and exposed for 3 s, collecting 18 frames at 20 °C. Data was collected using a Pilatus Dectris 2M detector. Background was manually subtracted using ScÅtter.[69] Form factor modelling was done using SASfit.[70]

4.4.9 Cytotoxicity Studies

The cytotoxicity of both the [poly(L-tyrosine$_{4-5}$)-*b*-(PEO 2.5k)]$_4$ and [poly(L-tyrosine$_{3-4}$)-*b*-(PEO 5k)]$_4$ was examined. In vitro cell culture was conducted using 161Br (ECACC), a human skin fibroblast cell line. Cells were cultured in EMEM, with 2 mM glutamine, enriched with 15% fetal bovine serum (FBS) and 1% non-essential amino acids (NEAA). Cells were maintained in a humidified atmosphere of 37 °C, 5% CO_2.

Potential cytotoxic effects were examined using the MTT (3-(4,5-dimethylthiazol-2-yl)-2,5-diphenyltetrazolium bromide) assay. The polymers [poly(L-tyrosine$_{4-5}$)-*b*-(PEO 2.5k)]$_4$ and [poly(L-tyrosine$_{3-4}$)-*b*-(PEO 5k)]$_4$ were dissolved in complete medium and 2% DMSO, and sterile filtered. Cells were seeded into a 96-well plate at $4x10^4$ cells/mL and allowed to adhere for 24 hours in 100 µL complete medium. After this, 100 µL of either complete media and/or peptide solution was added, to give either control solution (complete media, 1% DMSO), and solutions containing 5 mg/mL, 1 mg/mL, 0.5 mg/mL, 0.1 mg/mL and 0.05 mg/mL peptide (1% DMSO).

Cells were incubated for 67 hours. After this, 20 µL MTT (5 mg/ mL, in PBS) was added to each well plate and allowed to incubate for 5 hours. After a further 5 hours of MTT addition (72 hours total) the solution was removed from the wells and replaced with 100 µL DMSO per well, which dissolves the formazan crystals. Plates were incubated for 30 minutes, and then analysed using the UV microplate reader (λ=570 nm). Results are reported as a % cell viability compared to control (untreated) values.

4.4.10 Peptide-functionalised Gels

Peptide conjugate decorated gels were prepared by adding poly(L-tyrosine$_{4\text{-}5}$)-*b*-(PEO 2.5k)]$_4$ and [poly(L-tyrosine$_{3\text{-}4}$)-*b*-(PEO 5k)]$_4$ to a solution of 1 wt% sodium alginate, in the final concentrations of 0.1 wt%, 1 wt% and 5 wt% (excluding poly(L-tyrosine$_{4\text{-}5}$)-*b*-(PEO 2.5k)]$_4$ as it was not soluble at this concentration). To each solution, $CaCl_2$ was added up to a concentration of 0.1 wt%. The solutions were vortexed for 3 minutes, and left at room temperature for 24 hours to allow gel formation.

4.5 References

(1) Schlaad, H. Solution Properties of Polypeptide-Based Copolymers. *Adv. Polym. Sci.* **2006**, *202* (1), 53–73.

(2) Heredia, K. L.; Maynard, H. D. Synthesis of Protein-Polymer Conjugates. *Org. Biomol. Chem.* **2007**, *5* (1), 45–53.

(3) Canalle, L. a; Löwik, D. W. P. M.; van Hest, J. C. M. Polypeptide-Polymer Bioconjugates. *Chem. Soc. Rev.* **2010**, *39* (1), 329–353.

(4) Nicolas, J.; Mantovani, G.; Haddleton, D. M. Living Radical Polymerization as a Tool for the Synthesis of Polymer-Protein/Peptide Bioconjugates. *Macromol. Rapid Commun.* **2007**, *28* (10), 1083–1111.

(5) Gauthier, M. a; Klok, H.-A. Peptide/Protein-Polymer Conjugates: Synthetic Strategies and Design Concepts. *Chem. Commun. (Camb).* **2008**, No. 23, 2591–2611.

(6) Klok, H. A. Peptide/Protein-Synthetic Polymer Conjugates: Quo Vadis. *Macromolecules* **2009**, *42* (21), 7990–8000.

(7) Rabotyagova, O. S.; Cebe, P.; Kaplan, D. L. Protein-Based Block Copolymers. *Biomacromolecules* **2011**, *12* (2), 269–289.

(8) Hamley, I. W. PEG-Peptide Conjugates. *Biomacromolecules* **2014**, *15* (5), 1543–1559.

(9) Petka, W. A.; Harden, J. L.; Mcgrath, K. P.; Wirtz, D.; Tirrell, D. A. Reversible Hydrogels from Self-Assembling Artificial Proteins. *Science (80-.).* **1998**, *281* (5375), 389–392.

(10) Shen, W.; Zhang, K.; Kornfield, J. a; Tirrell, D. a. Tuning the Erosion Rate of Artificial Protein Hydrogels through Control of Network Topology. *Nat. Mater.* **2006**, *5* (2), 153–158.

(11) Hamley, I. W.; Cheng, G.; Castelletto, V. A Thermoresponsive Hydrogel Based on Telechelic PEG End-Capped with Hydrophobic Dipeptides. *Macromol. Biosci.* **2011**, *11* (8), 1068–1078.

(12) Stahl, P. J.; Romano, N. H.; Wirtz, D.; Yu, S. M. PEG-Based Hydrogels with Collagen Mimetic Peptide-Mediated and Tunable Physical Cross-Links. *Biomacromolecules* **2010**, *11* (9), 2336–2344.

(13) Jing, P.; Rudra, J. S.; Herr, A. B.; Collier, J. H. Self-Assembling Peptide-Polymer Hydrogels Designed from the Coiled Coil Region of Fibrin. *Biomacromolecules* **2008**, *9* (9), 2438–2446.

(14) Tzokova, N.; Fernyhough, C. M.; Topham, P. D.; Sandon, N.; Adams, D. J.; Butler, M. F.; Armes, S. P.; Ryan, A. J. Soft Hydrogels from Nanotubes of Poly(Ethylene Oxide)-Tetraphenylalanine Conjugates Prepared by Click Chemistry. *Langmuir* **2009**, *25* (4), 2479–2485.

(15) Nishiyama, N.; Okazaki, S.; Cabral, H.; Miyamoto, M.; Kato, Y.; Sugiyama, Y.; Nishio, K.; Matsumura, Y.; Kataoka, K. Novel Cisplatin-Incorporated Polymeric Micelles Can Eradicate Solid Tumors in Mice. *Cancer Res.* **2003**, *63* (24), 8977–8983.

(16) Hu, F. Q.; Zhang, Y. Y.; You, J.; Yuan, H.; Du, Y. Z. PH Triggered Doxorubicin Delivery of PEGylated Glycolipid Conjugate Micelles for Tumor Targeting Therapy. *Mol. Pharm.* **2012**, *9* (9), 2469–2478.

(17) Bae, Y.; Kataoka, K. Intelligent Polymeric Micelles from Functional Poly(Ethylene Glycol)-Poly(Amino Acid) Block Copolymers. *Adv. Drug Deliv. Rev.* **2009**, *61* (10), 768–784.

(18) Karakoti, A. S.; Das, S.; Thevuthasan, S.; Seal, S. Minireviews PEGylated Inorganic Nanoparticles. *Angew. Chem. Int. Ed.* **2011**, *50* (9), 1980–1994.

(19) Brown, S. D.; Nativo, P.; Smith, J. A.; Stirling, D.; Edwards, P. R.; Venugopal, B.; Flint, D. J.; Plumb, J. A.; Graham, D.; Wheate, N. J. Gold Nanoparticles for the Improved Anticancer Drug Delivery of the Active Component of Oxaliplatin. *J. Am. Chem. Soc.* **2010**, *132* (13), 4678–4684.

(20) Kolate, A.; Baradia, D.; Patil, S.; Vhora, I.; Kore, G.; Misra, A. PEG - A Versatile Conjugating Ligand for Drugs and Drug Delivery Systems. *J. Control. Release* **2014**, *192*, 67–81.

(21) Van Vlierberghe, S.; Dubruel, P.; Schacht, E. Biopolymer-Based Hydrogels as Scaffolds for Tissue Engineering Applications: A Review. *Biomacromolecules* **2011**, *12* (5), 1387–1408.

(22) DeForest, C. A.; Tirrell, D. A. A Photoreversible Protein-Patterning Approach for Guiding Stem Cell Fate in Three-Dimensional Gels. *Nat. Mater.* **2015**, *14* (5), 523–531.

(23) Yu, T. T.; Shoichet, M. S. Guided Cell Adhesion and Outgrowth in Peptide-Modified Channels for Neural Tissue Engineering. *Biomaterials* **2005**, *26* (13), 1507–1514.

(24) Castelletto, V.; Nutt, D. R.; Hamley, I. W.; Bucak, S.; Cenker, C.; Olsson, U. Structure of Single-Wall Peptide Nanotubes: In Situ Flow Aligning X-Ray Diffraction. *Chem Commun* **2010**, *46* (34), 6270–6272.

(25) Murphy, W. L.; McDevitt, T. C.; Engler, A. J. Materials as Stem Cell Regulators. *Nat. Mater.* **2014**, *13* (6), 547–557.

(26) Thiele, J.; Ma, Y.; Bruekers, S. M. C.; Ma, S.; Huck, W. T. S. 25th Anniversary Article: Designer Hydrogels for Cell Cultures: A Materials Selection Guide. *Adv. Mater.* **2014**, *26* (1), 125–148.

(27) Miller, J. S.; Shen, C. J.; Legant, W. R.; Baranski, J. D.; Blakely, B. L.; Chen, C. S. Bioactive Hydrogels Made from Step-Growth Derived PEG-Peptide Macromers. *Biomaterials* **2010**, *31* (13), 3736–3743.

(28) Wilson, M. J.; Liliensiek, S. J.; Murphy, C. J.; Murphy, W. L.; Nealey, P. F. Hydrogels with Well-Defined Peptide-Hydrogel Spacing and Concentration: Impact on Epithelial Cell Behavior(). *Soft Matter* **2012**, *8* (2), 390–398.

(29) Liu, S. Q.; Tay, R.; Khan, M.; Rachel Ee, P. L.; Hedrick, J. L.; Yang, Y. Y. Synthetic Hydrogels for Controlled Stem Cell Differentiation. *Soft Matter* **2010**, *6* (1), 67.

(30) Hersel, U.; Dahmen, C.; Kessler, H. RGD Modified Polymers: Biomaterials for Stimulated Cell Adhesion and Beyond. *Biomaterials* **2003**, *24* (24), 4385–4415.

(31) Cooke, M. J.; Vulic, K.; Shoichet, M. S. Design of Biomaterials to Enhance Stem Cell Survival When Transplanted into the Damaged Central Nervous System. *Soft Matter* **2010**, *6* (20), 4988.

(32) Slaughter, B. V; Khurshid, S. S.; Fisher, O. Z. Hydrogels in Regenerative Medicine. *Adv. Mater.* **2009**, *21* (0), 3307–3329.

(33) Annable, T. The Rheology of Solutions of Associating Polymers: Comparison of Experimental Behavior with Transient Network Theory. *J. Rheol. (N. Y. N. Y).* **1993**, *37* (4), 695.

(34) Winnik, M. A.; Yekta, A. Associative Polymers in Aqueous Solution. *Curr. Opin. Colloid Interface Sci.* **1997**, *2* (4), 424–436.

(35) Hamley, I. Block Copolymers in Solution: Fundamentals and Applications; Wiley, 2005.

(36) Dekker, F. J.; de Mol, N. J.; van Ameijde, J.; Fischer, M. J. E.; Ruijtenbeek, R.; Redegeld, F. A. M.; Liskamp, R. M. J. Replacement of the Intervening Amino Acid Sequence of a Syk-Binding Diphosphopeptide by a Nonpeptide Spacer with Preservation of High Affinity. *ChemBioChem* **2002**, *3* (2–3), 238–242.

(37) Pilkington-Miksa, M. A.; Sarkar, S.; Writer, M. J.; Barker, S. E.; Shamlou, P. A.; Hart, S. L.; Hailes, H. C.; Tabor, A. B. Synthesis of Bifunctional Integrin-Binding Peptides Containing PEG Spacers of Defined Length for Non-Viral Gene Delivery. *European J. Org. Chem.* **2008**, *2008* (17), 2900–2914.

(38) Huang, J.; Hastings, C. L.; Duffy, G. P.; Kelly, H. M.; Raeburn, J.; Adams, D. J.; Heise, A. Supramolecular Hydrogels with Reverse Thermal Gelation Properties from (Oligo)Tyrosine Containing Block Copolymers. *Biomacromolecules* **2013**, *14* (1), 200–206.

(39) Kirkham, S.; Castelletto, V.; Hamley, I. W.; Reza, M.; Ruokolainen, J.; Hermida-Merino, D.; Bilalis, P.; Iatrou, H. Self-Assembly of Telechelic Tyrosine End-Capped PEO and Poly(Alanine) Polymers in Aqueous Solution. *Biomacromolecules* **2016**, *17* (3), 1186–1197.

(40) Julich-Gruner, K. K.; Neffe, A. T.; Lendlein, A. Synthesis and Characterization of Oligo(Ethylene Glycol)s Functionalized with Desaminotyrosine or Desaminotyrosyltyrosine. *J. Appl. Biomater. Funct. Mater.* **2012**, *10* (3), 170–176.

(41) Zaupa, A.; Neffe, A. T.; Pierce, B. F.; Nöchel, U.; Lendlein, A. Influence of Tyrosine-Derived Moieties and Drying Conditions on the Formation of Helices in Gelatin. *Biomacromolecules* **2011**, *12* (1), 75–81.

(42) Neffe, A. T.; Zaupa, A.; Pierce, B. F.; Hofmann, D.; Lendlein, A. Knowledge-Based Tailoring of Gelatin-Based Materials by Functionalization with Tyrosine-Derived Groups. *Macromol. Rapid Commun.* **2010**, *31* (17), 1534–1539.

(43) Popescu, M.-T.; Liontos, G.; Avgeropoulos, A.; Tsitsilianis, C. Stimuli Responsive Fibrous Hydrogels from Hierarchical Self-Assembly of a Triblock Copolypeptide. *Soft Matter* **2015**, *11* (2), 331–342.

(44) Edwards-Gayle, C. J. C.; Greco, F.; Hamley, I. W.; Rambo, R. P.; Reza, M.; Ruokolainen, J.; Skoulas, D.; Iatrou, H. Self-Assembly of Telechelic Tyrosine End-Capped PEO Star Polymers in Aqueous Solution. *Biomacromolecules* **2018**, *19* (1), 167–177.

(45) Black, S. D.; Mould, D. R. Development of Hydrophobicity Parameters to Analyze Proteins Which Bear Post- or Cotranslational Modifications. *Anal. Biochem.* **1991**, *193* (1), 72–82.

(46) White, S. H.; Wimley, W. C. Membrane Protein Folding and Stability: Physical Principles. *Annu. Rev. Biophys. Biomol. Struct.* **1999**, *28*, 319–365.

(47) Kyte, J.; Doolittle, R. F. A Simple Method for Displaying the Hydropathic Character of a Protein. *J. Mol. Biol.* **1982**, *157* (1), 105–132.

(48) Lamorte, L.; Park, M. The Receptor Tyrosine Kinases: Role in Cancer Progression. *Surg.Oncol.Clin.N.Am.* **2001**, *10* (2), 271–288.

(49) Gschwind, A.; Fischer, O. M.; Ullrich, A. The Discovery of Receptor Tyrosine Kinases: Targets for Cancer Therapy. *Nat. Rev. Cancer* **2004**, *4* (5), 361–370.

(50) Lindgren, M.; Sörgjerd, K.; Hammarström, P. Detection and Characterization of Aggregates, Prefibrillar Amyloidogenic Oligomers, and Protofibrils Using Fluorescence Spectroscopy. *Biophys. J.* **2005**, *88* (6), 4200–4212.

(51) Gasymov, O. K.; Glasgow, B. J. ANS Fluorescence: Potential to Augment the Identification of the External Binding Sites of Proteins. *Biochim. Biophys. Acta - Proteins Proteomics* **2007**, *1774* (3), 403–411.

(52) Hawe, A.; Sutter, M.; Jiskoot, W. Extrinsic Fluorescent Dyes as Tools for Protein Characterization. *Pharm. Res.* **2008**, *25* (7), 1487–1499.

(53) Castelletto, V.; Gouveia, R. M.; Connon, C. J.; Hamley, I. W. New RGD-Peptide Amphiphile Mixtures Containing a Negatively Charged Diluent. *Faraday Discuss.* **2013**, *166*, 381–397.

(54) Castelletto, V.; Kirkham, S.; Hamley, I. W.; Kowalczyk, R.; Rabe, M.; Reza, M.; Ruokolainen, J. Self-Assembly of the Toll-Like Receptor Agonist Macrophage-Activating Lipopeptide MALP-2 and of Its Constituent Peptide. *Biomacromolecules* **2016**, *17* (2), 631–640.

(55) Barth, A. The Infrared Absorption of Amino Acid Side Chains. *Prog. Biophys. Mol. Biol.* **2000**, *74* (3–5), 141–173.

(56) Barth, A.; Haris, P. I. Biological and Biomedical Infrared Spectroscopy; IOS Press, 2009; Vol. 2.

(57) Barth, A. The Infrared Absorption of Amino Acid Side Chains. *Prog. Biophys. Mol. Biol.* **2001**, *74* (2000), 141–173.

(58) Stuart, B. H. Infrared Spectroscopy: Fundamentals and Applications; Wiley, 2004.

(59) Dehsorkhi, A.; Castelletto, V.; Hamley, I. W.; Harris, P. J. F. Multiple Hydrogen Bonds Induce Formation of Nanoparticles with Internal Microemulsion Structure by an Amphiphilic Copolymer. *Soft Matter* **2011**, *7* (21), 10116.

(60) Hamley, I. W. Peptide Fibrillization. *Angew. Chemie - Int. Ed.* **2007**, *46* (43), 8128–8147.

(61) Giri, K.; Bhattacharyya, N. P.; Basak, S. PH-Dependent Self-Assembly of Polyalanine Peptides. *Biophys. J.* **2007**, *92* (1), 293–302.

(62) Hamley, I. W.; Castelletto, V.; Moulton, C. M.; Rodríguez-Pérez, J.; Squires, A. M.; Eralp, T.; Held, G.; Hicks, M. R.; Rodger, A. Alignment of a Model Amyloid Peptide Fragment in Bulk and at a Solid Surface. *J. Phys. Chem. B* **2010**, *114* (24), 8244–8254.

(63) Smail, E. H.; Briza, P.; Panagos, A.; Berenfeld, L. Candida Albicans Cell Walls Contain the Fluorescent Cross-Linking Amino Acid Dityrosine. *Infect. Immun.* **1995**, *63* (10), 4078–4083.

(64) Castelletto, V.; Hamley, I. W. Self Assembly of a Model Amphiphilic Phenylalanine Peptide/Polyethylene Glycol Block Copolymer in Aqueous Solution. *Biophys. Chem.* **2009**, *141* (2–3), 169–174.

(65) Teraoka, I. Polymer Solutions: An Introduction to Physical Properties; Wiley, 2002.

(66) Li, B.; Dong, X.; Fang, S.; Gao, J.; Yang, G.; Zhao, H. Systemic Toxicity and Toxicokinetics of

a High Dose of Polyethylene Glycol 400 in Dogs Following Intravenous Injection. *Drug Chem. Toxicol.* **2011**, *34* (2), 208–212.

(67) Khattak, S. F.; Chin, K. S.; Bhatia, S. R.; Roberts, S. C. Enhancing Oxygen Tension and Cellular Function in Alginate Cell Encapsulation Devices through the Use of Perfluorocarbons. *Biotechnol. Bioeng.* **2007**, *96* (1), 156–166.

(68) Hamley, I. W.; Kirkham, S.; Dehsorkhi, A.; Castelletto, V.; Adamcik, J.; Mezzenga, R.; Ruokolainen, J.; Mazzuca, C.; Gatto, E.; Venanzi, M.; et al. Self-Assembly of a Model Peptide Incorporating a Hexa-Histidine Sequence Attached to an Oligo-Alanine Sequence, and Binding to Gold NTA/Nickel Nanoparticles. *Biomacromolecules* **2014**, *15* (9), 3412–3420.

(69) Rambo, R. P. Http://Www.Bioisis.Net/.

(70) Breßler, I.; Kohlbrecher, J.; Thünemann, A. F. *SASfit* : A Tool for Small-Angle Scattering Data Analysis Using a Library of Analytical Expressions. *J. Appl. Crystallogr.* **2015**, *48* (5), 1587–1598.

Chapter 5.

The Self-Assembly of Oxytocin, Carbetocin and Derivatives in Water and Ethanol

5.1 Introduction

Self-assembly is the ability of molecules to organise into ordered structures from a bottom up approach. This process is fundamentally important for life, and has a range of applications including material science and biotechnology.[1–5] Self-assembling peptides which form nanotube structures are of high interest due to their many applications including antimicrobials, biomineralization, photosystem models, biosensors and biomaterials.[6,7]

The ability of short sequenced cyclised peptides consisting of alternating -L and -D amino acids has been extensively examined. Ghandiri and co-workers demonstrated controlled nanotube formation of cyclo(L-Gln-D-Ala-L-Glu-D-Ala) based on pH variation, characterised by a range of biophysical techniques and modelling.[8–10] Lambert and co-workers confirmed pH variation as a method to control nanotube formation of an -L,-D-alternating octapeptide containing two Asp units.[11] Cyclic peptides containing β-amino acids have also been shown to form nanotubes with a similar stacking interaction to -L, -D-alternating nanotubes[12] that can form ion channels in bilayers. These may act as affinity sites for different proteins.[13] Another class of cyclic peptide that forms nanotubes are those consisting of D-amino acids and γ-aminocyclohexanecarboxylic acid, which gives the core of the nanotubes hydrophobic cavities, providing potential functionalisation capabilities.[14–18]

Lanreotide, (NH_3-(D)Nap-Cys-Tyr-(D)Trp-Lys-Val-Cys-Thr-$CONH_2$), is a synthetic peptide and a growth hormone inhibitor, used to treat acromegaly. It forms a hydrogel which is administered as a long acting implant in patients. The self-assembly of Lanreotide has been extensively examined.[19,20] The pathway of assembly is β-hairpin structures, which dimerise to form open ribbons, followed by the formation of helical ribbons, which later close to form nanotubes.[21,22] The self-assembly is driven by amphiphilicity, and the segregation of the aromatic side chains which leads to β-sheet associations. A series of mutational studies found that D(Napj) and Tyr were the drives of the self-assembly into nanotubes.[23] At 10 wt%, these nanotubes are monodisperse.,[19] with higher concentrations having polydispersity and embedded tubes.[19,20] Double walled Lanreotide nanotubes have been observed when combined with silica[24] and divalent counterions, the latter of which was shown to affect the diameter.[25,26] These can have applications in biomineralization.

Recently the self-assembly of the peptide hormone oxyntomodulin, a 37 long amino acid, was examined.[27] Oxyntomodulin is an agonist to glucagon and GLP-1 receptors, with promise to be a treatment for obesity, as it suppresses appetite and increases energy expenditure.[28–31] Oxyntomodulin was found to form nanofibers of ~10 nm diameter and up to 1 µm length in water at 1 wt%, forming a gel-like structure. These fibres were shown to be stable at 0.1 wt%, and were shown to release oxyntomodulin slowly in rat models, prolonging exposure compared to free oxyntomodulin from 4 hours to 5 days.[27]

Oxytocin (CYIQNCPLG) is a nine amino-acid neuropeptide which has been well characterised biologically.[32,33] Oxytocin has both physiological actions as well as psychological actions in many species, and is a critical hormone in the central and peripheral nervous systems. This includes childbirth and lactation in mammals, bonding, modulation of anxiety and roles in autism development.[32,33] Oxytocin has a disulphide salt bridge between the two cysteine residues which cause cyclisation.

Oxytocin is also administered to mothers who have just given birth to prevent the loss of blood postpartum.[34] Although oxytocin is effective for this, it is unstable at higher temperatures, due to the disulphide and amide bonding within its structure. This is an issue in countries where Oxytocin cannot be stored at lower temperatures. To overcome this, an analogue of oxytocin, carbetocin, (Butyryl-Tyr(Me)-Ile-Gln-Asn-Cys-Pro-Leu-Gly-NH_2) which does not have these heat stable regions, has been shown to be as effective as oxytocin for preventing excessive bleeding during childbirth.[35,36]

This chapter focuses on the self-assembly behaviour of oxytocin and carbetocin at native pH and pH 12 in aqueous conditions. The peptides are examined using an array of biophysical characterisation techniques to include: Fluorescence CD, SAXS, FTIR, Cryo-TEM and TEM. Finally, the behaviour of a lipidated variant of oxytocin (named LOT-1) is examined in ethanol (as it is insoluble in water) and compared to the self-assembly of oxytocin in ethanol.

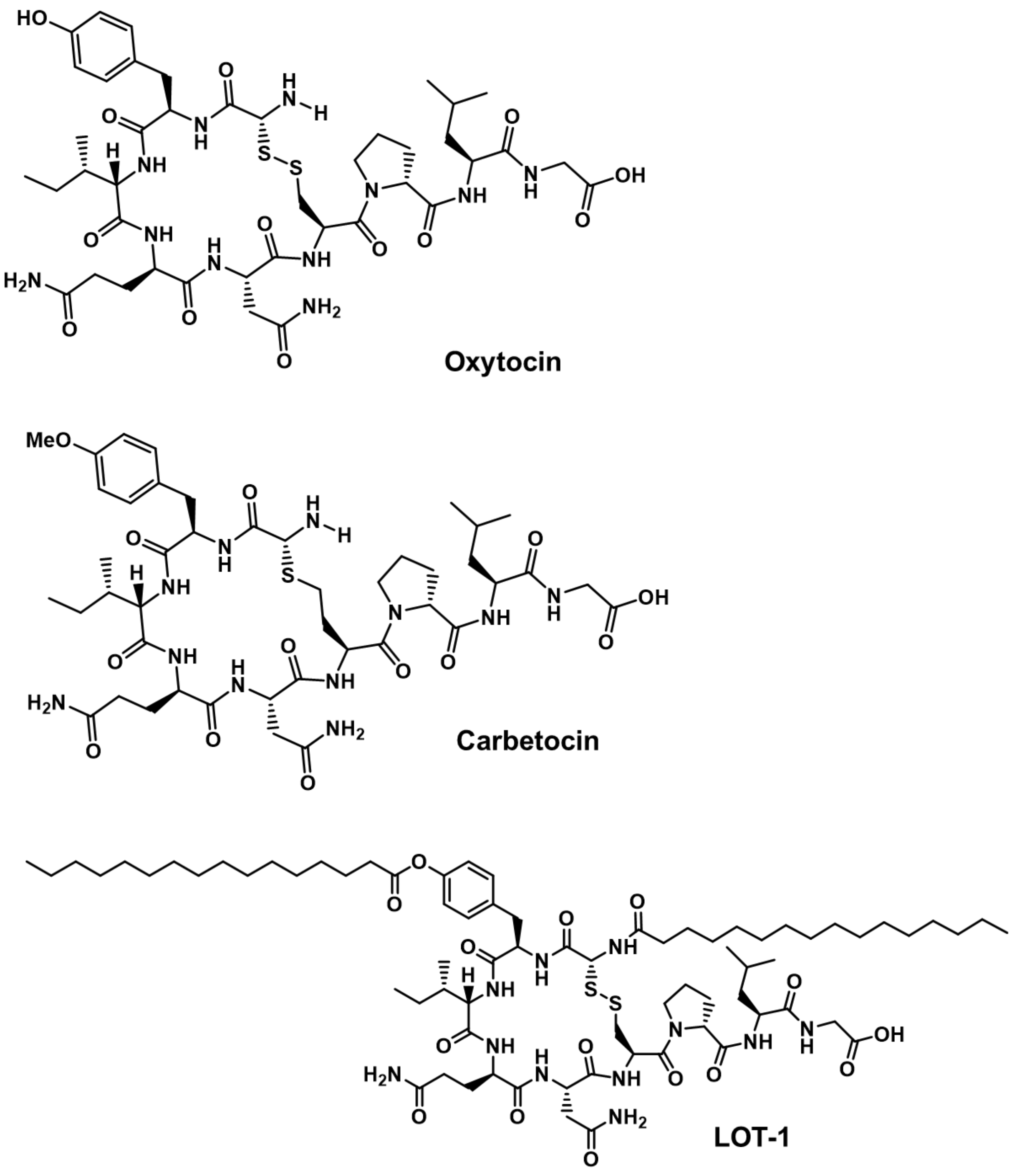

Scheme 5.1. *Structures of oxytocin, carbetocin and LOT-1*

5.2 Results

5.2.1 Self-assembly of carbetocin and oxytocin in water.

The self-assembly of both oxytocin and carbetocin at native and pH 12 was examined. To ensure that the peptides did not lyse at pH 12, mass spectroscopy was used. No distinguishable changes were found between native pH and pH 12 (Appendix Figure 3 and 4).

The critical aggregation concentration for oxytocin and carbetocin in water was determined using ANS. ANS binds to the hydrophobic environment, indicating hydrophobic collapse.[37,38] Oxytocin has a *cac* of 0.04 wt%, and carbetocin was found to have a *cac* of 0.09 wt%. The increase in ANS intensity was much more distinguishable with oxytocin than with carbetocin which could mean that carbetocin has a less defined aggregation concentration. This implies that the loss of the S-S disulphide bridge, and the methylation of the tyrosine reduce the aggregation propensity. Methylation of the tyrosine may affect the ability of the ring to have strong π-π stacking interactions.

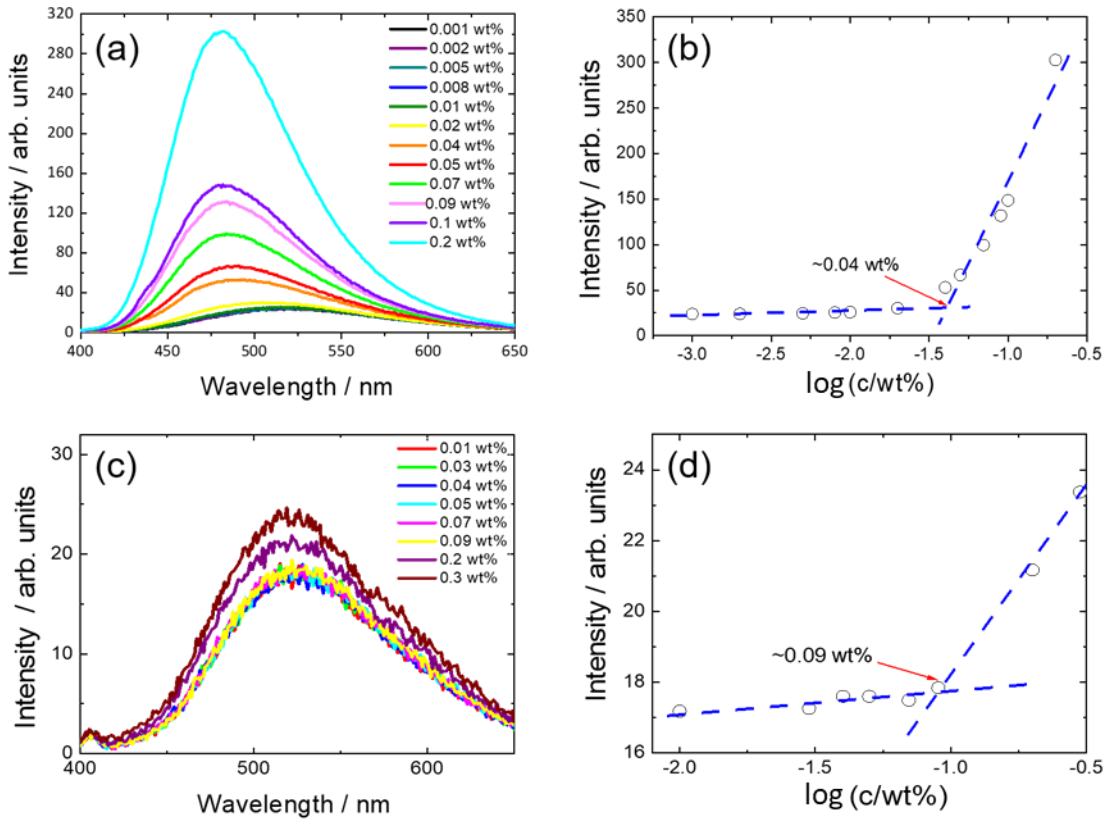

Figure 5.1. *cac values determined by ANS of a) and b) Oxytocin and c) and d) Carbetocin.*

To assess the secondary structure, circular dichroism (CD) and Fourier transform infrared spectroscopy (FTIR) were used. Samples of 1 wt% oxytocin or carbetocin samples were measured. At native pH, oxytocin has a minimum of 205 nm, indicating a disordered secondary structure. The 230 nm peak corresponds to tyrosine. Adjustment to pH 12 causes a shift and broadening of the 230 nm peak present in the native pH to 240 nm, and an increased molar ellipticity of the negative 200 nm peak, indicating disordered secondary structure.[39–41] Temperature CD for oxytocin at native pH showed irreversibility, as the minimum did not return to the original shape. When adjusted to pH 12, oxytocin was temperature reversible. carbetocin at native pH has a minimum peak at 210 nm, with no positive β-sheet band, indicating that carbetocin is disordered.[39–41] The negative molar ellipticity at 210 nm is slightly reduced when adjusted to pH 12, however at pH 12 there is an increase in the 230 nm tyrosine band.[42–44] Both carbetocin at native pH and pH 12 showed reversibility to the original molar ellipticity after heating, unlike oxytocin at native pH. This is expected as oxytocin is reported to be heat sensitive.[35]

At 2 wt% pH 12 oxytocin forms a self-standing gel. Figure 5.3 shows the CD spectrum of oxytocin gel, which shows a minimum peak at 218 nm, indicating that there is a shift from disordered structure to β-sheet secondary structure when adjusting pH.[39–41] Moreover, the shifted tyrosine peak has a significant increase in molar ellipticity indicating the tyrosine rings are stacking together strongly, which could imply that π-stacking is important in the hydrogelation process.

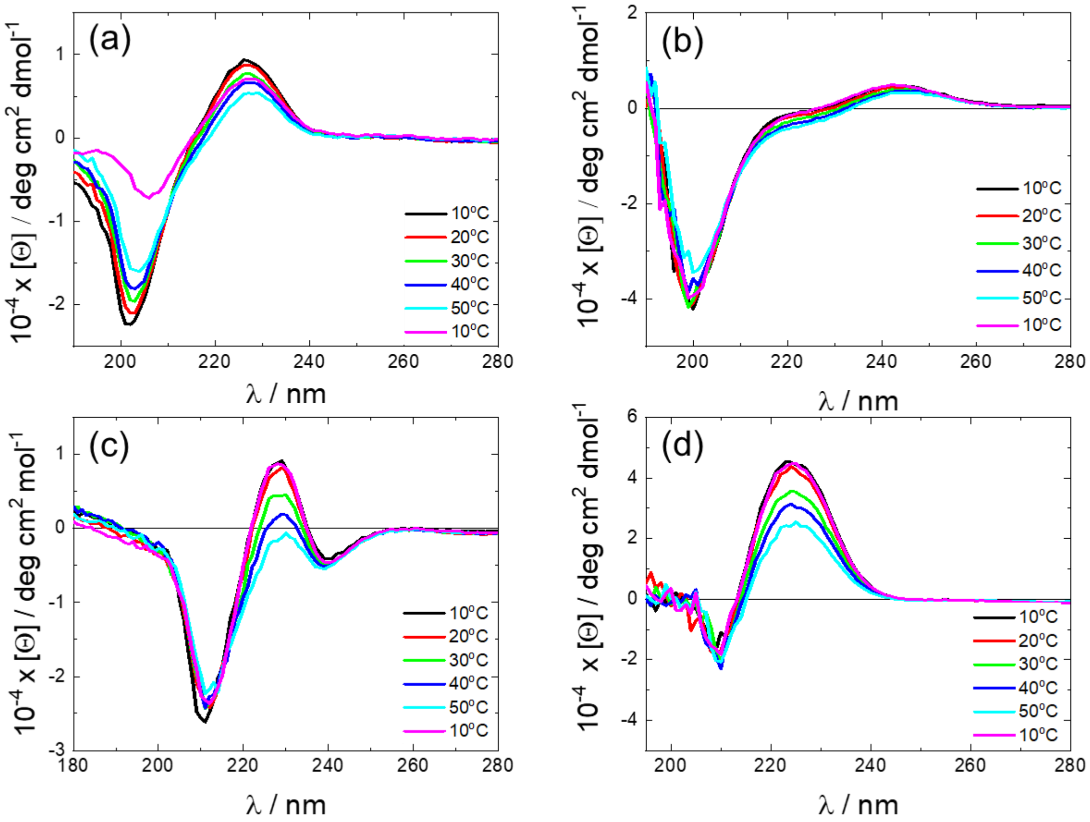

Figure 5.2. CD spectrum of a) 1 wt% oxytocin, pH native, b) 1 wt% oxytocin pH 12, c) 1wt% carbetocin pH native, d) 1 wt% carbetocin pH 12.

FTIR was measured for oxytocin and carbetocin at native pH. The 1458 cm^{-1} peak corresponds to the proline C-N bond vibration.[45] The 1516 cm^{-1} peak corresponds to tyrosine bond vibrations in the C-C and C-H bonds.[45] The third peak at 1559 cm^{-1} corresponds to asparagine side chains.[45] The amide I’ region for both carbetocin and oxytocin is dominated by a large peak around 1643 cm^{-1} at native pH which corresponds to disordered secondary structure, confirming the circular dichroism.[45,46]

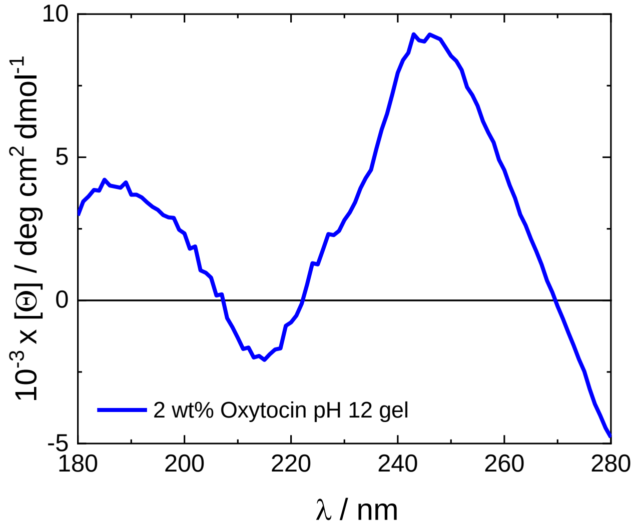

Figure 5.3. *CD spectrum for 2 wt% oxytocin gel.*

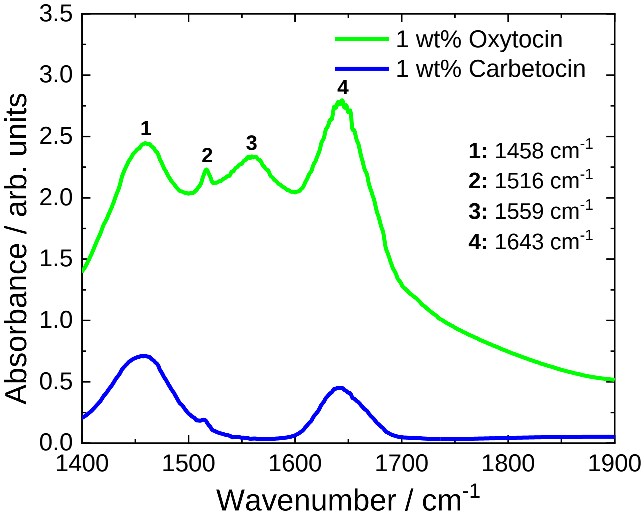

Figure 5.4. *FTIR spectra of 1 wt% oxytocin and 1 wt% carbetocin at native pH*

To examine the self-assembled morphology, SAXS, TEM and cryo-TEM were used for both oxytocin and carbetocin. Cryo-TEM for 1 wt% oxytocin at native pH showed small globular structures with a radius of 21 nm (± 5 nm); these are potentially vesicles. For a 2 wt% sample, TEM revealed that there was a large polydispersity in globular size, ranging from 19 nm to 152 nm. SAXS data for 1 and 2 wt% oxytocin was fitted to a model for monomers, using a generalised Gaussian coil form factor which accounts for clusters of monomers. This fits the data very well. The radius of gyration was found to be 6.8 nm for a 1 wt% sample and 5.8 nm for 2 wt%, with a v of 0.55 for 1 wt%, and 0.19 for the 2wt% sample, showing that at 1 wt% the structure is swollen and 2wt% the structure is more folded.

Cryo-TEM for 1 wt% oxytocin at pH 12 (Figure 5.5), shows a change in the tertiary structure to polydisperse fibrils. These fibrils have a radius of 17 nm ± 6.3, with lengths ranging from 150 nm - 800 nm. Thus, adjustment to pH 12 promotes fibril formation. SAXS data shown in Figure 5.6, did not agree with the cryo-TEM data, showing monomers at 1 wt% pH 12 which was fitted to a Gaussian coil form factor.[47] The discrepancy between native pH and pH 12 oxytocin by cryo-TEM and SAXS requires further investigation, but potentially can be explained by radiation damage, as oxytocin is known to degrade at high temperatures[35] and may be sensitive to X-ray radiation.

The oxytocin hydrogel (2 wt% oxytocin, pH 12) is formed of large fibrils, visualised by TEM (Figure 5.6) and cryo-SEM (Figure 5.7). In TEM these fibrils range from 2.7 μm to 5.3 μm, with radius of 72 nm ± 16 nm. SAXS data shows a low intensity scaling of $I \sim -2.7$, implying that the aggregated particle is larger than the resolution limit, and the data should be remeasured with an increased q range. At high q, there is a Bragg peak at d = 21.2 Å which corresponds approximately to the size of an oxytocin molecule.

For solutions of 1 wt% and 2wt% Carbetocin at native pH and 1 wt% Carbetocin pH 12, no self-assembly at native pH was observed through cryo-TEM, SAXS or TEM. However, as shown in Figure 5.6, 2 wt% Carbetocin shows large spherical structures at low magnification which could also be visualised via light microscope. These aggregates appear to be crystalline in TEM.

When stained with Congo red dye, a dye commonly used to detect amyloid like fibres, both Carbetocin and Oxytocin at 2 wt% adjusted to pH 12 show birefringence through polarised light microscopy (Figure 5.7). As Carbetocin is slightly crystalline at this pH it could imply that the crystal structures are non-cubic.

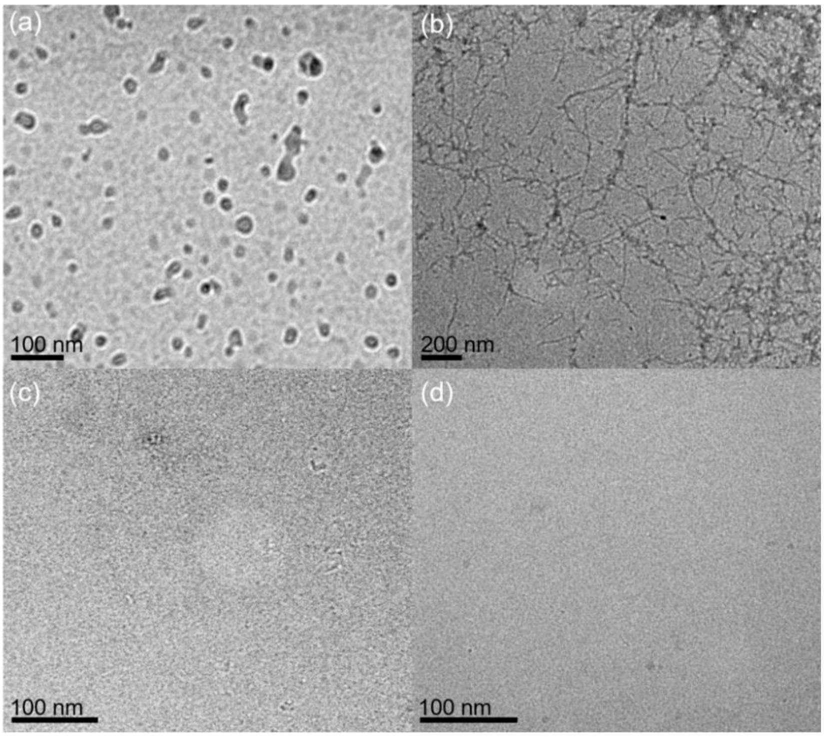

Figure 5.5. *Cryo-TEM images of a) 1 wt% oxytocin, native pH, b) 1 wt% oxytocin, pH 12, c) 1 wt% carbetocin, pH native, d) 1 wt% carbetocin pH 12*

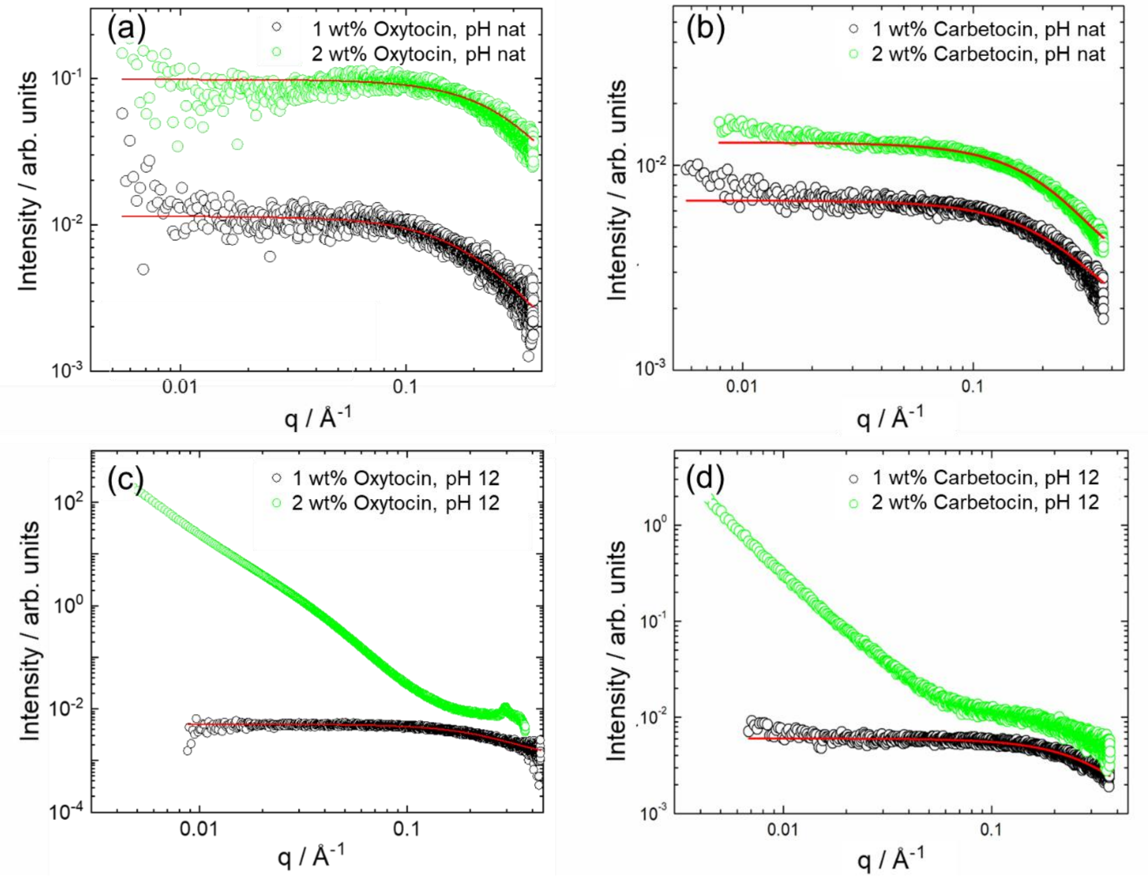

Figure 5.6. *SAXS data for oxytocin and carbetocin.*

Table 5.1. *Fits of oxytocin and carbetocin.*

	1 wt% Oxytocin, pH nat	1 wt% Oxytocin, pH 12	2 wt% Oxytocin, pH nat	1 wt% Carbetocin pH nat	1 wt% Carbetocin pH 12	2 wt% Carbetocin pH nat
R_g	6.8	6.9	5.8	6.5	7.3	5.4
v	0.20	0.24	0.19	0.60	0.27	0.31
I(0)	0.03	0.01	0.03	0.01	0.10	0.01
N	0.15	0.27	0.27	0.52	0.10	0.50
BG	9.28×10^{-4}	1.20×10^{-3}	1.74×10^{-3}	7.513×10^{-4}	2.85×10^{-3}	6.84×10^{-4}

Where v = Flory exponent, R_g is the radius of gyration and I(0) is the forward scattering.

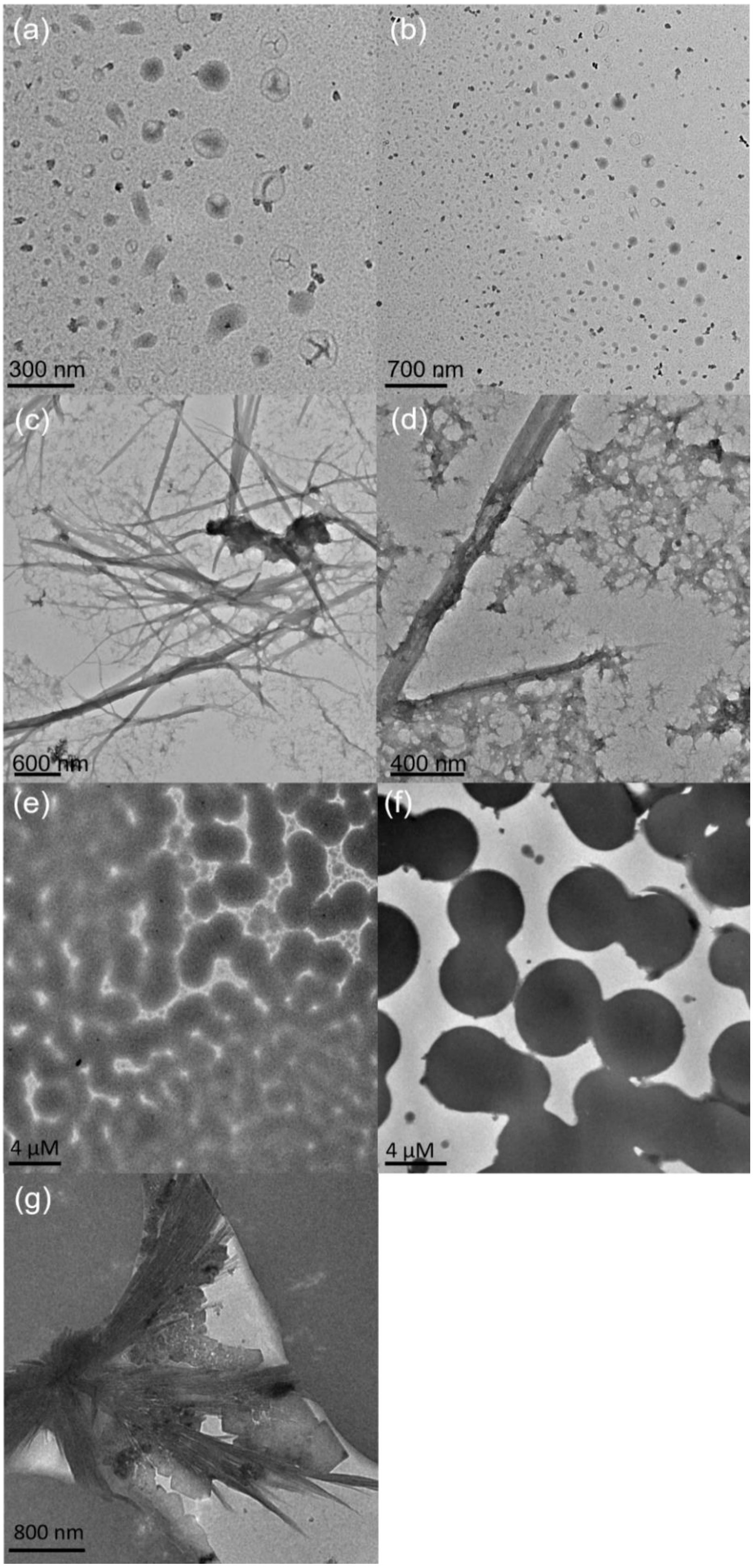

Figure 5.6. *TEM images of a) and b) 2 wt% oxytocin at native pH and c and d) 2 wt% oxytocin at pH 12. e) 2 wt% carbetocin native pH and f) and g) 2 wt% carbetocin pH 12*

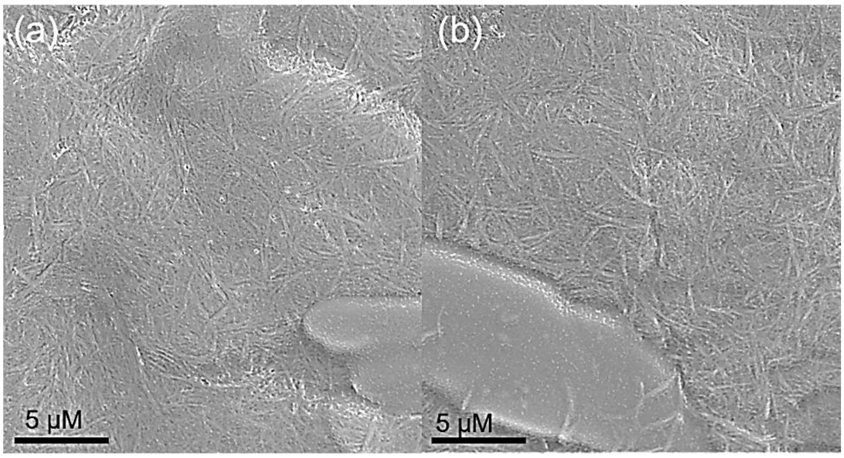

Figure 5.7. *cryo-SEM images of 2wt% Oxytocin pH 12 hydrogel showing fibres.*

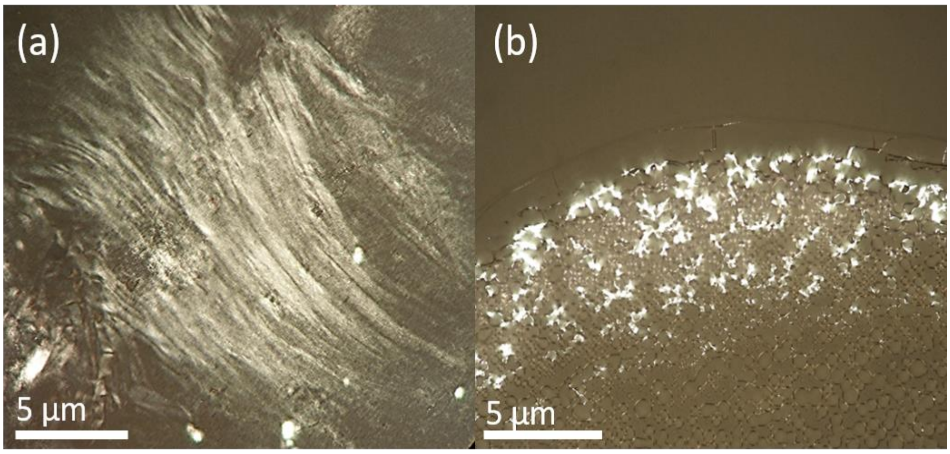

Figure 5.8. *Polarised optical microscopy images of peptides stained with Congo red a) 2 wt% oxytocin pH 12 hydrogel and b) 2 wt% carbetocin pH 12 solution.*

5.2.2 Self-assembly of Oxytocin and LOT-1 in Ethanol

LOT-1 is a lipidated version of oxytocin (Scheme 5.1) which has been modified with two C_{16} palmitoyl chains C_{16}-CY(C_{16})IQNCPLG-NH_2. Due to this lipidation, LOT-1 is not soluble in H_2O, or combinations of H_2O/Ethanol at 0.1 wt%. Therefore, self-assembly was examined in ethanol, and oxytocin was re-examined in ethanol solvent to compare the change in assembly.

Circular dichroism was used to characterise secondary structure. Oxytocin was found to form a poly-proline helix characterised by a double minimum (Figure 5.9a), in the CD spectra, at 220 nm and 205 nm.[48–50] This differs from the secondary structure observed in H_2O which was disordered. Oxytocin in ethanol has a tyrosine peak at 230 nm like that observed in water, however LOT-1 has lost this peak perhaps due to the lipidation of the tyrosine, which may affect the polarity of the ring. LOT-1 had a disordered structure at low temperature characterised by a peak at 205 nm (Figure 5.9b). When the temperature was raised above 30°C, there was an irreversible change in structure, indicating a loss of secondary structure.

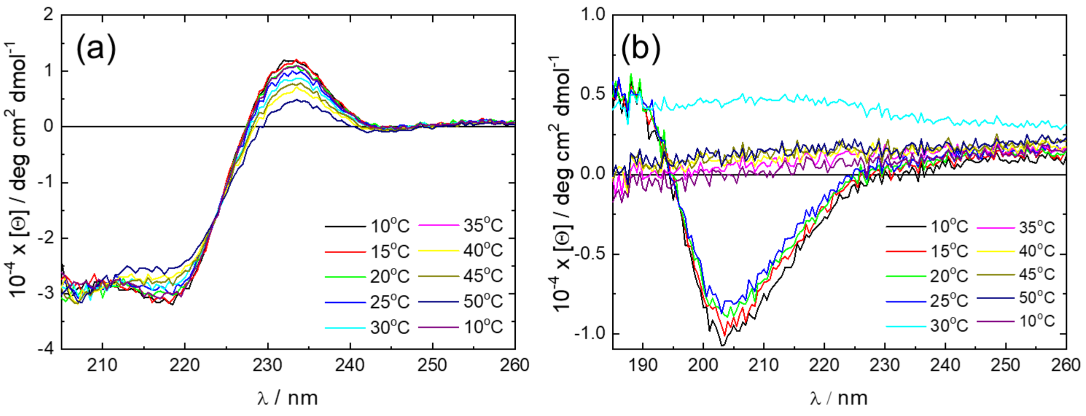

Figure 5.9. *Circular Dichroism of a) 0.5 wt% oxytocin and b) 0.5 wt% LOT-1*

Cryo-TEM and SAXS were used to probe the tertiary structure of LOT-1 and oxytocin in ethanol. Interestingly, the cryo-TEM of Oxytocin in ethanol revealed a mixture of long fibres with a diameter of 6.2 ± 2.5 nm, and spherical globular structures with an average diameter of 17 ± 4.5 nm. The lipidated peptide shows a preference to irregular shaped clusters, with an average diameter of 26.5 ± 4.7 nm. These clusters were seen to aggregate into large fibrillar particles as show in Figure 5.10b.

SAXS for oxytocin was fitted to a long cylindrical shell model. [47] Intensity profiles for Oxytocin fibrils were fitted with a length of 50 nm, compared to LOT-1 which was fitted with a smaller fixed length based on the cryo-TEM showing different fibril morphologies. The radius for these fibres were all roughly around 3 nm, with a shell thickness between 2.0 nm and 2.5 nm. The fit parameters are listed in Table 5.2.

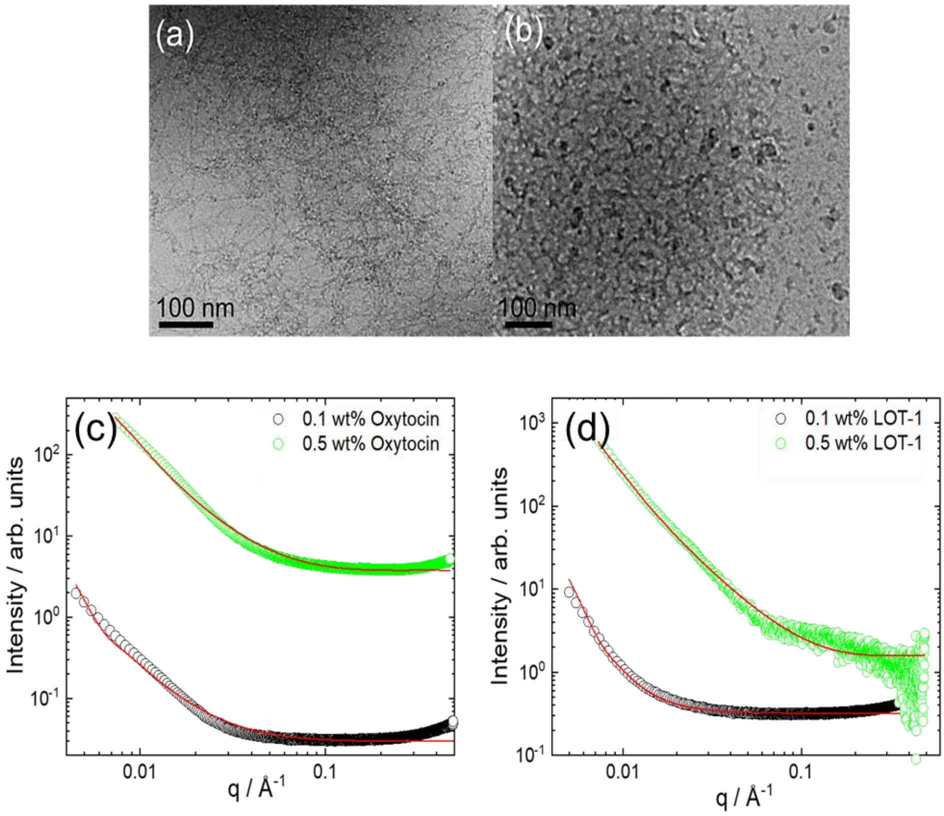

Figure 5.10. *a) Cryo-TEM of 0.5 wt% oxytocin in ethanol b) cryo-TEM of 0.5 wt% LOT-1, and c) and d) SAXS profiles.*

Table 5.2. *SAXS fits parameters for oxytocin and LOT-1 in ethanol fitted using long cylindrical shell form factor.*

	0.1 wt% Oxytocin	0.5 wt% Oxytocin	0.1 wt% LOT-1	0.5 wt% LOT-1
N	0.02	1	0.11	0.19
***R* ± *Δ R* (Å)**	30 ±15	33 ± 15	34 ± 15	30 ± 15
D_r (Å)	2.5	2.5	2.0	2.0
L	500	500	100	100
η_{core} (a.u.)	$9.10x10^{-4}$	$2.58x10^{-3}$	$6.00x10^{-4}$	$6.18x10^{-4}$
η_{shell} (a.u.)	$4.97x10^{-3}$	$1.54x10^{-3}$	$2.60x10^{-3}$	$4.20x10^{-3}$
η_{solv} (a.u.)	$5.79x10^{-5}$	$2.95x10^{-5}$	$3.0x10^{-5}$	$3.12x10^{-5}$
BG	0.014	0.037	0.032	0.15

Here N denotes scaling parameter, R denotes core radius, D_r denotes shell thickness, and η_{core}, η_{shell} and η_{core} denote the scattering length density of the core, shell and solvent, and BG denotes background.

5.3 Conclusions

Overall the self-assembly of oxytocin and carbetocin in aqueous solution, and the self-assembly of LOT-1 and oxytocin in ethanol was examined. Oxytocin at 1 wt% native pH and pH 12 showed conflicting results with cryo-TEM and SAXS, requiring further experiments to understand reasons for the observed discrepancy. Oxytocin is known to degrade at higher temperatures, which limits the current clinical use. This could mean that oxytocin is also radiation sensitive. Thus, other techniques, for example atomic force microscopy (AFM) could be used to examine self-assembly, to complement the cryo-TEM or SAXS studies. Interestingly, Oxytocin forms a β-sheet hydrogel at 2 wt% and pH 12. This hydrogel exhibits anisotropic SAXS patterns and has birefringent properties.

Carbetocin has very weak self-assembly, remaining as a monomer (confirmed by cryo-TEM and SAXS) until adjusted to pH 12 for a 2 wt% solution, for which large birefringent crystalline structures are seen with TEM and polarised light microscopy. This is confirmed by SAXS through a low q intensity scaling with n = -3 decay indicating large particle structures.

Interestingly, in ethanol oxytocin forms poly-proline helical long fibril structures, as confirmed by SAXS and TEM. Lipidation of oxytocin (LOT-1) has poor water solubility and assembles irregularly into clustered fibrils.

5.4 Materials and methods

5.4.1 Materials

Oxytocin, CYIQNCPLG-NH2, M_w=1007.2 cyclised with a disulphide bridge was purchased as an acetate salt from CS Bio at >98% purity. Carbetocin, N(4-Mercapto-1-oxobutyl)-O-methyl-YIQNCPLG-thioester acetate Mw = 988 LOT-1, M_w=1484.02, C_{16}-CY(C_{16})IQNCPLG-NH2 was synthesised at Hokkaido University, and received as a acetate salt, as a gift. Mixtures were made by adding 0.5 wt%, 1 wt% 2 wt% in nano-pure water or EtOH. Adjustment of pH was done using 0.5M NaOH solutions.

5.4.2 Fluorescence Assays

The presence of any critical aggregation concentration (*cac*) was assayed using fluorescence probes, measuring spectra for a series of peptide concentrations. Fluorescence spectra were recorded with a Varian Cary Eclipse fluorescence spectrometer with samples in 4 mm inner width quartz cuvettes. ANS (8-anilinonaphthalene-1-sulfonic acid) was further used to examine whether there is a *cac* for oxytocin and carbetocin in water.

5.4.3. Circular Dichroism (CD) Spectroscopy

CD spectra were recorded using a Chirascan spectropolarimeter (Applied Photophysics, UK) in the wavelength range 180 – 260 nm. Samples containing 1 wt% Carbetocin and Oxytocin in pure H_2O or oxytocin or 0.5 wt% LOT-1 in ethanol at were pipetted into 0.1 mm pathlength quartz cuvettes. Data with absorbance less than 2 at any point only are reported. Measurements were recorded with a 0.5 nm bandwidth, 1 nm step and 1 s collection time per point. The CD signal for the background solution was subtracted from the CD signal of the sample, and molar ellipticity was calculated.

5.4.4. Fourier Transform Infrared (FTIR) Spectroscopy

Spectra were recorded using a Thermo Scientific Nicolet IS5 instrument equipped with a DTGS detector, with a PEARL liquid cell (sample contained between fixed CaF_2 plates). Aliquots containing 80 μL of 1 wt% oxytocin or carbetocin in D_2O were prepared and added to a PEARL liquid cell. Spectra were scanned 128 times over the range of 900 − 4000 cm^{-1}. The peptide signal was background corrected with the FTIR spectra of D_2O.

5.4.5. Cryogenic Transmission Electron Microscopy (cryo-TEM)

Cryo-TEM measurements were performed by Mehedi Reza and Jani Seitsanen at Aalto University, Finland. Vitrified specimens were prepared using an automated FEI Vitrobot device using Quantifoil 3.5/1 holey carbon copper grids with a hole size of 3.5 µm. Prior to use, grids were plasma cleaned using a Gatan Solarus 9500 plasma cleaner and then transferred into the environmental chamber of a FEI Vitrobot at room temperature and 100% humidity. After this, sample solutions were applied onto a grid, and were blotted twice for 5 s and then vitrified in a 1/1 mixture of liquid ethane and propane at a temperature of −180 °C. The grids with vitrified sample solution were maintained at liquid nitrogen temperature and then cryo-transferred to the microscope. Imaging was carried out using a field emission cryo-electron microscope (JEOL JEM-3200FSC) operating at 200 kV. Images were taken in bright field mode and using zero loss energy filtering (Ω type) with a slit width of 20 eV. Micrographs were recorded using a Gatan Ultrascan 4000 CCD camera. The specimen temperature was maintained at −187 °C during the imaging.

5.4.6. Cryo-SEM

Cryo-SEM was performed using an FEI Quanta 600F instrument in the EM CAF laboratory at Reading University. The oxytocin gel was mounted onto aluminium stubs and frozen in a liquid-nitrogen slush at −210°C. Once frozen, the sample was transferred under vacuum to a sample preparation chamber and allowed to equilibrate to the appropriate temperature prior to fracturing. The gel was fractured at −140°C and allowed to sublime at−90°C for approximately 5 minutes. The sample was cooled to −140°C and then coated with platinum and imaged at 5 keV

5.4.7 Transmission Electron Microscopy (TEM)

TEM imaging was performed in the EM CAF laboratory at Reading University, using a JEOL 2100Plus TEM microscope operated at 200 kV. Droplets of sample were placed on Cu grids coated with a carbon film (Agar Scientific, UK), stained with uranyl acetate (1 wt %) (Sigma-Aldrich, UK) and dried. Specimens were then loaded into the microscope.

5.4.8 Optical polarised Microscopy (POM)

Congo Red Staining and Birefringence Monitored by Polarized Optical Microscopy (POM). A filtered solution of 0.5 wt % Congo red solution was pipetted onto a glass microscope slide with oxytocin hydrogel or carbetocin solution, and stained for approximately 2 min. Images of the sample placed between crossed polarizers were obtained with an Olympus CX-41 microscope

5.4.9. Small-angle X-ray scattering (SAXS)

Data from solutions was collected on the bioSAXS beamlines B21 (Diamond Light Source, UK). Peptide solutions were loaded into PCR tubes in an automated sample changer, then 30 μL was delivered into a temperature-controlled quartz capillary and 28 frames (1 s each) of SAXS data were acquired at 20 ^{o}C. For hydrogels, samples were loaded into a custom designed gel cell holder at B21, and measured at ambient temperature. The camera length was 3.9 m, and the X-ray wavelength was λ= 1.02 Å. Data was collected using a Dectris PILATUS 2M detector and processed using ScÅtter,[51]and is presented as a function of $q = 4\pi\sin\theta/\lambda$.

5.5 References

(1) Dehsorkhi, A.; Castelletto, V.; Hamley, I. W. Self-Assembling Amphiphilic Peptides. *J. Pept. Sci.* **2014**, *20* (7), 453–467.

(2) Hamley, I. W. Self-Assembly of Amphiphilic Peptides. *Soft Matter* **2011**, *7*, 4122–4138.

(3) Hamley, I. W. Lipopeptides: From Self-Assembly to Bioactivity. *Chem. Commun.* **2015**, *51* (41), 8574–8583.

(4) Hutchinson, J. A.; Burholt, S.; Hamley, I. W. Peptide Hormones and Lipopeptides: From Self-Assembly to Therapeutic Applications. *J. Pept. Sci.* **2017**, *23* (2), 82–94.

(5) Hamley, I. W.; Castelletto, V. Self-Assembly of Peptide Bioconjugates: Selected Recent Research Highlights. *Bioconjugate Chemistry*. 2017.

(6) Hamley, I. W. Peptide Nanotubes. *Angew. Chemie - Int. Ed.* **2014**, *53* (27), 6866–6881.

(7) Scanlon, S.; Aggeli, A. Self-Assembling Peptide Nanotubes. *Nano Today* **2008**, *3* (3–4), 22–30.

(8) De Santis, P.; Morosetti, S.; Rizzo, R. Conformational Analysis of Regular Enantiomeric Sequences. *Macromolecules* **1974**, *7* (1), 52–58.

(9) Ghadiri, M. R.; Granja, J. R.; Milligan, R. A.; McRee, D. E.; Khazanovich, N. Self-Assembling Organic Nanotubes Based on a Cyclic Peptide Architecture. *Nature* **1993**, *336*, 324–327.

(10) Khazanovich, N.; Granja, J. R.; McRee, D. E.; Milligan, R. A.; Ghadiri, M. R. Nanoscale Tubular Ensembles with Specified Internal Diameters. Design of a Self-Assembled Nanotube with a 13-Å Pore. *J. Am. Chem. Soc.* **1994**, *116* (13), 6011–6012.

(11) Polaskova, M. E.; Ede, N. J.; Lambert, J. N. Synthesis of Nanotubule-Forming Cyclic Octapeptides via an Fmoc Strategy. *Aust. J. Chem.* **1998**, *51* (7), 535–540.

(12) Seebach, D.; Matthews, J. L.; Meden, A.; Wessels, T.; Baerlocher, C.; McCusker, L. B. Cyclo-β-Peptides: Structure and Tubular Stacking of Cyclic Tetramers of 3-Aminobutanoic Acid as Determined from Powder Diffraction Data. *Helv. Chim. Acta* **1997**, *80*, 173.

(13) Clark, T. D.; Buehler, L. K.; Ghadiri, M. R. Self-Assembling Cyclic B3-Peptide Nanotubes as Artificial Transmembrane Ion Channels. *J. Am. Chem. Soc.* **1998**, *120* (4), 651–656.

(14) Amorín, M.; Castedo, L.; Granja, J. R. New Cyclic Peptide Assemblies with Hydrophobic Cavities: The Structural and Thermodynamic Basis of a New Class of Peptide Nanotubes. *J. Am. Chem. Soc.* **2003**, *125* (10), 2844–2845.

(15) Brea, R. J.; Amorín, M.; Castedo, L.; Granja, J. R. Methyl-Blocked Dimeric α,γ-Peptide Nanotube Segments: Formation of a Peptide Heterodimer through Backbone-Backbone Interactions. *Angew. Chemie - Int. Ed.* **2005**, *44* (35), 5710–5713.

(16) Amorín, M.; Brea, R. J.; Castedo, L.; Granja, J. R. The Smallest α,γ-Peptide Nanotubulet Segments: Cyclic α,γ-Tetrapeptide Dimers. *Org. Lett.* **2005**, *7* (21), 4681–4684.

(17) Brea, R. J.; Castedo, L.; Granja, J. R. Large-Diameter Self-Assembled Dimers of α,γ-Cyclic Peptides, with the Nanotubular Solid-State Structure of Cyclo-[(L-Leu-D- MeN-γ-Acp)4-]·4CHCl2COOH. *Chem. Commun.* **2007**, No. 31, 3267–3269.

(18) Reiriz, C.; Amorín, M.; García-Fandiño, R.; Castedo, L.; Granja, J. R. α,γ-Cyclic Peptide Ensembles with a Hydroxylated Cavity. *Org. Biomol. Chem.* **2009**, *7* (21), 4358–4361.

(19) Valéry, C.; Paternostre, M.; Robert, B.; Gulik-Krzywicki, T.; Narayanan, T.; Dedieu, J. C.; Keller, G.; Torres, M. L.; Cherif-Cheikh, R.; Calvo, P.; et al. Biomimetic Organization:

Octapeptide Self-Assembly into Nanotubes of Viral Capsid-like Dimension. *Proc. Natl. Acad. Sci. U. S. A.* **2003**, *100* (18), 10258–10262.

(20) Valéry, C.; Artzner, F.; Robert, B.; Gulick, T.; Keller, G.; Grabielle-Madelmont, C.; Torres, M. L.; Cherif-Cheikh, R.; Paternostre, M. Self-Association Process of a Peptide in Solution: From β-Sheet Filaments to Large Embedded Nanotubes. *Biophys. J.* **2004**, *86* (4), 2484–2501.

(21) Tarabout, C.; Roux, S.; Gobeaux, F.; Fay, N.; Pouget, E.; Meriadec, C.; Ligeti, M.; Thomas, D.; IJsselstijn, M.; Besselievre, F.; et al. Control of Peptide Nanotube Diameter by Chemical Modifications of an Aromatic Residue Involved in a Single Close Contact. *Proc. Natl. Acad. Sci. U. S. A.* **2011**, *108* (19), 7679–7684.

(22) Pouget, E.; Fay, N.; Dujardin, E.; Jamin, N.; Berthault, P.; Perrin, L.; Pandit, A.; Rose, T.; Valéry, C.; Thomas, D.; et al. Elucidation of the Self-Assembly Pathway of Lanreotide Octapeptide into β-Sheet Nanotubes: Role of Two Stable Intermediates. *J. Am. Chem. Soc.* **2010**, *132* (12), 4230–4241.

(23) Valéry, C.; Pouget, E.; Pandit, A.; Verbavatz, J. M.; Bordes, L.; Boisde, I.; Cherif-Cheikh, R.; Artzner, F.; Paternostre, M. Molecular Origin of the Self-Assembly of Lanreotide into Nanotubes: A Mutational Approach. *Biophys. J.* **2008**, *94* (5), 1782–1795.

(24) Pouget, E.; Dujardin, E.; Cavalier, A.; Moreac, A.; Valéry, C.; Marchi-Artzner, V.; Weiss, T.; Renault, A.; Paternostre, M.; Artzner, F. Hierarchical Architectures by Synergy between Dynamical Template Self-Assembly and Biomineralization. *Nat. Mater.* **2007**, *6*, 434–439.

(25) Gobeaux, F.; Fay, N.; Tarabout, C.; Mériadec, C.; Meneau, F.; Ligeti, M.; Buisson, D. A.; Cintrat, J. C.; Nguyen, K. M. H.; Perrin, L.; et al. Structural Role of Counterions Adsorbed on Self-Assembled Peptide Nanotubes. *J. Am. Chem. Soc.* **2012**, *134* (1), 723–733.

(26) Gobeaux, F.; Fay, N.; Tarabout, C.; Meneau, F.; Mériadec, C.; Delvaux, C.; Cintrat, J. C.; Valéry, C.; Artzner, F.; Paternostre, M. Experimental Observation of Double-Walled Peptide Nanotubes and Monodispersity Modeling of the Number of Walls. *Langmuir* **2013**, *29* (8), 2739–2745.

(27) Ouberai, M. M.; Dos Santos, A. L. G.; Kinna, S.; Madalli, S.; Hornigold, D. C.; Baker, D.; Naylor, J.; Sheldrake, L.; Corkill, D. J.; Hood, J.; et al. Controlling the Bioactivity of a Peptide Hormone in Vivo by Reversible Self-Assembly. *Nat. Commun.* **2017**, *8* (1), 41467–017.

(28) Wynne, K.; Park, A. J.; Small, C. J.; Patterson, M.; Ellis, S. M.; Murphy, K. G.; Wren, A. M.; Frost, G. S.; Meeran, K.; Ghatei, M. A.; et al. Subcutaneous Oxyntomodulin Reduces Body Weight in Overweight and Obese Subjects. *Diabetes* **2005**, *54* (8), 2390–2395.

(29) Pocai, A. Unraveling Oxyntomodulin, GLP1's Enigmatic Brother. *J. Endocrinol.* **2012**, *215* (3), 335–346.

(30) Kosinski, J. R.; Hubert, J.; Carrington, P. E.; Chicchi, G. G.; Mu., J.; Miller, C.; Cao, J.; Bianchi., E.; Pessi, A.; Sinharoy, R.; et al. The Glucagon Receptor Is Involved in Mediating the Body Weight-Lowering Effects of Oxyntomodulin. *Obesity* **2012**, *20* (8), 1566–1571.

(31) Pocai, A. Action and Therapeutic Potential of Oxyntomodulin. *Mol. Metab.* **2014**, *3* (3), 241–251.

(32) Lintner, K.; Peschard, O. Biologically Active Peptides: From a Laboratory Bench Curiosity to a Functional Skin Care Product. *Int. J. Cosmet. Sci.* **2000**, *22* (3), 207–218.

(33) Striepens, N.; Kendrick, K. M.; Maier, W.; Hurlemann, R. Prosocial Effects of Oxytocin and Clinical Evidence for Its Therapeutic Potential. *Front. Neuroendocrinol.* **2011**, *32* (4), 426–450.

(34) Gallos, I. D.; Papadopoulou, A.; Man, R.; Athanasopoulos, N.; Tobias, A.; Price, M. J.; Williams, M. J.; Diaz, V.; Pasquale, J.; Chamillard, M.; et al. Uterotonic Agents for Preventing Postpartum Haemorrhage: A Network Meta-Analysis. *Cochrane Database Syst. Rev.* **2018**, *2018* (12).

(35) Attilakos, G.; Psaroudakis, D.; Ash, J.; Buchanan, R.; Winter, C.; Donald, F.; Hunt, L. P.; Draycott, T. Carbetocin versus Oxytocin for the Prevention of Postpartum Haemorrhage Following Caesarean Section: The Results of a Double-Blind Randomised Trial. *BJOG An Int. J. Obstet. Gynaecol.* **2010**, *117* (8), 929–936.

(36) Su, L.-L.; Chong, Y.-S.; Samuel, M. Carbetocin for Preventing Postpartum Haemorrhage. *Cochrane Database Syst. Rev.* **2012**, *15* (2), CD005457.

(37) Hawe, A.; Sutter, M.; Jiskoot, W. Extrinsic Fluorescent Dyes as Tools for Protein Characterization. *Pharm. Res.* **2008**, *25* (7), 1487–1499.

(38) Gasymov, O. K.; Glasgow, B. J. ANS Fluorescence: Potential to Augment the Identification of the External Binding Sites of Proteins. *Biochim. Biophys. Acta - Proteins Proteomics* **2007**, *1774* (3), 403–411.

(39) Greenfield, N. J. Applications of Circular Dichroism in Protein and Peptide Analysis. *TrAC - Trends Anal. Chem.* **1999**, *18* (4), 236–245.

(40) Castelletto, V.; Hamley, I. W. Methods to Characterize the Nanostructure and Molecular Organization of Amphiphilic Peptide Assemblies. In *Peptide Self-Assembly: Methods and Protocols*; Nilsson, B. L., Doran, T. M., Eds.; Springer New York: New York, NY, 2018; pp 3–21.

(41) Greenfield, N. J. Using Circular Dichroism Spectra to Estimate Protein Secondary Structure. *Nat. Protoc.* **2007**, *1* (6), 2876–2890.

(42) Kirkham, S.; Castelletto, V.; Hamley, I. W.; Reza, M.; Ruokolainen, J.; Hermida-Merino, D.; Bilalis, P.; Iatrou, H. Self-Assembly of Telechelic Tyrosine End-Capped PEO and Poly(Alanine) Polymers in Aqueous Solution. *Biomacromolecules* **2016**, *17* (3), 1186–1197.

(43) Edwards-Gayle, C. J. C.; Greco, F.; Hamley, I. W.; Rambo, R. P.; Reza, M.; Ruokolainen, J.; Skoulas, D.; Iatrou, H. Self-Assembly of Telechelic Tyrosine End-Capped PEO Star Polymers in Aqueous Solution. *Biomacromolecules* **2018**, *19* (1), 167–177.

(44) Hamley, I. W.; Cheng, G.; Castelletto, V. A Thermoresponsive Hydrogel Based on Telechelic PEG End-Capped with Hydrophobic Dipeptides. *Macromol. Biosci.* **2011**, *11* (8), 1068–1078.

(45) Barth, A. Infrared Spectroscopy of Proteins. *Biochim. Biophys. Acta* **2007**, *1767* (9), 1073–1101.

(46) Barth, A.; Zscherp, C. What Vibrations Tell Us about Proteins. *Q. Rev. Biophys.* **2002**, *35* (4), 369–430.

(47) Breßler, I.; Kohlbrecher, J.; Thünemann, A. F. *SASfit* : A Tool for Small-Angle Scattering Data Analysis Using a Library of Analytical Expressions. *J. Appl. Crystallogr.* **2015**, *48* (5), 1587–1598.

(48) Hirst, J. D.; Colella, K.; Gilbert, A. T. B. Electronic Circular Dichroism of Proteins from First-Principles Calculations. *J. Phys. Chem. B* **2003**, *107* (42), 11813–11819.

(49) Woody, R. W. Circular Dichroism Spectrum of Peptides in the Poly (Pro) II Conformation. *J. Am. Chem. Soc.* **2009**, *131* (23), 8234–8245.

(50) Falla, T. J.; Nedra Karunaratne, D.; Hancock, R. E. W. Mode of Action of the Antimicrobial Peptide Indolicidin. *J. Biol. Chem.* **1996**, *271* (31), 19298–203.

(51) Rambo, R. P. Http://Www.Bioisis.Net/.

Chapter 6

Conclusions and Future Work

6.1 Conclusions

This thesis extensively examines the self-assembling behaviour, membrane interactions and biological activity of different peptides for therapeutic use including antimicrobials, enzyme responsive materials and peptide hormones.

Chapter 2 focuses on the self-assembly and bioactivity of arginine and alanine rich surfactant like peptides (SLP's) and bola-amphiphiles, with constructs A_nR and RA_nR. Bola-amphiphiles with longer alanine chains were shown to have greater aggregation propensity, where RA_3R and RA_6R do not self-assemble into regular structures, whereas RA_9R and $RA_{12}R$ assembled into fibres, and form hydrogels at concentrations at or above 5 wt%. The SLPs self-assembled to form fibres. The cytocompatibility of the bola-amphiphiles did not depend on molecular weight, and can be classified in order of most toxic to least: RA_9R, RA_3R, $RA_{12}R$ and RA_6R, where RA_6R is the most tolerated. The SLPs were generally more cytocompatibile, with all the SLPs having IC_{50} concentrations above 0.5 wt%, apart from $A_{12}R_2$. These peptides were screened against several strains of bacteria at concentrations below the IC_{50}, and displayed strong activity against *P.aeruginosa*. Interactions with lipid membrane models based on DPPG/DPPE examined through DSC, SAXS and Cryo-TEM showed evidence of peptide de-mixing and ordering of bilayers, which was assumed to be the origin of their antimicrobial properties.

Chapter 3 focuses on the self-assembling behaviour of two symmetrical short peptides, rich in arginine and phenylalanine. These peptides, R_3F_3 and R_4F_4, have disordered secondary structure with SAXS measurements revealing monomers. TEM shows the occasional large aggregated structure of long tapes for R_3F_3 and sheets for R_4F_4. These peptides were screened with several strains of bacteria at cytocompatible concentrations and displayed selective activity to the *Pseudomonas* species. R_4F_4 was particularly active, displaying activity against a range of plant *Pseudomonas* as well as clinically relevant *Pseudomonas aeruginosa*. Peptide interaction with lipid membranes revealed reordering of lipid DPPG/DPPE membrane models. Interesting R_4F_4 completely disrupted the formation of DPPG/DPPE liposomes, when the PG/PE ratio was most similar to the *P.aeruginosa* membrane composition. Finally, the effect of R_3F_3 and R_4F_4 on biofilm formation of *P.aeruginosa* was measured using a crystal violet assay. The peptide R_4F_4 was found to reduce biofilm formation by 70%. Both peptides showed interactions with c-di-GMP, visualised through TEM and SAXS. Attempts to indirectly measure c-di-GMP in bacteria using Congo red stain showed flocculation of the bacteria. The RNFN peptides showed interesting antimicrobial properties.

Chapter 4 focuses on the self-assembly of telechelic PEO-star conjugates functionalised with tyrosine. These conjugates showed changes in self-assembly upon pH adjustment. The [poly(L-tyrosine$_{4\text{-}5}$)-*b*-(PEO 2.5k)]$_4$ conjugate showed clustered structures at native pH, and disrupted self-assembly visualised through cryo-TEM at pH 12. The larger conjugate, [poly(L-tyrosine$_{3\text{-}4}$)-*b*-(PEO 5k)]$_4$ showed changes in self-assembly, from fibril worm-like globules, to long straight fibres and small globules. The self-assembly of these branched conjugates were polydisperse, which may be due to the star architecture. These conjugates were found to be cytocompatible at sufficiently high concentration.

Finally, Chapter 5 focuses on the self-assembly of peptide hormones oxytocin, analogue Carbetocin and lipidated oxytocin (LOT-1). Oxytocin in aqueous solution had conflicting results. SAXS measurements showed monomers at 1 wt% Oxytocin at native pH and pH 12. However, cryo-TEM and TEM, revealed vesicle formation at native pH and fibril formation at pH 12. This may be due to Oxytocin being heat sensitive, which may also mean it is radiation sensitive. At 2 wt% pH 12, oxytocin forms a β-sheet hydrogel, visualised by SAXS, TEM, cryo-SEM which is birefringent. Carbetocin had a very weak aggregation, at native pH and pH 12, consistently displayed by cryo-TEM, SAXS and TEM. At 2 wt% peptide solution, the peptide formed large birefringent crystalline structures. LOT-1 was insoluble in water, due to increased hydrophobicity of the lipid chain, thus LOT-1 and Oxytocin were studied in ethanol. LOT-1 formed irregular clusters of fibrils, visualised by cryo-TEM and SAXS. Oxytocin in ethanol formed poly-proline II helical secondary structure and assembled into fibrils.

The work carried out in this thesis has demonstrated the capabilities of peptides for a range of therapeutic applications. The results demonstrate the promise of small synthetic oligopeptides for antimicrobial applications, the properties of telechelic star polymers for enzyme responsive material development, and the characterisation of peptide hormone oxytocin and analogues, which contributes to the understanding of enhancing stability in the future.

6.2. Future work

Considering the antimicrobial peptides discussed in chapters 2 and 3, with structures RA_NR, A_NR, and F_NR_N, future work should focus firstly understanding in greater detail the mechanism of action, and secondly improving constructs to enhance activity. To understand further the mechanism of interactions, SEM and TEM could be undertaken on bacteria to see visually whether there are any changes to the bacterial membrane at a range of concentrations below the MIC concentration. This could give information on whether the peptide is membrane disruptive or whether it interacts with downstream intracellular targets. A further method to be considered is to fluorescently label the peptide and use a technique such as confocal microscopy to trace the peptide's movement within the cell. Further to this, to explore the effect on peptides on gene expression (if the peptides do interact with intracellular targets), techniques like bioarray or qPCR could be used to examine whether the peptides lead to up or down regulation of specific genes. This could provide us with further useful information on interactions between peptides and intracellular targets. This may then lead to informed modification of the sequence, increasing the specificity of the peptides to any targets.

A factor that was noticeable during the antimicrobial screening was that the peptides reduced the CFU of the bacteria within the first 2 hours of exposure. A method to track whether the peptide has been degraded by the bacteria within this time could be mass spec analysis, or NMR if a part-deuterium labelled version of the peptide was used. Further to this, the peptides could then be modified with D-amino acids, lipids or PEG chains to improve stability. Particularly for R_4F_4, the strongest AMP examined, assaying R_5F_5, or changing the sequence to examine the effects of alternating [RF] units or bola-amphiphile like units (RF_NR) have on antimicrobial activity and cell viability could prove to beneficial for therapeutic development. Additionally, incorporating other amino acid residues which are important to antimicrobial activity, such as K, W, C, H, or P, could be of interest to see whether this creates a broader range of activity.

Moreover, examining the peptides in a more physiologically relevant buffers such as PBS, and screening them against different cell lines including blood platelet cell lines, could be important in determining their suitability as a proposed candidate for clinical use.

Considering the tyrosine functionalised telechelic PEO-star conjugates, increasing the number of arms may be of interest, with potential to function as a more dendrimer like material could be interesting for applications as a delivery vehicle. Moreover, examining whether tyrosine kinases phosphorylates the conjugate and if these conjugates could have anticancer applications could be of interest, as many tyrosine kinases are upregulated in many types of cancer. It is possible that cancer cell lines with high tyrosine kinase activity may be affected by this conjugate.

Finally, in the instance of peptide hormone oxytocin, more analytical methods to resolve the self-assembly, such as AFM, could be used. Although the hydrogel forms at pH 12, it would be interesting to see whether this could be ‘seeded’ into a solution at a physiological pH to establish whether this could promote fibre formation. This may be of interest as self-assembled oxytocin may be more stable than monomeric oxytocin and may assist with delivery.

7. Appendix

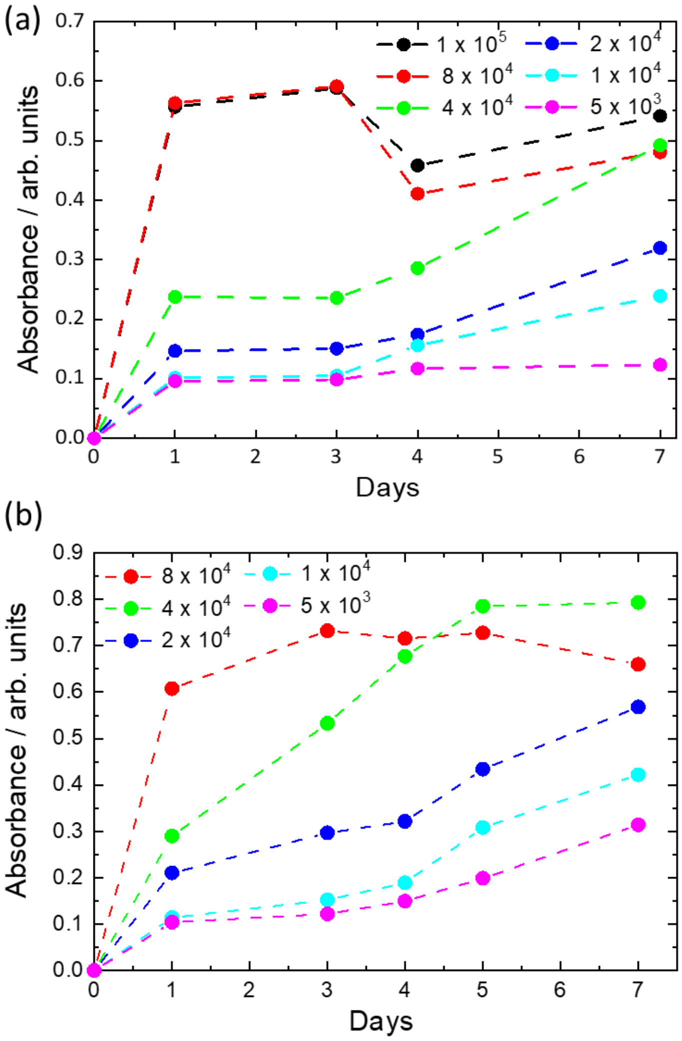

Figure A1. *Seeding density of a) 161BR cells and b) HDFa cells. The seeding density selected for assays based on this was 4 x* 10^4 *for both cell lines.*

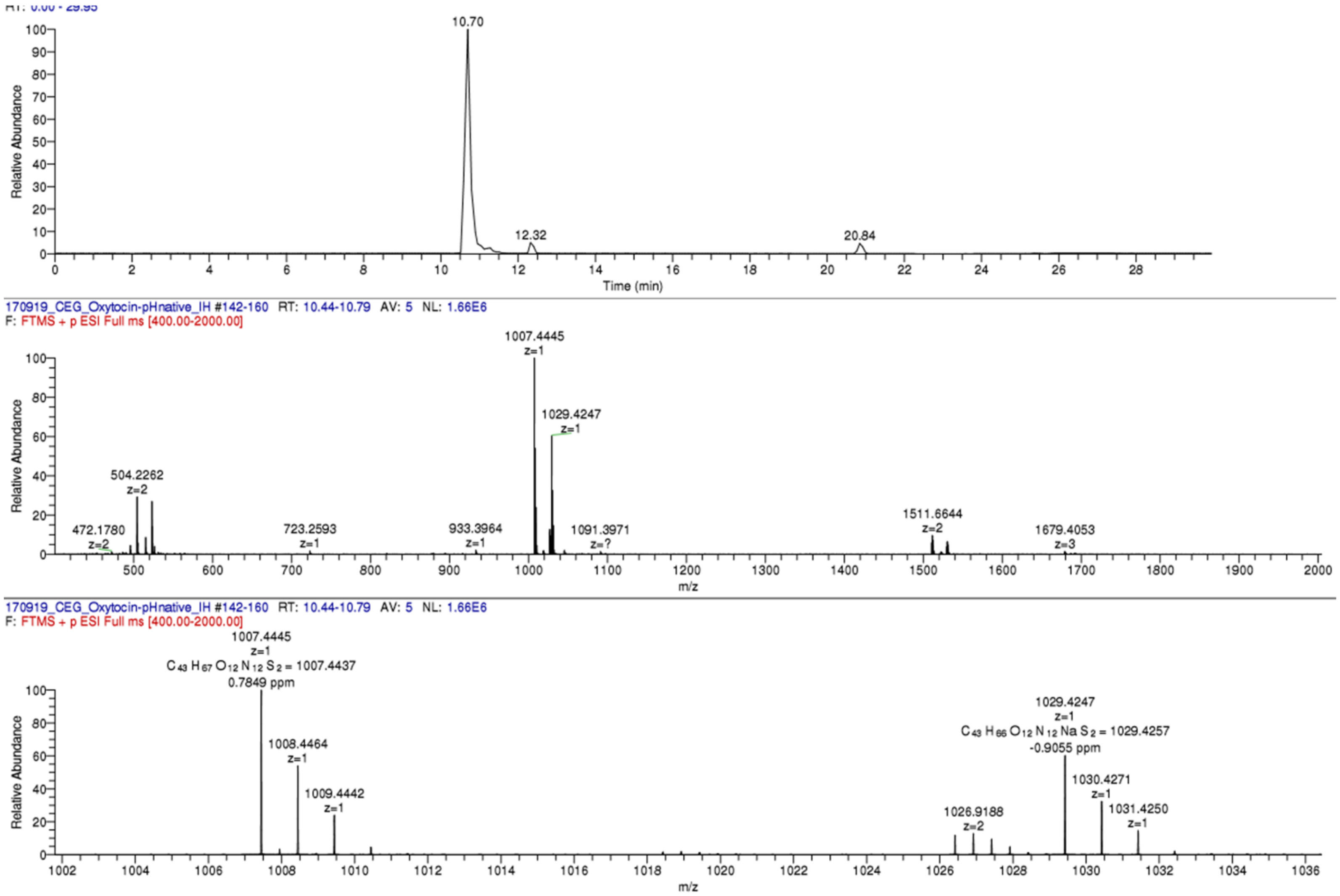

Figure A2. *Mass Specta of Oxytocin, pH native, 0.01 wt%.*

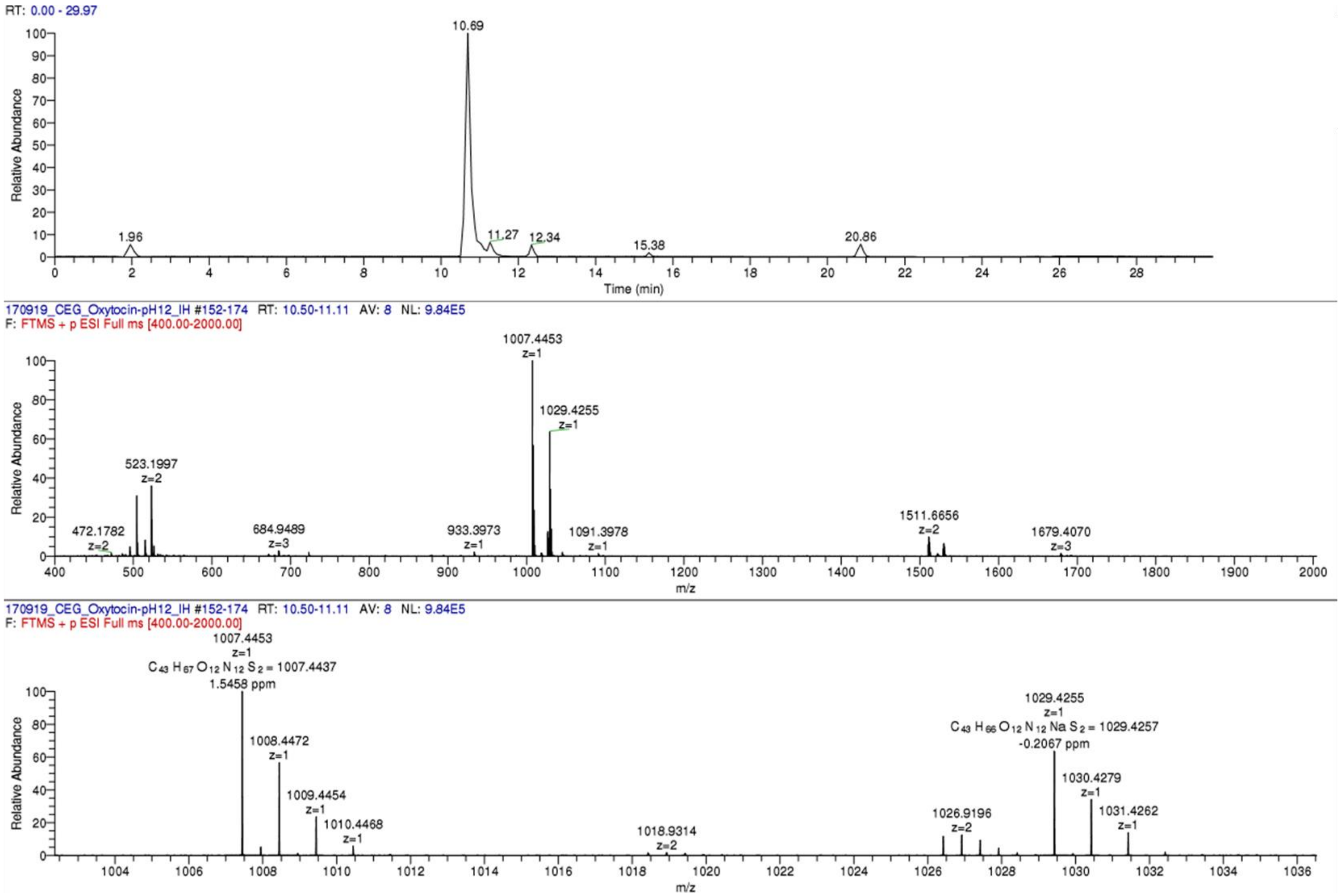

Figure A3. *Mass Specta of Oxytocin, pH 12, 0.01 wt%.*

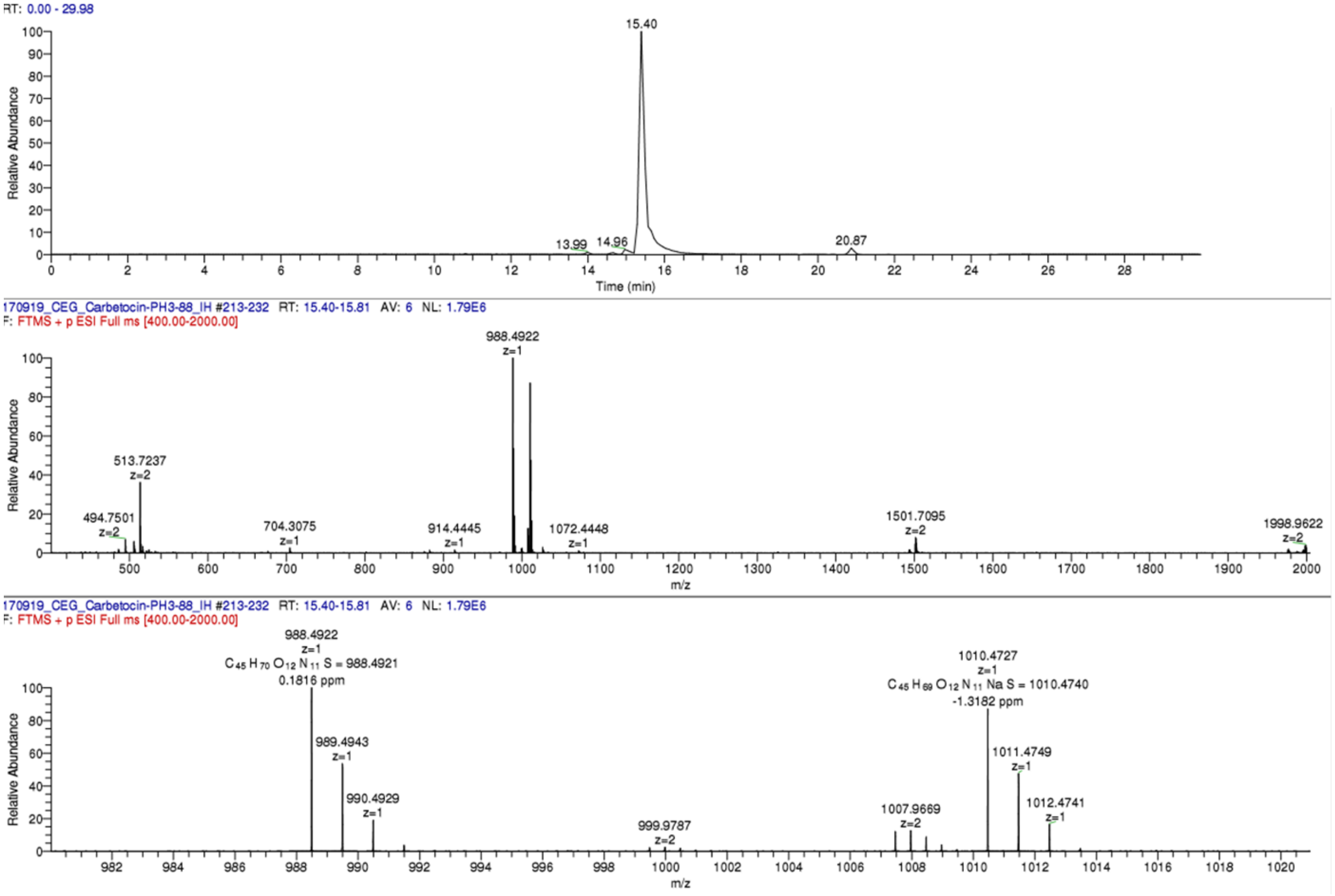

Figure A4. *Mass Specta of Carbetocin, pH native, 0.01 wt%.*

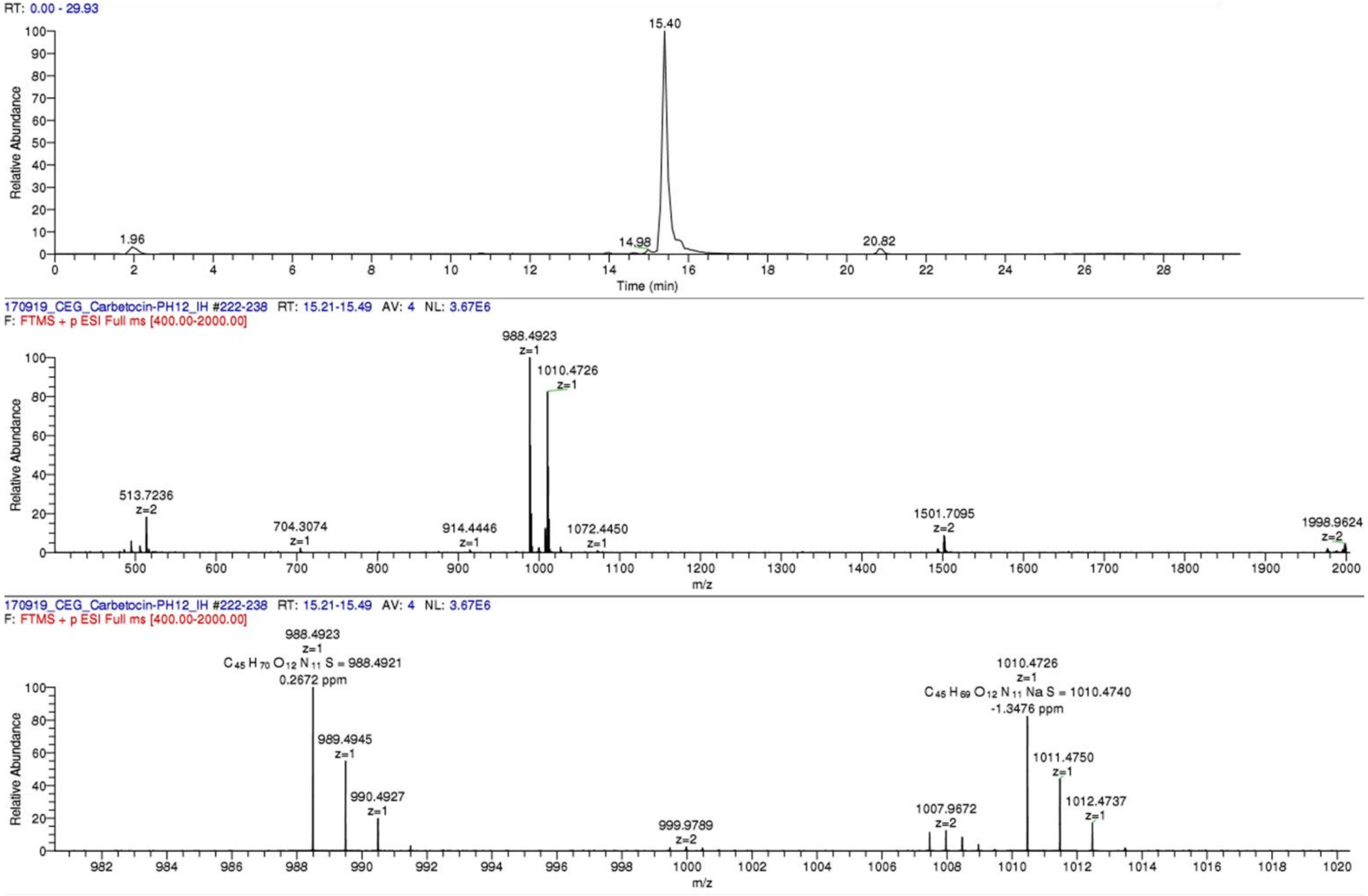

Figure A5. *Mass Specta of Carbetocin, pH 12, 0.01 wt%.*